technische universität dortmund

JÜLICH Forschungszentrum

Nanowire Transistor Structures for Advanced Biosensing

Vorgelegt in der Fakultät Physik der Technische Universität Dortmund zur Erlangung des akademischen Grades eines Doktors der Naturwissenschaften

von

Master of Science

Ihor Zadorozhnyi

aus Chemerivtsi
Khmelnytskyi Region, Ukraine

Dedicated to
my beloved mother, father,
and all my family

Table of Contents

Table of Contents **5**

Abstract **7**

Zusammenfassung **9**

Acknowledgements **13**

1 Introduction **15**

2 Fundamentals and Theory **19**

2.1 Biosensor Detection Principles 19

2.1.1 Label-Based Detection Technique 19

2.1.2 Label-Free Detection Technique 20

2.1.3 Biomarkers of Cardiovascular Disease 21

2.1.4 Biosensors Based on Field-Effect Transistors 22

2.2 Field-Effect Transistor 24

2.3 Electrical Double-Layer 28

2.4 Electrophysiology of Cells 30

2.4.1 The Action Potential 32

2.4.2 Cellular Communication 33

2.4.3 Extracellular Recordings 33

2.5 Noise Fundamentals 37

2.5.1 Thermal Noise 38

2.5.2 Dielectric-Polarization Noise 39

2.5.3 Shot Noise 39

2.5.4 Flicker Noise 40

2.5.5 Generation-Recombination Noise 44

2.5.6 Random Telegraph Signal Noise 44

2.5.7 Analysis of Noise Components 46

3 Materials, Methods, and Setup Development **47**

3.1 Current - Voltage (I-V) Characterization of FETs 47

3.2 Noise Spectroscopy 50

3.3 Multichannel BioMAS Setup 55

3.4 Surface Modification for Troponin Detection 57

3.5 Cell Culture and Imaging 58

3.5.1 Cardiomyocyte Cell Culture 58

3.5.2 Fluorescent Imaging of Cardiomyocytes 58

3.6 Summary 59

4 Transport Phenomena in Silicon Nanostructures **61**

4.1 Design of Nanostructures 61

4.2 Optimization of Fabrication Technology 63

4.3 Chip Encapsulation 73

4.3.1 Reservoir for Cell Culture 73

4.3.2 Microfluidic for Biomarker Detection 74

4.4 Silicon Nanowire Devices Characterization 75

4.5 Gate Coupling Effect(GCE) for Advanced FET Properties 78

4.5.1 GCE in Si NW Array FETs . . . 79
4.5.2 GCE in Single Si NW FETs . . . 84
4.5.3 TCAD Simulation and Analysis of GCE . . . 85
4.6 Noise Spectroscopy of NW FETs . . . 87
4.7 Single Trap Phenomena for Development of Nanowire Sensor . . . 94
4.7.1 Enhanced Capture Kinetics Behavior . . . 95
4.7.2 Understanding the Coulomb Blockade Energy . . . 101
4.7.3 Impact of Gamma Radiation on Single Trap Parameters . . . 106
4.7.4 Simulation of RTS Noise for Sensor Optimization . . . 112
4.8 Summary . . . 118

5 Space-Charge Phenomena in GaN Nanostructures for Biosensing . . . 121
5.1 Space-Charge Phenomena in GaN Nanowires . . . 121
5.2 Patterning of AlGaN/GaN Nanoribbons . . . 122
5.3 Depletion Effects in Low-Voltage Regime . . . 125
5.3.1 Current–Voltage Characteristics of GaN NR Structures . . . 125
5.3.2 Electronic Edge-State Phenomena . . . 126
5.4 Space-Charge Phenomena in Long GaN Nanoribbons . . . 131
5.5 Noise Spectroscopy of GaN Nanoribbons . . . 133
5.6 Summary . . . 135

6 Silicon Nanostructures Toward the Development of Biosensors . . . 137
6.1 pH Sensitivity . . . 137
6.1.1 Effect of the Channel Length on pH Sensitivity . . . 139
6.1.2 Simulation of pH Biosensor . . . 141
6.2 Single Trap Phenomena for Enhanced Biosensing . . . 142
6.3 Cardiac Troponin Detection . . . 144
6.3.1 Sensor Reusability . . . 146
6.3.2 Noise Spectroscopy for Biomolecular Detection . . . 147
6.4 Nanostructures for the Detection of Ascorbate and Gluthathione Solutions 151
6.5 Silicon NW FET Structures for Analysis of Cellular Activity . . . 152
6.5.1 Chip Characterization for Cellular Measurements . . . 154
6.5.2 In Vitro HL-1 Cell Measurement . . . 156
6.5.3 Combination of Electrical Monitoring with Fluorescent Microscopy 160
6.6 Neuronal Interfacing . . . 162
6.7 Summary . . . 164

7 Conclusions and Outlook . . . 165

Appendix A Silicon Nanowire Fabrication Protocol . . . 170

Appendix B Silicon Nanowire Description . . . 175

Appendix C Software Development . . . 178

List of Abbreviations . . . 179

References . . . 180

Personal Publication List . . . 196

Abstract

Modern bioelectronics addresses challenges for the development of tools capable of ultimate detection at down to single molecule level and recording of extremely small signals from electrogenic cells like cardiac cells and neurons at the subcellular level. With the achievements of nanotechnology liquid-gated silicon nanowires emerged as a basis for the development of reliable, high-speed and highly sensitive biosensors. In spite of conventional field-effect transistors (FETs), liquid-gated silicon nanowires have the potential for single charge detection and demonstrate improved electrical coupling with living cells. Among the major challenges, the achievement of stable long-term operation in a liquid environment with abilities to recover small signals have still to be addressed. In this work, we designed and fabricated silicon nanostructures, including single nanowires, nanowire arrays, and nanoribbons, and studied their transport properties using noise spectroscopy. We focused on the ways to achieve enhanced signal-to-noise ratio (SNR) and novel approaches for the detection of signals from biological objects.

An optimized approach for the nanowire patterning has been developed to reduce leakage currents in the liquid-gated configuration. To apply different concentrations of target analytes the microfluidic system with on-chip reference electrode has been developed. Fabricated nanowires demonstrate good scaling abilities with the subthreshold swing of 160 mV/dec for $p^+ - p - p^+$ and 250 mV/dec for $n^+ - p - n^+$ structures, indicating on a good quality of liquid-gated FETs. Transistors operate under a relatively low threshold voltage of around 1.5 V.

Silicon nanostructures were fabricated on the basis of silicon-on-insulator (SOI) wafers enabling the utilization of both liquid and back gates. We reveal the possibility of gate-coupling effect utilization for up to 100% enhanced signal-to-noise ratio for comparable with neuronal signals. The results are in good agreement with simulations performed in technology computer-aided design (TCAD) software.

The comprehensive studies of noise properties demonstrate that in $p^+ - p - p^+$ structures it is mainly caused by the mobility fluctuations while in $n^+ - p - n^+$ structures the interaction with traps in gate dielectric plays a dominant role. Furthermore, the input-referred noise of fabricated devices was around $1 \times 10^{-7}\,V^2$ at 10 Hz for nanowires with gate area larger than $0.03\,\mu m^2$ and increased with area decrease following the general law observed in different nanostructures. From calculated charge noise dependencies, nanowires with gate area less than $0.1\,\mu m^2$ demonstrate the ability to detect single charges. It should be emphasized that with scaling nanowires down, a single trap phenomenon was registered as a strong modulation of channel current. Extracted time characteristics of two-level fluctuations demonstrate enhanced capture time dependencies on the current with unusual for the standard Shockley-Read-Hall (SRH) model slopes in the range from (-1) to (-14), indicating enhanced sensitivity to surface potential change. Due to the strong dependence of capture time on the surface potential change single trap phenomena was considered for enhanced biosensing applications. Coulomb blockade energy was considered

to explain the enhanced capture time behavior. To control the trap dynamics parameters, gamma irradiation was used. At the same conditions, capture time decreased from 5 ms to 0.1 ms, which can be considered for tuning the speed of the detection process. We developed a model for the simulation of single trap behavior and suggested a new approach for understandnding random telegraph signal (RTS) fluctuations as a useful signal. Since the response time of a biosensor is a critical parameter, we estimate that 10 sec is the lower limit for the recording of useful RTS signal.

Along with established silicon-based technologies, a wide bandgap GaN becomes a promising material for biosensing applications. We studied the transport and noise properties of planar GaN nanoribbons and revealed the space-charge phenomena. Due to the spatial separation of charge carriers, electric fields are generated outside the nanoribbon. The feature turns out to be beneficial for biosensing applications as it changes the dynamics of the molecular diffusion towards the surface.

Fabricated silicon nanostructures were employed in biosensing experiments. The response to changes of solution pH reached up to 59.5 mV/pH (Nernst limit) with increasing area sensing area. The response around the Nernst limit was obtained from the TCAD simulation using the developed model of an ideal liquid-gated silicon nanowire. The model can be further used for simulations of biosensors based on liquid-gated silicon nanowires. While the pH response is limited by Nernst limit, a single trap phenomenon was employed to achieve an enhanced response from capture time as a sensitive parameter. The slope of capture time was 10 times larger than for current change, which is promising for biosensing applications.

Silicon nanowires were used for the detection of troponin molecules, a biomarker specific to acute myocardial infacrction. The lowest detected concentration was as low as 20 pM. Furthermore, reusability of troponin biosensor was shown by applying glycine-HCl buffer. The features observed in the noise behavior was explained as a formation of the membrane on the surface of the biosensor which allows the penetration for only specific ions.

The recording of extracellular action potentials (APs) from cardiac cells is important for fundamental studies of AP propagation features reflecting cellular activity and the influence of pharmacological substances on the signal. We applied a novel approach of using fabricated Si nanowire (NW) FETs in combination with fluorescent marker techniques to evaluate the functional activity of cardiac cells. High-quality AP signal recordings from HL-1 cardiomyocytes were demonstrated. The propagation of APs across the confluent cellular layer with the speed of around 10-13 mm/sec was shown using spacialy distributed Si NW FETs. This method was supplemented by studies of the pharmacological effects of stimulations using noradrenaline (NorA) as a modulator of functional activity on a cellular and subcellular level, which were also tested using fluorescent marker techniques. The addition of NorA resulted in the increase of beating frequency in cardiomyocyte cellular community. The role of calcium alteration and membrane potential were revealed and analyzed using fluorescent microscopy. The results open prospects for the application of fabricated Si NW FET sensors as a tool for the recording of cellular network activity, interfacing with living systems, and analysis of pharmacological agent influence on cells.

Zusammenfassung

Die moderne Bioelektronik stellt sich den Herausforderungen bei der Entwicklung von Werkzeugen, die eine Detektion auf Einzelmolekülebene und die Erfassung extrem kleiner Signale von elektrogenen Zellen wie Herzzellen und Neuronen auf subzellulärer Ebene ermöglichen. Mit den Errungenschaften der Nanotechnologie sind Silizium-Nanodrähte als Grundlage für die Entwicklung zuverlässiger, schneller und hochempfindlicher Biosensoren entstanden. Trotz herkömmlicher Feldeffekttransistoren (FETs) haben flüssiggesteuerte Silizium-Nanodrähte das Potenzial zur Einzelaufladung und zeigen eine verbesserte elektrische Kopplung mit lebenden Zellen. Zu den großen Herausforderungen gehört die Erreichung eines stabilen Langzeitbetriebs in einer flüssigen Umgebung mit der Fähigkeit, kleine Signale detektieren zu können. In dieser Arbeit wurden Silizium-Nanostrukturen entworfen und hergestellt, darunter einzelne Nanodrähte, Nanodraht-Arrays und Nanoribbons, und ihre Transporteigenschaften mittels Rauschspektroskopie untersucht. Hauptentwicklungsziele waren insbesondere die Verbesserung des Signal-Rausch-Verhältnis, und neue Methodiken für die Erkennung von biologischen Signalen.

Ein optimierter Ansatz für die Nanodrahtstrukturierung wurde entwickelt, um Leckströme in der flüssigkeitsgesteuerten Konfiguration zu reduzieren. Um verschiedene Konzentrationen von Analyten zu messen, wurde ein Mikrofluidiksystem mit On-Chip-Referenzelektrode entwickelt. Gefertigte Nanodrähte zeigen gute Skalierungsfähigkeiten mit dem Ladungsträgermobilität von 160 mV/dec für $p^+ - p - p^+$ und 250 mV/dec für $n^+ - p - n^+$ Strukturen, was auf eine gute Qualität flüssigkeitsgesteuerter FETs hinweist. Transistoren arbeiten mit einer relativ niedrigen Schwellenspannung von etwa 1.5 V. Die Silizium-Nanostrukturen wurden auf der Basis von Silicon-on-Insulator(SOI)-Wafern hergestellt, die die Verwendung von Front- und Backgates ermöglichen, wobei das Frontgate vom Elektrolyt gesteuert wird. Wir zeigen die Möglichkeit der Nutzung des Gate-Coupling-Effekts für ein bis zu 100% verbessertes Signal-Rausch-Verhältnis, für vergleichbar mit neuronalen Signalen. Die Ergebnisse stimmen gut mit Simulationen überein, die mit Hilfe von TCAD-Software (Technology Computer-Aided Design) durchgeführt werden.

Die umfassenden Untersuchungen der Rauscheigenschaften zeigen, dass in $p^+ - p - p^+$ Strukturen hauptsächlich durch die Mobilitätsschwankungen verursacht werden, während in $n^+ - p - n^+$ Strukturen die Wechselwirkung mit Traps in Gate-Dielektrikum eine dominante Rolle spielt. Darüber hinaus betrug das eingangsbezogene Rauschen der Transistoren etwa $1 \times 10^{-7}\,\mathrm{V}^2$ bei 10 Hz für Nanodrähte mit einer Gate-Fläche größer als $0.03\,\mu\mathrm{m}^2$ und erhöhte sich mit abnehmender Fläche gemäß dem allgemeinen Gesetz, das in verschiedenen Nanostrukturen beobachtet wurde. Aus berechneten Ladungsrauschabhängigkeiten zeigen Nanodrähte mit einer Gate-Fläche von weniger als $0.1\,\mu\mathrm{m}^2$ die Fähigkeit, einzelne Ladungen zu erkennen. Es ist hervorzuheben, dass mit der Verkleinerung von Nanodrähten ein einzelnes Trap-Phänomen als starke Modulation des Kanalstroms registriert wurde. Extrahierte Zeitmerkmale von zweistufigen Schwankungen zeigen eine verbesserte Abhängigkeit der Erfassungszeit vom Strom, wobei die für das Standard-Shockley-

Read-Hall (SRH)-Modell ungewöhnlichen Steigungen im Bereich von (-1) bis (-14) eine erhöhte Empfindlichkeit gegenüber Oberflächenpotentialänderungen anzeigen. Aufgrund der starken Abhängigkeit der Erfassungszeit von der Oberflächenpotentialänderung wurden Single Trap Phänomene für erweiterte Biosensorik-Anwendungen berücksichtigt. Die Coulomb-Blockadenergie wurde als Erklärung für das verbesserte Erfassungszeitverhalten betrachtet. Um die Dynamikparameter der Traps zu kontrollieren, wurde Gammabestrahlung verwendet. Unter den gleichen Bedingungen verringerte sich die Erfassungszeit von 5 ms auf 0.1 ms, was für die Abstimmung der Geschwindigkeit des Erfassungsprozesses berücksichtigt werden kann. Darauf aufbauend wurde ein Modell für die Simulation des Single Trap-Verhaltens entwickelt und einen neuen Ansatz vorgeschlagen, um Schwankungen des Random Telegraph Signal (RTS) als informationstragendes Signal zu verstehen. Da die Ansprechzeit eines Biosensors ein kritischer Parameter ist, schätzen wir, dass 10 sec die untere Grenze für die Aufzeichnung des nützlichen RTS-Signals ist.

Neben etablierten siliziumbasierten Technologien wird GaN, welches über eine großes Bandlücke verfügt zu einem vielversprechenden Material für Biosensorik-Anwendungen. Wir untersuchten die Transport- und Rauscheigenschaften planarer GaN-Nanoribbon und zeigten die Raumladungsphänomene. Durch die räumliche Trennung der Ladungsträger werden außerhalb des Nanoribbons elektrische Felder erzeugt. Die Funktion erweist sich als vorteilhaft für Biosensor-Anwendungen, da sie die Dynamik der molekularen Diffusion zur Oberfläche verändert.

Die fabrizierten Silizium-Nanostrukturen wurden in Biosensorik-Experimenten eingesetzt. Die Reaktion auf Änderungen des pH-Wertes erreichte bis zu 59,5 mV/pH (Nernst-Grenze) bei zunehmender Fläche. Das Resultat um die Nernst-Grenze wurde aus der TCAD-Simulation mit dem entwickelten Modell eines idealen flüssiggesteuerten Silizium-Nanodrahtes gewonnen. Das Modell kann für die Simulation von Biosensoren auf Basis von flüssiggesteuerten Silizium-Nanodrähten weiterverwendet werden. Während die pH-Reaktion durch den Nernst-Grenzwert begrenzt ist, wurde ein Single Trap Phänomen eingesetzt, um eine verbesserte Reaktion der Erfassungszeit als empfindlicher Parameter zu erreichen. Die Steigung der Erfassungszeit war 10 mal größer als bei der Stromänderung, was für Biosensorik-Anwendungen vielversprechend ist.

Silizium-Nanodrähte wurden für den Nachweis von Troponinmolekülen verwendet, einem Biomarker, der speziell für den akuten Myokardinfarkt entwickelt wurde. Die niedrigste nachgewiesene Konzentration lag bei nur 20 pM. Darüber hinaus wurde die Wiederverwendbarkeit des Troponin-Biosensors durch den Einsatz von Glycin-HCl-Puffer nachgewiesen. Die im Rauschverhalten beobachteten Merkmale wurden als eine Bildung der Membran auf der Oberfläche des Biosensors erklärt, die die Ionen-selektive Permabilität begründet.

Die Erfassung von extrazellulären Aktionspotentialen (APs) aus Herzzellen ist wichtig für grundlegende Untersuchungen von AP-Ausbreitungsmerkmalen, die die Zellaktivität und den Einfluss pharmakologischer Substanzen auf das Signal widerspiegeln. Wir haben einen neuartigen Ansatz zur Verwendung von fabrizierten Si Nanowire (NW)-FETs in Kombination mit Fluoreszenzmarker-Techniken angewandt, um die funktionelle Aktivität von Herzzellen zu bewerten. Es wurden Rauscharm AP-Signalaufzeichnungen von HL-1-Kardiomyozyten nachgewiesen. Die Ausbreitung von APs über die konfluente Zellschicht mit einer Geschwindigkeit von etwa 10-13 mm/sec wurde mit Hilfe von räumlich verteilten Si-NW-FETs gezeigt. Diese Methode wurde durch Studien über die pharmakologischen Effekte von Stimulationen mit Noradrenalin (NorA) als Modulator der funktionellen Aktivität auf zellulärer und subzellulärer Ebene ergänzt, die ebenfalls mit Fluoreszenzmarker-

Techniken getestet wurden. Die Zugabe von NorA führte zu einer Erhöhung der Schlagfrequenz in der Zellgemeinschaft der Kardiomyozyten. Die Rolle der Kalziumveränderung und des Membranpotentials wurde aufgedeckt und mit Hilfe der Fluoreszenzmikroskopie analysiert. Die Ergebnisse eröffnen Perspektiven für die Anwendung von gefertigten Si-NW-FET-Sensoren als Plattform für die Erfassung der Aktivität von zellulären Netzwerken, die Kopplung mit lebenden Systemen und die Analyse des Einflusses pharmakologischer Wirkstoffe auf Zellen.

Acknowledgements

During the time of my PhD thesis work I faced dozens of obstacles and here I would like to express my gratitude to the people, who were always helping me to fight the challenges, encoraging and supporting me.

I would like to thank my supervisor **Prof. Dr. Svetlana Vitusevich** for being a guiding star along my PhD life in Forschungszentrum Jülich. Your endless positive energy and optimistic attitude never allowed to give up, but only encouraged for progressive motion towards the scientific achievements. Thank you for all possibilities and collaborations you organized to enrich my scientific skills. Thank you for being ready to help anytime.

I would like to thank **Prof. Dr. Andreas Offenhäusser**, for the possibility to perform my PhD work at the Institute of Complex Systems (ICS-8), Forschungszentrum Jülich. Thank you for your friendly attitude and warm atmosphere in the institute. It was a pleasure for me to discuss results with you and obtain valuable advises. Thank you for organizing amazing summer and winter schools, workshops and retreats, for the great time spent there.

I thank my second supervisor **Prof. Dr. Manfred Bayer** for reviewing my thesis as well as for his support, and contribution.

Dr. Mykhaylo Petrychuk, I enjoyed each period of your stay in Forschungszentrum Jülich. Thank you for sharing your knowledge and experience in the lab as well as in the theoretical aspects of our research. All discussions with you were extremely valuable to gain my scientific skills.

I highly appreciate the collaboration with **Dr. Nicolas Clement**. You made a huge contribution into my scientific development.

I would like to thank my colleagues **Dr. Sergii Pud**, **Dr. Dmitry Kireev**, **Dr. Nataliia Naumova**, **Dr. Viktor Sydoruk**, **Jan Schnitker**, **Dr. Volodymyr Piatnytsia** for valuable discussions and sharing with me their experince, for their genius ideas and collaboration on interesting projects. It was a great pleasure to learn from you.

I highly appreciate the scientific input from **Maristella Coppola**, **Irina Tihaa**, **Fabian Brings**, **Mykola Fomin**, **Pegah Shokoohimehr**, **Frano Milos**. Thank you for valuable discussions, and work together on the interesting projects.

Especially I would like to express my gratitude to one of my best friends and my colleague **Volodymyr Handziuk**. I was lucky enough to work on my PhD thesis in the same place and at the same time. Thank you for your valuable contributions and endless support, encouragement and patience.

I thank my friends and colleagues **Hanna Hlukhova** and **Yurii Kutovyi** for their support and being ready to help anytime, and also for the fun part.

I would like to thank **Nazarii Boichuk**, **Dr. Jie Li**, **Nataliia Piechniakova**, **Rasel Ferdaus**, and all members of our **Electronic Sensing** group for the fruitful cooperation and nice time working together.

I also thank **all the members** of our institute for their input, valuable discussions

and help.

Especially I thank the Helmholtz Nano Facility(HNF) **cleanroom team** for their help and support. Without you this thesis would have been much shorter.

I thank the **electronic workshop** for their help with development and implementation of our devices, and **IT department** for solving endless software- and hardware-related issues.

Of course, I would like to thank **my parents**, **all my family**, and **friends** for their endless support, encouragement, understanding, and warm attitude. Thank you for keeping me optimistic even at my most desperate moments.

Chapter 1

Introduction

Biosensing has been rapidly evolving over the last decades and became a highly developed field of research with a great potential for applications in the life sciences and health care.

Recent trends in medicine demonstrate a transition towards personalized services. Such way declares the individual approach to each patient and disease treatment based on person's unique biomarker profile in order to reduce the risk of disease aggravation at early stages.

Therefore, scientific community is focused on the development of compact point-of-care devices, allowing the doctor to constantly monitor the patient's condition. The core component of the product should be a reliable, stable, and highly sensitive biosensor, enabling to permanently track the changes of physiological parameters of the human body. For example, when myocardial infarction occurs, the troponin molecules are released into the blood indicating on the cardiac dysfunction. To prevent the heart attack and to save the patient's life, such biosensing systems should detect the disease markers at the smallest concentration level possible. For the precise determination of this markers, the high-cost equipment, trained personal, and long sample preparation time are usually required. Till now, a variety of studies have been performed in order to develop the highly sensitive sensors to be available in the markets worldwide. There are, however, only a few biosensing techniques, including optical-based techniques, such as enzyme-linked immunosorbent assay (ELISA), which have been successfully introduced to the market. The major drawbacks of such systems are the bulky equipment and, what is more important, the inevitable requirement for the biomarker labelling, which significantly affects the effectiveness and response time of such type of sensors.

Meanwhile, the modern bioelectronics challenges existing tools for the investigation of living systems and organisms to understand biochemical reactions and internal communication patterns, which define their behavior. The task is very complex and requires to study much more simple objects first. Electrogenic cells play a crucial role in the functional activity of main human organs - brain and heart. Generated by the cells extracellular potential changes are extremely small, which makes their recording very challenging. The investigation of cellular functional activity allows to find patterns which enable to distinguish between normal and anomalous behavior, opening prospects for prediction, and prevention of possible disease development. Novel biosensors are already capable of such signal monitoring, however still suffer from low signal-to-noise ratio (SNR) and stability issues.

Low-dimensional nanostructures have been intensively studied over last decades aiming at the development of new high-performance electronic devices. Silicon nanowires

(NWs), in particular, are a remarkable example of such structures, demonstrating unique electrical, optical, thermoelectric, and structural properties. In addition, they are usually fabricated using complementary metal-oxide-semiconductor (CMOS) compatible technology, thus becoming attractive not only for the fundamental studies, but also for a variety of applications such as high-performance advanced transistors, cost-efficient photovoltaic devices, and ultrahigh-sensitive chemical and biological sensors. Silicon nanowires are also often regarded as key structures of modern nanoelectronics. The high aspect ratio and nanoscale diameter enable the improved interfacing to living cells, and provide an instrument for highly sensitive and selective analysis of molecular-scale objects. Their property of directly translating interactions with target biological objects into a readable electrical signal allows the real-time observation of biochemical processes. Liquid-gated silicon NW field-effect transistors (FETs) were studied for the development of new type biosensors [1–3]. They demonstrate unique possibilities for sensing of small analyte concentrations with the sensitivity approaching the single molecule level. What is more important, the electrical properties of such structures are tremendously sensitive to the changes of surface charge. Thus, interactions with charged analyte molecules can considerably effect the electrical behavior of NW FETs, which makes such devices perfect for the label-free sensing of biochemical species. Furthermore, demonstrating the enhanced interfacing properties with living cells [4], silicon NW FETs are the active devices, enabling to adjust the working point to achieve better SNR for the recording of extracellular electrical activity from such electrogenic cells as cardiomyocytes and neurons. The nanoscale sizes of such devices allow to reach cellular and even sub-cellular spatial resolution for signal monitoring [5].

Therefore, Si NW FETs are perfect candidates for the detection and studies of nanoscale biochemical analytes, including single biomolecules, and their binding kinetics, as well as for extracellular activity monitoring of electrically active cells.

To implement an exclusive specificity of silicon NW-based biosensors to target analyte, their surface has to be modified with the special linker molecules and analyte-specific receptors. This step plays crucial role determining the performance of the biosensor. Because of the electrical double layer, which forms, when the liquid is getting in contact with the surface of such sensors, only charges located closer than the Debye screening length can be effectively detected. Therefore, the linker and receptor molecules should be as small as possible. In this respect, there are several ways to enhance the sensitivity of such biosensors, either by enhancing the performance of the biorecognition layer, involving the utilization of smaller linker and receptor molecules, or by optimizing the sensor working regimes, or utilizing novel effects and device parameters.

The optimization of biorecognition layer requires comprehensive biochemical studies, synthesis of smaller receptors, improvement of immobilization protocol, which is a complicated and time-consuming task. On the other hand, the investigation of nanowire FET operation regimes, study the device geometry impact on the sensitivity, as well as utilization of novel effects and phenomena opens prospects for the development of advanced biosensors.

Recently, single electron effects in FET devices have emerged as a promising tool for quantum information processing and biosensing [1, 6–8]. Silicon NW FET devices are known for their ultimate scaling abilities. Together with the gate area reduction, the amount of traps in the gate dielectric also decreases. At the characteristic size of $0.1\,\mu m^2$, only a single trap can influence the channel conductivity by capturing and emitting a single charge carrier. The strong modulation appears as a two level fluctuations known as the random telegraph signal (RTS) noise. Such a trap is usually treated as the source of an

unwanted excess noise in electronic nanoscale devices. Typically, the statistical behavior of such a trap can be explained in the framework of the Shockley-Read-Hall (SRH) model, where the capture time has a power dependence on the channel current with the power of 1. However, this is not always the case, and much stronger power dependencies were reported in literature [1, 9, 10]. The fact of enhanced dependency observation indicates on the strong influence of the surface potential on the single trap parameters. Therefore, the single trap approach can be directly applied to enhance the sensitivity of the biosensors. To understand such an enhanced behavior the quantization, charge carrier distribution in the channel, as well as Coulomb blockade energy have to be taken into account.

The understanding of enhanced single trap dynamics allows to develop a strategy for the achievement of the reliable single trap formation, and its application in fundamental studies as well as in applied fields of research, particularly, in biosensing. It should be noted that when this step is solved, suggested approach can be applied to the large scale CMOS-compatible production, which reasonably reduces costs of sensor fabrication.

In this thesis we designed and fabricated silicon nanostructures including nanowires, nanowire arrays, and nanoribbons. We targeted our research on the investigation of transport properties of fabricated devices using noise spectroscopy with respect to the implementation of novel effects and phenomena into advanced biosensing techniques. Our silicon NW FET structures fabricated on the basis of silicon-on-insulator (SOI) wafers enable the utilization of both liquid and back gates. The gate coupling effect was demonstrated as a powerful tool for tuning the conductive channel of the nanowires, resulting in the twofold increase of SNR for comparable to neuronal signals. The results are supported by the comprehensive simulations in technology computer-aided design (TCAD) software.

The analysis of transport properties demonstrates an excellent scaling abilities of our liquid-gated silicon NW FETs. The comprehensive studies of noise properties reveals the capability of single elementary charge detection for the devices with the gate area of less than $0.1\,\mu m^2$. Furthermore, at such dimensions single trap phenomenon was registered as a strong modulation of the FET channel current. Enhanced capture time dependencies on the drain current demonstrate extremely high slopes of up to (-14.13), unusual for the standard SRH model. The Coulomb blockade energy, quantization effects and charge carrier distribution were considered for the understanding of such enhanced bahavior in liquid-gated silicon NW FETs. It should be emphasized that the single trap phenomenon appears in the gate area range, where single charge sensitivity was obtained. The capture time dynamics has been approved to be highly sensitive to the surface potential change in solutions with different pH, thus opening the prospects for the development of novel biosensing approaches. Liquid-gated silicon NW FETs were used for the detection of troponin molecules, a gold standard markers of acute myocardial infarction (AMI). Developed sensors demonstrate good sensitivity with the lowest detected concentration of 20 pM. We reveal the possibility of sensor reusability by applying glycine-HCl buffer.

The stable and reliable biosensor operation is a guarantee of the proper device work and diagnosis for a long period of time. In this respect, new materials and compounds are also considered for the role of a transducer. The wide bandgap material have proven themselves to be a promising candidates for sensing application because of their mechanical robustness, environmental stability, and high tolerance to high temperatures as well as radiation [11]. We considered GaN nanoribbons fabricated on the basis of AlGaN/GaN heterostructure. The novel space-charge effects are revealed as a powerful tool for the enhancement of molecular diffusion processes towards the surface of the biosensor.

In addition, we demonstrate the recordings of extracellular activity from cardiac cells

and show the propagation of the action potentials (APs) across the confluent cellular layer with the speed of arounf 10-13 mm/sec, reflecting the cellular activity. We applied a novel approach of using fluorescent microscopy together with silicon NW FETs to evaluate the functional activity of cardiac cells. The pharmacological effect of noradrenaline (NorA), as a modulator of functional activity of the cells was tested by the suggested method. The addition of NorA caused the increase of the cellular beating frequency. The role of calcium alteration and membrane potential were analyzed in terms of fluorescent microscopy. Furthermore we investigated the compatibility of our silicon nanostructures with the neuronal cell culture. The results demonstrate that fabricated silicon NW FETs are the excellent choice for the broad area of application in biosensing with remarkable novel effects, such as the gate coupling effect, and single trap phenomena, for the investigation of different kinds of biological objects.

The thesis is structured in the following order. **Chapter 2** includes fundamentals on the biosensor detection principles, the operation principles and electrical characteristics of FET and biosensors based on FETs, and covers the topic of noise origins. The chapter describes features of the electrical double layer, its importance for detection of biological species using FET-based biosensors, as well as electrophysiology of cells. In **chapter 3**, methods, including surface modification and cell culture, measurement techniques and developed setups, as well as software are presented. **Chapter 4** is dedicated to the design, fabrication, and investigation of silicon nanostructures including nanowires, nanoribbons and nanowire arrays. The findings in gate-coupling effect as well as noise properties including single trap phenomena are considered in detail for the application in biosensing. In **chapter 5**, nanoribbons based on AlGaN/GaN heterostructure were studied. The characteristic features of the transport properties were revealed, and features of space-charge phenomena were considered for biosensing applications. In **chapter 6**, knowledge obtained from studies of different structures is applied for biosensing with advanced parameters. The experiments include the detection of troponin molecules, antioxidants specific to reactive-oxygen species, as well as in vitro recording of cardiac cell electrical activity. Conclusions and final remarks are presented in **chapter 7**.

Chapter 2

Fundamentals and Theory

2.1 Biosensor Detection Principles

The progress in the development of modern smart healthcare products including medical diagnostic tools, point-of-care devices as well as disease treatment optimization requires more and more comprehensive biosensors as a core component. To reach the maximum performance of the detection system and monitor the smallest changes of the analyte concentration it should be able to quantify target bio-molecules specifically and selectively with a high sensitivity and satisfying temporal resolution. Clinical samples under investigation typically contain a large number of components. Specific disease however can only be classified by monitoring a specific content of a single molecule or a certain group of target bio-markers and in real life examples many bio-molecules such as deoxyribonucleic acid (DNA), ribonucleic acid (RNA), various proteins or viruses appear in the concentration orders from fg/ml to pg/ml. Furthermore when personalized medicine becomes a foremost approach for medical diagnostics not only quantities but also a biomarker profiles play important role for accurate diagnosis. Meeting the aforementioned requirements is an advanced task of the modern bioelectronics including the development of both highly sensitive and selective functional layers and multichannel biosensing platform [12]. Techniques used for the detection can generally be classified into two big groups [13]: label-based and label-free. Both detection techniques are schematically shown in figure 2.1.

2.1.1 Label-Based Detection Technique

Label-based biosensor techniques utilize so-called "labels" or "tags" for the detection of certain analyte among the other components (see figure 2.1(a)). There are three most popular approaches for detecting specific molecules utilizing such effects as fluorescence [15–19], chemiluminescence [20–24], and radioactivity [25–27].

The fluorescent labeling means that target molecules such as antigens modified with fluorophore are loaded on the surface immobilized probe molecules such as antibodies. After the antibody-antigen binding the analyte can be detected using fluorescent microscopy. Such approach, however, has its disadvantages. Firstly sample losses or occasional functionality losses might occur while the labeling and purification procedures. Secondly, the fluorescent activity of fluorophores tends to vanish fast upon exposure to the light and is very sensitive to the environment conditions such as pH of the solution [28]. In spite of mentioned facts fluorescent technique is popular and widely used method due to high

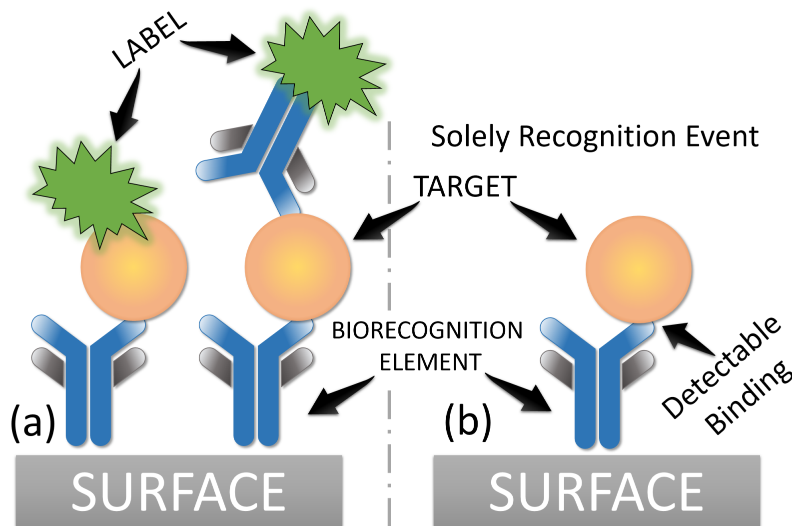

Figure 2.1: Schematic representation of two detection techniques with different working principle. (a) Label-based approach uses label activity, generated as a result of the recognition event. (b) label-free detection technique relies on the solely recognition event and properties of the target object. Figure is adapted from [14].

sensitivity, stability and possibility to utilize it in scanning array configuration [29].

Chemoluminescence is the process of light emission as a consequence of a chemical reaction. This phenomenon allows to detect target molecules with simple instruments without additional light sources. Method demonstrates high sensitivity and is attractive in environmental, biomedical and chemical analysis. Among the major drawbacks are the limited spacial resolution and limited dynamic range. Furthermore samples can be used for detection only once in comparison to the fluorescence technique where samples can be reused.

Another popular technique utilizes radioisotopes as labels. Method suggests ultimate sensitivity and resolution with well developed protocols providing high stability and reproducibility. Obviously method utilization is limited from the viewpoint of safe handling and therefore can be used only for low-throughput applications.

Label-based approach allows for highly sensitive and reliable detection in almost all assays. With all benefits labeling has several disadvantages. It provides the information on the target concentration or its location. However due to the underlying labeling principles continuous monitoring becomes impossible and the information regarding binding kinetics cannot be extracted. Furthermore usually multiple washing steps are required to complete the assay, thus reducing the effective throughput and increasing the cost. In this respect other approaches should be considered to overcome mentioned above challenges.

2.1.2 Label-Free Detection Technique

Label-free biosensors emerged as a novel platform to satisfy the strong requirement in continuous binding kinetics monitoring down to the single molecule level and precise quantification with the high throughput. The working principle of the label-free sensors relies on the interaction of the target molecule with the receptor-functionalized surface of

the transducer which converts the binding events into readable signal through the changes in physical properties of the sensor (see figure 2.1(b)). Label-free technique became very attractive and has been undergoing a great progress during the past decades since it simplifies the assay development. Because each target molecule requires only one recognition element the amount of functionalization steps and thus overall complexity is reduced making the cost of such tests lower. There are many label-free techniques developed which can be categorized into two groups based on the transducer type, namely optical-based and non-optical-based. Biosensors based on the surface plasmon resonance are leading in the field of commercially available label-free optical technologies. There are however several more worth mentioning approaches emerging recently and used in a various applications. They are the waveguide-based biosensors including optical slot-waveguide [30–32] optical resonator-based biosensors [33–36] interferometer-based biosensors [37, 38] bio-photonic sensing cells - based biosensors [39, 40] and porous materials for optical biosensing [41–44].

On the other hand-side there are non-optical-based label free biosensing techniques including acoustic waves [45–47] , micro-calorimetry [48, 49] and electrochemistry [50–53].

The strong push over the development of novel label-free techniques and transducer types has been made by recent advances in nanotechnology enabling the fabrication of high-throughput, highly sensitive label-free biosensors with low sample consumption as well as low damage to the analytes. The compatibility with the modern fabrication technology makes them attractive for the low-cost production. Furthermore the possibility to integrate them with modern electronics opens the prospects for the ultimate automation of the screening process. Because the thesis is mainly focused on the field effect transistors we will describe only principles behind this type of transducers in the following section.

2.1.3 Biomarkers of Cardiovascular Disease

Cardiovascular system is one of the most important in the human organism while ensuring a continuous blood flow and providing the organism with oxygen and nutrients, thus supporting the livelihood of the entire organism. That‘s why any dysfunctions might cause irreversible damage to the organism with even lethal outcome. Nowadays cardiovascular diseases are unfortunately widely spread and taking the leading positions by the mortality rates worldwide. Further uprising threat tendency is caused by many factors like tobacco use, physical inactivity, excessive alcohol consumption, unhealthy diet, obesity as well as often mentioned aging of the world population [54]. Acute myocardial infarction (AMI) is one of critical stages of coronary artery disease. The development of disease is accompanied with the lack of blood supplied and is followed by tissue death. Many biosensing techniques have been developed to be track such stages and apply appropriate treatment. This is however not enough for every case and to be able to prevent critical stages of AMI more sensitive techniques with high temporal resolution for realtime biosensing should be established. It is important to understand the dynamics of so-called biomarkers, the molecules which are typical to find in higher than normal concentration in blood serum when certain stage of disease appears. A comprehensive research together with dozens of clinical investigations have shown that c-reactive protein and troponin molecules express elevated concentrations [55, 56].

Troponin complex plays important role in regulation of striated muscle contraction process (see figure 2.2). The complex consist of three regulatory proteins, responsible for specific functions. troponin C (TnC) binds Ca^{2+}, troponin I (TnI) inhibits the ATPase activity of actomyosin, and troponin T (TnT) provides for the binding of troponin to

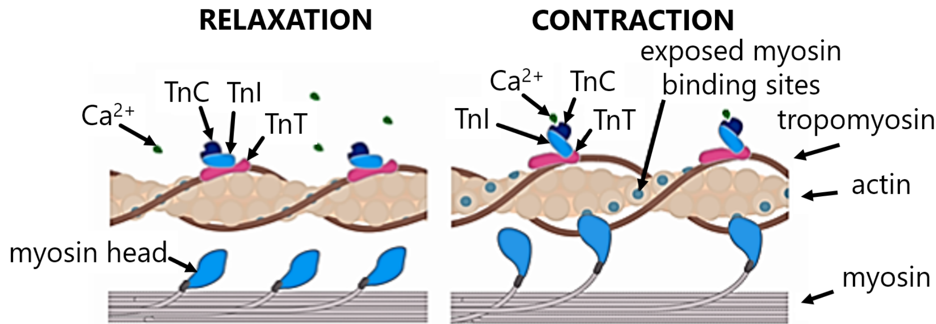

Figure 2.2: Schematic representation of actin-myosin complex. During the relaxation, binding sites of myosin on actin molecules are blocked by the tropomyosin. The contraction occurs when calcium molecules bind to troponin C, causing the conformation change in troponin I and troponin T. As a result the tropomyosin slides away, allowing myosin to bind to actin. This causes shortening of the complex resulting in the muscle contraction. When cardiac cell injury occurs, troponins are released into the blood, making them highly specific and sensitive biomarkers. Figure is adapted from [58]

.

tropomyosin [57]. The complex together with tropomyosin is located on actin filaments. The cardiovascular disease development and transition into a critical stage (i.e. myocardial infarction) is accompanied by the muscle cell destruction or necrosis and release of troponin molecules into the blood. Increased troponin concentration can be observer shortly after the myocardial injury in the range from 2 to 4 hours [59]. Troponin is released in two steps, first - from the cellular cytosol, and later from degrading myofilaments. In respect to the process kinetics, the troponin sensitivity is not maximal directly after the injury onset and reaches 90% after 1 hour. Due to further injury development the sensitivity increases in time and 99% sensitivity can be achieved after 6 or more hours of myocardial necrosis.

There are three isoforms of troponin I found for the striated muscle, where two are typical for skeletal fibers and one for cardiac muscle [60, 61]. The interesting fact is that cardiac TnI is larger than others due to additional 30-membered peptide [61]. troponin I is interesting not only because of high specificity to cardiac injury but also because of its properties. It has excess of positively charged residues and its estimated pI is aroung 9.9 [57]. This fact is attractive for the implementation of label free technique based on field effect transistors.

2.1.4 Biosensors Based on Field-Effect Transistors

Among the variety of structures suggested by nanotechnology the nanoscaled field-effect transistors became within the topmost perspective for the biosensing applications. The ability to directly translate the specific interactions of the analyte with the field-effect transistor (FET) surface into a readable signals makes them very attractive to become a transducer for the label-free detecion technique. Transistor-based biosensor is usually a three-terminal device including source, drain and gate, which is exposed to the sensing environment, often liquid, directly or through so-called extended gate. The operation of such transducer is very similar to the operation of metal-oxide semiconductor field-effect

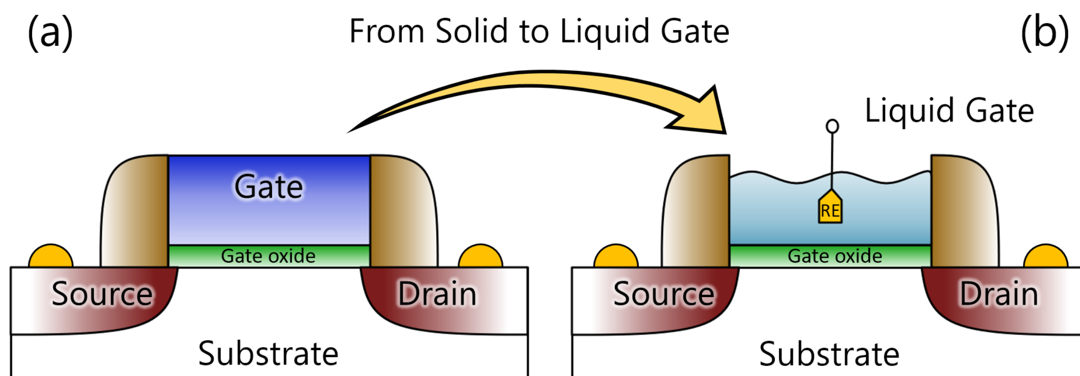

Figure 2.3: Schematic transition from solid (a) to liquid (b) gate towards the development of novel highly-sensitive biosensors.

.

transistor (MOSFET) device where the electrical conductance of the channel between source and drain reflects the changes of the gate surface potential(see figure 2.3. In biosensor such significant changes are caused by the influence of various chemicals, charged ions or by adsorption of target molecules on the surface of the transducer.

With special chemical treatment called surface modification or sometimes functionalization biosensor can be prepared for the specific interactions such as enzymatic reactions, DNA hybridization and antibody-antigen reactions. In this respect several types of FETs used for biosensing can be highlighted. Enzyme-based FETs are the core components of the biosensors where the products of biocatalytic reaction produce the surface potential changes corresponding to the enzyme concentration. One can find a variety of works where different enzymes were studied, for example glucose oxidase [62], urease [63] tyrosinase [64], etc. One of the most commonly used detection technique employs the binding of charged antigens to antibodies immobilized on the surface of the FET resulting in the changes of surface potential. Such transducers are also called ImmunoFETs since the application area often deals with the detection of disease markers. troponin I is considered as a gold standard marker for the detection of acute miocard infarction. There are however still several important challenges to overcome in order to implement a fully practical diagnostic platform useful for medical applications. One of them is the inability of detecting macromolecules in physiological solutions without pretreatment. Another problem is related to physical properties of the solid to liquid interface where Debye screening length, λ_D, is the limiting factor of biosensor sensitivity. λ_D is the distance from the surface at which electrical charge can be effectively recorded. Therefore it is important to control the Debye screening length which depends on the ionic content of the solution as well as the length on the receptor molecules in order to be sensitive enough to the captured molecules. Furthermore the working regime of the FET biosensor plays crucial role on the sensor performance, since the applied gate voltages should be in a safe range, where the antibody-modified surface is not degrading and can provide reproducible results. One more remarkable FET-based biosensor type allows to investigate the electrically active living systems containing for instance cardiomyocytes or neurons. An objects under investigation can be either cells cultured on the sensor surface(in vitro) or a tissue from the living organism (ex vitro) or even a living organism(in vivo). Cell-based FETs allow to monitor the metabolism of cells, the interaction of the drugs or even detect action

potential activity inside and outside the cell membrane. The requirements to biosensor's sensitivity, selectivity, spacial and temporal resolutions are growing rapidly. Therefore many candidates were considered to become an ideal candidate for label-free applications. In this race low-dimensional semiconducting structures such as silicon nanowires, carbon nanotubes or graphene outperformed the standard bulk FET devices by enhanced surface-to-volume ratio. This feature makes nanoscaled devices highly sensitive to charges close to the surface. Furthermore at nanoscale materials demonstrate unusual properties including quantization, ballistic transport or gate coupling effects which can be employed for the biosensor enhancement. Along with this, such devices can be scaled down to fit the dimensions of target molecules aiming the single molecule detection or investigation of electroactive cells on subcellular level.

2.2 Field-Effect Transistor

Field-effect transistor is a semiconductor device in which an electric field is used to control the current through the conductive channel. Single type charge carriers are involved in the formation of charge transport, in this respect FETs are also called as a unipolar transistors. It has three terminals for interfacing with electronic circuits, namely source, drain and gate. The current flows in the conductive channel between drain and source while controlled by the gate. By applying potential to the substrate transistor can be additionally body-biased or gated in silicon-on-insulator (SOI) configuration. There are many different implementations of field effect transistors, e.g. MOSFET, junction field-effect transistor (JFET), ion sensitive field-effect transistor (ISFET) and based on it biologically sensitive field-effect transistor (BioFET). The concductive channel is usually doped in order to form n-type semiconductor with electrons as a main charge carriers or p-type semiconductors where holes are the main charge carriers. Depending on the desired operation of the FET source and drain contacts may be doped with similar type dopant to form depletion mode FET or with opposite type to form enhancement mode FET.

Field Effect

The effect of changing charge carrier concentration in the layer near the interface between the dielectric and the semiconductor under the influence of external electrical field is called the field effect. The mode when near-interface layer contains increased concentration of major carriers is called accumulation. On the other hand when the concentration is decreased the device is in depletion mode. When increased concentration of minority carriers is increased the device operates in the inversion mode. In comparison to metals where electrical charge concentrates on the surface in semiconductors the charge is distributed into the volume of the crystal. The sign of the charge in semiconductor depends on the applied gate voltage.

Accumulation Mode

When negative voltage is applied formed charge is positive. In p-type semiconductor positive charge is caused by the holes attracted to the surface. Similarly electrons are pulled to the surface of n-type semiconductor when positive voltage is applied. Under such conditions the structure is operated in so-called accumulation mode.

Depletion Mode

On the contrary to the previous clause when changing voltage polarity to opposite, in p-type semiconductor the near-interface layer would be depleted by the major carriers and in n-type semiconductor when negative voltage applied would cause the electrons to push away from the surface. In this case devices are opereted in depletion mode.

Working Principle

To explain the working principle of the liquid-gated FET, we consider n-type device. A typical transfer curve is shown in figure 2.4(a). When zero voltage is applied between gate and source there is no conductive channel between source and drain since there are two reverse-biased p-n junctions (figure 2.4(b)). Therefore when applying drain-source voltage the current is negligibly small. If negative voltage is applied to the gate, the holes are accumulated close to the dielectric interface and the current will not change. On the contrary, when applying positive gate voltage the depletion region starts growing and then transforms to the inversion layer which forms the conductive channel (figure 2.4(c)). From this moment on the current gets the finite value and it is dependent on gate voltage. The gate voltage when the conductive channel forms is called threshold voltage, V_{Th}. When increasing gate voltage more and more transistor gets into working regime (figure 2.4(d)). In the linear operation mode, when $V_{DS} < V_G - V_{Th}$, the current through the channel can be described by the following equation:

$$I_D = \mu_n C_{ox} \frac{W}{L} \left((V_G - V_{Th}) V_{DS} - \frac{V_{DS}^2}{2} \right) \tag{2.1}$$

For the p-type FET the threshold voltage and the range of working voltages are negative.

Mobility

In solid-state physics when electric field is applied to the semiconducting material electrons and holes are moving across the material and collide with atoms in the crystal structure, impurities and defects causing electron and hole scattering. In between collisions electrons and holes gain velocity in applied electric field. Resulting average drift velocity of electrons and holes is a finite value proportional to applied electric field where μ is the constant of proportionality and is called mobility. This parameter is very important in semiconductor physics since it express how good is the movement of charge carriers resulting in the device performance and speed of operation. Because effective mass of electrons is lower than for holes, the mobility of electrons is approximately 3 times larger. Mobility depends on the set of parameters including temperature, impurity concentration and electrical field. The dependence of mobility on temperature is defined by the charge carrier scattering mechanisms. When scattering on lattice is stronger the dependence would be:

$$\mu_L = \mu_{0L}(T_0/T)^c \tag{2.2}$$

In the case when scattering on impurities is stronger the mobility would be defined as:

$$\mu_L = \mu_{0L}(T/T_0)^{3/2} \tag{2.3}$$

where μ_0 is the mobility at initial temperature (i.e. room temperature) and μ - mobility at temperature T. Power exponent c is different for different materials, for silicon in particular it is equal to 5/2. Taking into account two scattering processes the resulting mobility is defined as:

$$\frac{1}{\mu_L} = \frac{1}{\mu_L} + \frac{1}{\mu_I} \tag{2.4}$$

therefore overall mobility would be close to the smallest value of two components.

The conductivity of the material can be written as the combination of electron and hole components as

$$\sigma = q(n\mu_n + p\mu_p) \tag{2.5}$$

For the intrinsic semiconductor the conductivity is defined by the temperature dependence of intrinsic carrier concentration n_i and it is quite strong with exponential law. In working range of temperatures (from −60 °C to 125 °C) the the intrinsic silicon conductivity is changing in 5 orders of magnitude. Considering impurity semiconductor the concentration of charge carriers is defined by the donor or acceptor concentration and thus the effect of minority carriers can be neglected. In working temperature range the concentration of majority charge carriers is almost constant thus making the conductivity dependent on mobility which is a function of temperature.

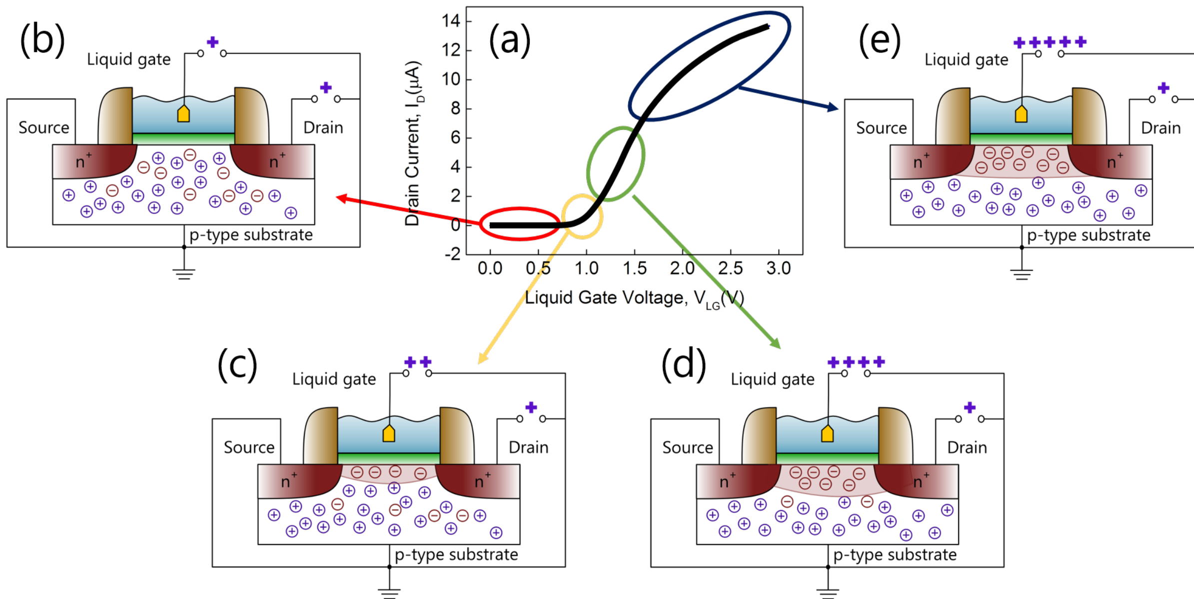

Figure 2.4: Schematic representation of FET working principle. (a) - shows typical transfer curve measured in liquid environment. Operation modes are highlighted on the curve, (b) - corresponds to the FET working in subthreshold regime where inversion channel is not yet formed and the current is not flowing through the channel, i.e., in closed state, (c) - when gate voltage reaches the value of threshold voltage a high concentration of inversion charge carriers is formed in a thin inversion layer next the the interface with gate dielectric and provides the current flow in the channel, (d) - further gate voltage increase produces more inversion charge carriers thus increasing current, (e) - at higher gate voltages when the resistance of the channel becomes smaller the current through the channel is limited by the resistances in the circuit.

Threshold Voltage

The voltage at which the current starts flowing through the transistor channel is called threshold voltage and it is designated as V_{Th}. In the case of metal-oxide semiconductor (MOS) transistors the influence of gate voltage on the channel is defined by the oxide capacity between the metal gate and the semiconductor. Therefore gate capacitance is one of the most important parameters in the device. The capacity itself is defined as

$$C_{ox} = \frac{\varepsilon_s \varepsilon_0}{d} \tag{2.6}$$

where ε_s is a permitivity of dielectric layer and d is the thickness of the layer. The thinner the layer the better control over the channel can be achieved. The limiting factor is the dielectric breakdown. The threshold voltage can be spitted into several components:

$$V_{Th} = V_{FB} + V_{BB} \tag{2.7}$$

where V_{FB} is the flat band voltage which compensates the equilibrium surface potential, V_{BB} is the band banding due to the space charge region and equals to the threshold voltage when surface potential equals to 0.

$$V_{FB} = \phi_{MS} + \frac{Q_s}{C_{ox}} \tag{2.8}$$

where ϕ_{MS} is the difference in metal and semiconductor work functions, Q_s is the equilibrium surface charge including charges accumulated in the gate dielectric and charges captured to the surface states. The band banding voltage is defined as follows:

$$V_{BB} = \phi_{sm} + \frac{\alpha}{C_{ox}} \sqrt{\phi_{sm}} \tag{2.9}$$

where

$$\alpha = \sqrt{2q\varepsilon_s\varepsilon_0 N} \tag{2.10}$$

and it indicates on the influence of volume charge in the substrate. Typically $\phi_{sm} = 2\phi_F$, here ϕ_F show the difference between Fermi level and electrostatic potential in the semiconductor volume. Overall the threshold voltage can be written as

$$V_{Th} = \frac{\phi_M - \phi_S}{q} + \frac{Q_s}{C_{ox}} + 2\phi_F \tag{2.11}$$

The typical threshold voltages are in the range from 0.5 V to 1.5 V. The key idea of the ISFET is to replace the metallic gate with electrolyte gate. In this configuration transistor can be used for a variety of applications including pH monitoring and biosensing. Now the role of gate electrode plays the electrolyte solution which is in direct contact with gate dielectric. The drain current is controlled by the electrical potential of the electrolyte solutions applied against the reference electrode. In comparison to the conventional MOSFET the role of metal workfunction plays the potential of reference electrode. Furthermore the threshold voltage includes also terms responsible for the surface potential of the interface between electrolyte and gate oxide:

$$V_{Th} = E_{ref} - \psi_0 + \chi_{sol} + \frac{\phi_S}{q} + \frac{Q_s}{C_{ox}} + 2\phi_F \tag{2.12}$$

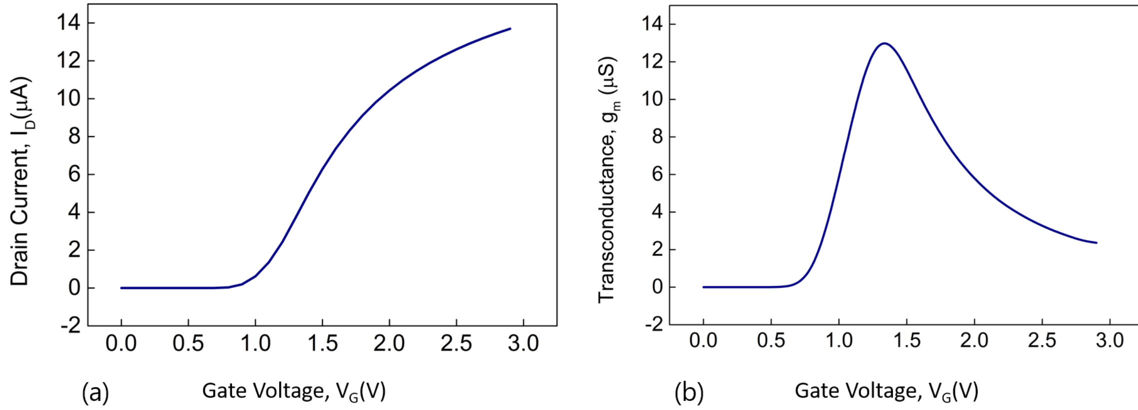

Figure 2.5: (a) Typical transfet curve of liquid-gated FET. (b) Transconductance of liquid-gated FET calculated as a derivative of a transfer curve.

where ψ_0 is the potential defined by the ion distribution near the interface and χ_{sol} is the surface dipole of a solvent. The changes of the surface potential are directly reflected in the threshold voltage and causes the changes of drain current at the same voltage applied to the reference electrode. Such changes might be the consequence of solution pH change or binding of analyte from the solution in BioFET configuration.

Transconductance

The parameter showing how strong the current through the channel is influenced by the corresponding changes in gate voltage is called as transcunductance, g_m, and is defined as

$$g_m = \frac{\partial I_D}{\partial V_G} \tag{2.13}$$

Typical transfer curve or FET device is shown in figure 2.5(a). Corresponding transconductance curve calculated using equation 2.13 is shown in the figure 2.5 (b).

2.3 Electrical Double-Layer

The interaction of surface with various liquids plays an important role in bioelectronics and defines the fundamental properties of interaction processes. When the object is brought into a contact with the fluid a so-called electrical double layer is formed at the interface between two materials. For instance the object can be represented by a surface of metal electrode or a dielectric covered nanowire. The electrical double layer refers to spacial charge separation at the interface of two phases. The formation of charge on the solid surface can be caused either by the ion absorption on the surface or by dissociation of surface compound or by electron density redistribution. In the case of biosensors the electrical double layer (EDL) is most often observed at the interface between a solid body and the electrolyte (see figure 2.6). For such configuration the adsorption of the ions of a certain type and sign turns out to be more beneficial. Such ions are called "potential determining ions" since they are bonded directly to the surface and determine its charge. The layer of absorbed co-ions is very dense and it has a permanent thickness comparable to

the atom radius. The appearance of the charges on the solid surface at the interface with liquid creates an electrical potential which can be calculated from the Nernst equation:

$$\varphi = \frac{RT}{Fz} ln \frac{\alpha_{(surface)}}{\alpha_{(solution)}} \tag{2.14}$$

where F - Faraday constant, z - ion charge, T - temperature, R - universal gas constant, $\alpha_{(surface)}$ and $\alpha_{(solution)}$ are the ion activities next to the surface and in the bulk fluid. The activity of ions can be related to the physical concentration C_{ion} as $\alpha_{(ion)} = \gamma_{(ion)} C(ion)$, where $\gamma_{(ion)}$ is the activity coefficient of certain ion type. At low concentrations the activity coefficient tend to unity and therefore can be replaced by simple concentrations. The charged surface is attracting the ions of the opposite sign from the solution by the electrostatic forces. Such ions are called "counter ions". By the configuration the system reminds the parallel plate capacitor and was generalized in Helmholtz model. Here the surface charge is compensated by the counter ions located at the distance from the surface to the center of the ion - i.e. the ion radius. The surface potential dissipates from the surface to the location of the counterions linearly. This is however a very rough estimation since the approach hypothesizes rigid layers of the opposite charges. This is not the case in nature. Because of thermal motion the mobile counter ions are diffusing into the electrolyte until the the tendency is suppressed by the counter potential. The thickness of formed diffusion layer is determined by the kinetic energy of ion motion. Gouy and

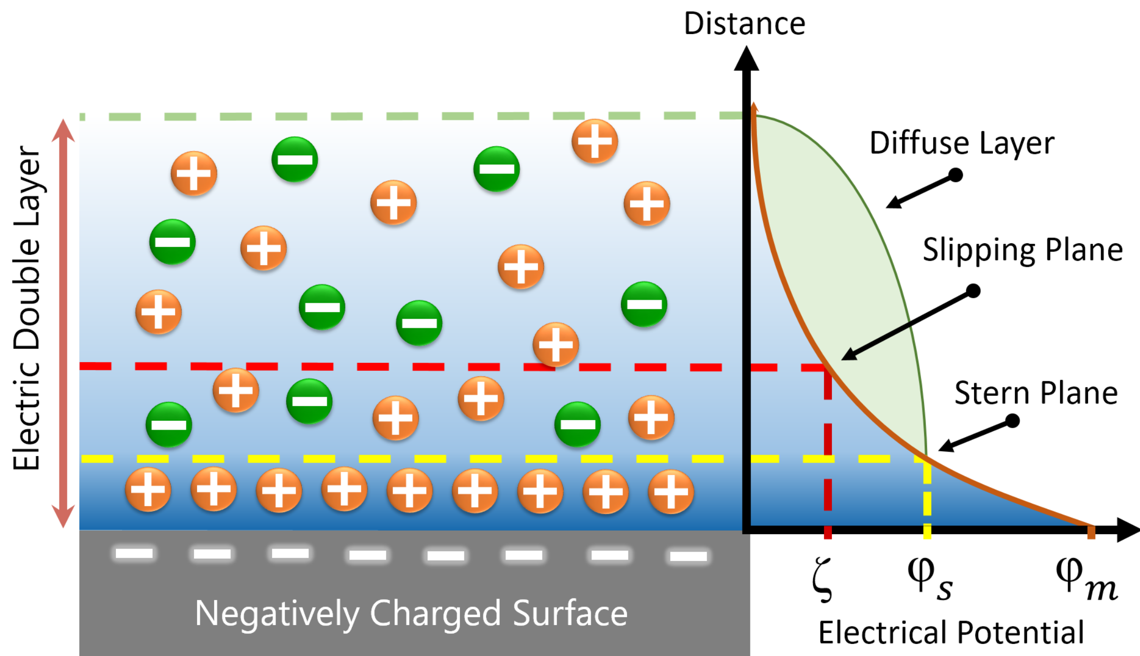

Figure 2.6: When liquid is brought into contact with charged surface the charge redistribution occurs in liquid resulting in a formation of electrical double layer - a spatially separated charges of opposite signs. Ions adsorbed onto the surface form rigid Stern layer where potential drops linearly as in parallel plate capacitor. The slipping plane separates mobile ions from those attached to the surface. Because of excess positive charge the potential in this plane drops to so-called ζ-potential. In diffuse layer ion concentration follows Botzmann distribution and potential here drops exponentially. In bulk liquid ions are evenly distributed.

Chapman independently came up with the idea of diffuse double layer where the charge in terms of counter ions concentration near the surface follows the Boltzmann distribution:

$$n = n_0 exp\left(-ze\varphi/kT\right) \tag{2.15}$$

where n_0 - is the bulk ion concentration, z - is the charge of the ion, e - charge on a proton, k - Boltzmann constant, φ - electrical potential. Such interpretation would be suitable to describe the behavior of bulk solution assuming that activity equals to molar concentration. This changes when approaching the charged surface and volume charge density should be considered when studying the coulombic interactions. The volume charge density can be calculated as:

$$\rho_i = \sum_i z_i e n_i \tag{2.16}$$

For the plane surface coulombic interactions can be written using Poisson equation:

$$d^2\varphi/dx^2 = -4\pi\rho/d \tag{2.17}$$

where φ varies from φ_m at the surface to 0 in the bulk solution. Solving the equation gives the potential distribution as a function of distance from the surface. The thickness of diffusive layer is found to be:

$$\lambda_{double} = \left[\varepsilon_r kT/\left(4\pi e^2 \sum_i n_{i0} z_i^2\right)\right]^{1/2} \tag{2.18}$$

As it derives from the equation the thickness of the double layer depends on the ion valence and the concentration. The theory suggested by Gouy and Chapman describes well the interactions within the system of a rigid charged surface and oppositely charged ions from the solution - known as diffuse double layer. The thickness of a double layer were experimentally found to be a little greater than predicted by a model. Stern in turn suggested additional modification of the theory by assuming that ions are not a point charges as it was postulated before and they cannot approach the surface closer than some distance, δ - the radius of the ion, which is in a range a few manometers. Therefore he assumed that some of ions are possibly adsorbed by the surface in the plane δ nowadays known as the Stern Layer. The potential drop of $\varphi_0 - \varphi_\delta$ will occur over the rigid layer of a "molecular capacitor" (Helmholtz Plane) and the rest φ_δ will drop over the diffuse layer. φ_δ has become known as a zeta(ζ) potential. The existence of the electrical double layer is of a fundamental importance for a variety of applications. In particular it plays a crucial role for the biosensors where target charged molecules are getting screened by the double layer.

2.4 Electrophysiology of Cells

The progress in understanding bioelectrical activities in the human body requires a deep understanding of a basic processes including information transmission and processing by the neural networks in brain, recognition and response to the light excitation by the ganglion cells in the eye as well as coordinated and synchronous beating of cardiomyocytes in the heart. The knowledge is especially valuable for medical purposes, in particular for

anomalous behavior detection and possible treatment or correction. To address challenges in the research area a new and more sophisticated electrophysiological techniques for high spatiotemporal resolution measurement has to be developed [65]. Electrophysiology as a branch of physiology studies the electrical properties of biological cells or tissues involving measurements of voltage changes or electric currents on a variety of scales from the whole organs down to single ion channels. The electrical activity of electrogenic cells(such as neurons or cardiomyocytes) originates from the properties of the cellular membrane. It is known that all eukaryotic cells are surrounded by a 5-8 nanometer thick membrane composed of a lipid(or phospholipid) bilayer with embedded transmembrane proteins. The pure phospholipid bilayer membrane does not contain free ions, thus preventing the charge transer, acting as a great insulator with a specific conductance per unit area of only around $1 \times 10^{-13}\,\Omega\,\mathrm{m}^{-2}$ [66]. On the other hand mentioned above transmembrane proteins, also known as ion pumps and ion channels, play a key role in the process of ion transfer inside/outside of the cell. Ion pumps, consuming energy in cellular currency of adenosine triphosphate (ATP), create a concentration gradients across the membrane by pushing specific ions through the membrane. Consequently the ion channels tend to compensate the excess charge and allow ions to move across the membrane following the gradient. A typical example is a Na^+/K^+ ion pump. When the cell is not experiencing any excitation, ions distribute across the membrane in a predictable way while the net charge remains neutral. The concentration of Na^+ is much greater outside the cell while K^+ concentration is greater inside the cell. The negative charge is mainly localized in the form of phosphate ions and charged proteins. Specialized phospholipids and proteins associated with the inner part of the membrane are the large source of negative charge.

In the equilibrium the charge separation results in the potential difference across the membrane, which can be explained by the Nernst equation:

$$E_m = \frac{RT}{zF} ln \frac{[X]_e}{[X]_i} \tag{2.19}$$

where $R = 8.314\,J\,mol^{-1}K^{-1}$ is the universal gas constant, T - the temperature in Kelvin, z - the valency of the ion, $F = 96485.33\,C\,mol^{-1}$ - Faraday's constant, $[X]_e$ and $[X]_i$ are the extra- and intracellular concentrations of the ion X, respectively.

However in reality membranes are permeable for several kinds of ions, like Na^+,K^+, Cl^-. Typical concentrations of major potential-determining ions and corresponding equilibrium membrane potentials are presented in the table 2.1.

In the case when multiple ions participate in the transmembrane transport they influence each other resulting in unequal distribution in the equilibrium. The membrane

Ion species	Ion concentrations(mM)	
	Intracellular	Extracellular
Na^+	8-30	145
K^+	100-155	5
Ca^{2+}	10^{-4}	2
Cl^-	4-30	120

Table 2.1: Typical concentrations of ions forming the membrane potential and participating in action potential generation[67–69].

potential in the state of dynamic balance of the ions which are continuously transferred through the membrane is called resting membrane potential. More accurate resting potential can be estimated from Goldman-Hodgkin-Katz equation [69]:

$$E_m = \frac{RT}{zF} ln \frac{P_K[K]_e + P_{Na}[Na]_e + P_{Cl}[Cl]_i}{P_K[K]_i + P_{Na}[Na]_i + P_{Cl}[Cl]_e} \tag{2.20}$$

taking into account the internal and external ion concentrations as well as relative permeability for each ion type (P_K,P_{Na} ,P_{Cl}). In living cells the value of resting membrane potential is in the range from $-90\,\mathrm{mV}$ to $-60\,\mathrm{mV}$.

2.4.1 The Action Potential

It should be mentioned that transmembrane ion channels can be classified to several types by the working principle, namely ligand-gated, mechanically-gated, leackage and voltage-gated. While leakage channels contribute to the resting potential, the voltage-gated channels play important role for the bioelectrical activity of the cell, since the ion transfer is activated by the changes in membrane potential. When the membrane potential rapidly rises or falls, as a result of external stimulus, electrogenic cell fires an action potential (AP) [70]. The remarkable feature of action potential formation is the requirement of the membrane potential to exceed the threshold potential. Otherwise the formation of AP is terminated resulting in failed initiation as it is shown in figure 2.7. In neuronal cells, when membrane potential raises from resting potential of around $-70\,\mathrm{mV}$ over the threshold potential of around $-50\,\mathrm{mV}$ channels start pushing Na^+ into the cell as its concentration is higher outside.

The membrane potential starts getting less negative and moves toward zero, causing membrane depolarization. The concentration gradient still remains so strong than Na^+continue entering the cell resulting in the membrane potential reaching around 30 mV. At this stage other voltage-gated channels open for potassium ions. Under the concentration gradient K^+ leaves the cell reducing the positive charge inside the cell leading to repolarization of the membrane. Membrane potential reaches resting potential of the

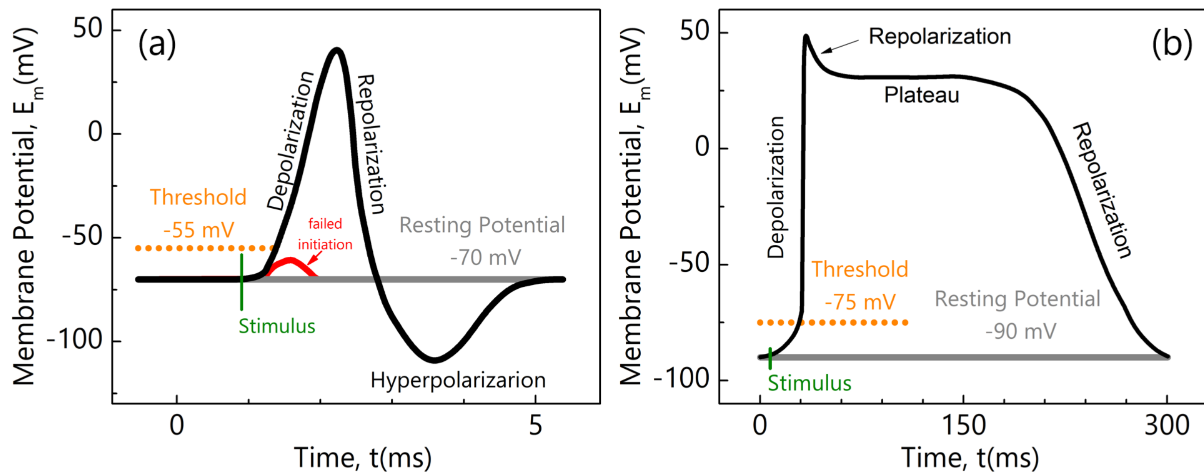

Figure 2.7: Action potentials typical for neuronal cell(a) and cardiac muscle cell(b). The action potential fires, when membrane potential increases over the threshold membrane potential(orange line) as a response to the external stimulus(green line). Otherwise the action potential generation will be terminated(red line).

cell, however with an overshoot. The period of time when the membrane potential gets lower than the resting potential is called hyperpolarization and occurs due to delayed closing of K^+ channels. Typical action potential of neurons last about 10 ms. The cardiac action potential differs from neuronal and also vary within the heart, which is caused by other ion channels present in the cellular membrane. It is worth mentioning that cardiac action potential is not initiated by the nervous activity but rather by the so-called pacemaker cells. Such cells possess the property of automatic action potential generation approximately 60-100 times a minute. As it can be seen from the figure 2.7, the shape of cardiac action potential is different from the one of neuronal cells. The resting potential of cardiac cells is around -90 mV. After the stimulus came from the pacemaker cells action potential starts with the depolarization assisted by the sodium iflux. The membrane potential reaches approximately 30 mV, where repolarization starts by the outflux of potassium ions. On the contrary to neuronal cells, the membrane potential reaches the plateau level where potassium outflux is balanced by calcium influx. The process induces so-called calcium-induced calcium release from sarcoplasmic reticulum which assists the contraction of muscle fibers [71]. Finally cell repolarizes due to K^+ outflux. Typically pacemaker action potential last in the range from 100 to 300 ms and action potentials in cardiomyocytes up to 500 ms.

2.4.2 Cellular Communication

Action potential, fired locally on the membrane, can trigger action potentials in the neighboring segments of the membrane as a result of ion currents, propagating across the membrane as a wave. Because action potentials are newly generated in every neighboring segment the signal propagates without dissipation [72]. After the peak of depolarization voltage-gated Na^+ channels are inactivated the action potential cannot propagate backwards. When it comes to signal transfer between cells there are several different mechanisms, including chemical and electrical. In the case of chemical synapses, the signal is transmitted using chemical messengers called neurotransmitters. When action potential reaches the synaptic knobs, the neurotransmitters are released into the synaptic cleft, the space between presynaptic and postsynaptic cells (see figure 2.8). After diffusion through the cleft, the binding of neurotransmitters to the receptors on the postsynaptic cells triggers the action potential. Taking into account that the cleft is usually from 20 nm to 40 nm the release, diffusion and recognition of the neurotransmitter causes the 1 ms to 5 ms delay in signal propagation. On the contrary, electrical synapses, also known as gap junctions, provide much faster transmission (see figure 2.8). Such beneficial signal propagation does not rely on the neurotransmitters rather on special hemichannels in the membrane called connexons. By connecting connexons, belonging to neighboring cells, a direct contact and cytoplasmic continuity allow ion currents to be directly transmitted between cells without directional restrictions. Both transmission mechanisms are typical for nervous system. Cardiac cells, however, make use of only electrical synapses.

2.4.3 Extracellular Recordings

The bioelectrical activity of electrogenic cells appears in the form of ionic currents flowing across the membrane as it was discussed previously. Changes of ion concentrations inside and outside the membrane influence on the electrical potentials on both sides of the membrane. In this respect, there are two approaches for measuring electrical cellular

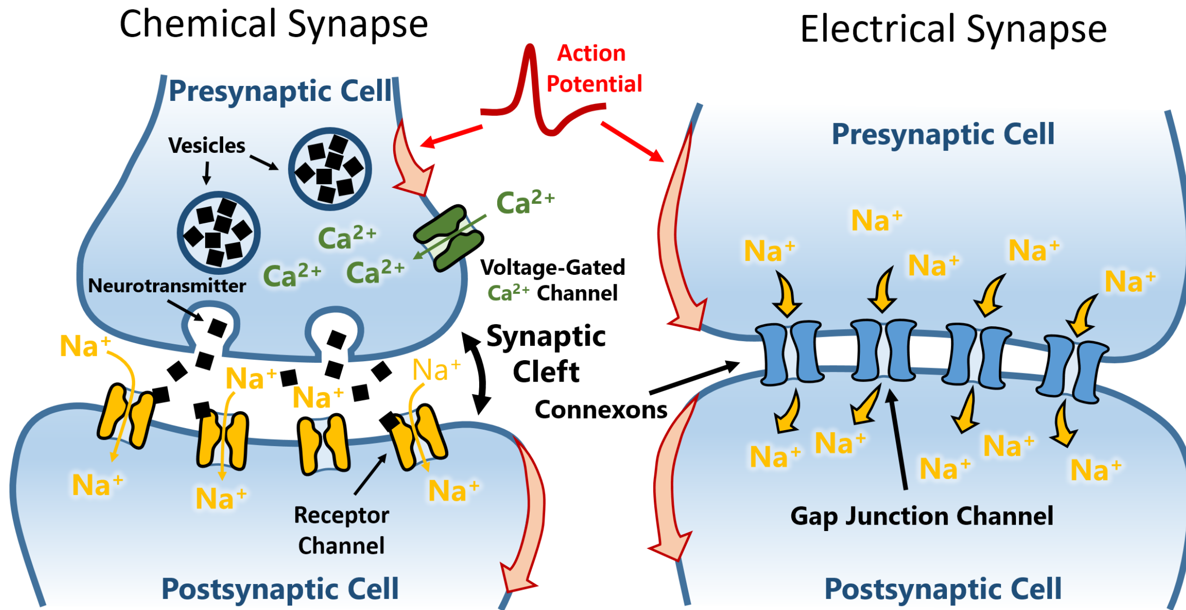

Figure 2.8: In chemical synapse (a) the action potential activates calcium channels which assist the release of neurotransmitters. Their binding to receptor channels in the post-synaptic cell triggers the sodium influx, thus firing the action potential. In electrical synapse (b) cells are directly connected through connexons, which allow the direct ion transmission from one cell into the other without directional limitations.

activity - intracellular and extracellular. The first one is represented by the patch-clamp technique, which is considered as a gold standard for the investigation of cell activity as well as single ion channel. This technique utilizes glass micropipette to penetrate through the cellular membrane and perform potential measurement inside the cell using incorporated Ag/AgCl reference electrode. The pipette itself is filled with intracellular patch solution(I-patch) which connects with intracellular solution while keeping the cell alive and maintaining the normal cell behavior for the time of measurement. The pipette detachment, however, results in the stress for the measurement cell, which can also cause the cell death. Not only the intracellular activity can be measured using patch-clamp, but also electrical stimulation can be applied from the inside of the cell. Usually this method provides high signal-to-noise ratio. Even though the technique is robust and reliable, there are several fundumental limitations. Firstly, cells do not survive long-term patch-clamping experiments. Secondly, the method does not allow recordings from multiple cells simultaneously, since pipettes are large enough to put many of them in the microscope field of view. With the development of micro- and nanoelectronics a novel approach has emerged as promising method for non-invasive electrical activity monitoring on relatively large area with cellular or even sub-cellular resolution utilizing multiple channels. Among a variety of devices, multielectrode array (MEA) and FET are most commonly used for this purpose. MEAs have attracted much attention due to the fabrication simplicity, possibility of electrical stimulation using the same electrodes as well as long-term stability in culture medium [73]. Even though high-resolution MEAs have been developed, the signal-to-noise ratio (SNR) is still limited while electrodes are becoming smaller [74, 75].

This creates a number of challenges in terms of achieving cellular and subcellu-

lar resolution for recording functional signals. Silicon (Si)-based devices, on the contrary, fabricated using technology compatible with modern complementary metal-oxide-semiconductor (CMOS) process, possess a lot of advantages due to their unique properties, which have been demonstrated by extensive research over the past few decades. Furthermore, a transition from conventional planar devices to nano-scaled structures such as nanowires (NWs) may improve the sensitivity down to the single molecule level. An enhanced sensitivity of biosensors based on Si NWs was confirmed for a variety of biological test objects, including proteins, nucleic acids, and viruses [65, 76]. The characteristic sizes of such structures allow much denser packaging, resulting in higher spatial resolution. It should be emphasized that recent research on interfacing between living cells and nanoscale objects demonstrates improved interface properties, without cleft between a cell and nanoscale structure in comparison to large-scale planar devices [4]. Furthermore the investigations of gate coupling effect in nanowire transistors demonstrate the possibility of enhanced signal-to-noise ratio(SNR) for cellular recordings [77]. A critical aspect of reliable cellular activity recording using MEA or FET devices is the coupling efficiency between the cell and the device sensing area. To analyze the abilities of cellular electrical activity monitoring by recording device analytical models have been developed. Following the Hodkin-Huxley model [70] the electrical characteristics of excitable cells like neurons or cardiomyocytes can be described by the set of nonlinear differencial equations. An equivalent circuit of cellular membrane is represented in the figure 2.9 ,where C_m is the membrane capacitance, determined by the properties of lipid bilayer, g_{Na}, g_K,g_L are conductivities of corresponding channels through the membrane, E_{Na}, E_K,E_L are

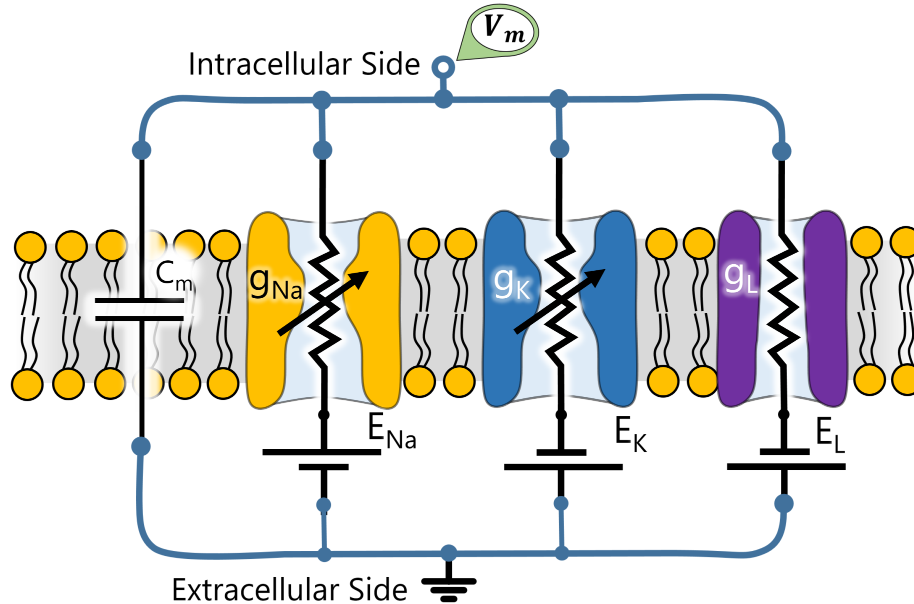

Figure 2.9: According to Hodgkin-Huxley model [70], the equivalent circuit of cellular membrane is represented by the membrane capacitance, C_m, pathways for ion transfer, represented by conductances, g_X, and voltage sources, corresponding to membrane potential formed by specific ions, E_X (X - stands for the specific ion, Na^+ , K^+ , and L - is the leakage channel). The membrane capacitance, C_m, is determined by the properties of lipid bilayer. The conductance of each channel is determined by concentrations and permeability of specific ions at each time point.

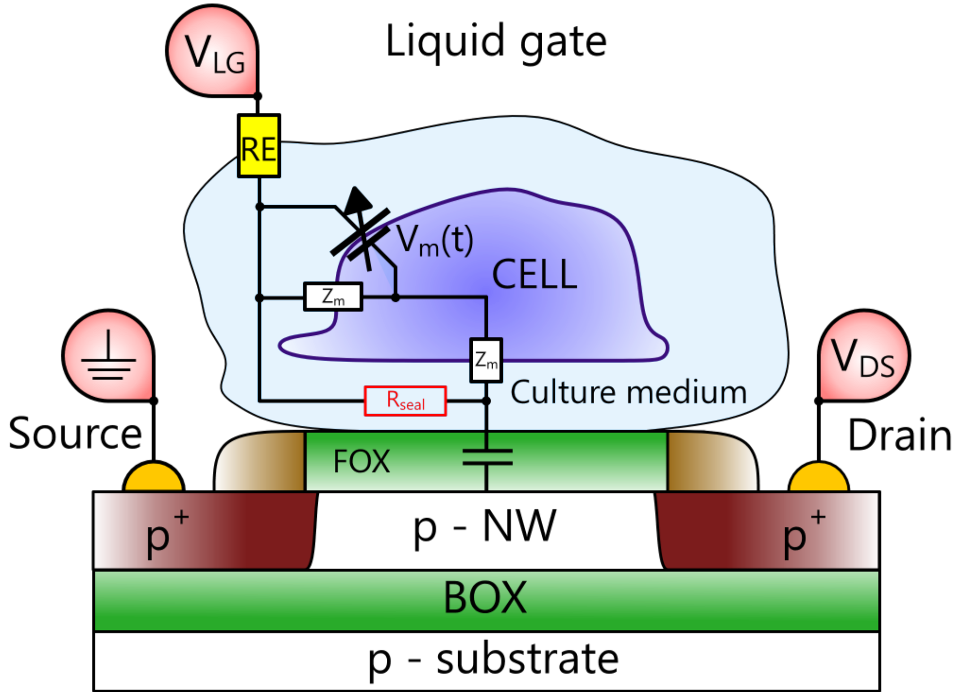

Figure 2.10: Schematic interface between the cell and nanowire FET. The higher values of sealing resistance, R_{seal}, represent the better coupling between the cell and electronic transducer, resulting in better signal transfer.

the potentials for each channel defined by the ion concentrations on both sides of the membrane.

A simplified representation of the cell interfacing the FET is shown in figure 2.10. The influence of cellular membrane potential change on the surface potential of the FET in the region of cell-transistor junction can be described by the following equation[78]:

$$\frac{dV_j}{dt} = \frac{C_M}{C_M + C_G}\frac{dV_m}{dt} - \frac{1}{R_{seal}\left(C_M + C_G\right)}V_j \tag{2.21}$$

,where C_M is the cell membrane capacity as described by Hodgkin-Huxley model, C_G is the gate capacitance of the FET, R_{seal} is the seal resistance.

Seal resistance reflects the quality of the cell-device coupling and is the most important parameter affecting measurement efficiency, determining the quality and the amplitude of recorded signals [79]. Typically action potential measured from neurons reach hundreds of microvolts [80]. R_{seal} depends on the distance between the cell and device surface, also called cleft, as well as sensing surface coverage by the cell. If sealing resistance is low, which means poor interface, the ionic currents inside the cleft will only slightly influence the surface potential of the sensor. Therefore the one of major challenges for extracellular electrophysiology is to achieve high sealing resistance, corresponding the good contact between cell and sensor surface. One possible way to address the issue is to utilize nanoscaled geometries and novel patterning. The nanowire FETs themselves satisfy the conditions by the nature and it has been shown that the cleft between nanowires and the cells is very small.

2.5 Noise Fundamentals

A variety of unusual effects take place when considering nanoscale objects such as nanowires, nanoribbons, nanosheets, core/shell devices. The understanding of underlying and fundamental physics require utilization of novel approaches. The method should be able to demonstrate and distinguish the impact of every material layer into transport properties of the entire system. Noise spectroscopy has recently emerged as a powerful tool for the investigation of transport features. In comparison to the standard methods this approach overcomes fundamental limits at nanoscale and does not require the fabrication of special structures, adjusted to the split capacitance-voltage methods [81, 82]. In general noise spectroscopy is known to be effective tool for understanding the main noise sources allowing to reduce or completely remove the reasons for exciting noise. Nowadays scientists draw more and more attention to noise considering it as a useful signal. This is mainly due to the fact that noise spectroscopy allows device characterization and transport properties analysis of nanostructures in nondestructive manner. In comparison to the bulk material structures on the basis of compositional material can express additional transport features reflected in noise spectra. As an example such structures can be represented by Si/SiO_2 structures, core-shell structures or in specific case semiconductor - organic passivation layers, metals or superconductors with passivation layers.

Noise in semiconductors and semiconductor-based devices can be described as fluctuation phenomena caused by random physical processes happening inside the material. Such fluctuations provide an information about any interactions within the system, about elementary particles taking part in the process as well as explain the abilities of the system to relax after perturbations, caused by such interactions. To describe the fluctuation phenomena the concept of spectral density is typically applied to fluctuating parameter $n(t)$ and defined as:

$$S_n(f) = \lim_{\Delta f \to 0} \frac{\overline{\Delta n^2(t)}}{\Delta f} \tag{2.22}$$

,where $\Delta n^2(t)$ is the variance of the fluctuating parameter $n(t)$ around the frequency f with the bandwidth of Δf. Typically current, I, or voltage, V, is considered fluctuating when dealing with semiconducting devices, therefore current, $S_I(f)$, and voltage, $S_V(f)$, spectral densities will be further analyzed.

The main task of noise spectroscopy is to figure out the origin of fluctuations using measured noise spectra. Often resulting spectra include several fundamental components corresponding to different physical mechanisms as it is shown in figure (2.11).

Noise properties are particularly important when considering detection applications such as biosensing. Often molecular attachment or action potential of electrogenic cells causes changes of sensor parameters, which are considered as a useful signal. Typically the magnitude of such response is very low, especially when speaking about ultra-low target molecule concentrations. Furthermore a transition towards real-time detection systems in a wide range of applications dictate a requirements of SNR to be higher than one. The ratio between useful signal amplitude and the noise level is a factor determining detection limits of the sensor. Considering nanowire FET biosensor the detection ability is determined by the transconductance(as defined by equation 2.13), g_m, as well as intrinsic noise of the device. Current fluctuations can be expressed as $\delta I = \delta I_S + \delta I_{fl}$, where δI_S is the result of surface potential change by δV_G caused by biological object and δI_{fl} is the

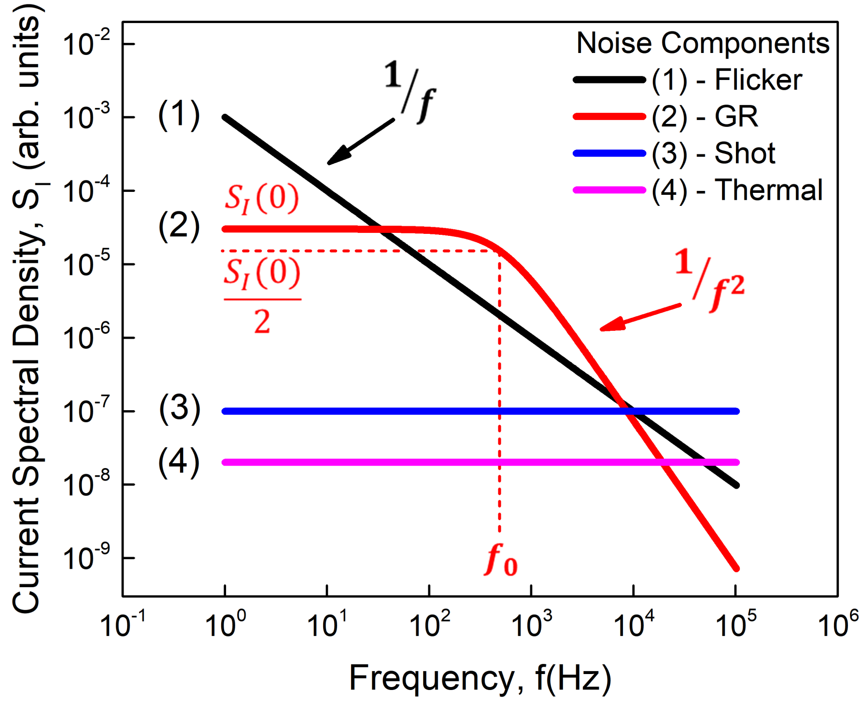

Figure 2.11: Schematic representation of the main noise components discussed in the chapter: flicker noise (1) with 1/f behavior, generation-recombination noise (2), where the plateau is followed by $1/f^2$ behavior, shot noise (3), and thermal noise(4) demonstrate frequency-independent behavior in a wide frequency range

.

noise related term. In such notation signal-to-noise ratio can be defined as:

$$SNR = \frac{\delta I_S}{\delta I_{fl}} \tag{2.23}$$

Because the impact of target biological objects on the current is usually extremely small, it is useful to consider equation 2.23 in terms of surface potential fluctuations,δV_G, and equivalent device noise at the input, δV_{fl}. The signal from sensors often undergoes filtering and frequency range restrictions where useful sensor response is observed. In this respect it is useful to switch into spectral representation of the equivalent input-referred noise [77].

$$SNR = \frac{\delta I_S}{\delta I_{fl}} = \frac{\delta V_{FG}}{\delta V_{fl}} = \frac{\delta V_{FG}}{\sqrt{\int_{f_1}^{f_2} S_U df}} = \delta V_{FG} \times \frac{g_m}{\sqrt{\int_{f_1}^{f_2} S_I df}} \tag{2.24}$$

,where S_I is the drain current spectral density, S_U is the equivalent input- referred voltage spectral density.

Therefore, to improve the detection abilities, simplify circuitry and lower cost signal-to-noise ratio should be carefully considered [83].

2.5.1 Thermal Noise

Thermal noise, also known as Johnson-Nyquist noise, is the result of random Brownian motion of the charge carriers in a semiconductor with resistance, R, at a certain absolute

temperature, T. Being a white noise by nature the power spectral density of thermal noise is independent on frequency up to a few gigahertz. The level of power spectral density (PSD) can be calculated as:

$$S_I(f) = 4kT/R \tag{2.25}$$

,where k is the Boltzmann constant, R is the differential resistance of the sample $R = dV/dI$, where V is the applied voltage, and I is the current through the sample. The spectral density does not depend neither on the current through the resistor nor on the material of the resistor. Thermal noise, however, can be used to analyze the effective carrier temperature, statistical fluctuations due to the finite number of carriers and their interactions with scattering particles [84].

2.5.2 Dielectric-Polarization Noise

A modification to Johnson-Nyquist noise has been made in terms of fluctuation-dissipation theorem by considering a complex impedance. For a lossy capacitor voltage spectral density has been derived to be:

$$S_V = \frac{2kTtg\delta}{\pi C_g f} \tag{2.26}$$

,where $tg\delta$ describes losses in the gate dielectric. From equation (2.26) voltage spectral density has obviously a 1/f dependence on the frequency. Dielectric-polarization noise concerns only ultralow-noise devices where trapping noise has almost no impact on the current fluctuations in the conductive channel[85]. For such devices together with regular thermal noise dielectric-polarization noise creates a thermal limit which addresses the challenge of the smallest sensitivity to surface potential changes.

2.5.3 Shot Noise

Shot noise, which is also white in nature, was conceptually introduced in 1918 by Schottky [86] and represents random independent transfer events of discrete charge carrier,e. It can be observed when the carrier flow is controlled by a potential barrier. The current power spectral density of the shot noise in relatively large NW diameters can be estimated according to Schottky equation:

$$S_I(f) = 2qI \tag{2.27}$$

,where q is the elementary charge and I is the current formed by the charge carriers being transferred. Current in the sample can be considered as a sum of short pulses due to discrete charge carriers randomly passing the potential barriers. If there is some correlation between pulses in a pulse sequence, then the deviation from the usual shot noise behavior is observed. The deviation can be registered, for example, when the interaction between electrons plays an important role. In such case, a decrease in noise can be registered which is a fundamental characteristic of any irregularity in the electron flow and reflects the quantum statistics of electrons in a single channel or multiple channels [87]. Usually the shot noise is registered at low temperatures, when the thermal noise is low enough and statistical fluctuations due to the finite number of particles can be detected.

2.5.4 Flicker Noise

The low-frequency part of the noise spectrum is of fundamental interest for the investigation of semiconducting devices. The appearance of different noise components depends strongly on the quality of semiconductor, features of fabrication technological process as well as physical processes happening in the structure and therefore are considered as excess noise.

Flicker noise is the dominant excess noise at low-frequency range of the spectrum. It represents the universal noise found in many systems, including electronic nanowire structures. Flicker noise is also known as $1/f$ (one over f) noise due to the characteristic behavior of spectral density as a function of frequency:

$$S_I(f) \sim 1/f^{\gamma} \tag{2.28}$$

, where γ is usually found to be around 1 in the interval from 0.7 to 1.3 for metallic and semiconducting nanowires. This component is typically investigated in the frequency range from 1 Hz to 10 kHz.[88–90] At higher frequencies flicker noise becomes lower than thermal noise level. Lower frequencies $1/f$ behavior is observed down to 1×10^{-6} Hz[91]. The origin of flicker noise is still under debates, however it is agreed that 1/f noise is the result of channel conductivity, σ, fluctuations [92]. The following equation can be used for evaluating the conductivity:

$$\sigma = nq\mu \tag{2.29}$$

here $n = N/WL$ is the concentration of free charge carriers, μ is their mobility, q is the elementary electron charge, W is the width and L is the length of the sample. From equation 2.29 the two parameters which can vary and influence the conductivity are the concentration and mobility. In this respect there are two main schools with different approaches for explaining the flicker noise.

$\Delta\mu$ model

The first, $\Delta\mu$ model, assumes that the charge carriers flowing in the volume of the sample are scattering on the acoustic fluctuations of crystalline lattice, known as acoustic phonons. The concentration of phonons also fluctuates with 1/f spectrum resulting in the charge carrier scattering and thus conductivity fluctuation with the same 1/f pattern. [88, 93, 94] Extensive investigations proved that this kind of noise is always present in many systems[88]. Hooge suggested that noise is caused by independent scattering events of charge carriers and mobility fluctuations of bulk carriers ($\Delta\mu$), which leads to $1/N$ dependence [88, 95]. Here N is the number of charge carriers. According to Hooge's empirical law:

$$\frac{S_I}{I^2} = \frac{\alpha_H}{Nf} \tag{2.30}$$

where α_H is the dimensionless Hooge's constant, which is used to quantitatively assess and compare the noise performance of NW devices. Here α_H/N describes the noise amplitude, A. $\alpha_H = 0.002$ was found in the first experimental studies of metallic systems at 300 K. However, later it was shown that this value can vary as a result of sample preparation, material, defect density, and other effects [88]. Typical α_H values for silicon are in the range from 5×10^{-6} to 2×10^{-3}. The Hooge's parameter may provide insights into the physical origin of the flicker noise and can be used as a dimensionless parameter to compare the noisiness of different systems. Analyzing equation 2.30 it is obvious that there is no

dependencies on the sample size, charge carrier concentrations. The fact indicates on the volume origins of the noise. Because of scattering on the lattice and mobility fluctuation Hooge's parameter can be written as:

$$\alpha_H \sim (\mu/\mu_{latt})^2 \tag{2.31}$$

,where μ_{latt} is the mobility limited by the lattice fluctuations. It should be mentioned that equation works on the assumption that all charge scattering process are independent and therefore result in the 1/f spectrum. Based on the Hooge's model equation explaining flicker noise in linear regime of SOI MOSFETs were derived[90, 92]:

$$S_I(f) = \frac{\alpha_H I^2}{f N_s Z L} \sim I \tag{2.32}$$

$$S_I(f) = \frac{\alpha_H q \mu^2 C_0 V^* V_{DS}^3 Z}{f L^3} \sim \frac{Z}{L^3} \tag{2.33}$$

$$S_{VG}(f) = \frac{q\alpha_H}{C_0 Z L f} V^* \sim \frac{1}{ZL} \tag{2.34}$$

,where N_s is the concentration of free charge carriers in the inversion layer, $V^* = (V_G - V_T h)$ - effective gate voltage.

ΔN model

Another model, introduced by McWhorter, describes 1/f noise as the result of the interaction between flowing charge carriers and traps located on the interface between semiconducting channel and dielectric layer[96]. The charge carriers are getting captured onto the traps causing the fluctuation of their number, ΔN. Each independent capture/emission act to/from the trap results in the Lorentzian-shape component:

$$S_I(f) = A_{GR} \frac{\tau_T}{1 + (2\pi f \tau_T)^2} \tag{2.35}$$

. Here $A_G R$ is the amplitude coefficient, $\tau_T = \tau_0 exp(x/\lambda)$, τ_0 - tunneling time constant, $\lambda = \sqrt{\hbar^2/2m_z^*\phi_B}$ is the tunneling parameter, m_z^* - effective electron mass in the dielectric perpendicularly to the current flow, ϕ_B barrier height which charge carriers should overcome to be captured onto the trap, $\hbar$ - Planck constant. Typical values for Si/SiO_2 interface are $\tau_0 = 1 \times 10^{-10}$ sec, $\lambda = 1 \times 10^{-8}$ cm. The superposition of all events happening on the traps which are uniformly distributed into the depth of the dielectric, x, starting from the interface as well as over energy, E, results in the 1/f noise[97]. It should be emphasized that the interactions between traps should be excluded, otherwise the resulting spectrum would look like a Lorentzian. According to the McWhorter's model the input referred noise in strong inversion is defined as:

$$S_{VG}(f) = \frac{kTq^2\lambda N_{ot}(E_F)}{f Z L C_0^2} \sim \frac{1}{ZL} \tag{2.36}$$

,where $C_{ox} = \varepsilon_{ox}/t_{ox}$ is the capacity of the dielectric layer, ε_{ox} is the dielectric permittivity, Z-channel width, $N_{ot}(E_F)$ is the oxide trap concentration which take part in the interactions (located in the range of several kT from Fermi level, E_F) This equation shows

the independence of the input-referred noise on the applied gate voltage and allows to estimate the active trap concentration.:

$$N_{ot} = S_{VG}(f)\frac{fZLC_0^2}{kTq^2\lambda} \tag{2.37}$$

When traps are non uniformly distributed in the depth of the dielectric, the spectrum will follow the law $S_I \sim 1/f^{\gamma}$, where $0.8 < \gamma < 1$ or $1 < \gamma < 1.2$. The input fluctuations can be converted into the current fluctuation using formula:

$$S_{VG}(f) = S_I(f)/g_m^2 \tag{2.38}$$

,where $g_m = \mu C_0 V_{DS}\frac{W}{L}$ is the transconductance of the FET. The current fluctuations can be written as:

$$S_I(f) = \frac{kTq^2\mu^2 V_{DS}^2 Z\lambda N_{ot}(E_F)}{fL^3} \sim \frac{Z}{L^3} \tag{2.39}$$

From equation 2.39 we can conclude that for uniform trap distribution the current spectral density will be determined by the mobility, $\mu(V_{FG})$.

Combination of Flicker Noise Mechanisms

Any model has its own application boundaries. McWhorter‘s model describes well the noise behavior for n-type channel where $S_{VG} \neq S_{VG}(V^*)$. On the other hand for p-type channel devices the input-referred noise typically increases with gate voltage increase. According to ΔN model this would indicate on the nonuniform distribution of traps in the dielectric. However the fact that p-type channels works more through the volume of the device leads towards the application of the other, $\Delta\mu$, model. Indeed because of increased distance between inversion layer and Si/SiO_2 interface the interaction of charge carriers with traps decreases whereas the barrier height increases. This explains lower flicker noise in p-type channel devices. It should be emphasized that it has now been established that the origin of 1/f-noise can be switched by means of the gate voltage applied from number fluctuations to mobility fluctuations in the NW structure with a characteristic size of about 50 nm [77]. Many efforts have been made to determine the applicability boundaries of one or the other theory of flicker noise. Meanwhile additional models combining some assumptions of ΔN and $\Delta\mu$ models arose, namely correlated ($\Delta N\Delta\mu$) and uncorrelated ($\Delta N + \Delta\mu$) models.

Uncorrelated Model

This model takes into account an independent impact of both ΔN and $\Delta\mu$ fluctuations on the flicker noise formation. The decisive factor indicating on the dominant mechanism remains the dimensionless Hooge’s parameter. Therefore several ranges can be pointed out (see figure 2.12):

- $\alpha_H \leq 2 \times 10^{-6}$ corresponds to the $\Delta\mu$ model;
- $2 \times 10^{-6} \leq \alpha_H \leq 10^{-3}$ the impact of both fluctuation types is observed;
- $\alpha_H \geq 10^{-3}$ corresponds to the surface ΔN noise. In this range all imperfections of the fabrication technology are observed as increased surface trap density. Modern SOI FETs with nitrated and high-k dielectrics belong to this area judging by the noise level.

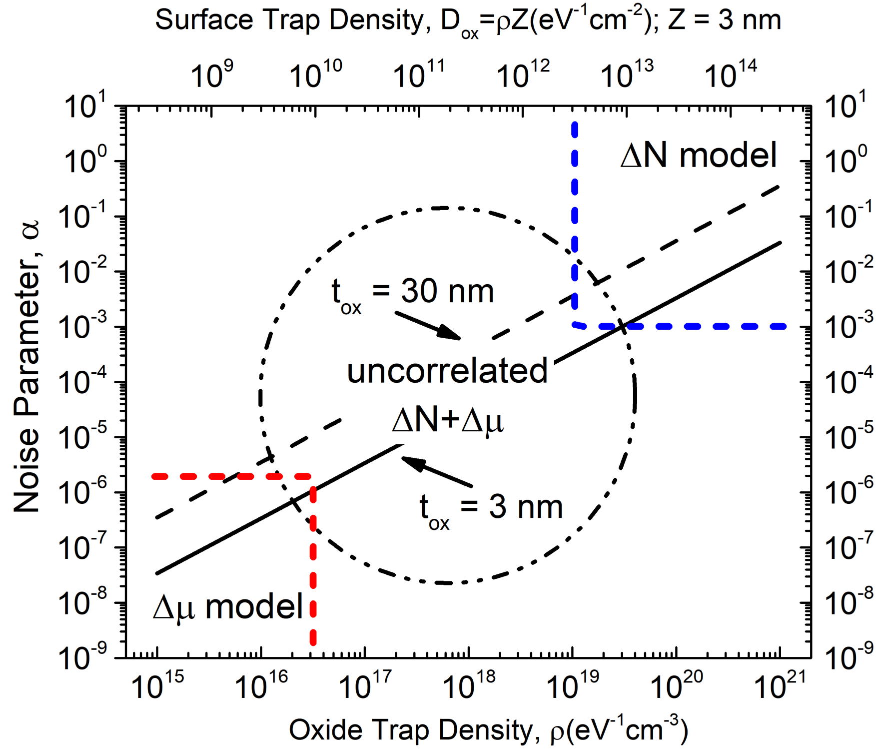

Figure 2.12: Noise parameter α versus oxide trap density calculated for oxide thicknesses of $t_{ox} = 3\,\text{nm}$ and $t_{ox} = 30\,\text{nm}$. Three regions can be highlighted, where mobility fluctuations are dominant, where number fluctuations are dominant and the region where one of uncorrelated noise sources can be dominant. Adapted from [90]

Correlated Model

Another approach takes into account experimental findings indicating on the correlated manner of ΔN and $\Delta\mu$ fluctuations[98–100]. The correlated model assumes that traps in the gate dielectric interact with the channel through capture and emission of charge carriers while changing scattering intensity within the channel. This means that changes in the charged state of the trap modulate the scattering cross section as well as influcence on the mobility of the charge carriers withing the channel. The following equation describes the current spectral density including aforementioned processes:

$$S_I(f) = \frac{kTI^2\lambda}{fZL}\left(\frac{1}{N_s} \pm \alpha_{sc}\mu\right)^2 N_{ot}(f) \sim \frac{1}{ZL} \tag{2.40}$$

,where $\alpha_{sc} \sim 2 \times 10^{-15}\,\text{V s}$ is the scattering parameter showing the influence of trap coulomb scattering on the mobility[99]. The sign under the brackets is selected depending on the charge state of the trap. The neutral center will support the mobility increase and thus "-" is appropriate in this case, otherwise "+" should be selected. From equation (2.40) one should expect the quadratic dependence of current spectral density, $S_I(f) \sim (V^*)^2$. Input referred noise in this case is described by the formula:

$$S_{VG}(f) = \frac{q^2kT\lambda N_{ot}(E_F)}{ZLC_0^2 f}\left[1 \pm \alpha_{sc}\mu C_0 V^*/q\right]^2 \sim \frac{1}{ZL} \tag{2.41}$$

It should be emphasized the mobility in the channel is limited by the coulomb scattering on the ionized impurities within inversion layer, on the charge captured at the interface, on the phonons and surface roughness. All the components depend on the temperature and electrical field adding physical sense to the $\Delta\mu$ part. The quadratic dependence of $S_I(f)$ might have a higher power when quantum-mechanical effects come into play[101, 102].

2.5.5 Generation-Recombination Noise

Generation-Recombination noise is a result of the individual random events of generation and recombination between one of allowed bands and traps in the bandgap of semiconductor. Such process causes the resistance modulation resulting in the current fluctuations with spectral density:

$$S_I(f) = \frac{S_I(0)}{1 + (2\pi f \tau)^2} \tag{2.42}$$

,where $S_I(0)$ is frequency-independent part of the spectral density $S_I(f)$, $\tau = 1/(2\pi f_0)$ is the fluctuation relaxation time constant, f_0 is the characteristic cutoff frequency of Lorentzian. It is seen from 2.42 that the spectral density has a plateau with the magnitude of $S_I(0)$ at frequencies $f \ll f_0$ and becomes frequency-dependent as $S_I(f) \sim 1/f^2$ at frequencies $f \gg f_0$. Investigation of generation-recombination (GR) noise using noise spectroscopy allows to study the trap density, their energy level, capture cross sections, etc. Recently, it was shown that the frequency shift of the GR noise component is also related to protein binding to the NW surface [103].

2.5.6 Random Telegraph Signal Noise

Scaling transistors down is the primary method to achieve better performance of microprocessors and memories. The miniaturization of transistors, in particular nanowires, leads to decreasing the effective gate area. In turn the amount of oxide traps which take part in the charge carrier exchange processes decreases. Experimental findings demonstrate that flicker noise generated by traps in the gate dielectric splits into several randomly distributed by frequency GR components as a result of downscaling process in submicron and nano-sized structures.[104]. Following the idea of defect number decrease at some critical area a single trap can influence on the current flow. The fact is also widely known as single trap phenomena. In this case current through the channel behaves similarly to random telegraph signal with two stable states corresponding to the charge carrier being captured or emitted from the trap(see figure 2.13(a)). random telegraph signal (RTS) fluctuations are characterized by average capture and emission times, the time which system spends before the carrier capture, τ_c, and the time before emission, τ_e, correspondingly. The histogram of such current fluctuations is shown in figure 2.13(b). Each stable state in the current fluctuations corresponds to the peak on the histogram curve and can be fitted as Gaussian distribution which is related to other fluctuations present in the systems including thermal noise fluctuations. Typically behavior of capture and emission times are described in terms of Shockley-Read-Hall (SRH) dynamics model. However in the case of strongly confined SOI FETs the behavior of capture time on the carrier concentration may vary from SRH behavior and become much stronger [1, 105–107]. The probability that the trap is occupied by an electron is given as:

$$g = \tau_e \,/\, (\tau_e + \tau_c) \tag{2.43}$$

Two level current fluctuations result in Lorentzian-shape spectrum(figure 2.13(c)) which can be described using Machlup equation[108]:

$$S_I(f) = \frac{4\,(\Delta I)^2}{(\tau_c + \tau_e)\left[\left(\frac{1}{\tau_c} + \frac{1}{\tau_e}\right)^2 + (2\pi f)^2\right]} \tag{2.44}$$

,where ΔI is the RTS amplitude, τ_c and τ_e are the trap capture and emission times and f is frequency. Analysis of RTS noise in various working regimes of device at different temperatures gives the information about single traps, allows to determine their energy levels, spacial location as well as the origin. There are several approaches for extracting useful information such as capture and emission times from measured RTS fluctuations. First one assumes relatively large signal-to-noise ratio and RTS amplitude. In this case it is possible to extract capture and emission times by averaging times in each state calculated directly from the timetrace. Another approach can be used when signal-to-noise ratio is small. This method involves analysis of both time and frequency domain data. To extract capture and emission times a system of equations is used:

$$\tau = 1\,/\,2\pi f_0 \tag{2.45}$$

$$\frac{\tau_c}{\tau_e} = \frac{Counts(capture)}{Counts(emission)} \tag{2.46}$$

$$\tau = \frac{\tau_c \tau_e}{\tau_c + \tau_e} \tag{2.47}$$

As RTS deals with single charge carriers this phenomenon becomes more popular in a number of research fields including quantum information processing and biosensing.

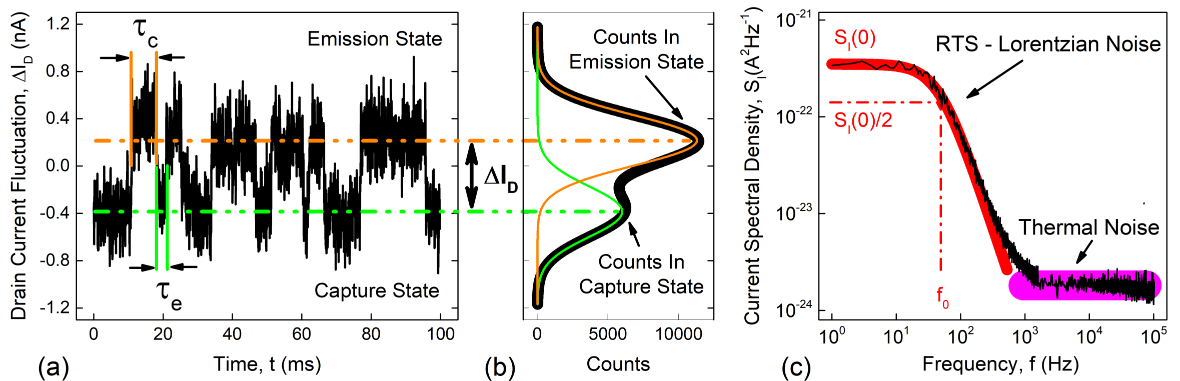

Figure 2.13: An example of random telegraph signal fluctuations. (a) Typical recorded timetrace with two current levels, corresponding to capture and emission states of the trap, ΔI_D is the amplitude of the RTS fluctuations. (b) Histogram of recorded timetrace demonstrating two distinct peaks, corresponding to each stable state in RTS fluctuations. (c) Noise spectrum corresponding to recorded timetrace. The Lorentzian-shape component is caused by the RTS fluctuations.

2.5.7 Analysis of Noise Components

The investigation of each individual noise component allows to extract an important information about the device performance and drives a fabrication technology towards improved device parameters, decreasing noise. In addition noise spectroscopy allows to find optimal operation regimes of FET devices, where profit for signal-to-noise ratio is achieved by lowering the overall noise of the system . Such situations are specifically desirable for any kind of amplifiers as well as sensors. Usually measured spectra contain several overlapping components, which simultaneously contribute to the noise level in the entire frequency range. Therefore each individual component has to be extracted from the spectra and analyzed separately. This can be achieved in two possible ways. First is to find the operation regime of the FET, where the interesting component is more pronounced and all the rest are low enough or completely suppressed. This is, however, difficult to achieve in many cases. Therefore, we often use the second approach. The procedure relies on the fitting of the noise spectra to customly created model, which contains all necessary noise components. The noise components with different origins were experimentally found to be independent on each other and, therefore, the overall noise can be considered as a sum of all present components. Such approach is implemented in the custom software developed during the work and described in section 3.2.

Chapter 3

Materials, Methods, and Setup Development

The development of biosensing platform based on field-effect transistors (FETs) requires a comprehensive tool set for the investigation of transport phenomena. In particular, at nanoscale, where device properties change very quickly following the external conditions, high accuracy measurements with precise control over the data acquisition process are required. For the transport evaluation of fabricated nanostructures, we utilize current - voltage as well as noise spectroscopy. The ability to detect target objects from the solution is the major task of a biosensor. To achieve the result the object has to be captured as close to the sensor surface as possible. Surface modification with specific chemicals, providing special linker groups allows to bind the target object from the solution and immobilize it next to the surface of the sensor, enabling to identify the binding event. In addition, the investigation of living systems (e.g. cardiac cells of neurons) is not possible without visualization techniques enabling to highlight different properties and aspects including live and dead cells as well as calcium content in cells and mitochondrial membrane potential.

In this chapter, we explain the key points in the development of measurement setups for the complex analysis of fabricated nanostructures. The software for setup control and further data analysis was developed using Python(Python, version 3.4.3) programming language in combination with Qt Framework (PyQt, version 4.11.4). A set of packages used for the development are mentioned in appendix C. We present the developed protocol of Si nanowire (NW) FET surface modification for the detection of cardiac troponin I using antibody-antigen reaction. Finally the methods of cardiomyocyte cell culture on the chip and fluorescent imaging techniques for live-dead staining as well as calcium content and mitochondrial membrane potential visualization are described.

3.1 Current - Voltage (I-V) Characterization of FETs

Current - Voltage (I-V) characterization was used for the device quality control and parameter extraction. Typically silicon-on-insulator (SOI) FET devices have 4 terminals, namely source, drain, front(or liquid) and back gates. The characterization consist of measuring output (dependence of drain current, I_D, on drain-source voltage, V_{DS}, at different liquid and back gate voltages, V_{LG} and V_{BG}) and transfer characteristics(dependence of drain current, I_D , on liquid or back gate voltage,V_{LG} or V_{BG} , at different drain-source voltages, V_{DS}). Current - voltage characterization was performed using two or three

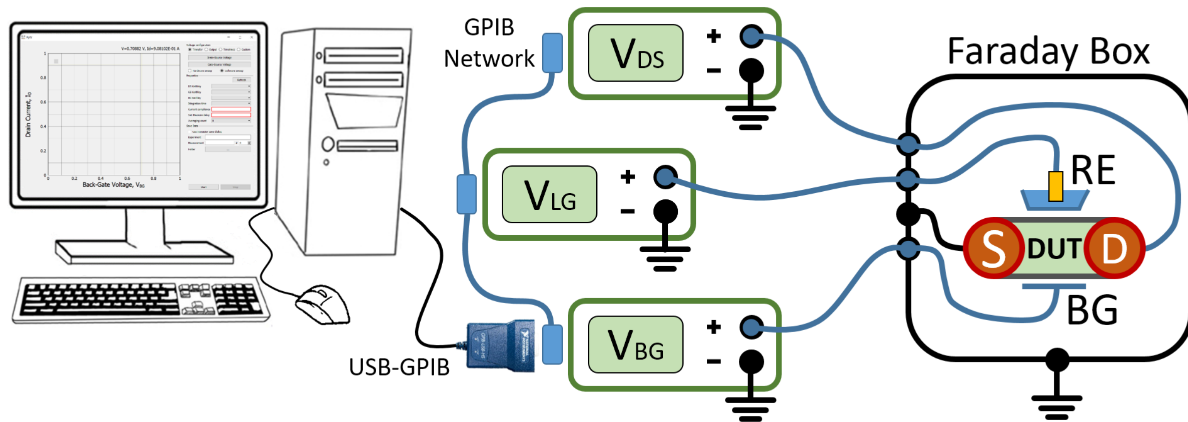

Figure 3.1: Schematic representation of I-V measurement setup. Device under test (DUT) is placed inside the Faraday box, which also serves as a common ground for all measurement devices. Source contact is connected to ground, other terminals are connected to corresponding source-meter units to set the voltage and measure current. Back gate contact is not always required therefore it can be omitted.

source-meter units (SMUs) as it is show in the figure 3.1 depending on the liquid- or back-gate characterization required. Device under test (DUT) is placed inside the Faraday shield formed by the continuous covering metal box which prevents the disturbances of possible external electromagnetic fields. Typically drain-source and gate-source voltages are applied using Keithley 2430 and Keithley 2400 correspondingly. Both of them correspond to 2400 series devices representing the Source Meter class with high-precision, low-noise and highly stable DC power supply together with low-noise and high-impedance multimeter. Devices allow simultaneous voltage sourcing and current measurement which allows evaluation of output and transfer curves for FET devices as well as measurement of leakage currents. To utilize available features of Keithley source-meter units and perform high-quality DUT characterization we developed a software package with the code name PyIV which runs on the computer and communicates with SMU devices using SCPI command protocol throught the GPIB-USB adapter. The program employs Keithley SMUs for measuring output and transfer curves. The simple user interface allows to select the SMU for setting drain-source and gate-source voltages, integration time, current compliance, set-measure delay and averaging (see figure 3.2). Important option is the possibility of hardware sweep which helps to eliminate the influence of data transfer between SMU and computer. Save data group box gives a flexibility to name the measurement and group them into the experiments. With switched advanced saving option on one can obtain more sophisticated name selection by introducing wafer and chip names and transistor number. After performed measurement the data is saved into selected folder in the way that each measurement is stored in separate ".dat" file and experiment summary is collected in the MeasurementData_.dat file. Such data organization provides easy access to any measurement made and thus is simple to analyze. For this purpose another package called IV_anallysis was written. It allows to extract the transconductance and calculate the channel resistance with respect to transistor configuration provided as the layout file. Developed software solution allows for automated transistor characterization. The characterization of all devices was carried out using the setup described previously. Structures used in the work have the possibilities of front and back gating. All voltages were applied agains the grounded source. Drain-source voltage was set in the range from 20 mV to

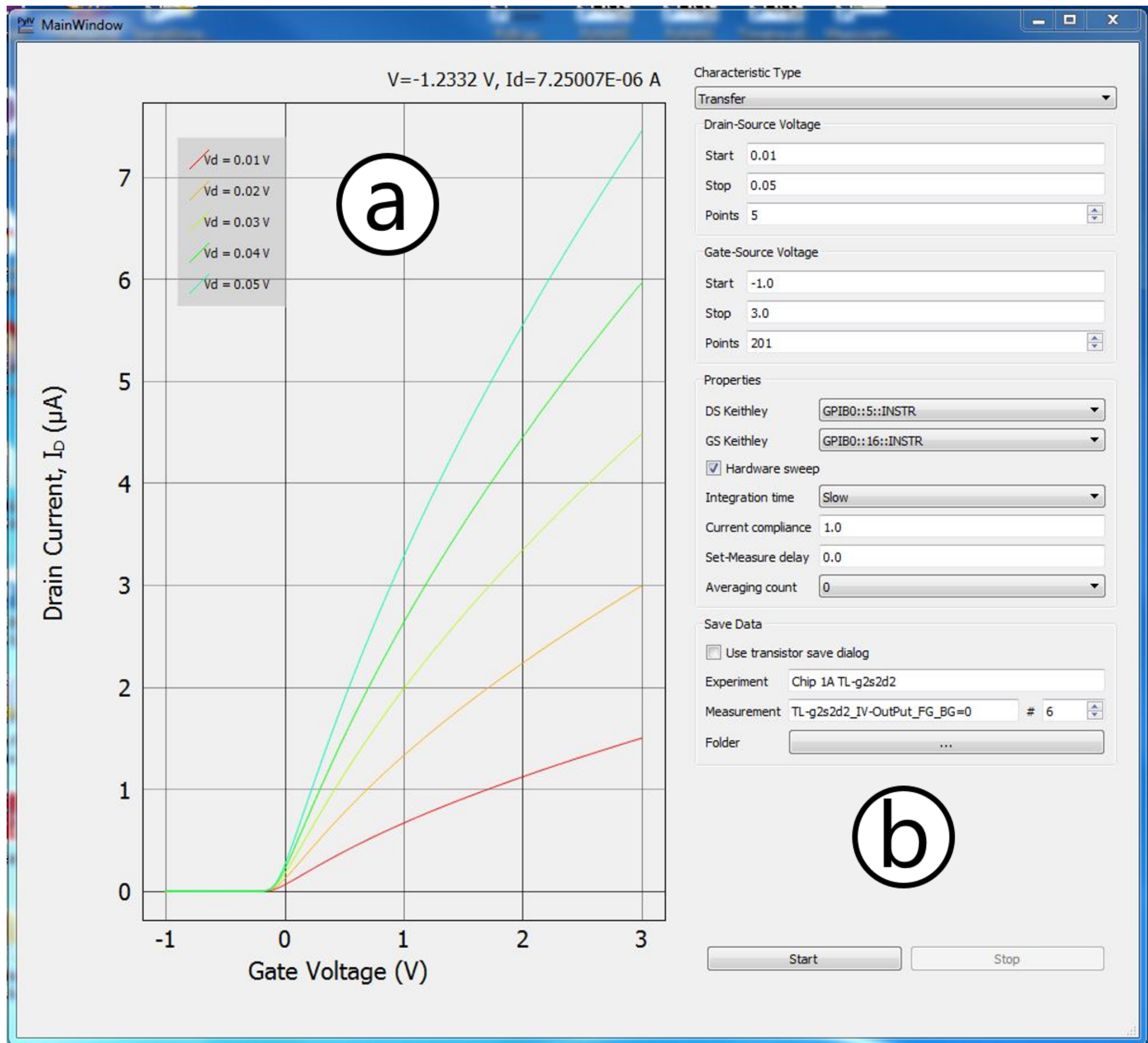

Figure 3.2: The user interface of developed program, PyIV, for the I-V characterization. The program is capable to perform output and transfer curve measurements, depending on selected characterization type. (a) The data plot, showing typical transfer curves at various drain-source voltages, measured for FET device. (b) The panel for selecting the sweeping parameters and SMU configurations.

100 mV to keep devices in linear operation mode or around 1 V for the saturation regime. In liquid-gate configuration gate voltage was applied against an Ag/AgCl reference electrode in the range from 0 V up to 5 V in positive or negative direction depending on the structure type ($n^+ - p - n^+$ or $p^+ - p - p^+$). As an electrolyte we used phosphate-buffered saline (PBS) with pH 7.4 and salt concentration of $\approx 10mM$ to make the conditions close to physiological. While the measurement reference electrode is dipped into electrolyte on top of the device or is built into the tubing of the microfluidic system. In the back-gate configuration the gate voltage was applied to the corresponding terminal, which typically is connected to the substrate of a device. On the contrary to the liquid top gate dielectric the one on the back gate is often much thicker. Therefore the range of applied voltages is extended approximately by one order of magnitude and reaches up to 15 V The results of measured characteristics allow to judge about the quality of fabricated devices and extract

important characteristics such as transconductance and threshold voltage. Furthermore at this stage the structures demonstrating leakage currents will be omitted from use.

3.2 Noise Spectroscopy

Another investigation activity involves noise spectroscopy of fabricated nanostructures as a powerful tool for transport properties characterization. The main noise properties were discussed in section 2.5. High precision and fine measurement process control are extremely important especially when speaking about low-dimensional systems where the processes are tending to change very fast with changing of external parameters such as applied voltage. For this purpose fully automated noise measurement setup (PyFANS) was developed aiming to perform the complete automation of the measurement process in order to provide high degree of measurement process automation and to eliminate the human influence on the process, thus increasing accuracy. The setup development was a continuation of the work, performed by Dr. Viktor Sydoruk [109] and Dr. Sergii Pud [110], and was also inspired by their suggestions and ideas. Further we will highlight the main point and issues during the development of hardware providing the fine tuning of applied voltages and controlling software parts.

The FANS system was built over the commercial data acquisition (DAQ) system Agilent U2542A as the main controlling unit. The module offers multifunction capabilities, in particular it can be used as a multimeter or a scope. Furthermore the module is able to source certain voltage level or even a defined waveform. DAQ module itself has 4 simultaneous analog input channels with 16-bit resolution and acquisition speed of up to 500 kSa/s, two 12-bit analog output channels and 24-bit programmable TTL input/output channels. The complete automation of noise measurement process, however, requires the system to be able to record both AC and DC coupled signals as well as source voltage to more than 2 channels in multiplexing manner. Therefore FANS system was equipped with the extension box for DAQ device schematically shown in figure 3.3.

The box allows to multiplex each of two DAQ output channels to 8, which are used to control motorized potentiometers (marked as M in figure 3.3), polarity switches, relays in the circuit and other controllable systems which require arbitrary voltage levels. All controlling signals are generally shown as control bus in figure 3.3 and yellow lines indicate a control flow direction to the units in the circuit. The box also enables to switch DAQ input to AC or DC coupled mode which depending on the selected configuration can serve as a voltmeter or a scope. All channels are switched using bipolar relays providing good and noiseless contact. The control over the FANS extension box is performed through the TTL-compatible digital outputs of the DAQ device. Major points required for DUT characterization are highlighted with a green spot in the figure 3.3 and green lines indicate the connection to measurement bus.

To set the working point of the DUT the system measures V_{main}, V_{DS}, V_{LG}, and uses them as a feedback loop for motorized potentiometers to set a desired voltage values. By measuring V_{main} and V_{DS} for selected load resistance, R_{load}, we can calculate the current through the channel of DUT as for simple voltage divider (as follows from figure 3.4(a)): $I_D = (V_{main} - V_{DS}) / R_{load}$. The load resistance is a high-precision, low-inductance resistance box with a possibility of nominal value change in the range from 1 Ohm to 1MOhm. Such circuit configuration allows to select the optimal working regime for measurement system, which often depends on the resistance of DUT.

Noise measurements were performed using analog input channel in AC configuration.

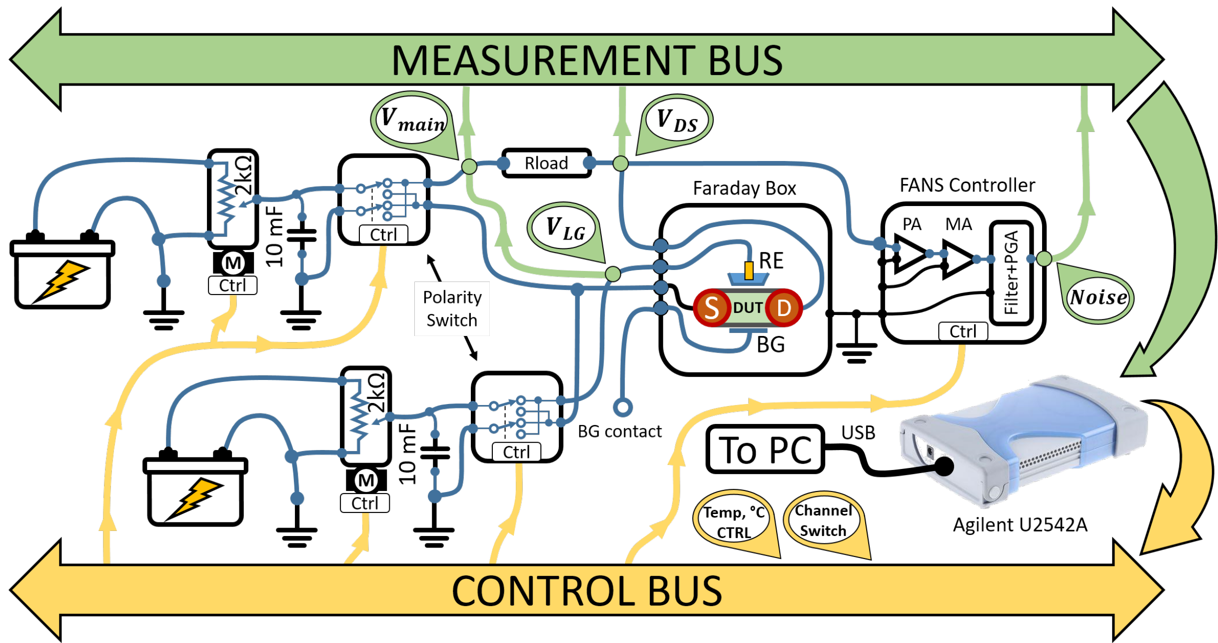

Figure 3.3: Schematic representation of FANS noise measurement setup. It incorporates circuitry for setting the working point of DUT in low-noise manner, using batteries and potentiometers. The system includes a set of amplifiers and filters as a part of FANS controller. Two buses, measurement and control, are used to perform voltage measurements on the required terminals and perform the control over the measurement circuitry. The control bus also enables the temperature control as well as measurement channel selection. The entire system in powered by Agilent U2542A data acquisition system.

Firstly signal was preamplified using an ultra-low noise homemade amplifier with gain of 172, since the first amplification step is very important for a proper noise measurement [109]. Then signal is passed through the commercial amplifier ITHACO 1201 with a variable gain from 1 to 100k. Further signal is amplified with low-noise general purpose

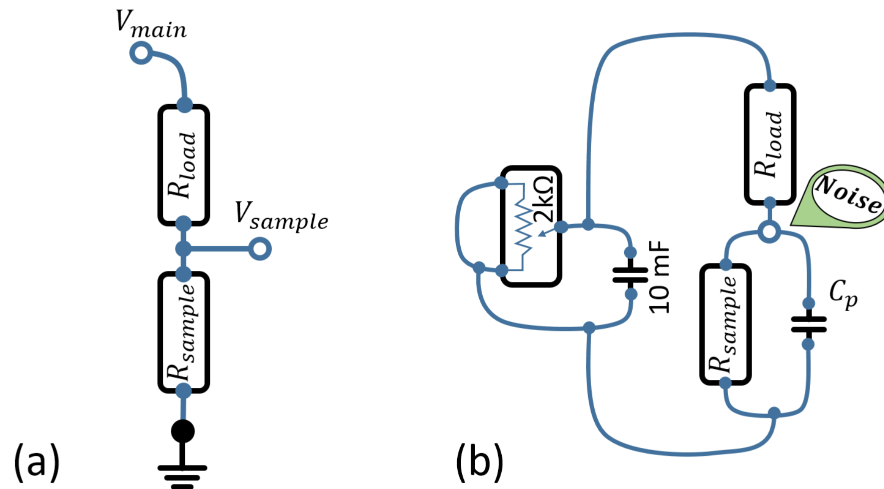

Figure 3.4: (a) A simplified circuit for setting voltage to the terminal of DUT. (b) The equivalent circuit of the DUT, during the noise measurements.

programmable-gain amplifier PGA-103 which are capable of digitally selected 1,10 and 100 times signal amplification. At maximum amplification the noise level is as low as 16 $nV/\sqrt{Hz}$ at 10 Hz. Afterwards signal is filtered using digitally controlled antialiasing continuous time filter LTC 1564 with possible cutoff frequency ranging from 10 kHz to 150 kHz.Sampling rate was set to maximum of 500 kHz allowing the best possible time resolution for this hardware. In this respect the cut-off frequency was selected to be a 100 kHz which is enough for the low-frequency noise analysis and satisfies Nyquist theorem. Parasitic capacitance (around 350 pF) which comes mainly from the cables and connections together with equivalent circuit resistance form an RC circuit which results in a roll-off in the high-frequency range. At large sample resistance the equivalent resistance is defined by the load resistance. For $R_{load} = 5\,k\Omega$ the cuto-off frequency is around 91 kHz, and it should be taken into account.

Prior to noise measurements the system has been calibrated to exclude the influence of amplification cascade which also has non-thermal noise behavior at low frequencies because of used semiconductor components in the circuitry.

The voltage noise, $S_V^{(DUT)}$, cased by the DUT is extracted using the following equation:

$$S_V^{(DUT)}(f) = \frac{\dfrac{S_V^{(meas)}(f)}{k_{(amp)}(f)^2} - S_V^{(amp)}(f)}{k_{(preamp)}(f)^2} - S_V^{(preamp)}(f) \tag{3.1}$$

,where $S_V^{(meas)}$ is the voltage noise measured with FANS system, $S_V^{(preamp)}$ and $S_V^{(amp)}$ are the calibration curves for homemade amplifier and following amplification cascade, respectively, $k_{(preamp)}$ and $k_{(amp)}$ are the amplification gains for homemade amplifier and following amplification cascade, respectively. A picture of assembled setup is shown in figure 3.5. Assembled system is shown in the following figure. Equivalent circuit for AC signal recording is presented in figure (3.4(b)). Potentiometer together with 10 mF capacitance introduce negligibly small impact on the equivalent impedance of the circuit (less than 4.2 Ω at frequencies greater than 1 Hz).

Therefore the equivalent resistance of the circuit (figure 3.4b) can be calculated as parallel resistor connection:

$$R_{eq} = \frac{R_{load} Z_{sample}}{R_{load} + Z_{sample}} \tag{3.2}$$

,where R_{load} is the load resistance and Z_{sample} is the differential resistance of the sample. In this respect when circuit works in open regime, $R_{load} \gg Z_{sample}$ thus equivalent resistance will be defined by Z_{sample}. Otherwise, when $R_{load} \ll Z_{sample}$, i.e. in shortcut mode, equivalent resistance will be defined by R_{load}. The fact should be taken into account when performing noise measurements to simplify further data analysis. Often for noise evaluation current spectral density, S_I, is required. The value can be recalculated form measured voltage spectral density as:

$$S_I = \frac{S_V}{R_{eq}^2} \tag{3.3}$$

,where R_{eq} is equivalent resistance as defined by equation(3.2).

FANS setup is controlled using software, called PyFANS, developed using Python programming language(Python version 3.4.3). The main window of developed user interface is shown in figure 3.6.

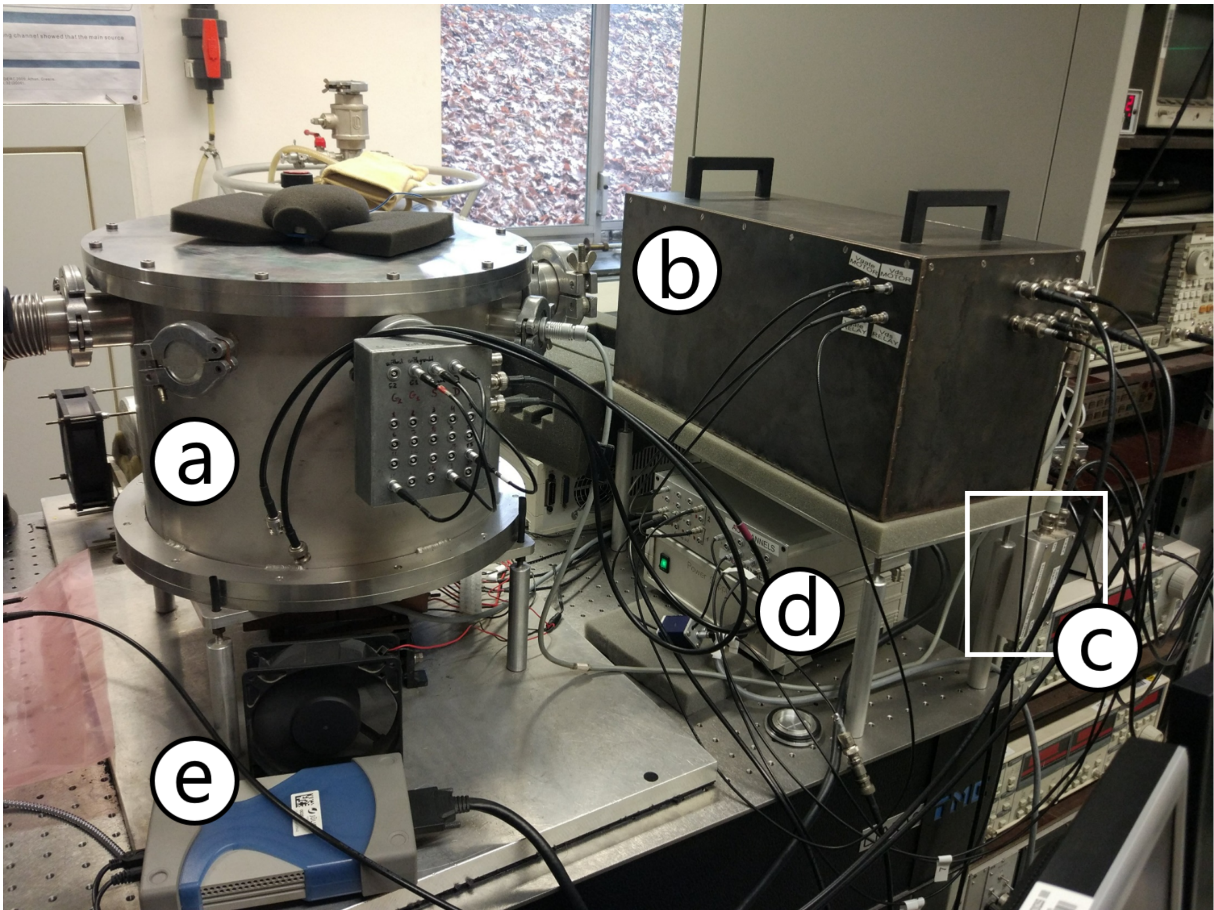

Figure 3.5: A photo of assembled FANS noise measurement setup. (a) Vacuum chamber for measurements at low temperatures. The system is based on the Stirling cooler, and is capable to reach as low as 70 K. (b) Enclosed in the Faraday box circuitry for the voltage control and noise measurement, including batteries and high precision set of resistors. (c) The homemade ultra-low noise amplifier. (d) The circuitry to control the voltage, applied to DUT, as well as amplifiers and filters for noise measurements. (e) Agilent U2542A DAQ system, controlling the noise measurement procedure.

Software allows to control all main components of the setup and is responsible for data acquisition and storage. Program automates all major processes in noise measurement experiment including setting voltages. This is organized through the motorized potentiometers which can be controlled with the feedback loop. In the settings section of PyFANS main window there are options which allow to define voltage ranges where noise spectra should be acquired. The system allows to record timetrace as well as noise spectra which are calculated using Fourier Transform in real time. The resulting noise spectrum is the average of a number of measured spectra predefined in settings section. The error at each point of noise spectrum inversely proportional to square root of the number of averaged spectra the resulting spectrum. Therefore for precise measurement it is recommended to use ≥ 100 spectra. Noise spectrum is a combination of two frequency ranges: 1 Hz to 3000 Hz with the frequency step of 1 Hz and 3 kHz to 250 kHz with frequency step of 10 Hz. This information is enough for a proper analysis of the noise spectra, while keeping the measurement file size acceptable for storage.

The information about each measurement is displayed in the Measurement Data section on the main window of PyFANS. Furthermore visual information can also be displayed

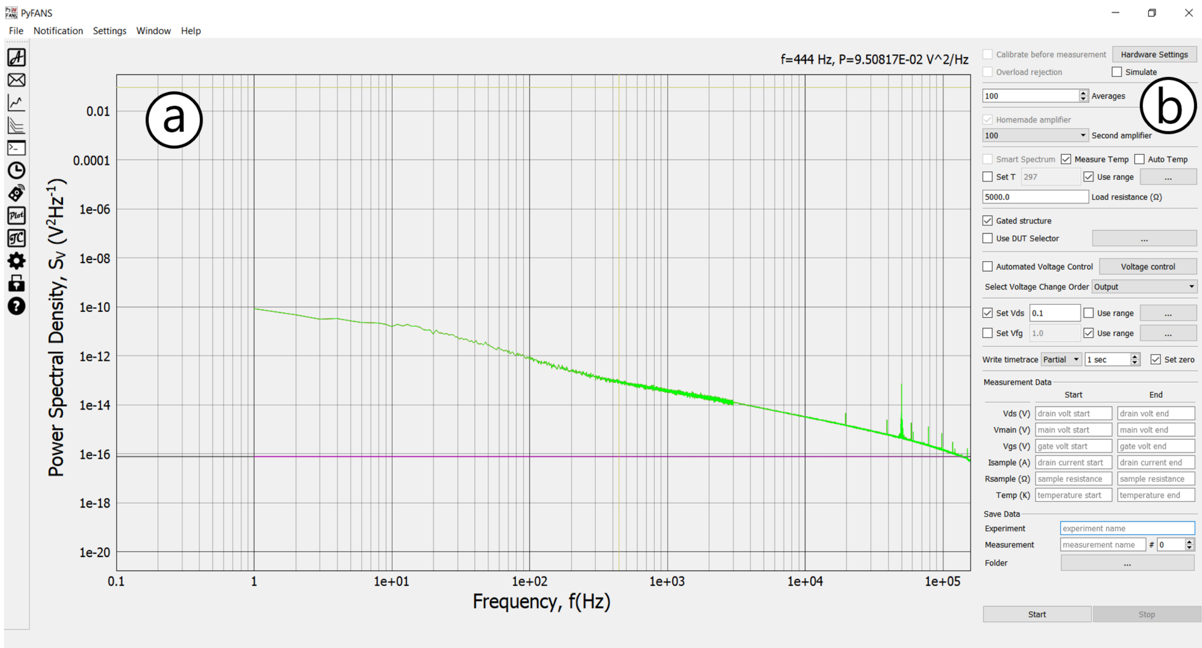

Figure 3.6: The main window of the noise measurement program, PyFANS, responsible for the complete automation of the process. Measured noise spectra appear in the plot(a). The configuration and measurement parameters can be set in the panel on the right hand side (b). An important measurement data is also displayed in the section "Measurement Data".

while measurement. It includes the noise spectrogram which shows the dynamic changes in noise spectra with time. This is interesting for observation of Lorentzian-shape components in spectra. Additionally I-V or other characteristics can be monitored on the plot

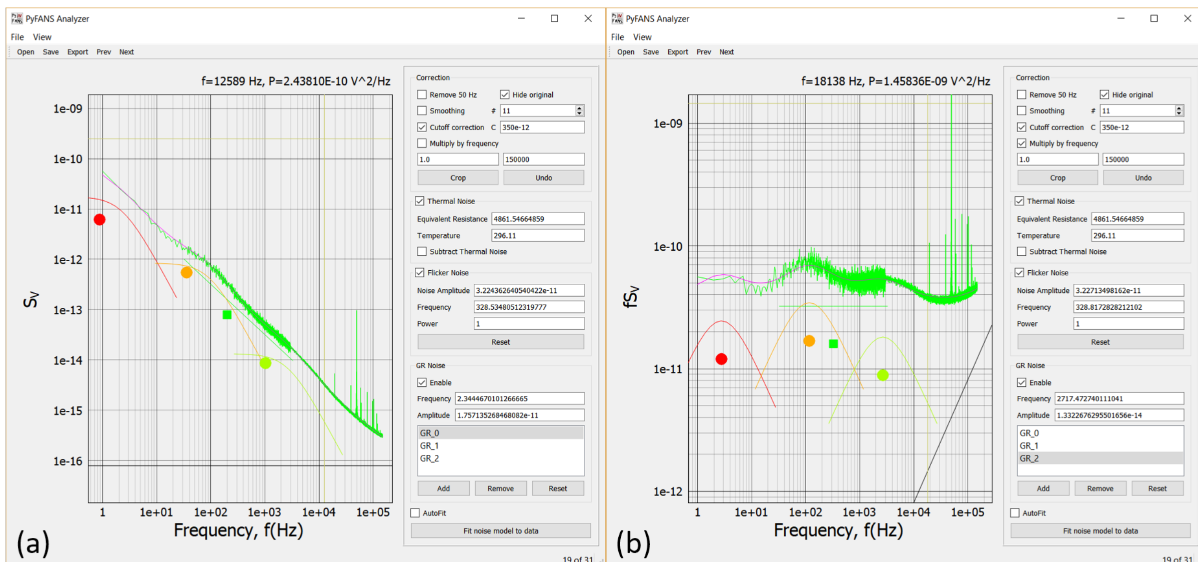

Figure 3.7: The main window of the noise analysis program, PyFANS Analyzer . (a) An example of noise spectrum fitting in log-log plot mode. (b) Data from (a) where y-axis is multiplied by the frequency. In this view GR-like components appear as bumps, thus easier to extract.

which can be defined by user.

Analysis of measured noise spectra can be performed using specially developed companion software, called PyFANS Analyzer. An example fitting performed in developed program is shown in figure (3.7).

The program allows to process the raw data obtained from FANS setup. Major features include data filtering, smoothing, cutoff correction and creating a noise model with a custom combination of flicker, thermal and several generation-recombination (GR) noise components. Furthermore program allows semi-automated fitting option. Figure 3.7 shows two coordinate modes where data can be fitted, $S_V(f)$ and $f \times S_V(f)$. The second one provides better and more convenient approach for Lorentzian-shape noise fitting since in this coordinates it is represented as a bump, while flicker noise component becomes a horizontal line. Program allows to visualize other parameters of the experiment, including I-V curve and highlights each point on the graph corresponding to noise spectrum. The noise model parameters are later saved into the file for further analysis.

3.3 Multichannel BioMAS Setup

Bioelectronic Multifunctional Amplifier System(BioMAS) is a developed in-house multichannel measurement setup, used for cellular activity recording. The system allows measurements on a variety of devices including multielectrode array (MEA) and FET by selecting appropriate adapter, called here as a headstage. Schematically system with FET configuration is shown in figure 3.8. The system enables I–V characterization as

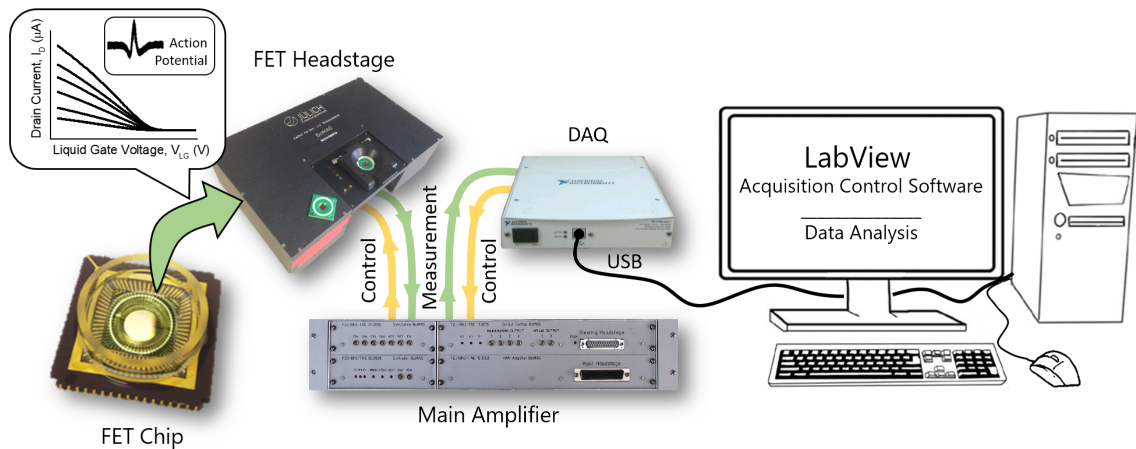

Figure 3.8: Schematic demonstration of BioMAS system. The system is capable of the measurements on a variety of devices, including FETs and MEAs. We present here a part responsible for FET measurements. It consists of the FET Headstage, where the chip is inserted. Analogue signal is passed to the main amplifier for further filtering and amplification. Data acquisition and control of the measurement circuits is performed through the commercial DAQ device. The System is controlled from a PC with LabView-based software.

well as time-series recordings in parallel from all 32 transistors on the chip [111]. The setup consist of an amplification cascade which includes a pre-amplifier and a main amplifier. For AC-coupled measurements, filters were used to prevent aliasing effects. The

amplified signal was then passed to the DAQ system for readout and further data processing on the computer. Commercially available DAQ system converts voltage, coming from the main amplifier into 16-bit digital values. The system provides the conversion bandwidth of 1.25×10^6 samples per second. Typically 10 kHz sampling rate is used when multichannel recordings are performed. The pre-amplifier consists of a corresponding operational amplifier and a Si NW FET on the chip (the "channel"). The resulting amplification depends on the feedback resistance (R_{FB}) connected to the operational amplifier and the actual transconductance of the FET defined by the selected working point: $V_{out} = V_{LG} \times g_m \times R_{FB}$.

It should be noted that for optimal signal amplification, RFB corresponds approximately to the FET channel resistance. In order to select the working point with the highest transconductance for the FETs, I–V characteristics are measured prior to the time trace studies. Optimized values for drain-source, liquid-gate, and back-gate voltages can be selected based on replotted derivative ($\partial I_D / \partial V_{LG}$) curves. Time series reported for cellular recordings are recalculated into the input voltage fluctuations using equation: $\Delta V_G = \Delta V_{out} / \left(g_m \times R_{FB} \right)$.

For data analysis we developed the software using Python programming language. It allows to find action potentials (APs) in the timetrace, extract them, align on the time axis and average for each available channel. The main window of the program is shown in figure 3.9.

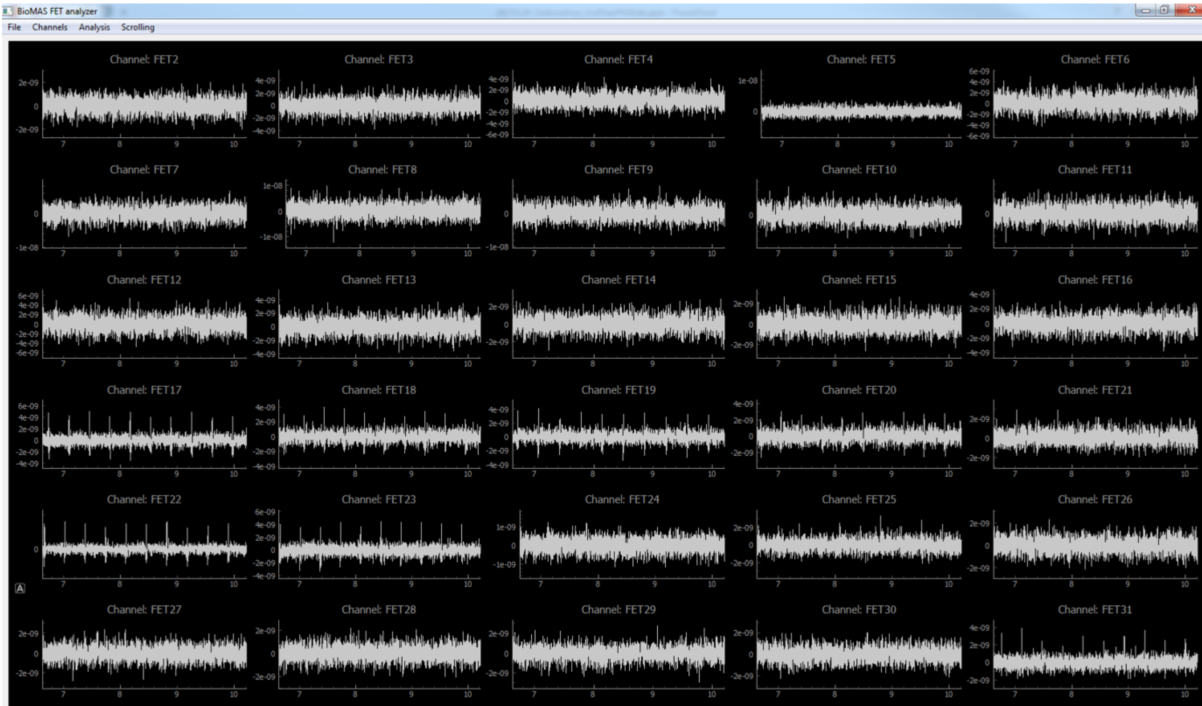

Figure 3.9: The main window of developed program for the analysis of data produced by BioMAS system. The plots demonstrate typical timetraces recorded from the FET device during experiments with cardiac muscle cells.

3.4 Surface Modification for Troponin Detection

As it was described in section 2.1.2 in order to make the detection of analyte from the solution it should be immobilized next to the surface of a biosensor, so that the electrical charge brought by a polar molecule influences on the surface potential.

For biosensing experiments we employ antibody-antigen reactions. This approach allows for a highly specific and selective binding of target molecules from the solution. To create such binding sites we performed surface modification with monoclonal cardiac Troponin I(cTnI) antibodies (see figure 3.10). During the first step devices are rinsed

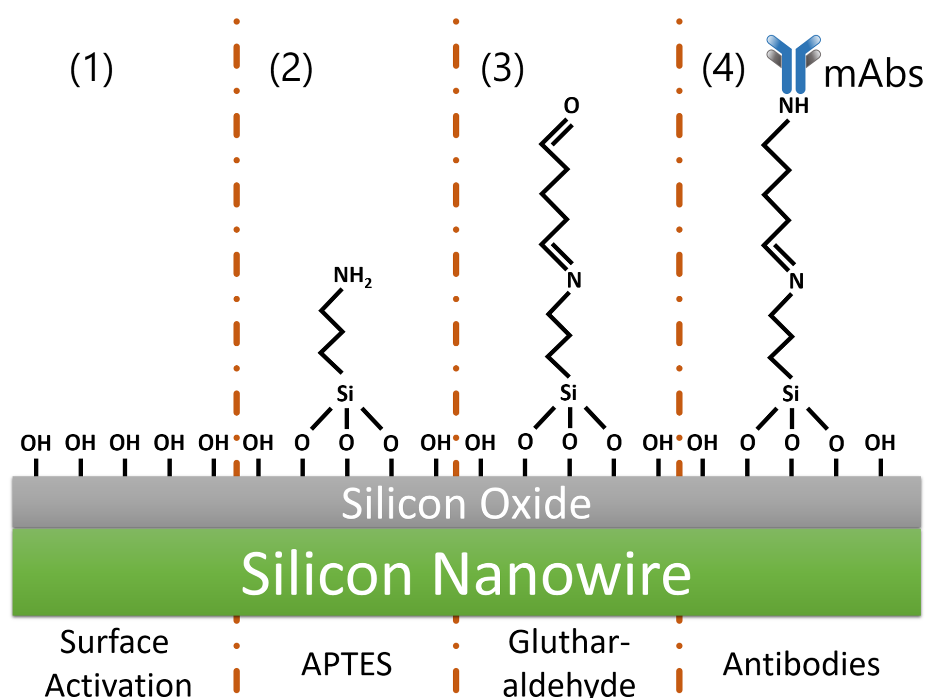

Figure 3.10: Schematic representation of the surface modification protocol for immobilization of monoclonal cardiac troponin antibodies on the silicon nanowire surface. The protocol allows to prepare the biosensor surface for the selective detection of cardiac troponin I from the solution.

with ethanol and dried with nitrogen flow to clean and prepare the surface for further treatment. In order to activate and form a dangling bonds on the surface devices were treated with oxygen plasma and dehydrated on the hotplate. To bind antibodies covalently to the surface several chemical steps should be performed. 3-aminopropyltriethoxysilane (APTES) was applied to the surface through the molecular layer deposition for 1 hour at room temperature. Then by dipping the chip into 5% glutaraldehyde solution the amino-terminated surface becomes aldehyde-terminated. Afterwards cTnI antibodies are covalently linked to the nanowire surface. To prevent the non-specific binding to the antibodies all unspesific binding sites as well as non-reacted aldehyde sites are blocked using ethanolamine.

3.5 Cell Culture and Imaging

3.5.1 Cardiomyocyte Cell Culture

As a model system for our investigations we used HL-1 mouse cardiomyocyte cell line. HL-1 is an immortilized cell line which is able to divide continuously and contract spontaneously. The cell line can be sequentially passaged keeping the morphological, biochemical and electrophysiological properties the same. The system has been proven to be excellent choice for studies of normal cardiomyocyte function including signaling, electrical, metabolic and transcriptional regulation as well as physiological and pathological cardiac conditions such as hypoxia, hyperglycemia, hyperinsulinemia, apoptosis, and ischemia-reperfusion injury. Cells were received in a frozen state, then thawed at room temperature and grown in T-25 flask until the full surface coverage. Before transfering cells onto the sensor surface, silicon nanowire chips were cleaned and disinfected with 70% ethanol solution. Afterwards the active sensing surface of nanowires was covered with a mixture of fibronectin ($5\,\mu g\,mL^{-1}$) and gelatin ($0.2\,\mu g\,mL^{-1}$) for 1 hour at 37 °C to improve the adhesion of cells to silicon dioxide dielectric surface. When cells formed a confluent layer in the flask a part of cells was separated and placed into the on-chip reservoir with the density approximately $150 cells/mm^2$. Afterwards chips were transferred into the incubator with the 5% flow of CO_2 gas at 37 °C. Such conditions are favorable for the normal culture growth and formation of confluent and contracting layers. The medium for cellular growth was a mixture of 100 U/ml penicilin, $100\,\mu g\,mL^{-1}$ streptomycin, 10% fetal bovine serum, 0.1 mM norepinephrine, and 2 mM L-glutamine. During the cell growth culture medium was exchanged on the daily basis and about 2 hour before the measurements.

3.5.2 Fluorescent Imaging of Cardiomyocytes

Live-Dead Staining. In order to visualize the vitality of grown cell culture we used a fluorescent live-dead staining technique involving calcein AM(calcein acetoxymethylester) and DAPI (4',6-diamidino-2-phenylidole) fluorescent dyes. Both dyes are able to penetrate through the cell membrane. In the case of calcein, when the molecule gets inside the cell esterases present internally are removing the acetomethoxy group and make the dye trapped inside the cell. When the cell is dead such active esterases are not supplied anymore. Therefore calcein produces a strong fluorescence at around 515 nm when excited at 495 nm. DAPI in turn binds only to adenine-tymine rich regions in deoxyribonucleic acid (DNA). When excited with ultraviolet light at wavelength of 358 nm, excited emission will occur at 461 nm(blue light). Both flyorescent dyes were used to label viable cells and recognize them through the fluorescent microscopy. The procedure begins with the washing of cells cultured on-chip with PBS for 3 times to prepare cells for addition of fluorescent dyes. Calcein AM (2 µM), green fluorescent dye, was introduced into the cells during 30 minutes incubation at 37 °C. The blue fluorescent dye DAPI(300 nM) was loaded during 5 minutes incubation at room temperature. After the incubation solutions were removed and chips were washed 3 times for 3 minutes. Labeled samples were then checked at ZEISS ApoTome with Axio Imager Z1 fluoresce microscope.

Calcium and Membrane Potential Imaging. One of important things to evaluate the functional activity of cells is to estimate the calcium content inside the cell as well as membrane potential of mitochondria - the main calcium storage within the cell. The

deviations from normal Calcium content, energetic deficit and oxidative streaa in cardiomyocytes are an important hallmarks in a wide range of cardiac diseases. For the investigation of calcium content inside of cells as well as mitochondria membrane potential together with extracellular electrical recordings we employed fluorescence microscopy. Method allows to monitor the current state of the confluent cellular network and detect the changes under the influence of pharmacological treatment. As the labels for the fluorescent microscopy we utilized the combination of calcium-sensitive Fluo-4 AM and membrane potential-sensitive TMRM fluorescent dyes. Fluo-4 AM is an AM ester which is able to penetrate through the cell membrane. After the hydrolization by the endogenous esterases Fluo-4 becomes trapped inside the cell. The marker allows to visualize the calcium content in the high-throughput drug screening. The emission at 506 nm is efficiently excited by the light at 494 nm.

TMRM is a cell-permeant membrane potential - sensitive dye which accumulates in active mitochondria. The dye is not actively interacting with membrane proteins and is not aggregating in the cell membranes. Therefore the transmembrane distribution of the marker is directly related to the membrane potential according to the Nernst equation.

Prior to the introduction of fluorescent dyes chips were washed with PBS solution. Green fluorescent dye Fluo-4 (10 µM) was loaded during the incubation for 30 minutes at 37 °C and red TMRM dye (200 nM) was loaded at room temperature for 5 minutes. The stain solution was then removes and samples were washed with PBS 3 times for 3 minutes each. s

3.6 Summary

In this chapter we discussed the development of tools for FET characterization, including I-V and noise measurements. Developed solutions allow to automate the data acquisition process for device transport properties investigation and simplify the analysis of obtained results. In addition a software package for analysis of data obtained from BioMAS multichannel FET measurements was developed. It enables to extract transport characteristics as well as cellular action potentials from timetraces, recorded on parallel FET channels.

We presented a method of the surface modification for cardiac troponin I detection using antibody-antigen reaction. Finally, we described the cardiomyocyte cell culture on chip and methods of their imaging. Furthermore, imaging methods of calcium content in the cell and membrane potential of mitochondria are presented.

Discussed materials and methods were used to obtain and analyze the results discussed in present work.

Chapter 4

Transport Phenomena in Silicon Nanostructures

4.1 Design of Nanostructures

In current work we have developed and fabricated Silicon nanowire (NW) field-effect transistor (FET) structures for the investigation of novel effects which can be used for the sensitivity enhancement of biosensors. Layouts of the structures are defined by the requirements of microfluidic integration to the system, cell culture requirements as well as compatibility with multichannel measurement setup. Fabricated nanowire samples have different geometry configurations including single nanowires as well as nanowire arrays and nanoribbons. Here we introduce the layouts and geometries of devices.

Chip layouts were designed in two principal configurations: linear and grid (see figure 4.1). Si NW FET chips were designed to be fabricated on four inch wafers. Therefore chip dimentions were assigned to $11 \times 11\,\mathrm{mm}^2$. This allows to solve several issues. Such chip configurations allows the utilization of microfluidic channels with comparably big sizes which makes all the manipulations with fluidic relatively easy without the need of sophisticated placement equipment. Often patch-clamp micropipette together with microscope are necessary for the control of cell culture and simultaneous recording of intracellular and extracellular cell action potentials. Therefore, cellular measurements require more space on the chip in comparison to ion sensitive field-effect transistor (ISFET) measurements. Moreover, spatially distributed FET structures, implemented in linear and grid layouts chips, allow the investigation of cellular communication, involving the recording of action potential (AP) propagation across the cellular networks. Such layout design configuration yields 50 chips per wafer. Each layout contains 32 transistors for both single nanowire chips and nanowire array/nanoribbon chips.

Single Silicon Nanowire FETs were selected for the implementation of novel biosensing approaches including single trap phenomena which allows sensitivity enhancement. In this respect the dimensions of nanowires should be small enough when only a single trap can influence the conducting channel resulting in random telegraph signal noise. Considering this designed single nanowire chips contain nanowires with different geometries containing nanowires with the same length and varying width as well as nanowires with same width and varying length. Such configuration gives an opportunity to find optimal geometries for increasing the propability of random telegraph signal (RTS) fluctuations caused by a single trap. Designed nanowire widths are in the range from 70 nm to 500 nm

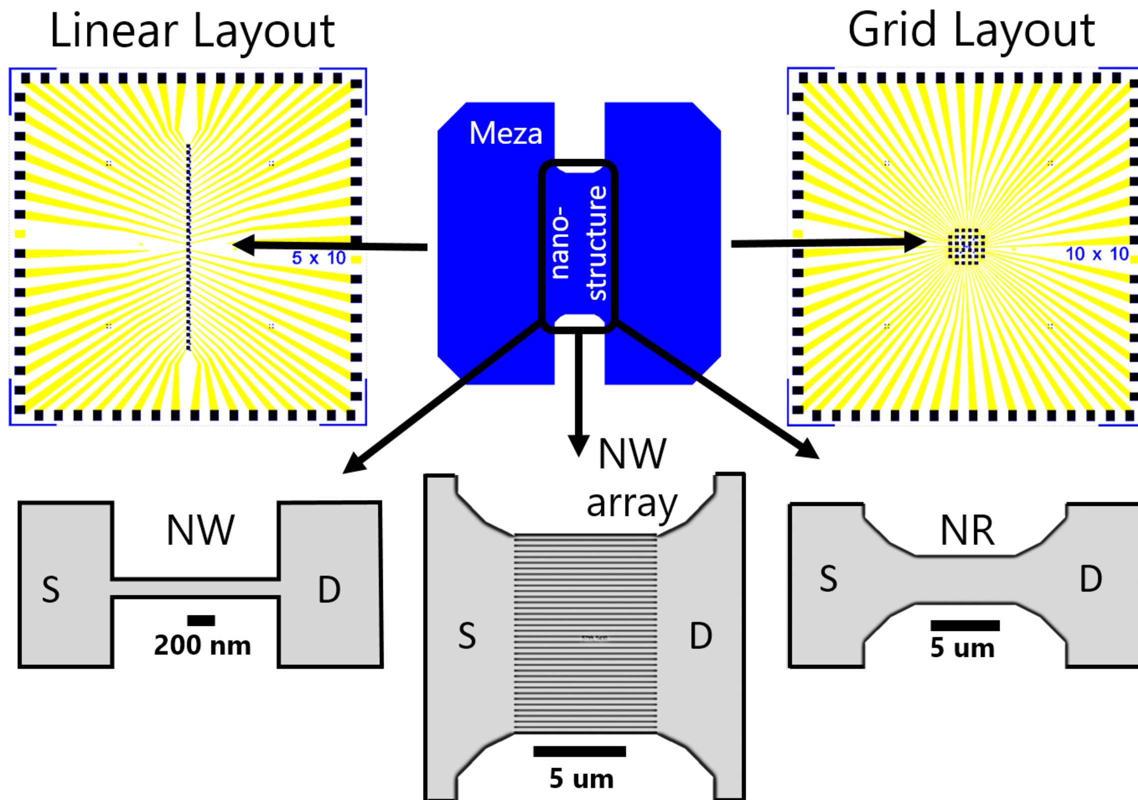

Figure 4.1: Chips were designed in two layouts - linear and grid. Each of them contains 32 transistors, which are located in the middle part of the chip, while the metal feedlines extend the metal contacts to the edges. Each transistor consists of a meza structure shown as a blue shape, where the middle part(assigned as nanostructure) is patterned respectively to the planned nanostructure - single nanowire, nanowire array or nanoribbon.

and lengths vary in the range from 100 nm to 4 µm. The complete set of single silicon nanowire dimensions as well as location of various chip types and their layouts over the wafer can be found in the appendix B.

Silicon Nanowire Array and Nanoribbon Chips were designed specifically for the recording of extracellular electrical activity of electrogenic cells like cardiomyocytes or neurons. In this case the layout represents the chip with 32 mapping sites for the measuremetns. The wafer contains chips with the same dimensions for all transistors for the measurements of cellular activity as well as chips with varied widths and lengths for principal structure investigations. NW array chips contain structures with length ranging 2 µm to 20 µm and widths in the range 100 nm to 250 nm with spacing of 250 nm. In turn nanoribbon (NR) structures have the same length range while the width is in the range 2 µm to 20 µm. In the next subsection the fabrication technology of Si NW FETs will be discussed.

4.2 Optimization of Fabrication Technology

All fabrication steps were performed at Helmholtz Nanoelectronic Facility (HNF), Forschungszentrum Jülich. Overall, the process consists of 9 major technological steps presented in figure 4.2. Each step has a crucial impact on the quality of final biosensor devices. Therefore, considering all possible precautions, we have fabricated high-quality Si NW FETs. During the fabrication process we combined photolithography together with electron-beam lithography for patterning of nanowires. Such combination allows the reduction of production costs and improves the fabrication speed, while a single step wafer illumination through the mask is much faster than writing the structure with electron beam point-by-point. Further, we discuss fabrication process in details, step-by-step. A complete set of steps and parameters used for the recent fabrication of silicon nanowires can be found in appendix A.

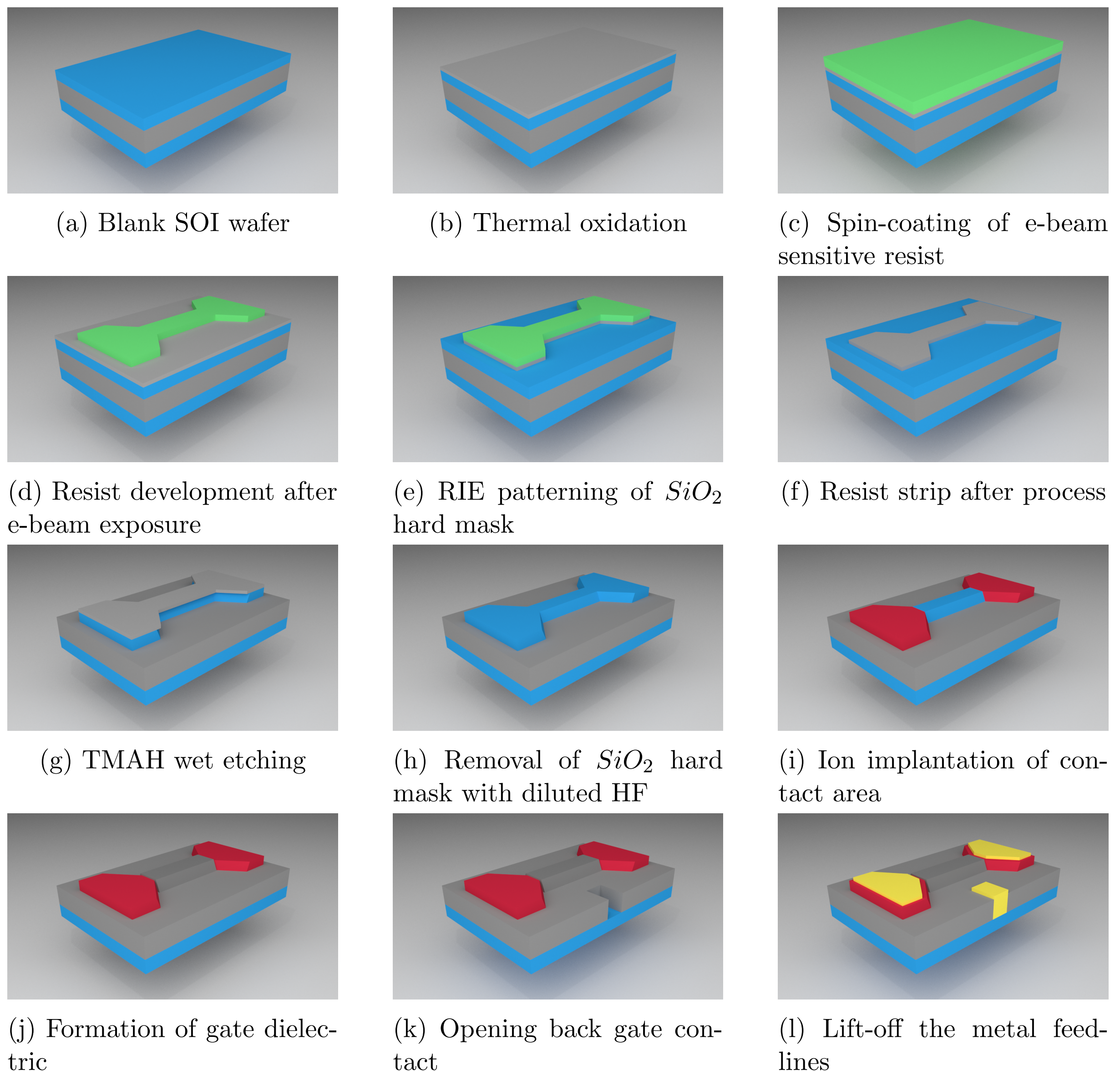

(a) Blank SOI wafer

(b) Thermal oxidation

(c) Spin-coating of e-beam sensitive resist

(d) Resist development after e-beam exposure

(e) RIE patterning of SiO_2 hard mask

(f) Resist strip after process

(g) TMAH wet etching

(h) Removal of SiO_2 hard mask with diluted HF

(i) Ion implantation of contact area

(j) Formation of gate dielectric

(k) Opening back gate contact

(l) Lift-off the metal feed-lines

Figure 4.2: The process flow used for the fabrication of silicon nanowire FETs.

Substrate selection

For the fabrication of biosensor devices silicon-on-insulator (SOI) wafers were selected. Wafers with <100>orientation were purchased from SOITEC, France. The utilization of such substrate has several advantages in comparison to conventional silicon substrates. Firstly it allows to lower parasitic capacitance due to isolation from the bulk silicon and thus improving power consumption. Secondly, thanks to the thin active silicon thickness the transistor channel is fully depleted and thus allows much more efficient and faster transistor control. Finally, the presence of buried oxide efficiently confines the charge carrier flowing from source to drain, dramatically reducing performance-degrading leakage currents. Furthermore SOI technology allows the control of transistor behavior not only through the gate but also by biasing the substrate underneath the device. The thickness of active silicon layer was 50 nm or 75 nm and buried oxide layer was 145 nm. Before the process the wafers were cut into 100 mm wafers using laser. The resistivity of wafers was 14 Ω cm to 18.9 Ω cm. In all structures the active layer was 50 nm. Wafers with active silicon layer thickness of 75 nm were thinned down to fit desired value. Initial wafer in the process flows is depicted in figure 4.2(a).

Formation of SiO_2 hard mask

In order to pattern silicon nanowires it is required to create the hard mask which is stable enough to survive the wet chemical etching of structures (figure 4.2(b)). Thermal SiO_2 layer is useful when the hard mask is created together with thinning active silicon layer from 75 nm down to 50 nm. The optimal value of hard mask thickness was found to be 20 nm. In order to achieve this for 75 nm Si wafers thermal oxidation was done in two steps. First was performed to thin the wafer down. Grown SiO_2 layer was then removed with diluted HF solution. Second thermal oxidation was done to form desired hard mask thickness The oxidation itself was performed in dry oxygen atmosphere at 940 °C for

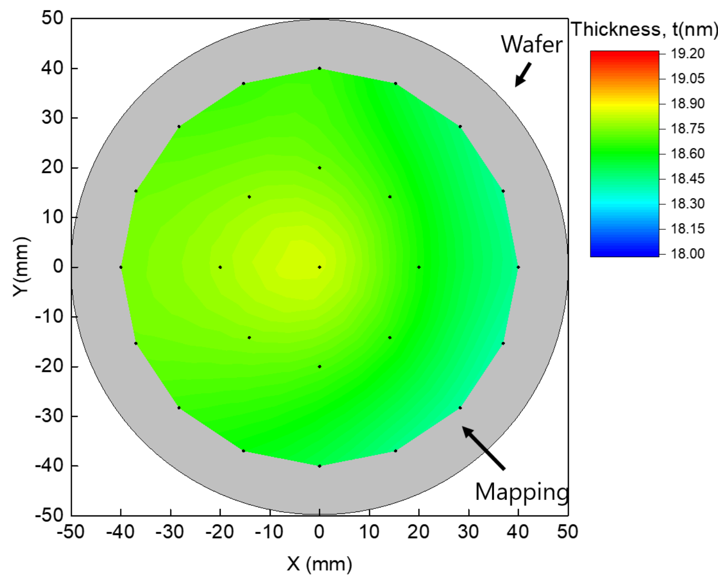

Figure 4.3: The mapping of PECVD-deposited SiO_2 layer thickness across the wafer using ellipsometer. The results demonstrate that SiO_2 layer was homogeneously deposited with the thickness of around 18.7 nm.

45 min resulting in uniform and high quality silicon dioxide surface. For 50 nm Si wafers plasma-enhanced chemical vapor deposition (PECVD) 20 nm SiO_2 was deposited in the chamber at 350 °C. The thickness of deposited oxide later is shown in figure 4.3.

Approaches to nanowire patterning

Patterning of the nanowires consists of several steps among which two main stages of defining nanowires and meza structure should be emphasized. In the first case(see figure 4.4(a)), after hard mask formation we pattern meza structure using photo lithography with consequent hard mask etching using reactive ion etching. After this we transfer meza structure from hard mask into silicon using wet chemical etching in tetramethylammonium hydroxide (TMAH) solution. During this process, negative markers for further patterning of nanowires are etched. Markers itself are 4 squares with the side of 20 µm and spacing of 100 µm located in the corners of the chip. Afterwards the nanowires are defined using e-beam lithography. In this case the positive tone e-beam sensitive resist is used. At this lithography step we define the areas for etching in hard mask of meza structure and define the nanowires of various geometries. Afterwards etching steps including reactive-ion etching (RIE) and TMAH are performed again to pattern nano-structures. Such approach of nanowire patterning causes the excess etching of buried oxide (BOX) layer. This further results in additional roughness of the BOX layer and consequently leakage current. To solve the problem we rearranged the process steps to reduce etching times in TMAH and HF solutions which introduce damage to the burried insulator layer. In the second case (see figure 4.4(a)), we firstly define positive tone markers(see section 4.2) for e-beam lithography with the same dimensions as in the first case together with high-precision

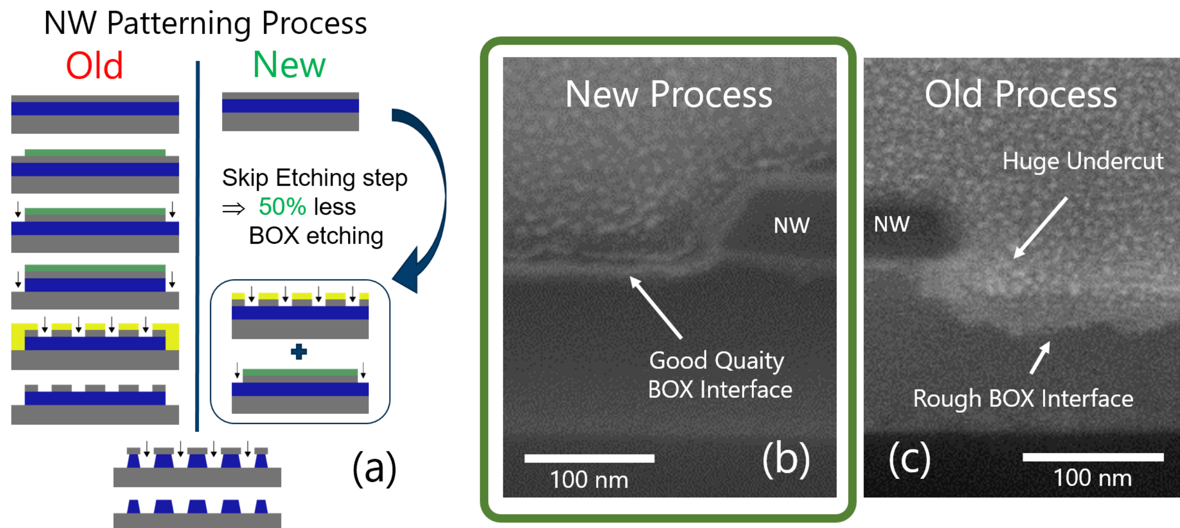

Figure 4.4: (a) A comparison of two approaches for nanowire pattering. (b) and (c) are the SEM images of structure cross sections fabricated by the new and old processes, correspondingly. The old process in (a) required two-step etching procedure for sequantial patterning of meza and nanowires. The new approach in(a) combines two etching steps into one, resulting in less underetching of the new structures (b) in comparison to the old ones (c). Furthermore the quality and the roughness of the BOX surface is much improved in the new process(b). The new process allowed to reduce leakage currents drastically.

markers for further alignment of meza structure. For this we use photolithography followed by RIE. The final markers were etched into the substrate on 600 nm. Using prepared markers we pattern nanowires in hard mask using electron-beam lithography and dry RIE etching. Afterwards we pattern meza structure into the same hard mask using high-precision markers. The advantage of such approach is the transfer of NW and meza structure into silicon simultaneously which allows to keep the high-quality of BOX layer as it is shown in figure 4.4(b-c). Moreover this approach allowed to reduce leakage currents drastically. In this respect, the second approach was figured out to be much more beneficial for the quality of fabricated structures as well as for optimization of fabrication process from the viewpoint of chemicals utilization. Therefore we discuss the second approach in more detail.

E-beam markers for the nanowire alignment

The first step is to define markers for fine alignment of e-beam written silicon nanowires with meza structure of transistors. Marker layer contains both markers for e-beam lithography and markers for photo lithography. E-beam markers are 4 squares with the side of 20 µm and spacing of 100 µm are located in the corners of the chip far from the fine structures in order not to influence the quality of lithography while the process of marker search(see figure 4.5(a)). Photolithography markers contain structures for high precision alignment with accuracy of 100 nm. The marker layer is defined by terms of photolithography. Wafers are first dehydrated at 180 °C for 5 minutes. Then hexamethyldisilazane (HMDS) adhesion promoter monolayer is formed on the surface through the deposition from vapor phase at substrate temperature of 130 °C. After applying the adhesion promoter the negative tone photoresist AZ nlof 2020 (MicroChemicals GmbH) is spin-coated onto the wafers surface at 4000 rpm with further soft bake at 110 °C for 1 minute. The resist is patterned using photolithography (Süss MicroTec, MA/BA GEN4 with 365 nm UV light source) with constant exposure dose of 40 mJ cm^{-2}. After the post-exposure bake at 110 °C for 60 s wafers are then developed for 45 s with AZ 326 MIF developer. The process of development is immediately stopped by dipping wafers into DI water. After patterning

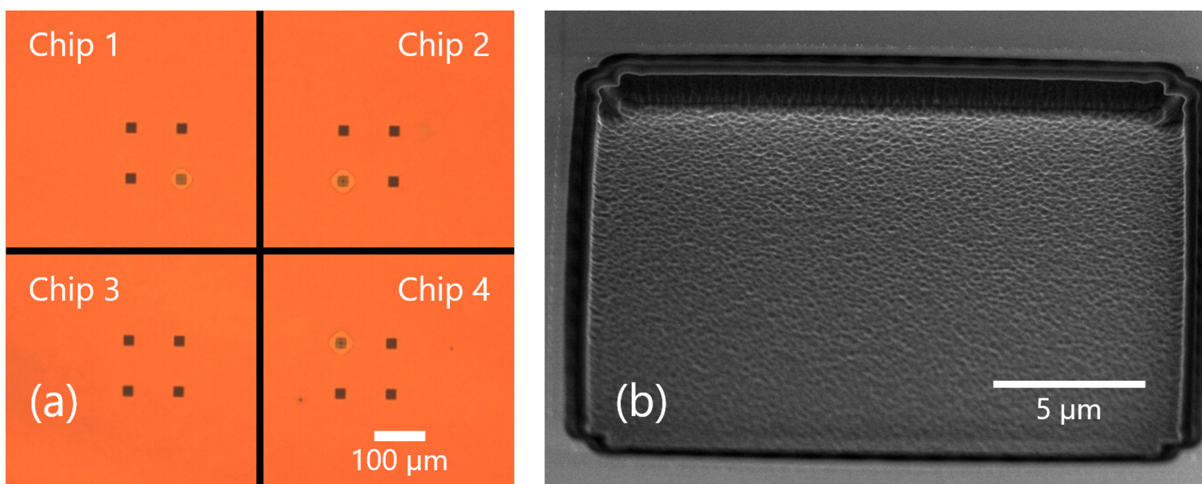

Figure 4.5: A new approach for nanowire patterning required markers to align meza structure with nanowires. We used a positive square-shape markers(a) with the side of 20 µm and spacing of 100 µm. Each chip has four markers in each corner. (b) The scanning electron microscopy (SEM) image of etched marker for nanowire patterning.

the photoresist we transfer it into the substrate by terms of dry RIE etching. The process of marker etching into the substrate involves several-step RIE process using CHF_3 and SF_6/O_2 gas mixtures which provide highly anisotropic and selective etching of silicon and silicon dioxide correspondingly. Beforehand the etching rates are calibrated. Furthermore the etching process can be controlled by the laser beam. Firstly 20 nm SiO_2 hard mask is etched for 40 s in CHF_3 plasma. Then active Si layer is etched in SF_6/O_2 plasma for 15 s. Later BOX layer(145 nm) is etched through with CHF_3 plasma for 7 min. Then Silicon substrate is etched with SF_6/O_2 plasma for 20 s. Finally the photoresist mask is removed with oxygen plasma for 90 s. SEM picture of etched marker is shown in figure 4.5(b). The resulting depth of markers was controlled by stylus profiler and was measured to be around 590 nm.

Patterning of nanowires

The patterning of single nanowires starts with e-beam lithography as it is shown in figure 4.2(d). From the previous experience of the fabrication technology two approaches for nanowire patterning have to be considered. The first one suggests the silicon approaching the nanowire should be patterned in triangular-like manner as it is shown in figure 4.6(a). Such approach suggests less expensive e-beam procedure since more coarse patterns can be introduced. However, it has a drawback limiting the lowest nanowire size. The limiting factor is an anisotropic etching rate of silicon in TMAH solution. Threfore the triangular approaching part is etched very fast along the nanowire thus making it longer than designed. The precise dimension control is required for the size-dependent effects in the nanowires, especially for the single trap phenomena as it will be shown further. In this respect we switched to the rectangular approaching parts, where the walls are perpendicular to the nanowire. In this crystallographic direction the etching rate of TMAH solution is the slowest, allowing the precise control of the nanowire dimensions (see figure 4.6(b)). It should be emphasized that both nanowires presented in figure 4.6 are designed to be 100 nm in length. Considering the aforementioned issue we decided to utilize a rectangular approaching parts. For the precise alignment we use markers defined

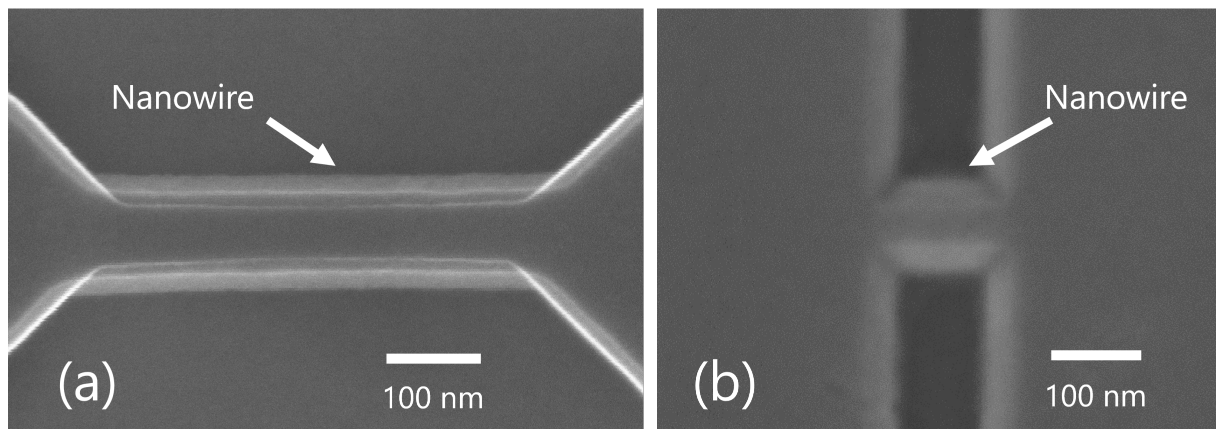

Figure 4.6: The impact of nanowire approaching part shape on the resulting nanowire size (nanowires were designed to be 100 nm in length). (a) With triangular-shape approaching parts the nanowire becomes much longer than designed due to anisotropic wet chemical etching with TMAH. (b) In the case of rectangular approaching part the etching speed is limited by the crystallographic orientation providing designed nanowire sizes after etching.

in previous step. Firstly, the wafers are dehydrated at 180 °C for 5 min. Then e-beam sensitive resist PMMA (AR-P 640.04) is spin-coated onto the wafer at 4000 rpm. After the resist was applied, the wafer had been soft baked at 180 °C for 5 min. The thickness of the resist layer should satisfy the requirement of holding the RIE etching of SiO_2 hard mask for 40 s and holding the vertical aspect ratio of our structures. In our case the resist thickness was about 150 nm which is in a good agreement with the datasheet. The next step is to transfer the nanowire pattern into hard mask. Further we patterned NW with e-beam. The PMMA is a positive tone resist. Therefore we expose with e-beam areas which should be subtracted from mesa structure in order to form nanowires. Since the area is relatively large in comparison to nanowire sizes the nanowire area gets also partially exposed to the scattered electrons in PMMA layer. This is called proximity effect and it can be compensated by the procedure of proximity correction. In this case the e-beam dose is corrected for the entire writing pattern in the way that at each point the dose is the same regardless the proximity effect. For the writing we used the dose of 270 µC cm^{-2} with the beam step size of 5 nm. After writing the e-beam pattern the samples were developed with AR-P 600-55 solution for 1 minute and immediately dipped into isopropanol for 1 minute in order to stop the development. The patterned nanowire structures are then transferred to hard mask using RIE etching in CHF_3 plasma (figure 4.2(e)). The etching rate for SiO_2 was measured to be around 29.832 nm min^{-1}. Therefore it takes around 40 s to etch through the hard mask. The resist was stripped with O_2 plasma afterwards (figure 4.2(f)). After the nanowires are patterned into the hard mask, we continue with patterning of meza structure.

Meza structure patterning

The next step is to pattern meza structure as it is shown in figure 4.7. For this purpose we use photolithography with defined previously high-precision markers. The wafers are dehydrated at 180 °C for 5 min. Then HMDS adhesion promoter is applied to the surface

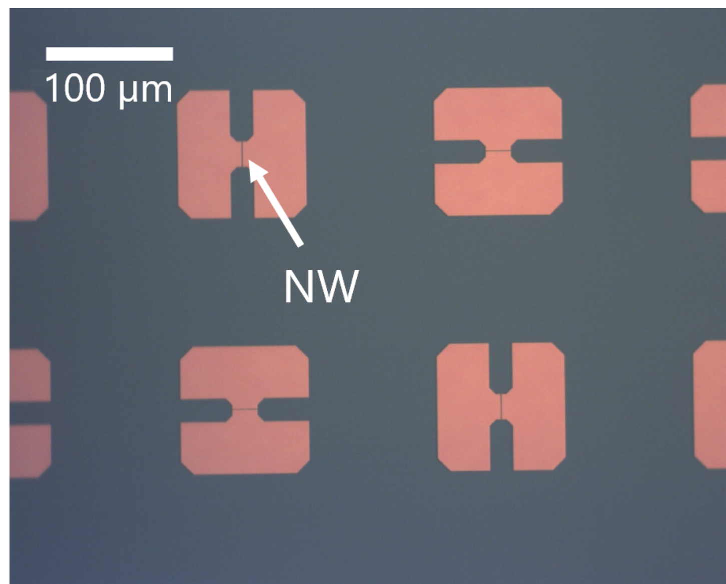

Figure 4.7: Microscope image of the meza and nanowire structures after wet chemical etching. The background corresponds to the burried oxide, red colored shapes are meza structures with nanowires etched into the silicon active layer.

from vapor phase at 130 °C to create better adhesion of photoresist. AZ 5214 E positive photoresist is spin-coated at 4000 rpm and then soft-baked at 110 °C for 60 seconds. Then the resist was exposed to UV light with the constant dose of 75 mJ cm^{-2}. After development in AZ 326 MIF solution for 55 seconds the pattern is transferred into hard mask using RIE as it was described for nanowire patterning. When silicon oxide hard mask is patterned with nanowire and meza structure, it is transferred into active silicon layer by terms of anisotropic wet chemical etching with TMAH solution (4.2(g)). This etchant has been shown to produce ultrahigh quality of fabricated structures resulting in reduced noise properties in comparison to RIE patterning [112]. TMAH solution provides highly selective and anisotropic etching of silicon. The etching parameters depend on TMAH concentration and temperature. In our case we used 5% TMAH solution at a temperature of 80 °C which results in the etching rate of 13 nm min^{-1} in <111>plane and 630 nm min^{-1} in <100>plane. Prior to silicon etching we removed native silicon oxide layer by dipping wafers for 30 seconds into 1% HF solution followed by DI water rinse and immediately dipping into TMAH solution for 15 seconds. The etch is stopped by rinsing wafers in DI water. Because of anisotropic etching considering the angle of 54.7° between <100>and <111>planes the nanowires become trapezoidal in cross-section. The hard mask is removed in 1% HF solution(4.2(h)). The resulting structures are examined by SEM and typical images of nanowires with scaling length are shown in figure 4.8

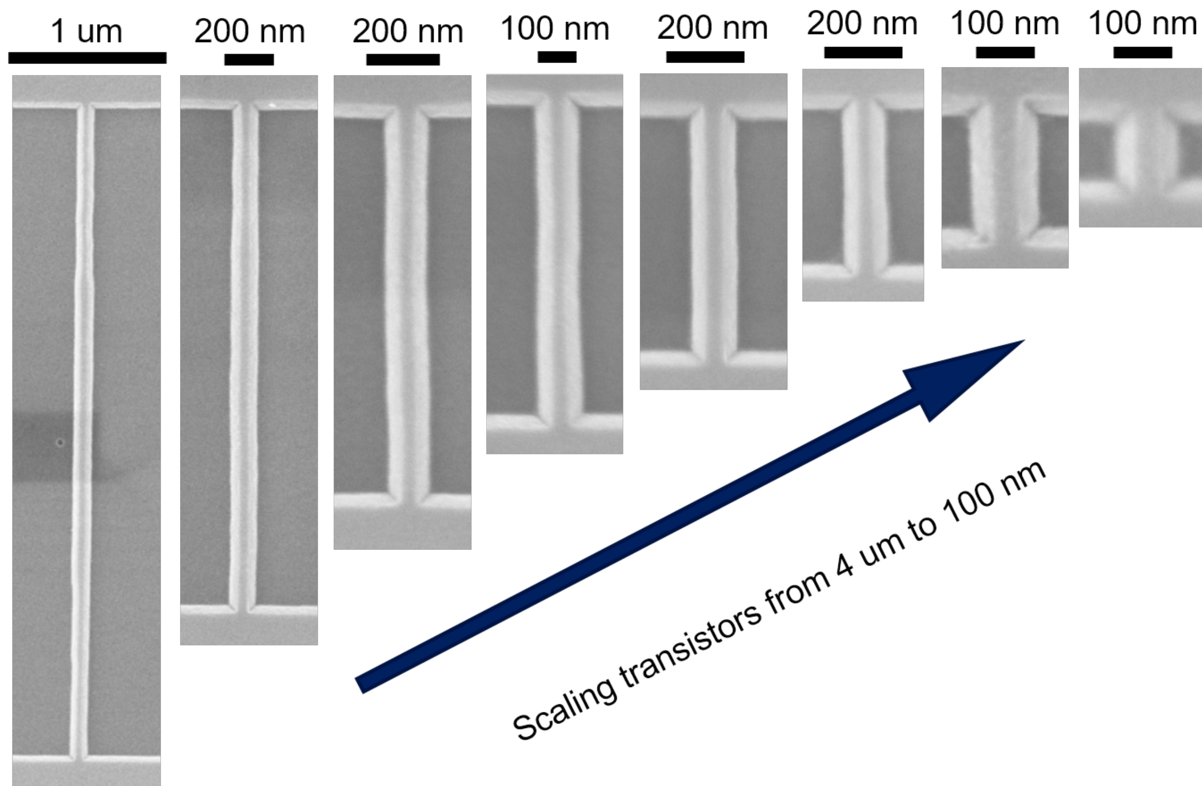

Figure 4.8: SEM images of fabricated nanowires with lengths ranging from 100 nm to 4 µm

Ion implantation

In order to create good ohmic contacts we perform ion implantation with Boron or Arsenic atoms which results in accumulation mode FETs ($p^+ - p - p^+$) and inversion mode FETs ($n^+ - p - n^+$) correspondingly. The process step is schematically shown in figure 4.2(i) The implantation area is defined in terms of photolithography with AZ 5214 E resist as it was described previously. In order to protect silicon meza from damage introduced by ion implantation we first perform protective oxidation. For this we first perform standard RCA cleaning. Meanwhile after Piranha cleaning we remove hard mask used in previous step by dipping wafers into 1% HF solution for 3 minutes and 30 seconds. After cleaning step we grow thermally 5 nm of silicon dioxide. Depending on the ion to be implanted we use different parameters. For Boron we use ion energy of 6 keV with the dose of $1 \times 10^{15}\,\text{cm}^{-2}$ while for Arsenic we use 8 keV with the dose of $5 \times 10^{14}\,\text{cm}^{-2}$. After the ion implantation the samples are cleaned from the photoresist with acetone for 12 hours. This allows to remove highly cross-linked top layer of the resist. The full RCA cleaning is then performed in order to remove all organic and inorganic residues as well as protective oxide from the surface of the wafer. The dopant is later activated with rapid thermal annealing (RTA): for Boron ion implantation 5 seconds at 1000 °C and 30 seconds at 950 °C for Arsenic ion implantation.

Gate oxide formation

The next step is to create the gate dielectric which will also serve as a protection of silicon channel of biosensor from the liquid environment. For this dry thermal oxidation is used in order to grow uniform oxide layer(see 4.2(j)). Prior to the oxidation native silicon oxide is removed from wafers by dipping into 1% HF for 40 seconds. The process at 850 °C for 44 minutes at oxygen flow results in around 8 nanometers of oxide. Such low oxidation rate of 10 nanometers per hour is selected in order of obtain high quality oxide layer with better stability required for operation of Si NW sensor in liquid environment.

Back gate opening

The layouts are designed with possibility of back gate utilization for additional control of silicon nanowires. In our structures we use highly doped substrate of SOI wafer as a back gate. To create the contact to the substrate we etch the via through the buried oxide of SOI wafer (4.2(k)). In order to do this we use photolithography with AZ 5214 E as it was described previously. Additionally after development we perform additional bake of the photoresist at 120 °C for 2 minutes in order to increase the stability of resist film to the etchant. In our case we used buffered oxide etch (BOE) since it allows better process control as well as reduced peeling of resist from the surface of the wafer in comparison to concentrated HF solution. With etching rate of around $100\,\text{nm}\,\text{min}^{-1}$ the etching time to create a via through BOX was around 70 seconds. The resist was then striped with acetone for 20 minutes followed by isopropanol dip for 1 minute and dried by nitrogen gun. The successful etching process is controlled by stylus profilometry.

Metallization

After the back gate opening metal contacts to Si NW FETs are formed with the lift-off process (figure 4.2(l)). Prior to this thin SiI_2 gate dielectric film should be etched

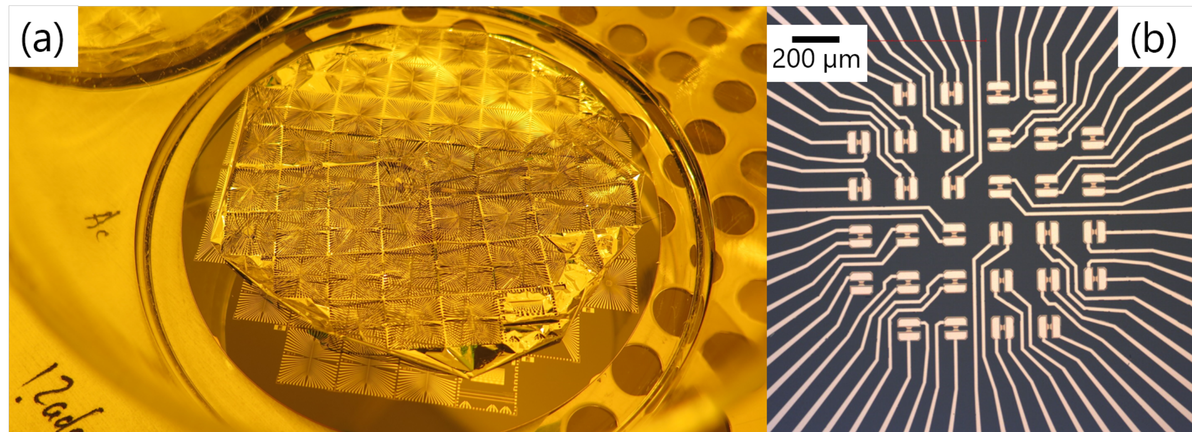

Figure 4.9: Metallization was performed using lift-off method. (a) Wafer in the beaker with acetone to dissolve negative photoresist and lift the excess metal off. (b) Microscope image of the chip after metallization procedure.

down to open access to highly doped silicon area. The photolithography was used in the same manner as it was for back gate opening. The gate oxide was etched with BOE for 10 seconds. Wafers were then rinsed in DI water and dried with nitrogen flow. The resist was then stripped with acetone. Metallization pattern was defined by the next photolithography. Wafers were dehydrated at 180 °C for 5 minutes. Negative tone lift-off resist AZ 2020 nlof was spin-coated at 4000 rpm and baked at 110 °C for 1 minute. After the UV exposure with the dose of $40\,\mathrm{mJ\,cm^{-2}}$ through the mask defining metal feedlines wafers were developed for 45 seconds in AZ 326 MIF developer solution. The wafers were dipped into 1% HF solution directly before metal deposition in order to strip native oxide layer. The stack of 5 nm TiN and 200 nm of Al was then deposited by sputtering. Wafers were then put into Acetone for 12 hours making the metal parts which cover the resist to lift-off as it is shown in figure 4.9(a). Afterwards we cleaned wafers with acetone, isopropanol and DI water. When resist is not completely removed from the surface of the wafer additional Oxygen plasma step can be used to remove residues. Metal contacts are then annealed in forming gas atmosphere($N_2 : H_2 = 10{:}1$) for 1 minutes at 450 °C to form good ohmic contacts between aluminum and silicon. The chip after metallization is shown in figure 4.9(b). In addition metal contact pads can be later adjusted with the deposition of another metal in order to improve the adhesion to the chip carried for further flip-chip encapsultation or improve the wire bonding quality and reliability.

Passivation

The last fabrication step is the feedline passivation against the liquid environment. The access of liquid solution to silicon nanowires is provided by patterning the passivation layer with photolithography. Polyimide was selected for this process since after hard-bake it was proved to be stable in liquid environment and highly bio-compatible material. Passivation starts with wafer dehydration at 180 °C for 20 minutes on the hotplate. The adhesion promoter VM-652 is then spin-coated at 3000rpm onto the wafer surface in order to enhance the adhesion between organic materials and silicon substrate. It is then baked at 110 °C for 60 seconds. Immediately after this polyimide (PI 2545) was spin-coated at 5000 rpm which results in layer thickness of approximately 1.5 µm. Wafers are then baked on the hotplate at 140 °C for 6 minutes. Mentioned series of polyimide layer

is non-photodefinable. Therefore additional negative tone resist AZ 2020 nlof is used to define openings to silicon nanowires and metal bondpads. The resist is spin-coated at 4000rpm onto the baked polyimide layer and baked at 110 °C for 1 minute. It is patterned with photolithography as described previously. The opening pattern is transferred into polyimide layer during the development step with the same AZ 326 MIF developer. This takes 38 seconds to etch through the passivation layer. It should be noted that the etching rate of PI in AZ 326 MIF solution is very fast. In this respect it is important to stop etching process immediately after the access to nanowires is opened. For this purpose several dummy wafers were used to check the etching time. The pattern resist is removed with acetone and cleaned with isopropanol and DI rinse. Finally wafers are hard baked in the furnace by ramping to 350 °C with the speed of 8 °C min^{-1} and hold at maximum temperature for 30 minutes under nitrogen flow of 10 l min^{-1}. Wafers are then cooled down to room temperature for 12 hours. The alternative process uses photo-definable HD 8820 polyimide layer. After the process chips are cut into chips which are further encapsulated and used for biosensing experiments.

On-chip reference electrode

An important element in the electrochemical system is the reference electrode which provides a stable potential. This is also critical for FET-based biosensors where the reference electrode potential determines the working point of the device. Typically Ag/AgCl reference electrode was used for measurements presented in this work. It provides high stability and is quite robust. The utilization of such external electrode is sometimes not convenient because of size limitations and setup configuration considerations. In this case on-chip reference electrode is a suitable substitution. Because of fabrication simplicity and clean-room compatibility we used lift-off patterned platinum(Pt) electrode. It was demonstrated that Pt electrode maintains permanent and stable potential for more than 12 hours immersed in molten NaCl/KCl. In this respect Pt electrode can be used as pseudo-reference electrode[113]. Fabricated reference electrode is shown in figure 4.10(a).

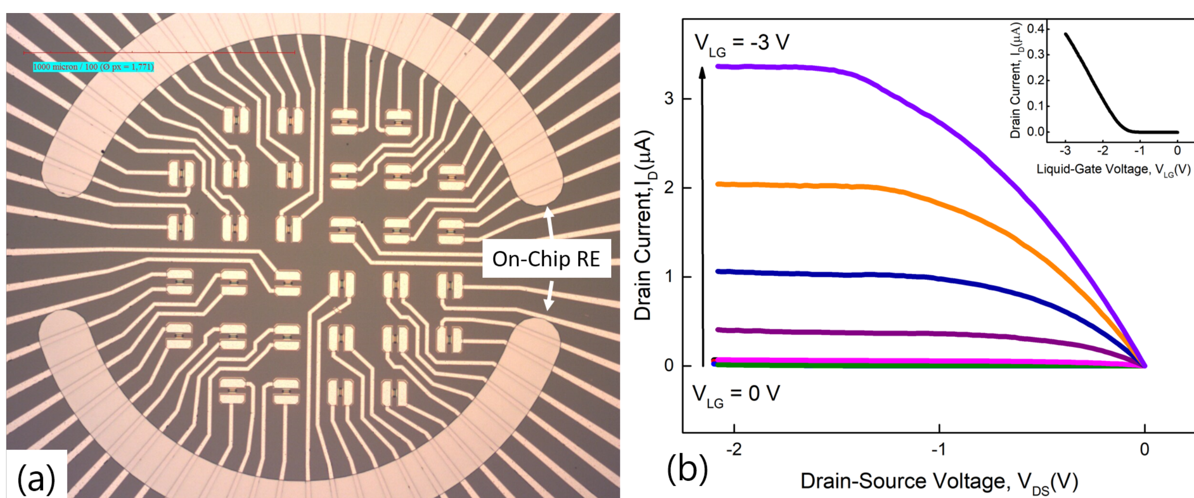

Figure 4.10: (a)Microscope image of fabricated Pt reference electrode on the chip. Metal layer is deposited on top of the passivation to prevent the electrical contact with metal feedlines. (b)Output and transfer characteristics of the chip measured using fabricated reference electrode.

To prove the working ability of reference electrode we performed output and transfer curves measurement. The results are shown in figure 4.10(b) and demonstrate a typical behavior for liquid gated devices as it will be further discussed.

Technology improvements

During the development and optimization of nanowire devices several major improvements were introduced. Nanowires were redesigned considering the approaching parts to the nanowires. This allowed to control the nanowire sizes much more precisely, which is critical in particular for single trap phenomena observation as it will be discussed in the following chapters. Fabrication flow has been reordered in order to improve the BOX layer quality after the nanowire etching. By introducing the alignment markers at the very beginning, it has become possible to combine meza and nanowire etching in one step and reduce BOX etching in the area of nanowire up to 50%. Fabrication of silicon nanowires with the new approach resulted in reduction of leakage currents which were a considerable problem for previous fabrication process. The minor tuning of the fabrication process has been performed at each step. Several iterations of the process optimization have been performed to introduce and test all improvements. A complete up to date technological process flow used for the fabrication of single nanowire FETs is presented in appendix A.

4.3 Chip Encapsulation

4.3.1 Reservoir for Cell Culture

Fabricated chips are typically glued and wire-bonded to the chip carrier with aluminum wire (see figure 4.11(a)). Because of liquid environment all exposed metal contacts should be covered and properly sealed in order to prevent gate-source or gate-drain leakage currents. The active area of the chip is separated with the glass ring of 5 mm inner

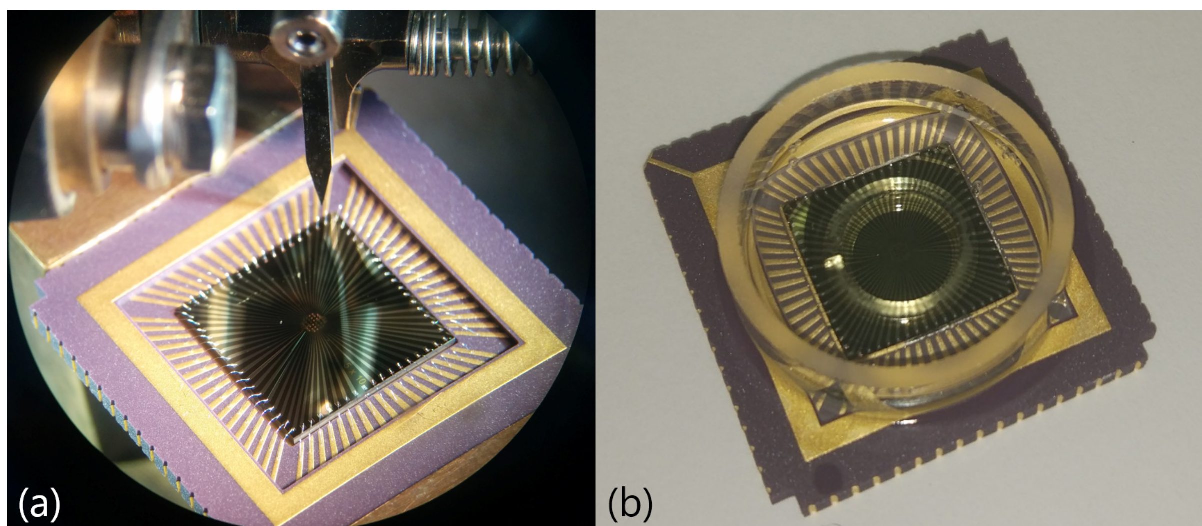

Figure 4.11: Chip encapsulation with reservoir:(a) - chip after wire bonding, (b) - chip with reservoir made of glass rings and metal wires covered with polydimethylsiloxane (PDMS)

diameter. Inner and outer glass rings are glued to the chip and chip carrier with PDMS. PDMS with 10:1 proportion of precursor and curing agent was prepared using standard protocol. Firstly inner and outer rings were glued using PDMS and pre-baked at 110 °C for 15 minutes. Then the volume between rings is filled with PDMS in order to cover wire bonds and put again into the oven for 1 hour. After the encapsulation samples are ready for liquid gated measurements. An example of prepared chip with reservoir is shown in figure 4.11(b). Depending on the application, chips can be alternatively encapslated for the use of microfluidic system.

4.3.2 Microfluidic for Biomarker Detection

For the easy of applying analyte solution to the nanowire surface microfluidic system was designed to fit the chip dimensions. Microfluidics can be fabricated on a large wafer scale using specially fabricated mold. The mold is then mounted into special holder which is filled with PDMS and baked in the oven at 110 °C for 1 hour. Then PDMS is detached from the mold and cut into separate fluidics which can be used on chip. When using microfluidic channels the chips glued and wire bonded to the chip carrier. The wires are covered with PDMS without glass rings as it is shown in figure 4.12(a). An inlet and outlet holes for liquid are made using biopsy puncher in the PDMS fluidic(see figure 4.12(b)). To perform the measurement, chip together with fluidic are assembled in the optimized holder, where the lid also serves as a clamp to fix the fluidic. With inserted tubing the system looks like it is shown in figure 4.12(c). Different solutions can be easily applied to the sensor using any kind of pump. External or on-chip reference electrodes can be used to define the gating voltage for liquid-gated silicon NW FETs.

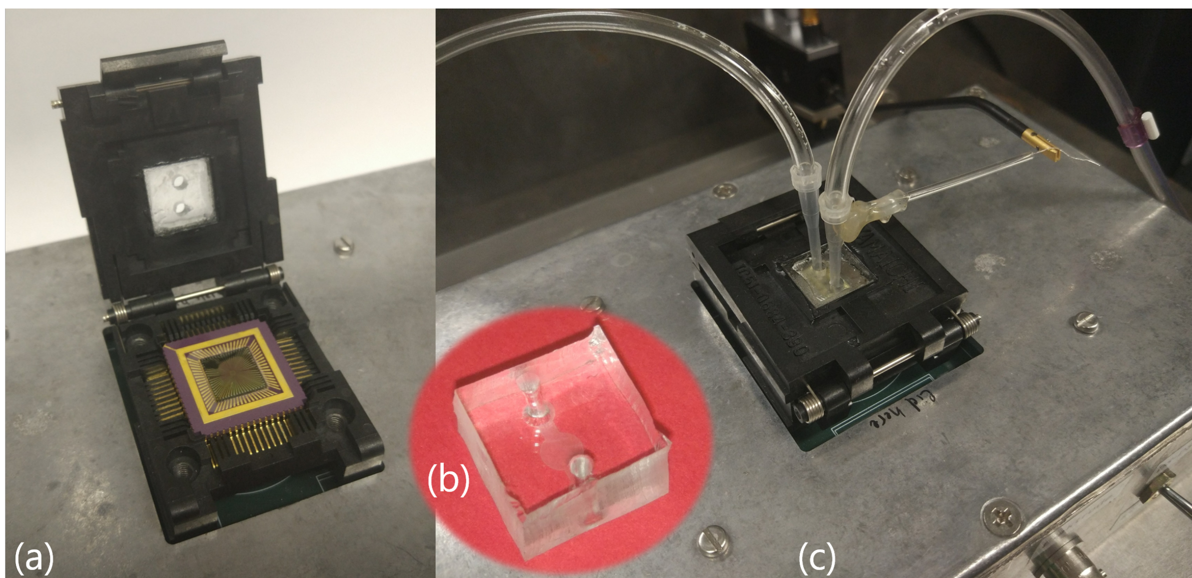

Figure 4.12: (a) - Chip, encapsulated with PDMS without glass rings, inserted into the socket for measurement, (b) - Microfluidic made of PDMS with inlet and outlet holes for the liquid flow, (c) - Microfluidic is placed over the chip in closed socket with inserted tubing. Reference electrode is mounted into the outlet tube

4.4 Silicon Nanowire Devices Characterization

Si NW FETs with outstanding electrical parameters are widely used as building blocks in modern electronics. A large surface-to-volume ratio is a distinctive feature of these structures allowing functionality which is extremely sensitive to the surface potential charges resulting in a considerable change of channel current. As a result, Si NW FETs are excellent candidates for biochemical sensor applications ensuring a high response signal level corresponding to bio-object binding events. The scaling of characteristic sizes allows ultra-low amounts of analyte to be registered down to the single molecule level. However, with NW size reduction the amplitude of the flicker (1/f) noise component usually increases. Moreover, the probability of RTS observation in noise spectra also increases. On the other hand, it was shown [114] that RTS noise parameters depend on gate potential and can be used as an informative signal for biosensing. Therefore the investigation of size-dependent features in NW FET biosensors is a challenging and extremely important task. We designed and fabricated Silicon nanowire structures as described in section 4.2. Transport properties of fabricated devices were studied in the FET configuration in liquid environment. phosphate-buffered saline (PBS) solution with pH 7.4 and ionic strength of 10 mM was used during liquid-gated measurements. The gate potential was set against an Ag/AgCl reference electrode.

Silicon nanowires with designed lengths in the range from 100 nm to 4 µm and widths from 70 nm to 500 nm were investigated from the viewpoint of scalability, device performance as well as noise properties. Typical transfer curves measured on $p^+ - p - p^+$ and $n^+ - p - n^+$ structures with length of 200 nm and width of 100 nm at various drain-source voltages, V_{DS} , are shown in figure 4.13(a). Output curves measured for the same set of nanowires FETs are shown in figure 4.13(b). Characteristics demonstrate stable metal-oxide semiconductor field-effect transistor (MOSFET)-like behavior with a typical transition from ohmic to saturation regime. It should be emphasized that the drain current axes scales for $n^+ - p - n^+$ structures are 3 times larger than for $p^+ - p - p^+$ structures for better visualization. At the same applied voltages drain current through the channel of $n^+ - p - n^+$-type nanowire is around 3 times larger than for $p^+ - p - p^+$-type nanowire. Which is reasonable from the viewpoint of charge carrier mobility. The major carriers in

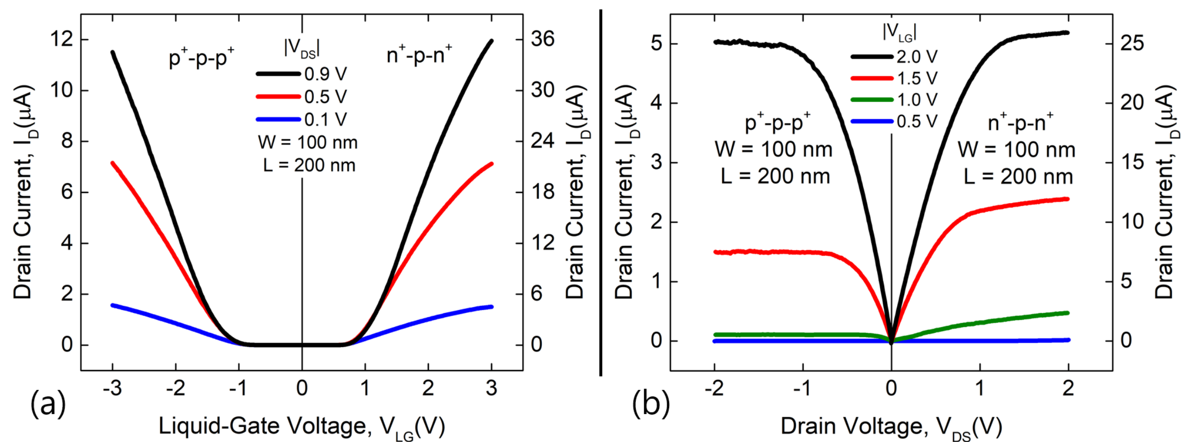

Figure 4.13: Transfer curves (a) measured at various drain-source voltages and output curves (b) measured at various liquid gate voltages for $p^+ - p - p^+$ and $n^+ - p - n^+$ liquid-gated nanowire FET structures with length of 200 nm and width 100 nm.

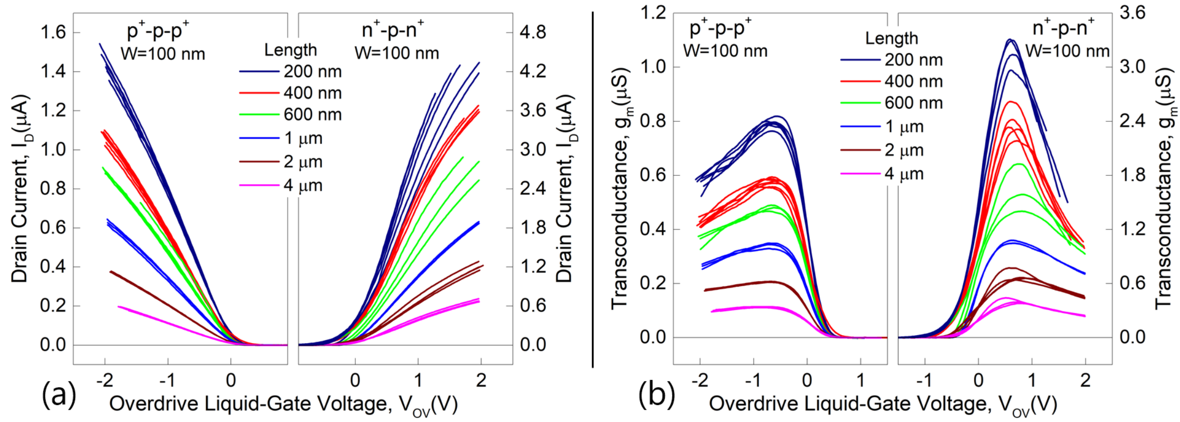

Figure 4.14: (a) Transfer curves measured for $p^+ - p - p^+$ and $n^+ - p - n^+$ structures with different lengths. (b)Transconductance recalculated as a derivative from the transfer curves, shown in (a). It should be mentioned that y scales for n-type devices are three times larger than for p-type devices.

$n^+ - p - n^+$ FET are electrons while for $p^+ - p - p^+$ FET - holes. It is known that for silicon electron mobility is around 3 times greater for electrons than for holes [115–118].

Transfer curves measured for $p^+ - p - p^+$ and $n^+ - p - n^+$ nanowire FETs of different length and width of 100 nm are shown in the figure 4.14(a). Characteristics were measured in linear operation regime at the absolute value of drain-source voltage $V_{DS} = 100\,\text{mV}$ (The sign is selected considering the conduction type: "-" for $p^+ - p - p^+$ and "+" for $n^+ - p - n^+$). Si NW FET structures demonstrate good scalability with length of the nanowire. This is also valid for transconductance(see figure 4.14(b)), recalculated as a derivative of transfer curves. It should be noted that transconductace maximum is also around three times larger for $n^+ - p - n^+$ structures in comparison to $p^+ - p - p^+$ analogues. Threshold voltage of nanowire FETs with different length were extracted from transfer curves as an intersection of a tangent line in the maximum of transconductance with voltage axis 4.15(a). Typical threshold voltage values lie around 1 V with a tendency to slightly increase(taking into account sign) at smaller lengths. Subthreshold swing of measured transistors was obtained from the slope of subthreshold current in the semi-logarithmic scale(see figure 4.15(b)). The median value for $p^+ - p - p^+$ structures is about 169 mV/dec while for $n^+ - p - n^+$ structures the median is about 250 mV/dec. The values obtained demonstrate a good quality of fabricated devices, considering the liquid-gate operation. Extracted mobilities were in the range from $40\,\text{cm}^2\,\text{V}^{-1}\,\text{s}$ to $116\,\text{cm}^2\,\text{V}^{-1}\,\text{s}$ for $p^+ - p - p^+$ structures and from $230\,\text{cm}^2\,\text{V}^{-1}\,\text{s}$ to $500\,\text{cm}^2\,\text{V}^{-1}\,\text{s}$. The contact resistance was analyzed for nanowires of different lengths using the transmission line measurement (TLM) approach. For that the resistance was plotted versus nanowire length at various overdrive gate voltages. The resistance of the nanowires depends linearly on the length and the extrapolation to zero gives the contact resistance defined by the geometry of the devices as well as quality of contact between metal feedlines and silicon. Channel resistace as a function of overdrive liquid-gate voltage is plotted in figure 4.16. Extracted contact resistance is several times smaller than the resistance for shortest nanowires. Therefore the impact of contact resistance on the transport phenomena is negligibly small. It should be noted that the contact resistance depends on the overdrive liquid-gate voltage. The decrease of contact resistance can be explained by thinning the Schottky barrier down

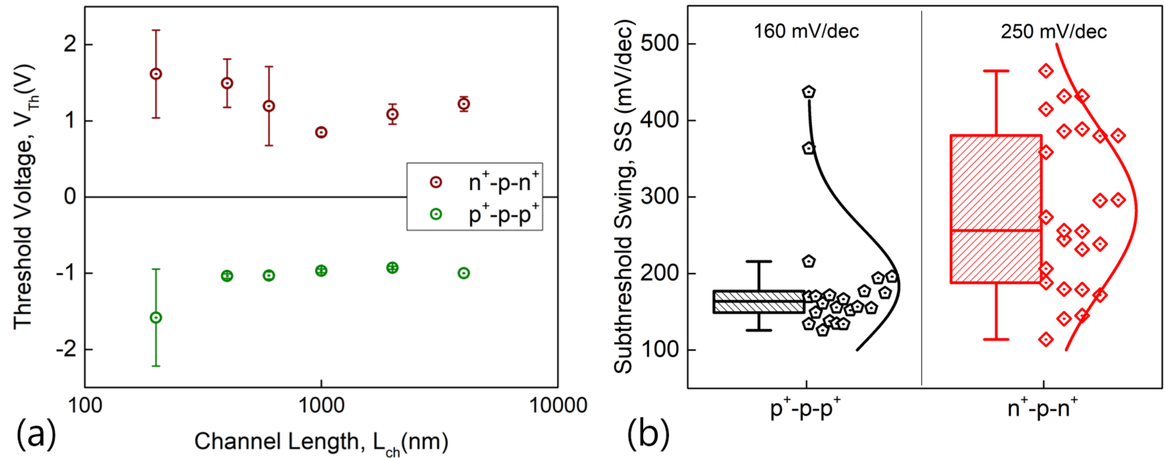

Figure 4.15: (a) Threshold voltages, extrated for the nanowires of different lengths, show that both n-type and p-type devices operate at relatively low gate voltage, under 1.5 V with respect to the sign. (b) Subthreshold swing calculated for $p^+ - p - p^+$ and $n^+ - p - n^+$ nanowire FETs shows a good quality of fabricated devices.

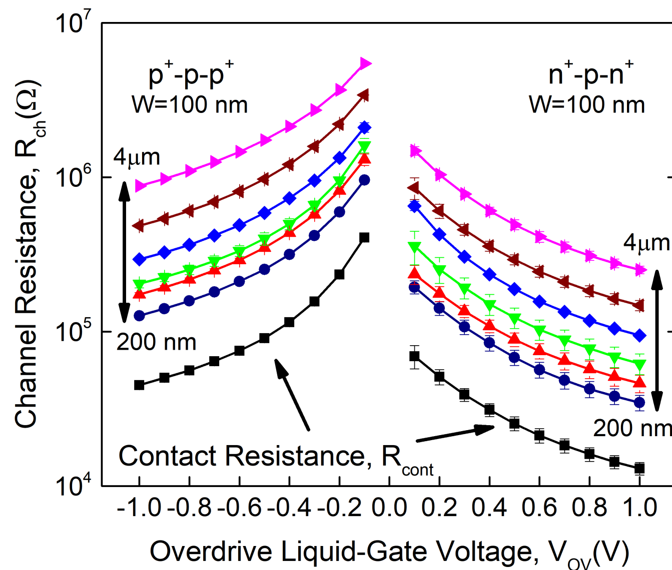

Figure 4.16: Channel resistance extracted for $p^+ - p - p^+$ and $n^+ - p - n^+$ nanowire FETs of different lengths and contact resistance extracted for corresponding device type using TLM method.

as a result of major charge carrier concentration increase in the area of the contact with increasing gate voltage.

Performed characterization of silicon nanowire devices demonstrate a good quality of fabricated nanowire devices with excellent scalability. In this respect fabricated Si NW FETs are a good candidates for both fundamental studies, including size-dependent effects and application in biosensing experiments.

4.5 Gate Coupling Effect(GCE) for Advanced FET Properties

Biosensing is nowadays a highly developed field of research with great potential for applications in the life sciences and health care. Within a wide range of biosensing applications we can emphasize several directions including the detection of biological markers, and the investigation of electrically active cells. Over the decades of extensive investigations silicon NWs attracted much attention because of the remarkable properties, including enhanced sensitivity to molecular-sized objects as well as improved interface to the living cells [1–4, 77].

Over the last few decades scientists have struggled to enlarge the dynamic detection ranges, improve the detection limit for a variety of bio-objects, reduce the noise level and improve signal-to-noise ratio. However, challenges regarding the reliability and stability of passivation layers in liquid environment as well as the noise property optimization in nanosized devices have still not been completely resolved.

Partially, problems can be overcome by studying a variety of device regimes and selecting the optimal one where the best performance can be achieved. Recently, it was demonstrated that the operation of $p^+ - p - p^+$ liquid-gated Si NW biosensors can be optimized by tuning the conducting channel position [77]. The utilization of both liquid and back gates in the case of p-type channels allows the dominant 1/f noise mechanism to be switched from the surface to the bulk of the nanowire, which results in significant noise suppression and improvement of the signal-to-noise ratio.

In this section, we evaluate the gate coupling effect of $n^+ - p - n^+$ Si NW FET structures using noise spectroscopy, technology computer-aided design (TCAD)simulations and utilizing both liquid and back gates to control the device conducting channel. In contrast to the accumulation mode, the inversion mode in Si NW FETs has the channel position localized much closer to the interface between the Si NW and dielectric layer. As it will be shown the structures provide improved sensitivity to the surface potential change of the NW biosensor.

To overcome several limitations including the short-channel effects [119–121], reduce the power consumption and increase the performance of the MOSFET devices ultra thin body (UTB) SOI design was introduced into nano-scaled complementary metal-oxide-semiconductor (CMOS) technology. As the transistor body gets thin enought the fundamental feature of charge coupling between front and back gates becomes more pronounced. Such behavior is also known as a gate coupling effect and it is related in particular to threshold voltage of the device [122, 123]. This means that the threshold voltage of the device controlled through the front gate can be adjusted by applying the back-gate bias. Such approach is often used for the characterization of FET devices. To date many models has been developed to explain the impact of gate coupling effect taking into account the high-field effects and dielectric breakdown, volume inversion and quantum mechanical effects as well as substrate depletion [124–126]. Often for the description of gate coupling effect various models are not using the analytical representation of the threshold voltage but instead the certain value at which the inversion carrier density reaches arbitrary taken value (e.g. $1 \times 10^{11}\,\mathrm{cm}^{-2}$). Typically it is used for the numerical simulations which causes difficulties extracting the experimental parameters [127].

Therefore the simplest Lim-Fossum model is still used for the characterization even though it was introduced already more than 30 years ago. Due to this model the threshold voltage of one gate linearly depends on the voltage applied to the opposite gate termi-

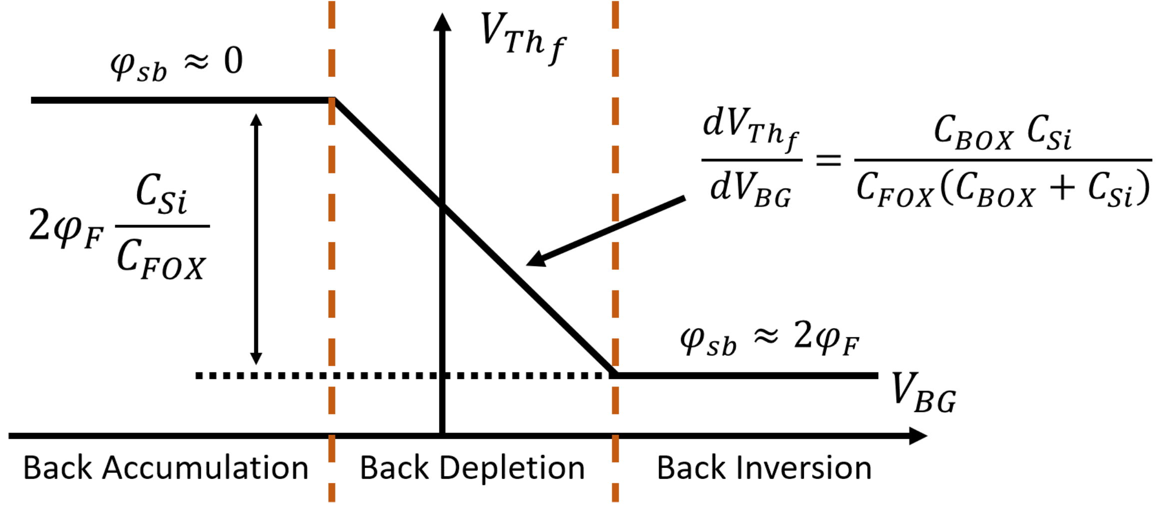

Figure 4.17: The dependence of threshold voltage at the front gate, V_{Th_f}, on the back gate voltage, V_{BG}, predicted by the Lim-Fossum model. Adapted from [128].

nal where depletion is established (figure 4.17). The dependence saturates when strong accumulation or inversion is reached at the other terminal.

The threshold voltage at the front interface depends on the back gate voltage as:

$$\frac{dV_{Th_f}}{dV_{BG}} = -\frac{C_{Si}C_{BOX}}{C_{FOX}(C_{Si}+C_{BOX})} \tag{4.1}$$

,where V_{Th_f} is the threshold voltage at the front interface, V_{BG} is the back gate voltage, C_{Si} is the capacitance of depleted silicon film, C_{FOX} and C_{BOX} are the capacitances of front gate oxide and back gate oxide, correspondingly. In our contribution we performed studies of the liquid-gated FET device for the purpose of the biosensor properties enhancement.

4.5.1 GCE in Si NW Array FETs

The impact of the gate coupling effect has been studied for the $n^+ - p - n^+$ Si nanowire FETs in liquid-gate configuration. We applied both liquid and back gates to control the device conducting channel and performed the investigations of transport properties involving noise spectroscopy. The structures under study were Si NW array FETs where the conducting channel is represented by 50 nanowires connected in parallel with the spacing of 250 nm. Nanowires were 100 nm wide and the length of the conducting channel varied in the range from 16 µm to 21 µm. The structures were fabricated on the basis of SOI wafers using CMOS-compatible technological process. The liquid-gate dielectric was 8 nm thin thermally grown SiO_2 layer. The thickness of the buried oxide was 145 nm. phosphate-buffered saline (PBS) was used as the electrolyte solution during the measurement. The liquid gate voltage was applied using the Ag/AgCl reference electrode. Highly doped silicon substrate of the wafer was used as a back-gate.

Firstly a proper operation of both back- and liquid-gate configured transistors we performed I-V measurements using corresponding gate terminals as it is shown in figure 4.18. The curves demonstrate a typical curves for FET device using both liquid- and back-gates which means that transistor can be controlled well using both gates.

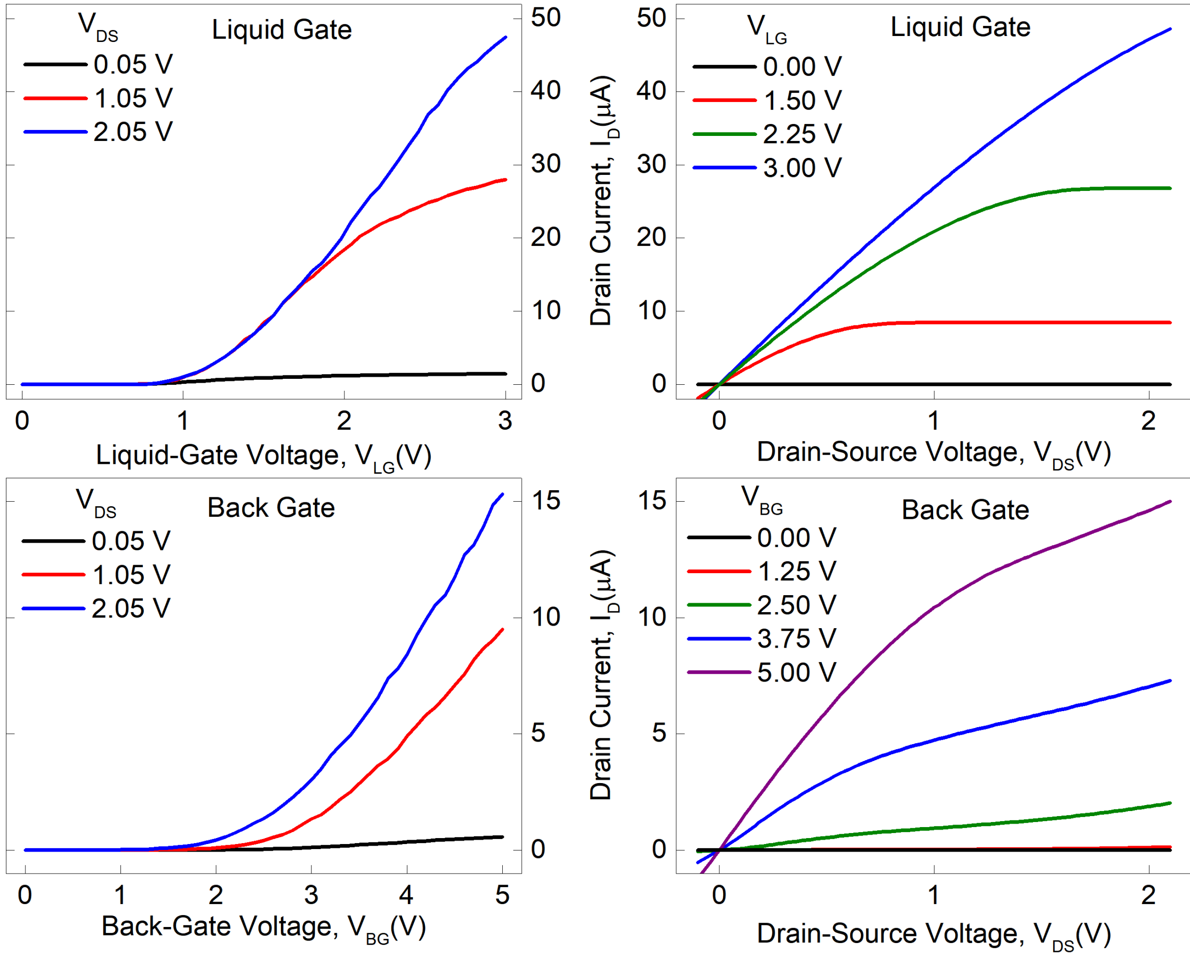

Figure 4.18: Transfer and output curves measured using both liquid and back gates demonstrate a good control over the current through the channel.

To check the impact of gate coupling effect on the channel conductivity we performed the IV characterization at varying back gate bias using the setup described in the section 3.1 where back gate voltage was additionally supplied with another source-meter unit. Drain-source voltage was set to 50 mV to keep the device in the linear operation regime. Transfer curves were measured at different back gate bias as it is shown in the figure 4.19(a).

Back gate voltage caused the shift of transfer curves towards lower threshold voltage of the transistor and fits well to the linear dependence predicted by the Lim-Fossum model [122]. In order to determine the optimal operation mode of fabricated devices we performed measurements of the device transconductance at different liquid- and back-gate voltages within the ranges where device demonstrate reproducible characteristics without irreversible changes as the result of dielectric damage. The transconductance color map for $n^+ - p - n^+$ liquid-gated Si NW FETstructure is presented in figure 4.19(b).

For the inversion n-type channel FET structure, no significant deviations from the traditional FET behavior were observed except of a shift of the threshold voltage with varying back-gate voltage. In order to study device transport properties at different channel locations, we performed noise measurements in the mode of constant current. Noise measurements were performed using a noise measurement system developed in-house. Schematic can be found in the section 3.2.

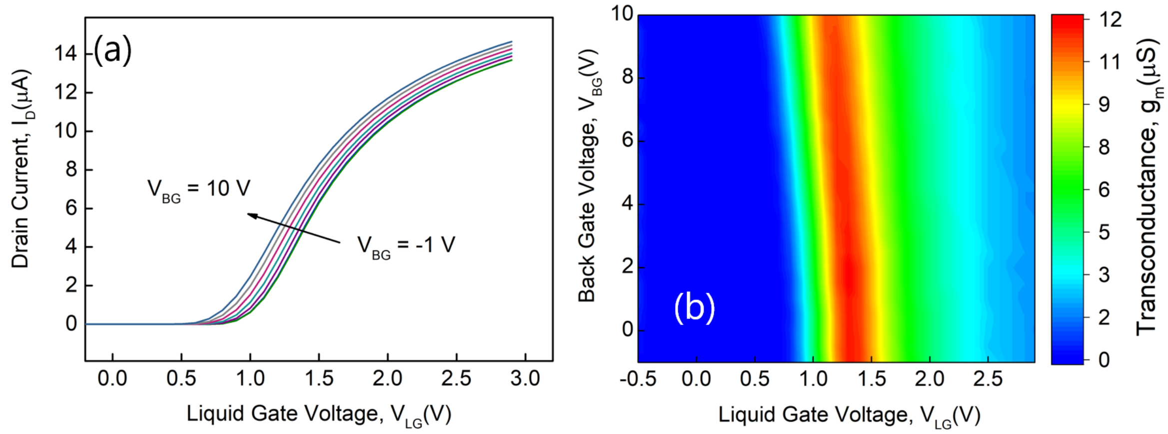

Figure 4.19: (a) Transfer curves of Si NW array FET measured at back gate voltages from −1 V to 10 V at $V_{DS} = 50$ mV. (b) Transconductance of the Si NW array FET measured at $V_{DS} = 50$ mV plotted as a color map versus V_{BG} and V_{LG} . Red color corresponds to the maximal values, while blue - for minimal.

The channel resistance was selected according to the maximum of the transconductance, g_m , at zero back-gate voltage and then both liquid- and back-gate voltages were swept in such a way that the drain current was kept constant and equal to 0.26 uA at 50 mV drain voltage. The voltage spectral densities obtained are presented in figure 4.20(a).

The measured spectra demonstrate small changes with gate voltages. This reflects a weak dependence of the device noise on the back-gate voltage, which is different from the behavior of an accumulation mode FET[77].

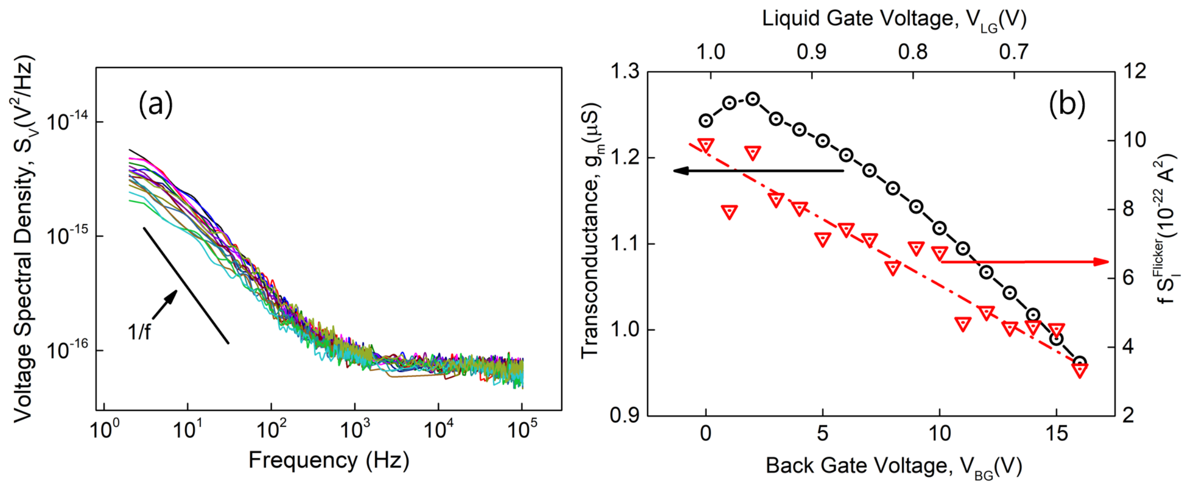

Figure 4.20: (a) Drain voltage noise spectral density, S_V , measured for Si NW array with a 100 nm wide nanowires and 20 µm length. Drain-source voltage was 50 mV. Liquid and back gate voltages were swept in a way that the current through the channel remained constant at 0.26 µA. (b)Transconductance (black circles) and flicker noise amplitude at 1 Hz(red triangles) measured in a constant current regime. Both dependencies are functions of both liquid and back gate voltages. Red line is plotted as a guide for eye.

The transconductance dependence on the liquid- and back-gate voltage demonstrates a monotonic decrease. The flicker noise component was extracted from the spectra by fitting and it is shown along with the transconductance in figure 4.20(b). The behavior of the 1/f noise follows the transconductance in a wide range of back-gate voltages and decreases with increasing back-gate voltage. This makes sense while the working point was selected initially at the maximum of transconductance. Thus the shift of transfer curves toward lower threshold voltage causes the decrease of the transconductance. As far as the measurements of figure 4.20 were performed in the constant current mode, changing of the gate voltages represents a slight displacement of the carrier distribution from the surface of the NW. Therefore the top dielectric layer is mainly responsible for the fluctuations in the channel of the nanowire. The equivalent input noise is a convenient parameter for making a decision about the dominant noise mechanism [90]:

$$S_U = \frac{S_I}{g_m^2} \tag{4.2}$$

where is the current spectral density and g_m is the transconductance. The behavior of S_U in the constant drain current mode is presented in figure 4.21.

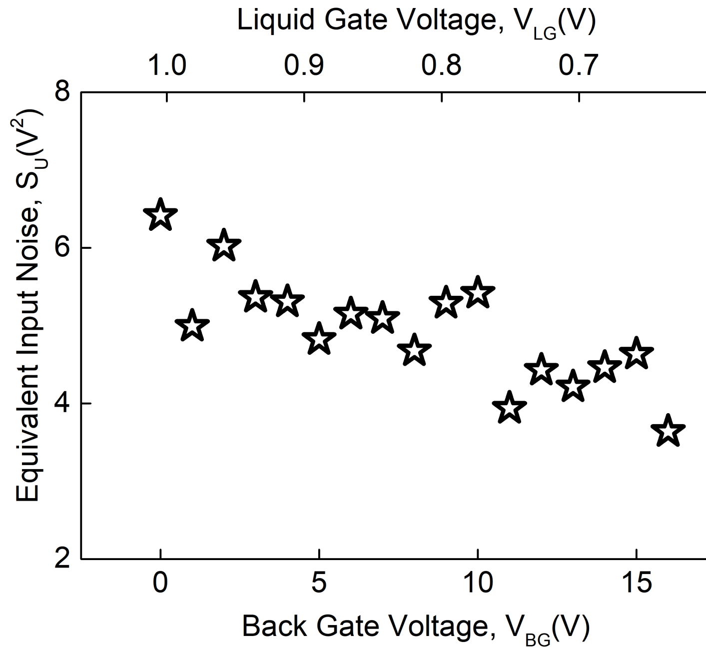

Figure 4.21: Equivalent input-referred noise calculated for noise spectra at 10 Hz and multiplied by frequency. Plotted as a function of both liquid and back gate.

It shows negligible changes at different front- and back-gate voltages. Therefore, we can conclude that in the fabricated liquid-gated Si NW array FETs noise at not too high V_{BG} is mainly determined by the number fluctuation model due to the carrier interactions with the traps located in the liquid gate dielectric. Thus, by moving the channel from the liquid gate toward the back gate we can see that the liquid gate dielectric – Si interface is more noisy than the back gate dielectric – Si interface.

To study the gate coupling phenomenon and its influence on device performance and noise characteristics, we performed an experiment where noise characteristics were measured along the transfer curves of liquid-gated FETs in linear and saturation regions with the influence of the back gate ($V_{BG} = 10$ V) and without ($V_{BG} = 0$ V). Noise spectra were

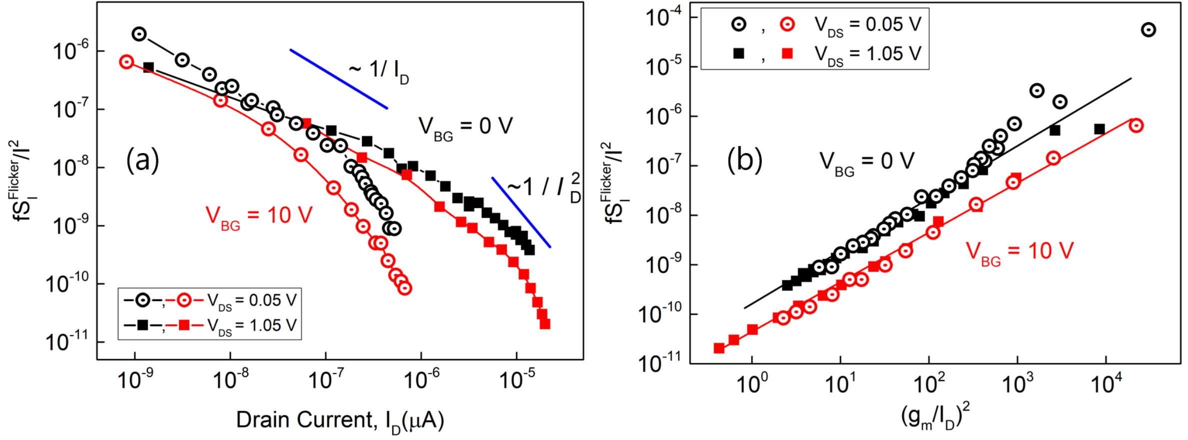

Figure 4.22: (a) Multiplied by frequency current noise spectral density measured in different operating regimes with and without back gate.(b) Normalized current noise spectral density as a function of $(g_m/I_D)^2$ at different applied back gate voltages.

acquired at different liquid gate voltages with and without using the back gate. Normalized flicker noise component multiplied by frequency is plotted against the drain current in 4.22(a). We observe the $1/I_D^2$ behavior. This reflects the trapping/detrapping model transformed to the correlated number/mobility fluctuation theory [129] for cases with and without back gate influence.

The input-referred noise presented in 4.23(a) demonstrates the shift of data point sets corresponding to the back gate influence in the direction of lower noise. Moreover, the dependence on gate voltage is not observed so that it can be concluded that the number fluctuations take place in the channel. The decrease in noise can be explained by the spread of the inversion layer within nanowire and the enhanced coupling effect, causing improved control of channel conductivity by the applied back gate voltage. We can show this by analyzing the flicker noise using the approach described in [130]. The contribution of the flicker noise of the two interfaces Si / SiO2 (Δn fluctuations): front, S_{Uf}, and back, S_{Ub}, to the overall noise considering the values g_m^2/I_D^2 can be described by equation 4.3.

$$\frac{S_{ID}}{I_D^2} = S_{Uf}(\frac{g_{mf}}{I_D})^2 + S_{Ub}(\frac{g_{mb}}{I_D})^2 \tag{4.3}$$

When sweeping the liquid-gate voltage we fixed back-gate voltage. Thus we can assume that $(g_{mb}/I_D)^2$ does not change very much. The normalized noise densities of the drain current (S_{ID}/I_D^2) as a function of $(g_m/I_D)^2$ with different back gate voltages are shown in figure 4.22(b). Two lines in figure 4.22(b) reflect the linear relationship of equation 4.3 for two cases: when using back gate and when it is set to zero.

Note that the larger values fS_I/I_D^2 correspond to noise normalized to a lower drain current value. By increasing the gate voltage, the FET transport in the channel is changed to a regime of strong inversion with increased electron density (for both classical and quantum considerations) shifted to the interface corresponding to the gate. This reflects the fact that, with respect to the inversion channel, by applying the back gate voltage the position of the channel is shifted in the direction of the substrate. This causes a decrease of the interaction rate with traps near the top dielectric thus lowering the noise level. Such a situation is extremely attractive for biosensor applications, in particular the extracellular

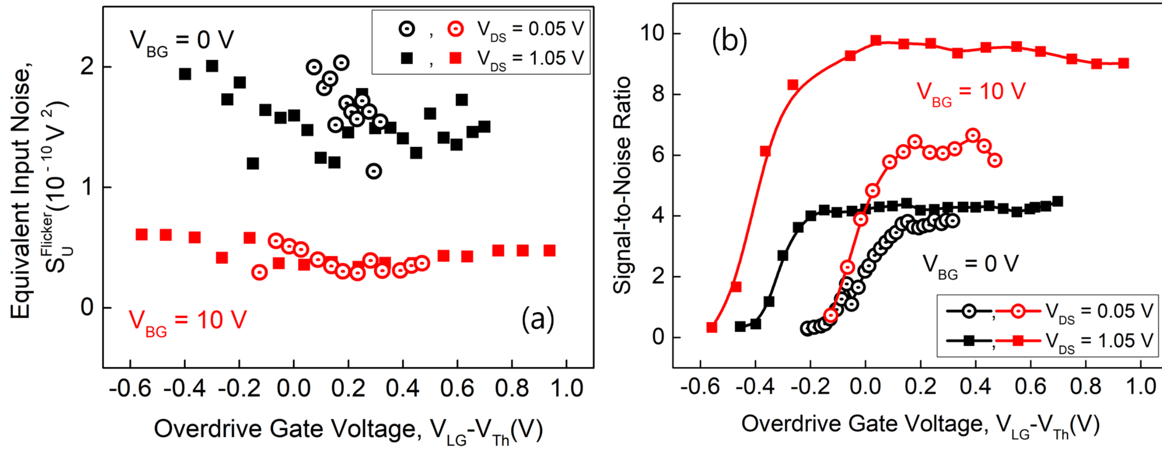

Figure 4.23: (a) Equivalent input-referred noise calculated from noise spectra at 1 Hz in different operation regimes.(b) Calculated signal-to-noise ratio (SNR) in different operation regimes for the bandwidth of 100 Hz and reference voltage fluctuations of 100 µV, typical for neuronal signals.

action potential detection of electroactive cells. Since the amplitude of typical neuronal cell action potential pulses are in the range of 100 µV, the signal-to-noise ratio of the detector has to be large enough to amplify this signal. In our study we demonstrated the possibility of lowering the noise level when applying the back gate voltage. This results in a change of the SNR, as shown in figure 4.23(b). The values of SNR were calculated using equation 2.24. The frequency bandwidth was selected at 100 Hz as suitable for recording of cellular signals, and reference voltage fluctuation was defined as 100 µV - typical amplitude for neuronal signal. For the same drain source voltages, the curves measured using the back gate voltage demonstrate an improved SNR compared to that obtained without back gate voltage. At the higher drain – source voltage of 1.05 V the SNR is twice larger in comparison to the case without back gate application.

4.5.2 GCE in Single Si NW FETs

In comparison to the long nanowire arrays, single silicon nanowire demonstrate enhanced gate coupling due to higher degree of electrical confinement. Transfer curves measured for $p^+ - p - p^+$ Si NW FET at back-gate voltages ranging from 0 V to −16.5 V are shown in figure 4.24(a). Back gate voltage causes the shift of transfer curves towards lower threshold voltages. Similar behavior is observed on the transconductance curves (figure 4.24(b)). Furthermore application of back gate voltage is accompanied by the increase of transconductance maximum. The effect indicates on tuning the position of conducting channel within the nanowire and supports the ideas of increased signal-to-noise ratio for the detection of biological signals [77]. The situation differs for the $n^+ - p - n^+$ type structures. Transfer curves measured for $n^+ - p - n^+$ Si NW FET are shown in figure 4.25(a). Together with curve shift towards lower threshold voltage the slope also changes. Transconductance curves demonstrate the shift together with the change of transconductance maximum (figure 4.25(b)). Furthermore at certain back-gate voltage additional bump appears. It is referred to the inversion at the back-gate interface and formations of another conductation channel. To understand the impact of

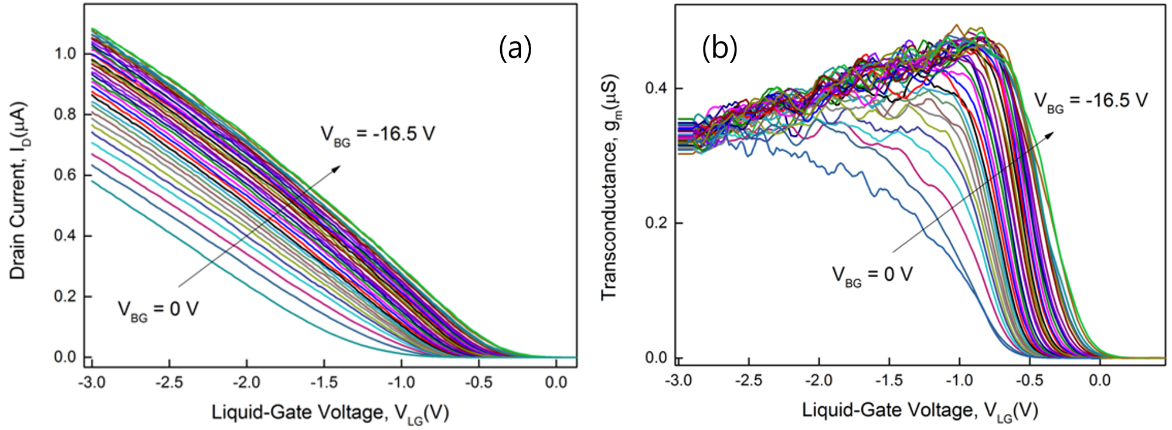

Figure 4.24: (a) Transfer curves measured for $p^+ - p - p^+$ nanowire structures. (b) Transconductance calculated from transfer curves.

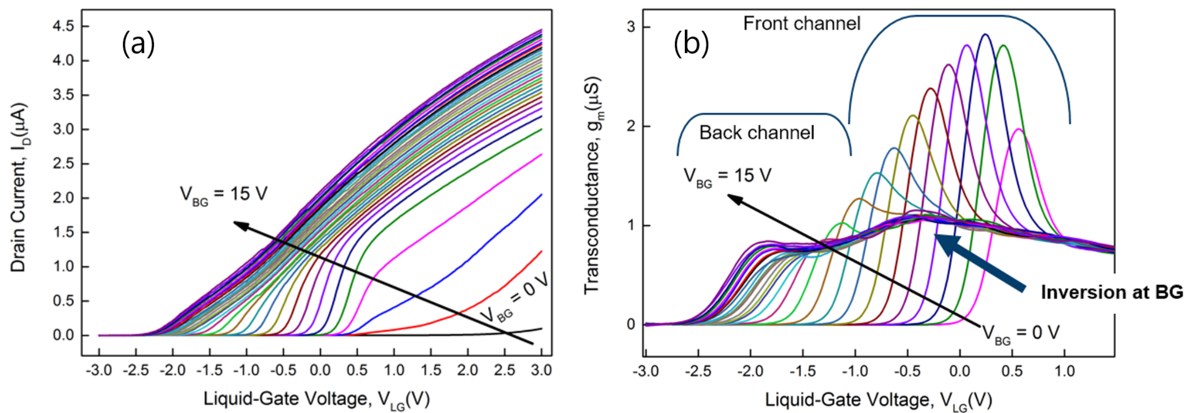

Figure 4.25: (a) Transfer curves measured for $n^+ - p - n^+$ nanowire structures. (b) Transconductance calculated from transfer curves.

back gate voltage on the charge carrier distribution we performed numerical simulations using TCAD software.

4.5.3 TCAD Simulation and Analysis of GCE

We implemented a 3D model of our $n^+ - p - n^+$ NW FET transistor in the Sentaurus TCAD software and simulated its behavior at different front- and back-gate voltages in order to study the front-back gate coupling effect in the inversion channel FET. Simulated nanowire device was 500 nm long and 100 nm wide as it is shown in figure 4.26.

The simulated transfer curves are shown in figure 4.27(a). The drain voltage was set to 100 mV to keep the device in linear operation regime. The back gate voltage was varied from -3 V to 15 V. As we can see, applying the back gate voltage affects the threshold voltage and shifts the transfer curves towards lower front-gate voltages. At higher back-gate voltages, the shape of the transfer curves also changes. At lower back-gate voltages ($V_{BG} < 5$ V), transfer curves have a linear region and sublinear region, caused by contact resistance and mobility degradation. At higher back-gate voltages, two linear modes are observed before the sublinear mode is reached. Such an effect may be explained by the

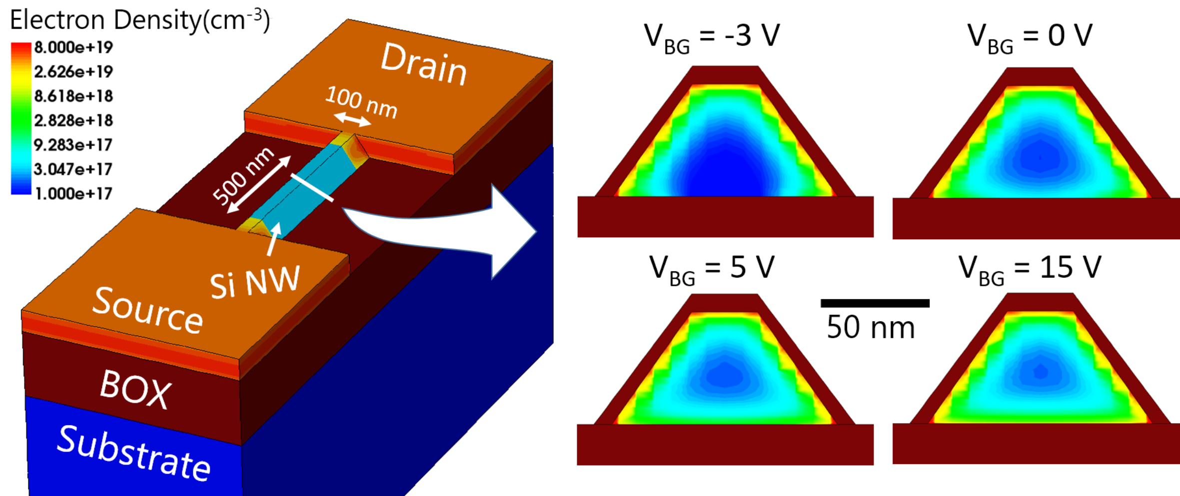

Figure 4.26: The simulated silicon nanowire structure(left) and the electron density (right) across the nanowire cross-section at different applied back gate voltages. With increasing positive back gate voltage the electron concentration at the back interface increases and forms the inversion channel.

formation of the second channel near the back-gate oxide.

The observation of the second conductive channel is also confirmed by transconductance of the NW FET, obtained as a derivative of the transfer curves (figure 4.27(b)). Indeed, for the case of higher V_{BG} , a plateau corresponding to the second linear region is clearly resolved on the transconductance curves. Such behavior was also observed for ultrathin SOI MOSFETs with a standard and ultrathin BOX layer [131]. It should be noted that the maximum value of transconductance increases with increasing back gate voltage.

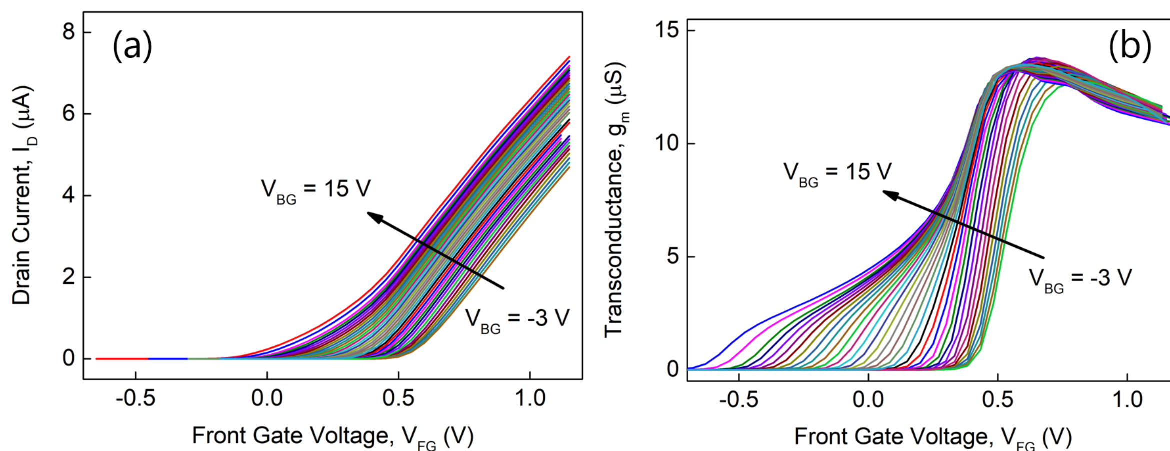

Figure 4.27: Transfer curves (a) and transconductance (b) calculated for the nanowire structure shown in figure 4.26. With back gate voltage increase the transfer curves shift towards lower threshold voltages. The curves also change the slope, which is reflected in transconductance curves(b) as a bump. The feature corresponds to the formation of inversion channel at the back gate interface.

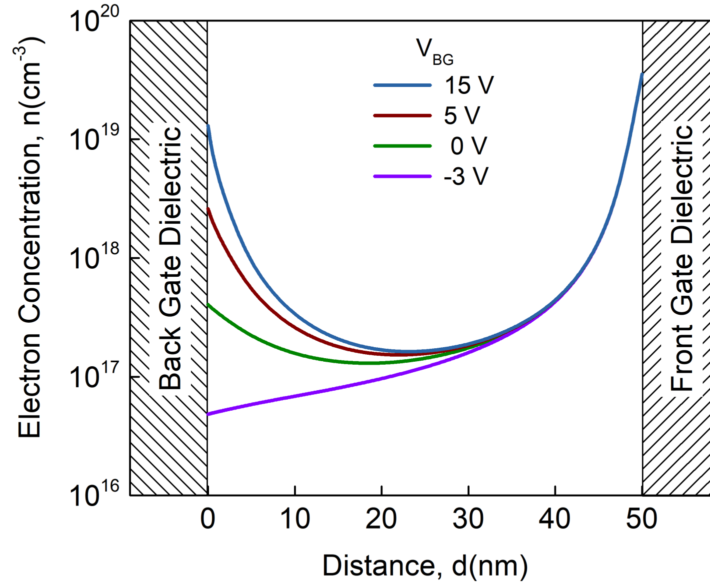

Figure 4.28: Electron concentration profile in the middle of nanowire channel

In order to investigate the phenomenon of front-back gate coupling effect on the transconductance, we simulated the charge carrier distributions at different back-gate voltages. The crossections of silicon nanowire demonstrating electron distributions at different back gate voltages are shown in figure 4.28. The front gate voltage was fixed at 3 V to keep the inversion mode of the device. Meanwhile the back gate voltage was swept from −3 V to 15 V. As it is shown in figure 4.28 the electron concentration changes with applied voltage. The back gate voltage of −3 V causes the accumulation next to the back dielectric, while at positive voltages the concentration of electrons next to the back dielectric increases leading to the inversion. The electron concentration profile is shown in figure 4.28. Under different applied back-gate voltages, the charge carriers are pulled towards both interfaces and causing the inversion at both back and fron dielectrics. The front-back gate coupling effect in the case of an n-type inversion FET is realized as the pumping of charge carriers between two potential wells: near the front-gate dielectric and near the back-gate dielectric. Also under certain conditions the formation of two channels (see figure 4.28) at the same time may be observed. It should be emphasized that in spite of applying a pulling voltage for the inversion carriers on the back gate there is still a conducting channel localized near the front gate. Therefore observing switching of the dominant noise mechanism from number fluctuations to mobility fluctuations is unlikely in the case of inversion channel NW FET.

4.6 Noise Spectroscopy of NW FETs

Noise characterization of silicon nanowire devices had been performed using the noise measurement setup described in section 3.2, including low-noise preamplifier. Measured voltage fluctuations were translated into a noise power spectrum, S_V , via the fast Fourier transform. Further voltage noise power spectra, S_V , in units of V^2/Hz are translated into current noise spectral density in units of A^2/Hz as $S_I = S_V/R_{eq}^2$, where R_{eq} is an equivalent resistance determined by the load resistance, R_{load} , and sample resistance in the circuit. Noise characteristics were measured in different operation modes for the

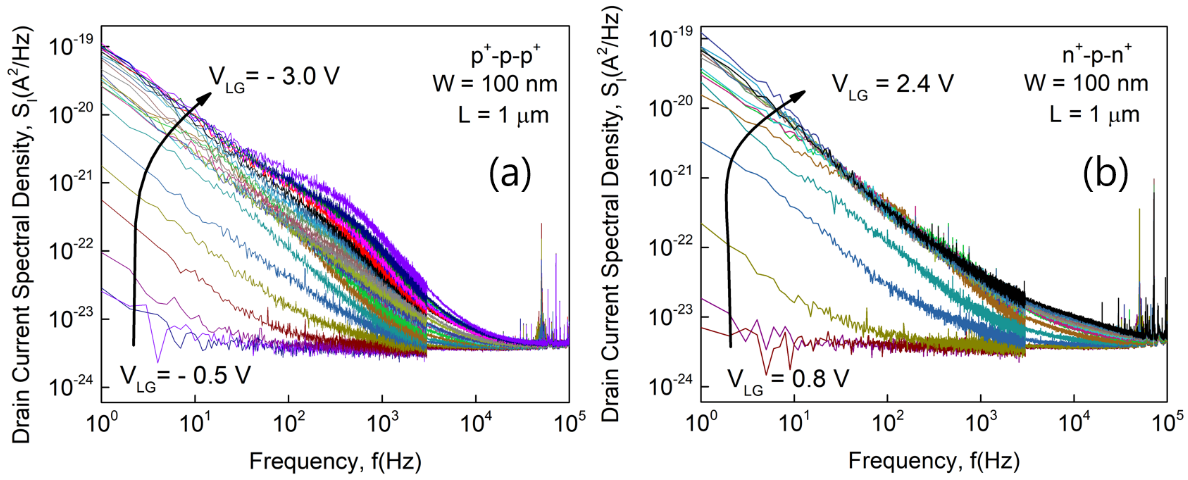

Figure 4.29: Drain current noise spectral density measured for 100 nm wide and 1 µm long nanowires in $p^+ - p - p^+$ and $n^+ - p - n^+$ configurations.

Si NW FET structures with various nanowire widths and lengths. A typical current noise power spectral density of both $n^+ - p - n^+$ and $p^+ - p - p^+$ device types with width of 100 nm and length of 1 µm are shown in figure 4.29. At low frequencies, noise spectra demonstrate the 1/f flicker noise behavior, which is dominant for major Si NW chips under investigation. generation-recombination (GR) noise components appearing in the noise spectra for nanowires with small characteristic sizes often correspond to single electron events resulting in random telegraph signal fluctuations of the current through the channel. To study the impact of nanowire size on noise properties we performed noise measurements on the nanowire sets with widths in the range from 70 nm to 500 nm and length - from 1 µm to 2 µm. The values of the current noise power spectral density at 10 Hz as a function of the overdrive gate voltage ($V_{OV} = V_{LG}{-}V_{Th}$) are plotted in figure 4.30.

The curves have several regions reflecting different noise behavior with respect to the operation mode. It should be emphasized that p-type devices demonstrate dependence on the overdrive liquid-gate voltage, while n-type devices demonstrate constant behavior in the strong inversion. The normalized current spectral density at 10 Hz is shown in figure 4.31. The p-type devices demonstrate I_D^{-1} behavior while n-type - I_D^{-2}. Such variation can be explained by different origins of noise for n- and p-type structures. Usually the input referred noise, S_U , is considered for an analysis of the noise sources in the devices. The value of S_U can be calculated according to the following expression: $S_U = S_I/g_m^2$. The input-referred noise of both device type is plotted in figure 4.32. The fact that the input-referred noise is independent of the overdrive gate voltage can be explained in the framework of the McWhorter number fluctuation model, where the interaction with traps in gate dielectric is most pronounced. On the other hand, when input-referred noise depends on the overdrive gate voltage, the intrinsic resistance fluctuations or volume noise behavior can be described by a phenomenological Hooge's model of mobility fluctuations. In p-type devices the hole concentration spreads into the volume of silicon channel where the noise behavior is determined by the charge carrier scattering on the lattice. Hooge's parameter, α_H , can be calculated using equation:

$$\frac{S_I}{I_D^2} = \frac{\alpha_H}{fN} \tag{4.4}$$

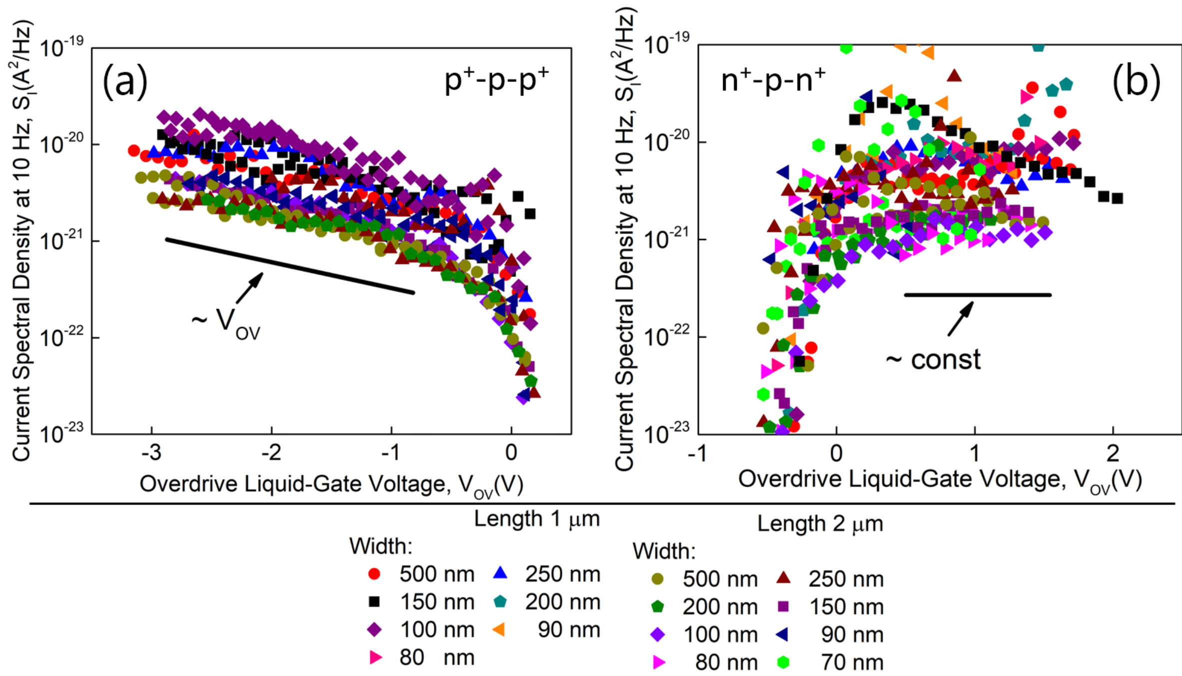

Figure 4.30: Current noise spectral density measured on the nanowires of different widths in the range from 70 nm to 500 nm and lengths of 1 and 2 microns for (a) $p^+ - p - p^+$ and (b) $n^+ - p - n^+$ configurations.

, where N is the number of charge carriers. The first suggested value of α_H was equal to 2×10^{-3}. Later the dimensionless parameter α_H , referred to as the Hooge's parameter, was found to be dependent on the crystal quality of the device and it was demonstrated

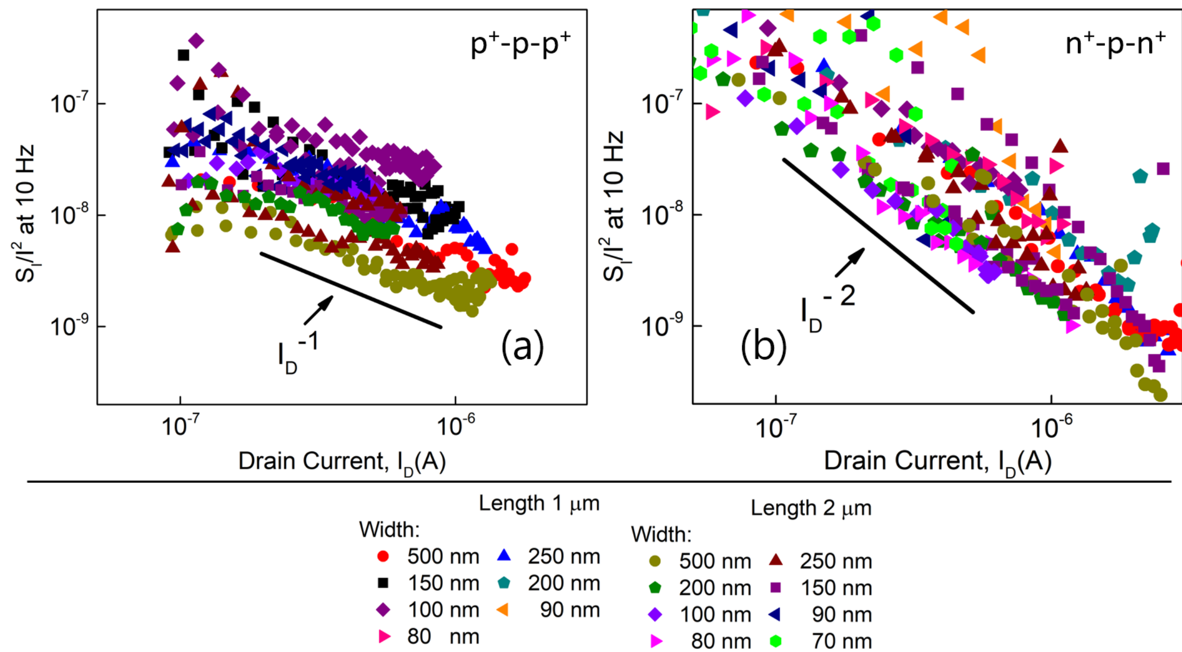

Figure 4.31: Normalized current noise spectral density measured on the nanowires of different widths in the range from 70 nm to 500 nm and lengths of 1 and 2 microns for (a) $p^+ - p - p^+$ and (b) $n^+ - p - n^+$ configurations.

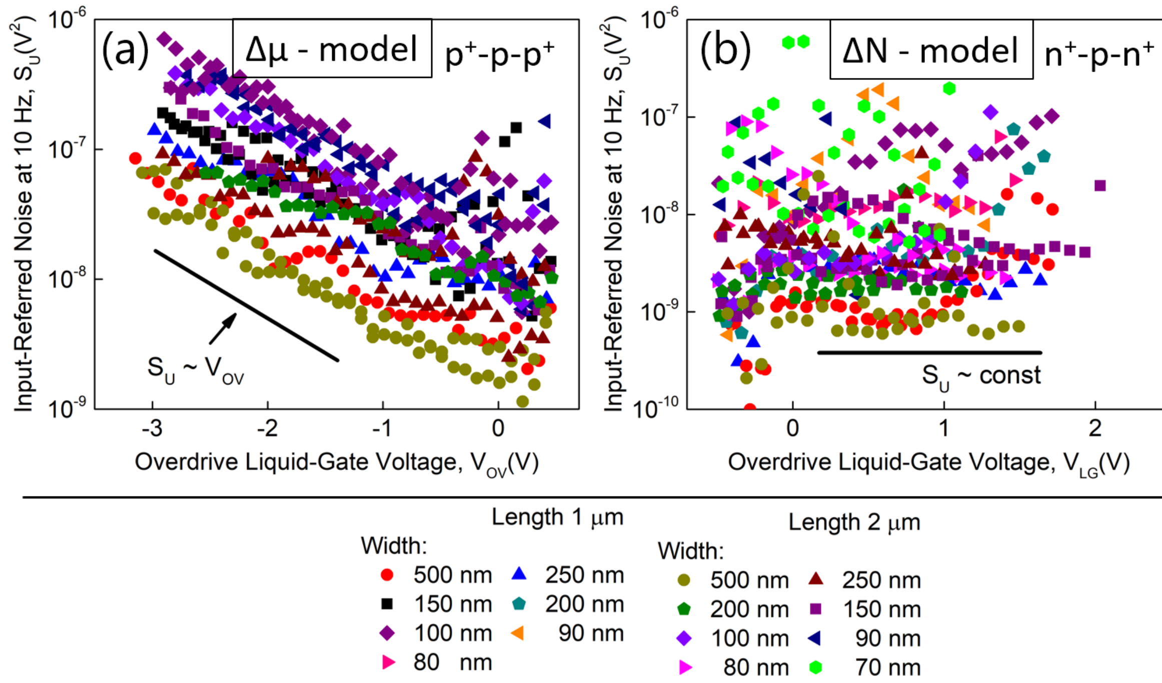

Figure 4.32: Input-referred noise recalculated from noise spectra measured on the nanowires of different widths in the range from 70 nm to 500 nm and lengths of 1 and 2 microns for (a) $p^+ - p - p^+$ and (b) $n^+ - p - n^+$ configurations.

to be 2-3 orders of magnitude lower for perfect devices [90]. Nowadays, α_H is often used for the comparison of noise levels and performance of a various devices, regardless of the materials they are made of. It should be noted that for nanowire biosensors the noise level, which can be expressed in terms of Hooge's parameter, is the critical factor determining the limit of detection and possibility of real-time molecular binding event extraction [132]. To analyze the origin of the noise, we calculated the input-referred noise according to the expression introduced above (see figure 4.32). The strong dependence of S_U on the overdrive gate voltage for p-type devices in accumulation ($V_{OV} < 0.5$ V) indicate that the 1/f noise measured is not McWhorter noise but rather volume noise described by Hooge's model of mobility fluctuation. The non-monotone behavior was registered in a weak accumulation. On the contrary, n-type devices demonstrate scattering around a constant value of input-referred noise, specific for each structure under study. Such a behavior is a signature of a surface noise, described by McWhorter noise model, where the inversion layer is closely located to the interface between gate oxide and silicon channel.

In order to estimate Hooge's parameter it is important to evaluate the number of charge carriers, N. In the linear regime of FET operation the current through the channel can be estimated as:

$$I_D = nq\mu_{FE}EWh \tag{4.5}$$

, where q is the electron charge, n - charge carrier concentration, μ_{FE} - field-effect carrier mobility, E - electrical field, W - width of the nanowire, h - is the thickness of the nanowire. $E = V_{DS}/L$, where L is the length of the nanowire. $n = N/V$, where V is the volume of the conduction channel, $V = W \times L \times h$. The total charge carrier number, N,

can be estimated taking into account equation 4.5 as:

$$N = \frac{I_D L^2}{q V_{DS} \mu_{FE}} \tag{4.6}$$

The field-effect mobility of charge carriers in linear operation mode can be extracted from the equation for the transconductance:

$$g_m = \mu_{FE} C_{ox} \frac{W}{L} V_{DS} \tag{4.7}$$

Based on the equation 4.7 the field-effect mobility can be estimated using following expression:

$$\mu_{FE} = \frac{L g_m}{W C_{ox} V_{DS}} \tag{4.8}$$

Here $C_{ox} = \varepsilon_{ox}\varepsilon_0/d$ is the gate capacitance. Extracted from noise measurement data values of field-effect mobility were in the range from $40\,\mathrm{cm^2\,V^{-1}\,s^{-1}}$ to $100\,\mathrm{cm^2\,V^{-1}\,s^{-1}}$ for $p^+ - p - p^+$ structures and from $100\,\mathrm{cm^2\,V^{-1}\,s^{-1}}$ to $300\,\mathrm{cm^2\,V^{-1}\,s^{-1}}$ for $n^+ - p - n^+$ structures.Taking into account aforementioned equations the Hooge's parameter can be calculated using the following equation:

$$\alpha_H = \frac{f S_I}{I_D^2} \frac{I_D L^2}{q \mu_{FE} V_{DS}} \tag{4.9}$$

We calculated the dimensionless Hooge's parameter using measured spectra in order to analyze the noise behavior. The dependencies on the overdrive gate voltage for $p^+ - p - p^+$ and $n^+ - p - n^+$ structures are shown in figure 4.33. In the case of the Hooge's model $\alpha_H = const$ while for the McWhorter's model the Hooge's parameter behaves as a function of the overdrive gate voltage $\alpha_H \sim (V_{OV})^{-1}$. For p-type devices(figure 4.33(a)) , there is the voltage range ($V_{OV} < 0.5\,\mathrm{V}$) where $\alpha_H = const$. This confirms the applicability of the Hooge's approach in the regime of strong accumulation. Moreover, in this voltage range we revealed that α_H depends on the width of the measured devices. The Hooge's parameter decreases with increasing width. This tendency does not change from weak to strong accumulation mode. The situation is opposite for n-type structures. In the inversion regime there is a strong dependence of α_H on overdrive gate voltage V_{OV} (see figure 4.33(b)), which is typical of McWhorter's noise model [133]. It is known that the noise level usually increases with decreasing characteristic device sizes [104]. To check the noise property on the samples under study we plot input-referred noise as a function of surface area (figure 4.34).

As it is predicted by noise models (see section 2.5) input referred noise for both n- and p-type FETs is inversely proportional on the surface area. As it is shown in figure 4.34 both device types follow predicted behavior. It should be emphasized that for $p^+ - p - p^+$ structure the input referred noise increases for smaller surface areas while the noise level also depends on the overdrive gate voltage. The overdrive voltage-dependence is, however, not observed for n-type structures. Therefore we can conclude that studies of liquid-gated FETs confirmed domination of Hooge's model of mobility fluctuations for $p^+ - p - p^+$ structures and McWhorter's model of number fluctuations for $n^+ - p - n^+$ structures.

Figure 4.35(a) shows the input-referred noise dependence on the surface area obtained for the fabricated devices in comparison to already published results obtained by other

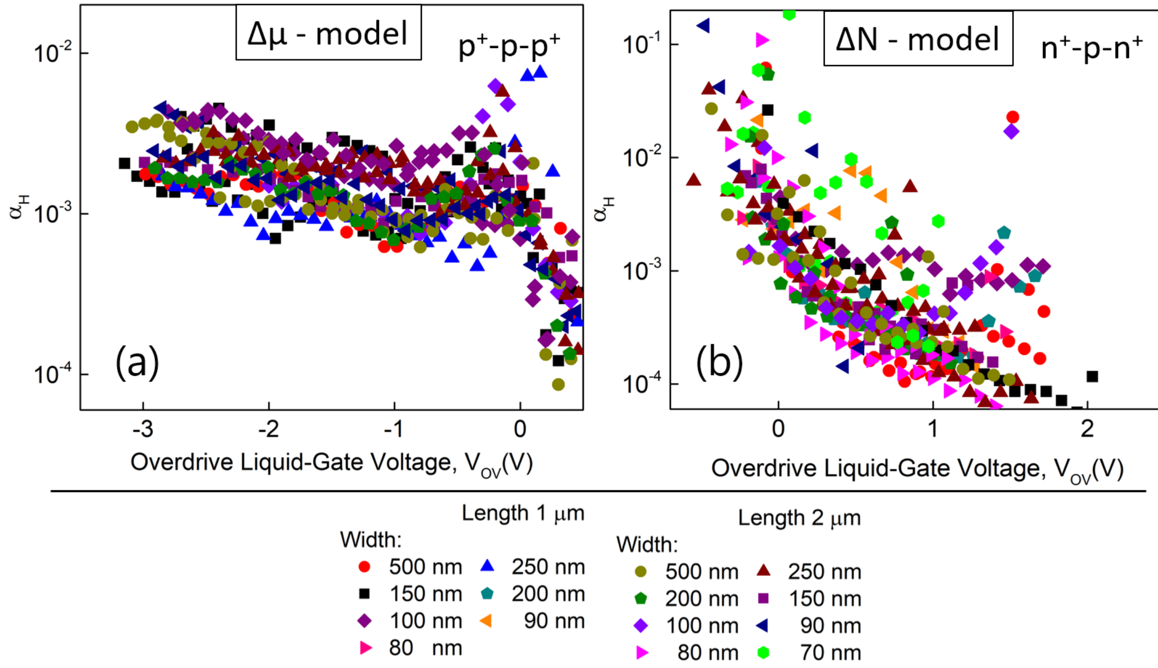

Figure 4.33: The dimensionless Hooge's parameter,α_H , recalculated from noise spectra measured on the nanowires of different widths in the range from 70 nm to 500 nm and lengths of 1 and 2 microns for (a) $p^+ - p - p^+$ and (b) $n^+ - p - n^+$ configurations.

research groups: N.Clement [134], C.Schönenberger [135], M.Reed [136], A. van den Berg [137], C. Dekker [138]. The plot shows that input-referred noise scales well with the active area of the device. Furthermore fabricated devices fit well to the scaling trends of the technological processes of the world-wide known groups. It should be emphasized that the majority of devices demonstrate the noise levels between the fundamental limit determined by the dielectric-polarization noise (estimated for ideal SiO_2 dielectric layer) and the trap-induced noise caused with the trap density of $1 \times 10^{10}\,\mathrm{cm}^{-2}$. When the

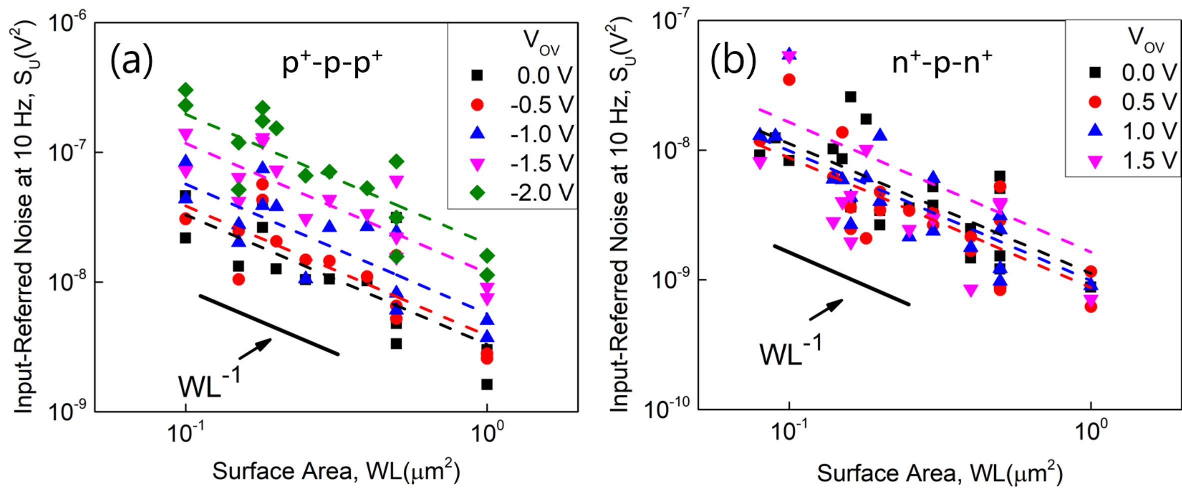

Figure 4.34: The input-referred noise as a function of gate surface area for (a) $p^+ - p - p^+$ and (b) $n^+ - p - n^+$ structures at different overdrive liquid-gate voltages.

active area of the device is scaled down there is a probability to obtain only a single trap which influences the current through the conducting channel by capturing and emitting a single charge carrier. Such behavior is often observed as two-level RTS fluctuations of current in nanowire FETs. The probability(see figure 4.35) was estimated for oxide trap density, $N_{ot} = 1 \times 10^9\,\mathrm{cm}^{-2}$ which approximates the noise over all devices under study. The area corresponding to the single trap is around $0.1\,\mu\mathrm{m}^2$. The probability might vary for much smaller areas since more sophisticated statistical model should be applied.

Biosensing capabilities of biosensors, in particular based on Si NW FETs, and therefore performance strongly depends on the noise properties of the device. In particular, the detection limit is directly influenced by the noise level in the system. As we can see from the figure 4.35, it strongly depends on the structure sizes. While the response of the FET-based system to the collective ion concentration change at the surface(Nernstian response) is defined by the Nernst limit, the sensitivity to single ions is limited by so-called charge noise of the device[134]. Charge noise is defined as:

$$S_q^{1/2} = \frac{C_{ox}}{q} S_U^{1/2} \tag{4.10}$$

,where C_{ox} is the gate capacitance, q is elementary charge, S_U is the input-referred noise. We estimate the charge noise for the data shown in figure 4.35(b) taking into account the gate dielectric capacitance. It should be emphasized that lower charge noise corresponds to the lower sensor area. Accordingly a major part of Si NW FET devices under study are capable of single elementary charge detection. The remarkable feature of Si NW FETs is that the gate area where sensors are capable of single charge detection intersect the area where random telegraph signal noise is likely to occur. Due to the RTS trapping/detrapping of charge carriers from the channel of Si NW FET to the gate oxide traps the process is highly sensitive to the external influence. It should be mentioned that majority of traps observed in the experiment as RTS fluctuations demonstrate non-SRH behavior with strong dependence on the channel current (see figure 4.36). The values of

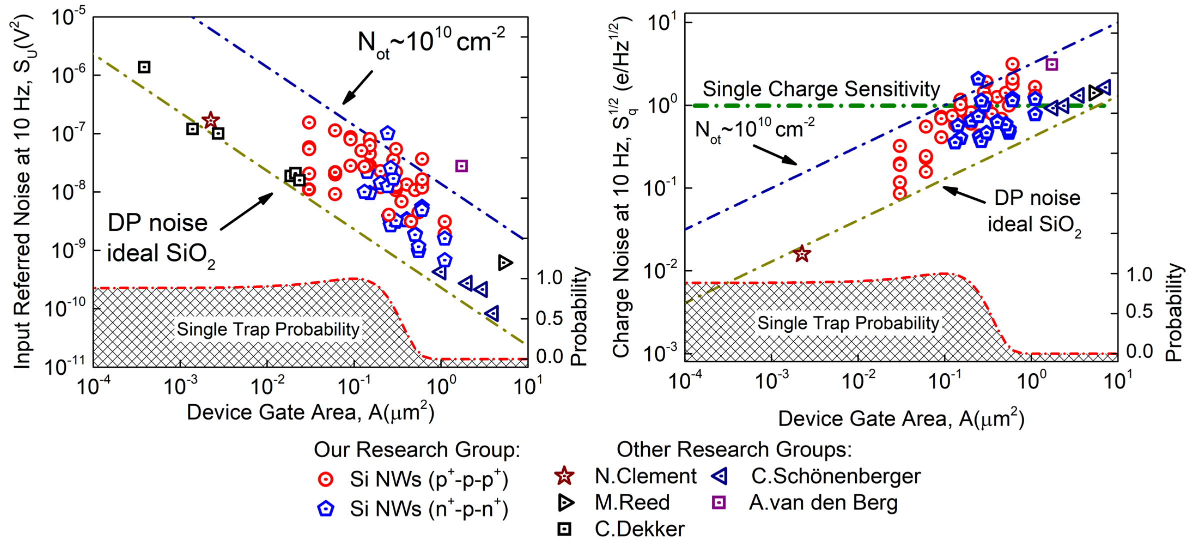

Figure 4.35: (a) The input-referred noise at 10 Hz and (b) the charge noise at 10 Hz as a function of the device gate area in comparison to the devices fabricated and investigated in a worldwide-known research groups.

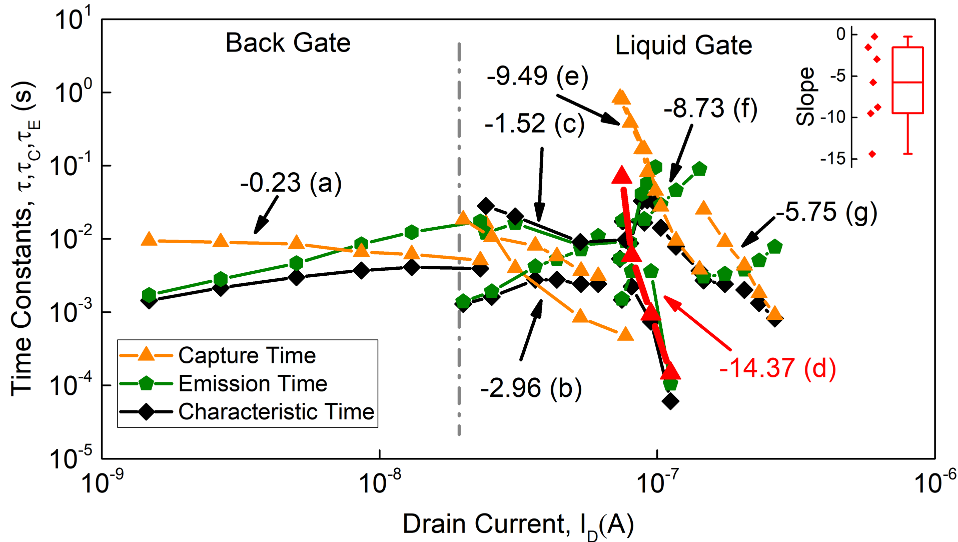

Figure 4.36: Characteristic time constants as a function of drain current recorded on different nanowires controlled by liquid-gate as well as back-gate. (a) slope (-0.23) corresponds to the measurements with back gate. (b)-(g) correspond to measurements with liquid gate. The inset shows the statistics of recorded capture time slopes. The slopes recorded with the liquid gate demonstrate much stronger behavior than predicted by Shockley-Read-Hall (SRH) model. The curve, highlighted with red color, demonstrates the strongest recorded capture time dependence. Such large slope value defines the target for the development of ultrahigh sensitive biosensors.

slope for liquid-gate measurements vary from (-1.52) up to extremely high (-14.37). Such strong behavior reflects very high sensitivity of single trap parameters to the surface potential change. Therefore the monitoring single trap capture dynamics is very promising for the development of highly sensitive biosensors with down to single ion detection limit.

4.7 Single Trap Phenomena for Development of Nanowire Sensor

Silicon nanowires, as a key elements of modern nanoelectronics, allowed to overcome challenges of planar CMOS technology [3, 139–141]. Due to their advanced performance and scalability silicon nanowires, configured as field-effect transistors, deserved one of a leading positions as a transducer for highly-sensitive biosensors. Typically for analyte detection the change of nanowire channel conductivity corresponds to the change of target molecules concentration. Depending on the application the sizes of silicon nanowire FETs may be adjusted to dimensions of a target object allowing the tuning of biosensor sensitivity [142]. Reducing the characteristic sizes noise level of the FET devices tend to increase as it was demonstrated in section 4.6. Furthermore at nanoscale, when characteristic sizes become comparable to the areas, where statistically only a single trap can be located at the interface between silicon channel and gate dielectric, the interaction between such trap and charge carriers in the channel becomes significant and is known as single trap phenomenon. Single charge carrier gets captured to the trap and released back into the channel thus significantly modulating the conductivity of the nanowire channel. Such process is observed as fluctuation of drain current in the nanowire FET channel between two

discrete levels and is also known as random telegraph signal noise. When discovered, RTS fluctuations were immediately classified as a noise component and research was focused on the development of methods to prevent the appearance of such single trap behavior. After decades of comprehensive investigation a number of techniques to reduce the RTS as well as 1/f noise have been suggested. However the possibility of fundamental and applied research using single trap phenomena makes it an object of interest rather than unwanted effect.

Furthermore single trap phenomena became extremely interesting as punctual, and highly sensitive atomic-size probe for nanoscale FETs and is nowadays considered as a promising candidate for many applications including quantum information processing, nanoscopic spin electronics as well as biosensing.

Indeed the processes happening at nanoscale are strongly influenced by various external factors especially electrical field and its changes caused for example by molecule attached to nanowire sensor surface.

Drain current of nanosized FETs can strongly alter the conductivity of the conductive channel. For the submicron FETs the capture kinetics was observed to deviate from the generally accepted SRH model due to geometrical factor or field effects [143–146]. Therefore single trap phenomenon can be considered as a smallest ever, atomic-size, highly sensitive sensor. The information about target objects can be extracted from the measured RTS fluctuations. Modern possibilities of fast data acquisition and processing allow real-time analysis and extraction of significant information and monitoring of the analyte concentration.

4.7.1 Enhanced Capture Kinetics Behavior

As mentioned before random telegraph signal noise is observed as two level fluctuations of the drain current of the FET device due the existance of single trap in the gate dielectric as it is shown in the figure 4.37. For nano-sized FETs the active volume is enough for only a small amount of charge carriers to flow. The removal of only a single charge

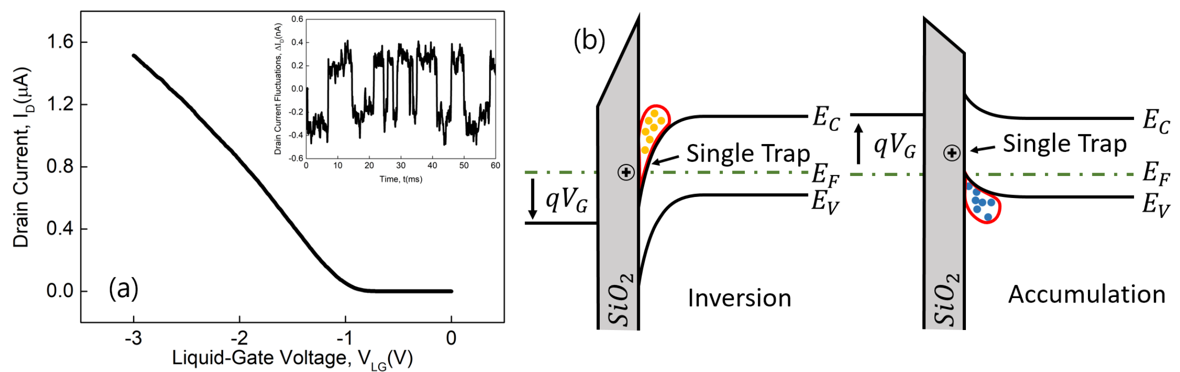

Figure 4.37: (a) A typical transfer curve of $p^+ - p - p^+$ liquid-gated Si NW FET. Inset shows typical RTS fluctuations of drain current. (b) Energy band diagrams for $n^+ - p - n^+$ structures in inversion regime and $p^+ - p - p^+$ structures in accumulation regime. Increased electron and hole concentrations are shown with red area. Electrons are shown as orange circles, holes - blue circles. A single trap in the oxide layer is shown as a "+" sign.

carrier from the channel causes a strong deviation of the current through the channel. The time which the charge carrier spends before being captured by the trap is called capture time and the time before the release of this carrier back into the channel is called emission time. The investigation of single trap phenomena over the last decade confirmed experimentally the deviation of the capture kinetics from predicted by the SRH model towards the stronger capture time, τ_c , dependence on the drain current. Such anomalous behavior is nowadays commonly explained considering the charge carrier distribution withing the channel dependent on the high electrical field near the interface [146] as well as Coulomb blockade effect [105, 147, 148].

In this respect quantization and tunneling of the charge carriers inside the conductive channel has to be considered to describe the basic reasons of the capture kinetics enhanced behavior.

The studies were performed on the single silicon nanowire structures with p-doped channel, while the contacts were highly implanted with either boron or arsenic to form n^+-p-n^+ (first group) or p^+-p-p^+ (second group) or type device correspondingly. The gate dielectric was thermally grown silicon dioxide with the thickness of 9 nm, the back-gate oxide was 145 nm thick. The thickness of the active layer was 50 nm. The nanowires under investigation were 200 nm long and 100 nm wide. Measurements were performed with liquid gate where PBS with pH=7.4 was used as an electrolyte solution. Devices of n^+-p-n^+ type were investigated in the inversion regime while the p^+-p-p^+ type in the accumulation regime. Typical transfer curves are shown in figure 4.37(a).

During the investigation of both device groups RTS fluctuations were measured as a part of noise measurement procedure(inset to figure 4.37(a)). Capture time slopes were estimated as (-1) for the FETs of a first group and (-2.8) for the second as it is shown in the figure 4.38. To explain the unusual behavior of capture time kinetics we employed theoretical predictions with respect to quantization and tunneling effects[149]. Calculated

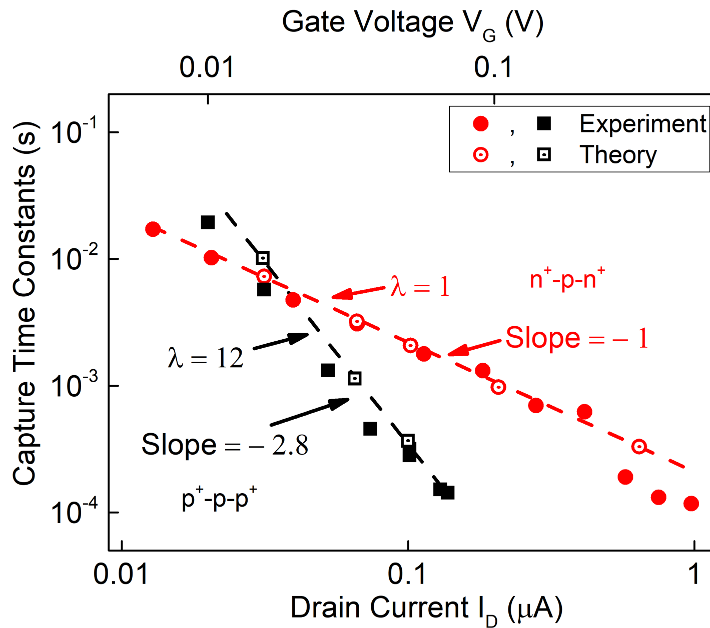

Figure 4.38: Measured(filled symbols) and calculated(empty symbols) capture time dependencies on the drain current. Red curves correspond to inversion regime n^+-p-n^+FETs, while black curves correspond to accumulation p^+-p-p^+ FETs.

capture time dependencies together with measured data are plotted in the figure 4.38. Results demonstrate a good agreement of measured and theoretically estimated values. The electron capture time slope was also predicted to be (-1) for n^+-p-n^+structures. To explain the enhanced slope for our p^+-p-p^+structures we assumed that the concentration of holes is considerably higher at the interface between silicon channel and gate dielectric. It should be mentioned that the sign of applied voltage does not influence the physical concept, since major charge carriers also change to the opposite sign. Charge carriers distributions were calculated for both structure types and plotted in figure 4.39. Several remarkable features of charge carrier distributions should be emphasized.

- The concentration of electrons is high in the inversion channel at the interface of $n^+ - p - n^+$ FET.
- There is a narrow (about 1 nm) gap between the peak electron concentration and the interface where the concentration of holes is low for the inversion regime n^+-p-n^+FET.
- The distribution of holes has a pronounced maximum in the accumulation regime of $p^+ - p - p^+$ FET

The electric field in the nanoscale channel is very high (1×10^5 V cm^{-1} to 1×10^6 V cm^{-1}). It should be noted that a strong exponential cross-section, σ, dependence on the field in the oxide was reported [150]. It can be represented as the following equation[98, 150]:

$$\sigma \propto exp\,(E_{OX}) \tag{4.11}$$

,where

$$E_{OX} = \frac{|V_G - V_{th}|}{d_{FOX}} \tag{4.12}$$

For the electron effective capture cross-section, we can rewrite relation 4.11 in the following form:

$$\sigma_n = \sigma_{n0} exp \left(\frac{|V_G - V_{th}|}{\epsilon_{cr} d_{FOX}} \right) \tag{4.13}$$

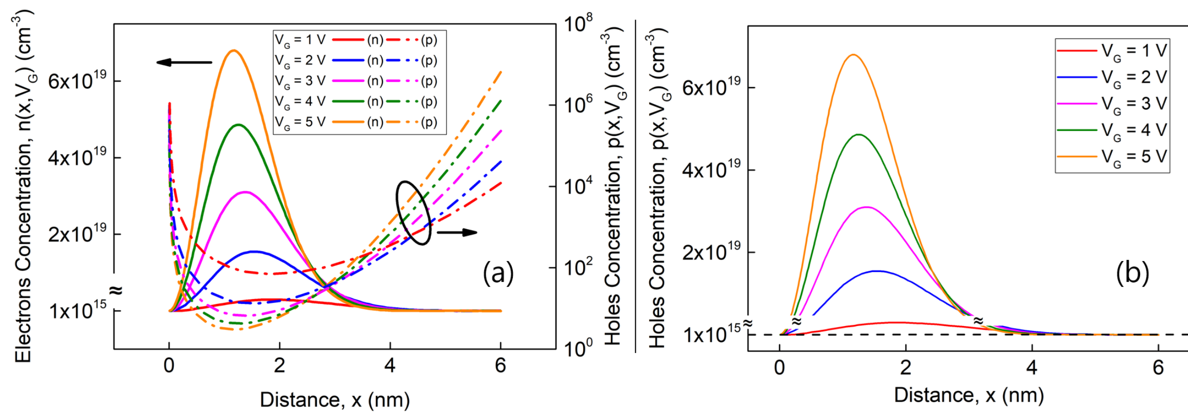

Figure 4.39: (a) Electron concentrations (solid line) and hole concentrations (dash-dot line) in $n^+ - p - n^+$ nanowire FET as a function of distance from the surface at different applied gate voltages. (b) Hole concentrations in $p^+ - p - p^+$ nanowire FET as a function of distance from the surface at different applied gate voltages(indicated absolute value)

Here V_G and V_{th} are the gate and threshold voltages, respectively; ϵ_{cr} is the critical field (for $E_{ox} = \epsilon_{cr}$ the cross-section, σ, is changed by e times). For $p^+ - p - p^+$ NW FETs, the effective capture cross-section grows with the strong decrease in carrier number (electrons) near the FOX-NW interface. To explain the enhanced behavior we introduce the the amplification factor $\lambda(\lambda \geq 1)$

$$\sigma_n' = \sigma_{n0} exp\left(\frac{\lambda(V_G - V_{th})}{\epsilon_{cr} d_{FOX}}\right) \tag{4.14}$$

On the contrary to the $n^+ - p - n^+$ structures, $p^+ - p - p^+$ FETs work in the accumulation mode. The surface region of the Si NW is depleted of the minor carriers — electrons (figure 4.39). The distance between the repulsive trap at the interface with oxide layer and the mobile electrons of the Si conductive band increases. Therefore the potential barrier for electrons to surmount in order to be captured by the trap increases simultaneously. In this respect the impact of the critical electrical field ϵ_{cr} becomes weaker. The physical interpretation of the amplification parameter, λ, is related to the amplification of the electron cross section determined by two factors. Firstly, the removal of an electron from the channel results in the weakener critical field influence. Secondly the potential barrier for electron capture also changes.

In the case of $n^+ - p - n^+$ structures, the electrons in the conductive band of Si NWs are located close to the interface. Therefore no considerable potential barrier changes are observed, and ϵ_{cr} does not change considerably, resulting in $\lambda = 1$. It is clear that the parameter λ has to be dependent on the gate voltage. Extraction of such dependence is another challenge which should be carefully considered. We found that in the $p^+ - p - p^+$ FETs, the cross section capture increases hundreds times for the critical field, $\epsilon_{cr} \propto 1 \times 10^5\,\mathrm{V\,cm^{-1}}$ to $1 \times 10^6\,\mathrm{V\,cm^{-1}}$ when compared to the low-field value, σ_{n0}, during variation of applied gate voltages on the order of 1 V.

Applying the electron capture time calculation method used in [149], and taking into account the quantization and tunneling effects of the mobile carriers from equation 4.14, we derived a new expression for τ_c :

$$\tau_c = \frac{exp\left[\gamma z_t + \beta z_{QM} - \frac{\lambda(V_G - V_{th})}{\epsilon_{cr} d_{FOX}}\right]}{ln\left[1 + \frac{1}{2}\left(\frac{V_G - V_{th}}{\eta \phi_T}\right)\right]} \times \tau_{c0} \tag{4.15}$$

where

$$\tau_{c0} = \frac{t}{2T_0 \sigma_{n0} v_{th} n_{st}}$$

For the case of $n^+ - p - n^+$ FETs, we have to take $\lambda = 1$ and for the case of the $p^+ - p - p^+$ FETs $\lambda > 1$. It should be noted that $\beta = 0.1\gamma$ and other denotations in equation 4.17 are the same as they were introduced in[148, 149]. The terms of equation 4.15 considering quantum approach are the following:

- $exp(\gamma z_t)$ — the trap location in the oxide [dependence $\tau_c \propto exp(\gamma z_t)$. γ is the attenuation coefficient of the electron wave function in the oxide layer and z_t is the trap distance from oxide – channel interface.

- $exp(\beta z_{QM})$ - tunneling of electrons. It depends on the depth of the maximal value of the carrier density at the channel-oxide interface.

- $\frac{\lambda(V_G - V_{th})}{\epsilon_{cr} d_{FOX}}$ — the field dependence of the crosssection in the oxide layer (equation 4.14).

- $ln\left[1+\frac{1}{2}\left(\frac{V_G-V_{th}}{\eta\phi_T}\right)\right]$ — the quantization and specific distribution of the mobile carriers in the channel.

Assuming that the FETs are working in the linear regime at low changes of applied gate voltage, $(|V_G - V_{th}|) \propto (0.1 \div 0.5)V$, we calculated the slope of τ_c versus drain current using following parameters: $\sigma_{n0} \approx 1 \times 10^{-20}\,\mathrm{cm}^{-2}$, $T_0 = 1$, $z_t = 2\,\mathrm{nm}$, $v_{th} = 2.3 \times 10^7\,\mathrm{cm\,s}^{-1}$, $\epsilon_{cr} \approx 4.5 \times 10^5\,\mathrm{V\,cm}^{-1}$, $d_{FOX} \approx 9\,\mathrm{nm}$, $z_{QM} = 1.21 + 165 \times exp(-0.88V_G)$, and remaining values from [149]. For the $n^+ - p - n^+$ FET, the capture time slope equals (-1) at $\lambda = 1$ and for the $p^+ - p - p^+$ FET, the slope equals (-2.8) at $\lambda = 12$.

Thus, the enhanced values of the τ_c slope can be described using equation (4.15), when considering the λ amplification factor, determined by accumulated carriers. Obviously, we can obtain higher slope values of capture time dependence with values of $\lambda > 12$.

Figure 4.40(a) shows the electron capture time slope's dependence on the amplification factor λ for $d_{FOX} = 9\,\mathrm{nm}$. For $\lambda = 1$, the slope equals (-1), while at $\lambda = 12$ the slope equals (-2.8). The capture time dependence on the oxide layer thickness is shown in figure 4.40(b).

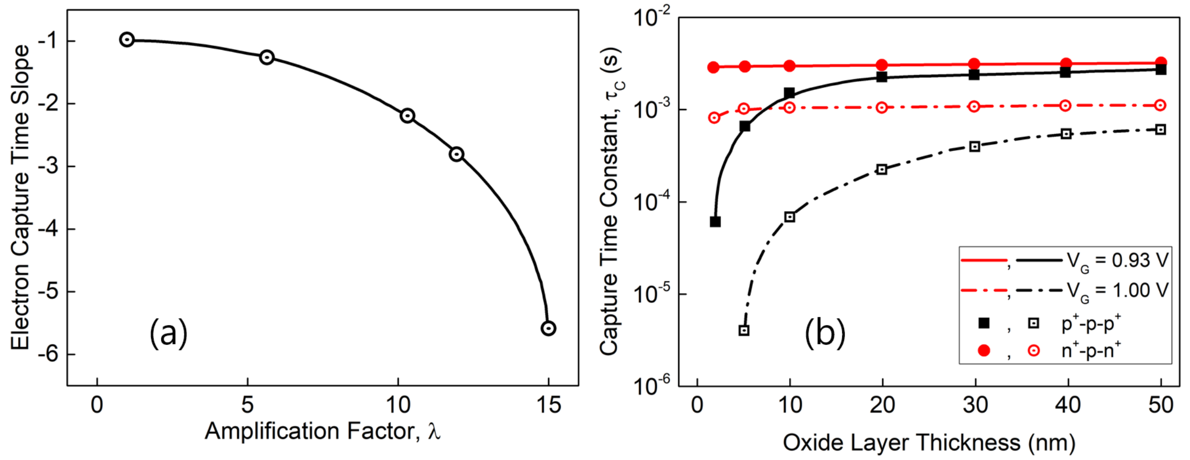

Figure 4.40: (a) The electron capture time slope as a function of the amplification factor, λ. (b) The electron capture time dependencies on the thickness of the gate oxide, using quantum-mechanical approach.

τ_c is almost constant for the $n^+ - p - n^+$ FETs. Moreover, $\tau_c = const$ at the $d_{FOX} \geq (5-8)nm$. For the $p^+ - p - p^+$ FETs, the exponential decrease is obtained with higher values of capture time slope beginning from $d_{FOX} \approx (20-40)nm$ and reaches $\tau_c = const$ for $d_{FOX} \geq 50\,\mathrm{nm}$. The decrease of τ_c strongly depends on the gate voltage determining the working point. Such behavior of τ_c can be explained by the rapid growth of the electron concentration in the inversion regime at the FOX-NW interface. In case when the $n^+ - p - n^+$ FET, the layer with high electron concentration blocks the influence of increasing E_{ox} on the capture time, which changes very slowly. On the contrary, for the $p^+ - p - p^+$ FET in the accumulation regime at very low electron concentrations increased E_{ox} influence results in a rapid decrease of τ_c. Figure 4.41 shows the electron capture time slope dependence on the front oxide thickness for the $p^+ - p - p^+$ FET. The characteristic slope value is calculated using equation (4.15) according to the following expression:

$$Slope = \frac{log(\tau_c)|_{V_{G,min}} - log(\tau_c)|_{V_{G,max}}}{log(V_{G,min}) - log(V_{G,max})} \tag{4.16}$$

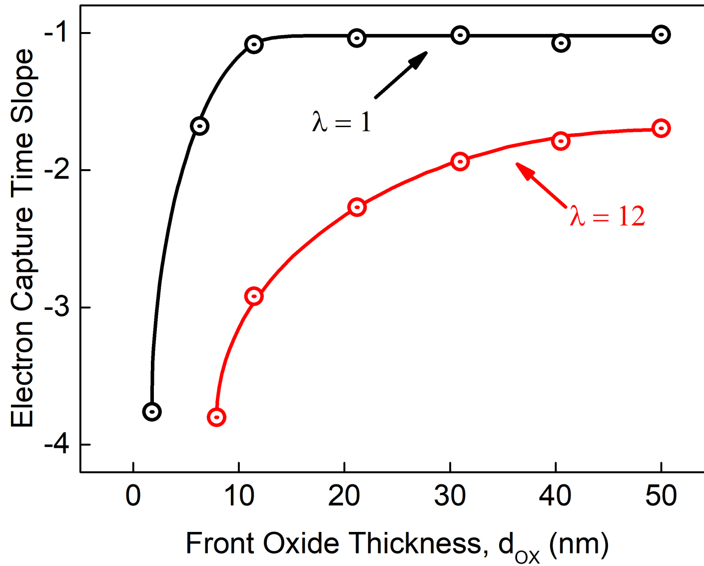

Figure 4.41: Electron capture time slope dependencies on the gate oxide thickness

The decrease of electron capture time slope strongly depends on the gate voltage determining working point and amplification factor. Thus, the key role of the quantization effect on the capture kinetics of the random telegraph signal is demonstrated. Considering the theoretical argumentation for the experimental results, this explanation represents a new way to analyze the increasing τ_c slope versus drain current for the case of a repulsive single trap for tunneling of the mobile carriers in the silicon oxide layer in the accumulation mode of a NW channel in a $p^+ - p - p^+$ FET. For a better explanation of the strong capture time slope dependence on drain current in nanowire FETs, in addition to already known factors, the following elements have to be taken into account:

- quantization of the mobile carriers in the channel;
- specific distribution of free carriers in the channel and tunneling of the electrons into the oxide single trap;
- sharp growth of the electron cross-section with the decrease of electron concentration at the oxide-NW interface.

It should be noted that the first two factors are determined by the electron concentration distribution in the plane perpendicular to the NW-FOX interface, which is in agreement with the data of Schulz and Mueller[151]. The last factor plays significant role in the formation of the capture time slope versus drain current in the strong accumulation regime. The value of the capture time slope as a function of drain current strongly increases with a decrease of the oxide thickness. Moreover, it plays a dominant role for the formation of the slope magnitude for $d_{FOX} < 5\,\mathrm{nm}$ ($n^+ - p - n^+$ FETs) and for $d_{FOX} < 50\,\mathrm{nm}$ in $p^+ - p - p^+$ FETs. It is shown that increased values of the slope can be explained by the strong increase of the effective capture cross-section, σ, with a decrease of the concentration of minor carriers in the channel. From our calculations, it follows that the high surface electric field plays an insignificant role in the accumulation regime.

4.7.2 Understanding the Coulomb Blockade Energy

As it was mentioned above the deviation of the single trap dynamics from generally accepted SRH model can be explained in frame of Coulomb blockade energy model. It was demonstrated for devices working in the inversion regime [145, 151]. The accumulation regime, however, was not considered previously. Coulomb blockade energy has a strong impact on the single trap capture and emission dynamics for both neutral and repulsive trap states. When the charge carrier gets captured by the single trap the screening region is formed by the change of trap charge state. The fact has a significant effect on the entire capture dynamics. The modulation of the current through the channel becomes even more pronounced when the single trap is located in the high-field region of the channel [8, 152]. Obviously single trap dynamics as well as current modulation amplitude is strongly influenced by the parameters of the trap including the geometrical location as well as energy level [152, 153]. Therefore to make use of single trap phenomena as well as to reduce its impact in the ultimate CMOS circuits it is important to study and further control the parameters of single trap.

In current studies we used $n^+ - p - n^+$ silicon nanowire structures with the length of 500 nm based on SOI wafer with buried oxide thickness of 150 nm. FET device was passivated with 100 nm thick PECVD layer of SiO_2 . Aluminum contacts were formed by evaporation of Aluminum with a lift-off patterning. Devices were first characterized using I-V characterization. Typical transfer curve is shown in the figure 4.42(a). Noise measurements were performed in the voltage range where FETs operated in the ohmic mode. Measured spectra confirm the 1/f flicker behavior of low-frequency noise which is also typical for MOSFETs. Single trap phenomena was registered as two-level fluctuations of drain current indicating the modulation of electron flow by the single trap (figure 4.42(b)). The histogram in figure 4.42(c) shows two distinct peaks due RTS fluctuations.

It is known that trapping is a temperature-activated process. Therefore experiment was performed in the temperature range from 200 K to 300 K. Extracted capture,τ_c , and emission,τ_e , time constants were analyzed as a dependencies on the drain-source and gate

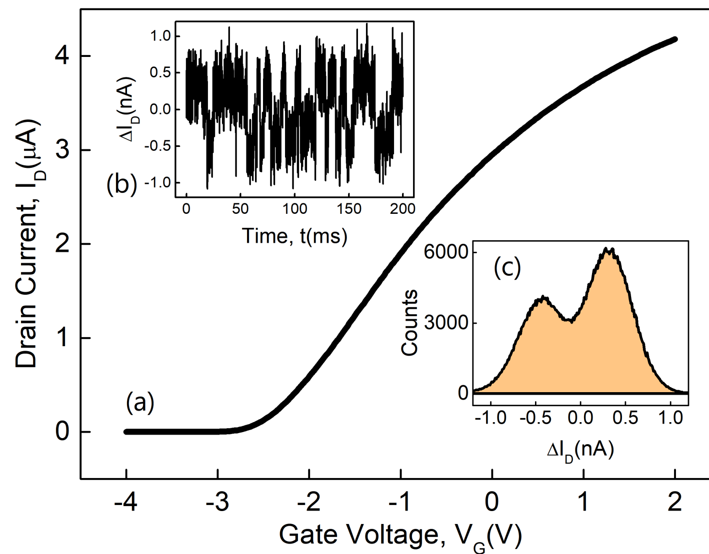

Figure 4.42: (a) Transfer curve measured for $500 \times 500nm^2$ Si NW glsfet.(b) Typical recorded timetrace with RTS noise fluctuations. (c) Histogram calculated from the time-trace, two peaks correspond to the stable levels in RTS noise

voltages as well as temperature. The capture time appears to be strongly dependent on the drain current while the emission time is almost constant. The temperature dependence is observed to be the opposite - the capture time is slightly influenced, while emission time has a strong dependence. When it comes to the analysis, capture and emission time dependencies are used to estimate the parameters of a single trap. Usually parameter extractions is performed using assumptions in frame of SRH model [154, 155]. According to this capture and emission times can be calculated as follows:

$$\tau_c = \frac{1}{\sigma_n v_{th} n} \tag{4.17}$$

$$\tau_e = \frac{1}{\sigma_n v_{th} n_1} = \frac{1}{\sigma_n v_{th} N_C} e^{\left(\frac{E_t}{kT}\right)} \tag{4.18}$$

,where σ_n is the capture cross section, v_{th} is the average thermal velocity, n is the concentration of free electrons (in the case of electron capture) at the Si/SiO_2 interface, n_1 is the statistical c-band factor for the trap (the electron concentration when the Fermi level equals the trap level), E_t is the energy level of the center relative to the bottom of the conduction band, N_C is the density of electron states at the bottom of the conduction band.

As it derives from equation 4.17 capture time depends on reciprocal electron concentration which determines the current through the channel. To judge about the applicability of SRH model capture time dependence on the drain current should be verified. Extracted from measured data characteristic capture (figure 4.43) time corresponding to the trapping-detrapping process demonstrated $\tau_C \approx I_D^{-5}$ behavior which is not typical for SRH model where the power is expected to be (-1).

The main reasons causing such deviation are still discussed in literature [98, 156, 157]. Concept of Coulomb blockade energy is considered as a most appropriate for explanation

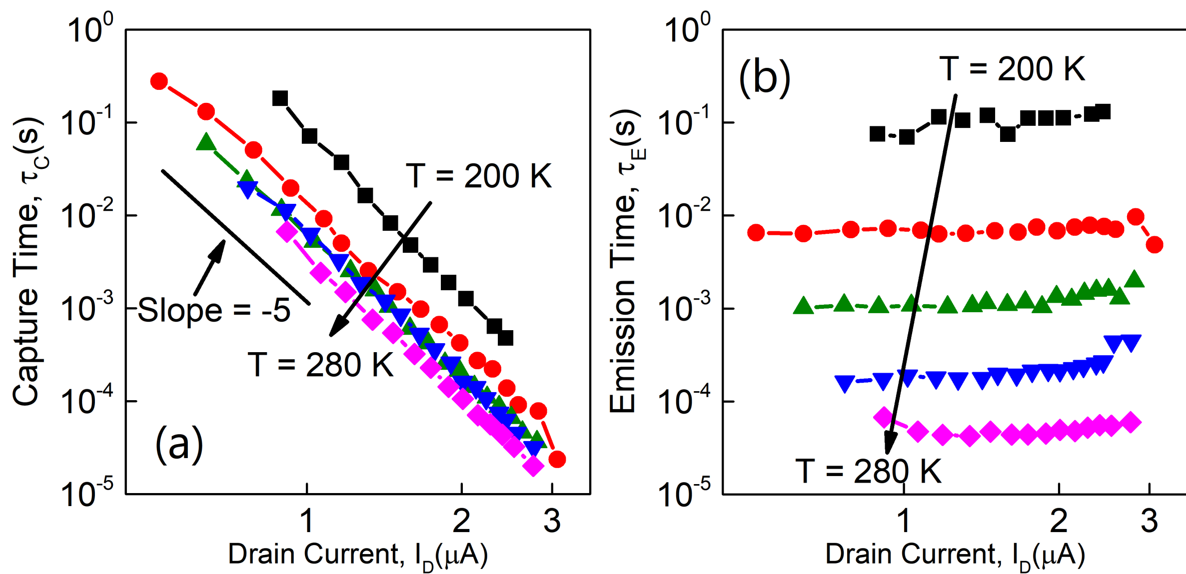

Figure 4.43: (a) Capture time constant, τ_c , and (b) emission time constant , τ_e , as a function of drain current, measured at different temperatures.

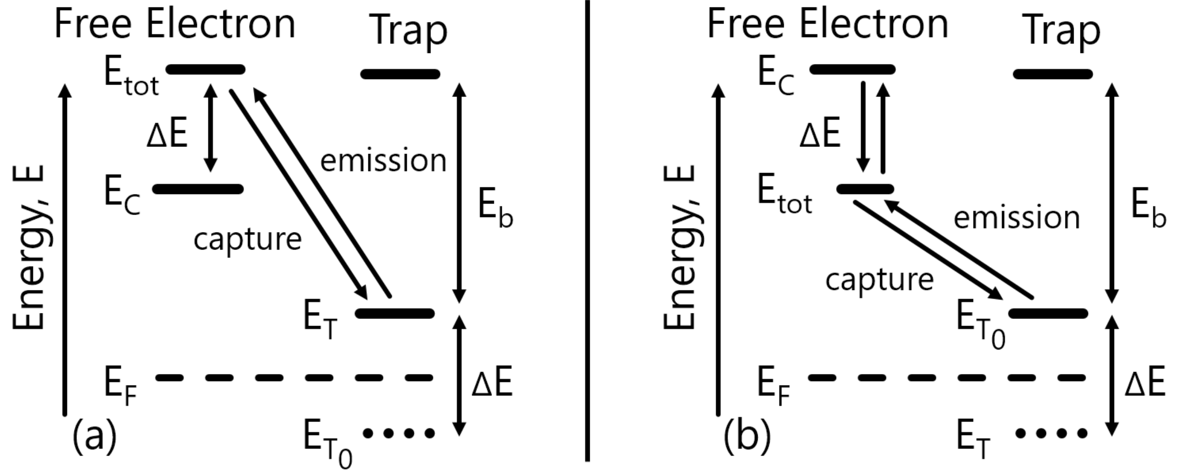

Figure 4.44: Energy level diagram of single electron in space-charge region. (a) The energy of an electron in the conduction band near the trap is shown on the left side, the energy of a neutral, E_{T_0}, or repulsive, E_T, charged trap is shown on the right side. E_b shows the binding energy of a trapped electron. (b) Charge state of the trap is attractive, E_T, or neutral, E_{T_0}, when the trap is unoccupied or occupied by an electron, respectively. Figure is adapted from [143]

of the capture kinetics. Capture and emission rates can be expressed as follows [143]:

$$\frac{1}{\tau_c} = C_n N_C e^{-(E_C - E_F)/kT - \Delta E/kT} \tag{4.19}$$

$$\frac{1}{\tau_e} = C_n N_C e^{-E_b/kT} \tag{4.20}$$

where $C_n = \sigma_n v_{th}$ is the coefficient of electron capture, N_C is the density of states at the bottom of the conduction band, E_C is the energy level of the conduction band, E_F is the Fermi level, T is the temperature of the electron gas, $E_b = E_C - E_{T0}$ is the binding energy of the center, E_{T0} is the energy position of the neutral (not occupied) center, ΔE is the Coulomb blockade energy (figure 4.44).

Anomalous enhanced capture dynamics of the single trap in accumulation mode has not been reported in literature. In this case equations 4.19 and 4.20 can be employed considering the additional energy, ΔE_{acc}, required for the charge carrier to be captured onto the trap.

The value of this energy component can be extracted from equations 4.19 and 4.20 by eliminating C_n and N_C. Dividing the capture rate by the emission we obtain the following expression:

$$\frac{\tau_e}{\tau_c} = e^{-(E_C - E_F - E_b + \Delta E_{acc})/kT} \tag{4.21}$$

The value of additional energy can be extracted from dependence 4.21. The unknown parameter, E_b can be determined from the temperature dependence of emission time, τ_e and calculation of $(E_C - E_F)$.

For calculations and estimation of additional energy we took into account the depen-

dence of electron mobility on the temperature:

$$\mu = \mu_0 \left(\frac{300}{T}\right)^{3/2} \tag{4.22}$$

,where $\mu = \mu_0$ at $T = 300\,\mathrm{K}$ and also the temperature dependence of the $C_n N_C \approx T^2$

Therefore, the data in figure 4.43 can be represented for convenience in temperature-normalized coordinates , as a function of the argument $I_D T^{3/2}$ and values of $\tau_e T^2$ and $\tau_c T^2$ instead of time constants. Using data from figure 4.43, we can now obtain the Arrhenius plot, figure 4.45, with the parameter $I_D T^{3/2} \sim n$.

Here we assume that the concentration of free electrons at the interface n_s is proportional to the average concentration, n. It should be noted that the energy E_b remains almost unchanged with the change of the $I_D T^{3/2}$ value. When $I_D T^{3/2} = 6mAK^{3/2}$, the temperature dependence of $\tau_e T^2$ is fitted to the data of the Arrhenius plot. Using this plot, the value of the trap energy was estimated to be $E_b = 0.41\,\mathrm{eV}$. With the obtained energy of the trap, we can calculate the other parameters of the trap including the additional energy and the capture cross section at different temperatures, considering that $C_n = \sigma_n v_{th}$ and taking into account the following equations:

$$v_{th} = \sqrt{\frac{3kT}{m_n^*}}, (m_n^* = 1.08 m_n) \tag{4.23}$$

$$N_C = 2\left(\frac{2\pi m_n^* kT}{h^2}\right)^{3/2} \tag{4.24}$$

$$\sigma_n = \frac{1}{\tau_e v_{th} N_C} e^{E_b/kT} \tag{4.25}$$

The results are summarized in Table 4.1.

It should be emphasized that the capture cross section is independent of temperature within the statistical error. The values of the capture cross sections reflect the fact that

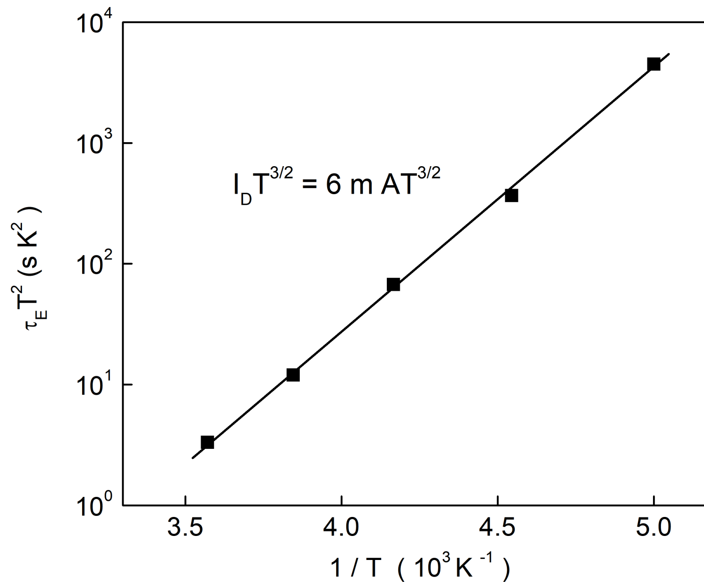

Figure 4.45: Arrhenius plot of $\tau_e T^2$ as a function of $1/T$

T[K]		v_{th} [cm s^{-1}]	N_C [cm^{-3}]	τ_e[s]	σ_n[cm^2]		v_{th} [cm s^{-1}]	N_C [cm^{-3}]	τ_e[s]	σ_n[cm^2]
200	Before Irradiation	5.30×10^{6}	1.53×10^{19}	1.10×10^{-1}	2.4×10^{-15}	After Irradiation				
220		5.56×10^{6}	1.98×10^{19}	7.15×10^{-3}	3.1×10^{-15}		5.56×10^{6}	1.98×10^{19}	3.60×10^{-1}	3.9×10^{-12}
240		5.81×10^{6}	2.16×10^{19}	1.10×10^{-3}	2.9×10^{-15}		5.81×10^{6}	2.16×10^{19}	1.60×10^{-2}	4.9×10^{-12}
260		6.05×10^{6}	2.26×10^{19}	1.81×10^{-4}	3.5×10^{-15}		6.05×10^{6}	2.26×10^{19}	1.50×10^{-3}	4.9×10^{-12}
280		6.27×10^{6}	2.53×10^{19}	4.30×10^{-5}	3.5×10^{-15}		6.27×10^{6}	2.53×10^{19}	1.58×10^{-4}	5.6×10^{-12}

Table 4.1: Table of single trap parameters in Si NW FET for comparison before and after gamma irradiation.

the center is in a neutral state while it is empty (i.e., no charge carrier captured by trap); and repels the carriers in the case of an occupied center[158]. Further, in accordance with equation 4.19, we calculated the value of ΔE_{acc} for all points, where values of τ_e and τ_c were measured. For this purpose the concentration of electrons in the channel has to be estimated.

Considering the distribution of electrons across the channel and taking into account equation 4.22, we determined the concentration of electrons in the following way:

$$n = \left(eR\mu_0 \left(\frac{300}{T} \right)^{3/2} \right)^{-1} L/Wd \tag{4.26}$$

where L, W, d are the length, width, and thickness of the sample, respectively; R is the resistance of the channel. Figure 4.46 shows the additional energy, ΔE_{acc}, as a function of carrier density.

It can be described using the following equation

$$\frac{\Delta E_{acc}}{T} = -\alpha \times ln \left(\frac{n}{n_0} \right) \tag{4.27}$$

where $\alpha = 3.45 \times 10^{-4}$ and $n_0 = 1.6 \times 10^{18}\,\text{cm}^{-3}$ were obtained from the fitting of the curves to the equation 4.27. The value of the additional energy reduces to almost zero

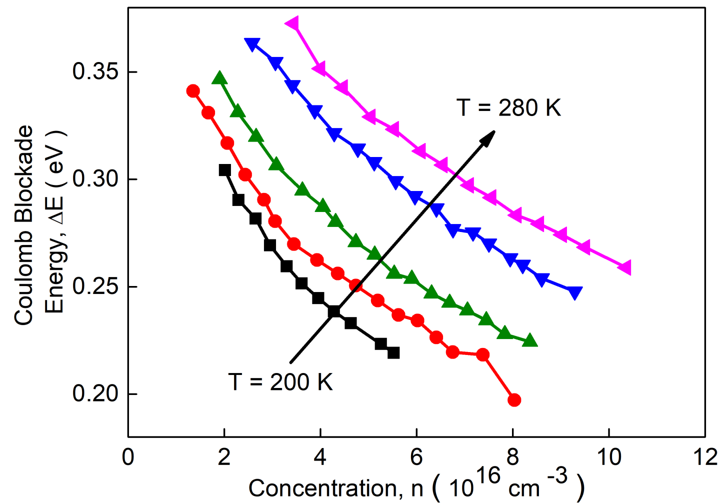

Figure 4.46: The additional energy, ΔE_{acc}, as a function of the average electron concentration at different temperatures.

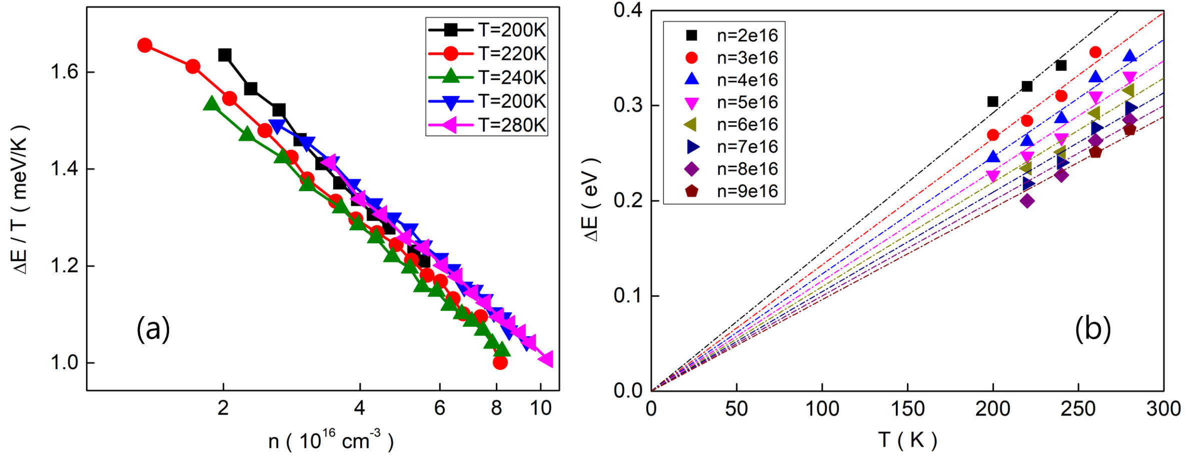

Figure 4.47: (a) Normalized additional energy ΔE_{acc} as a function of the average electron concentration in the channel at different temperatures. (b) Dependence of the additional energy ΔE_{acc} as a function of the temperature. Plotted lines follow the equation 4.27.

with increasing of free electron concentration in the channel. This can be explained by considering the electrostatic screening by free electrons [143, 151, 155, 159]. The calculated value of the additional energy as a function of the average electron concentration in the channel obtained at different temperatures follows the behavior described by equation (4.27), which can be shown by plotting in normalized coordinates (see figure 4.47).

4.7.3 Impact of Gamma Radiation on Single Trap Parameters

To implement our idea of control over dynamic processes related to a single trap, we analyzed the effect of γ-irradiation on the properties of a single trap center. We investigated the transport properties and RTS noise behavior in Si NW FETs after a low dose of 1×10^4 Gy irradiation. Transfer characteristics of the Si NW FET before and after irradiation are compared in the figure 4.48. It should be noted that the resistances of the sample measured at different temperatures demonstrated strong scattering before the gamma radiation treatment. At the same time the scattering was considerably reduced after irradiation. This indicates the positive effect of gamma irradiation leading to the stabilization of the sample characteristics. Transfer characteristics of Si NW FETs were measured before and after irradiation at different temperatures (Figure 4.48).

It should be emphasized, that before gamma treatment the threshold voltage, V_{th} , values were relatively high: from -0.65 V to -1.27 V. In contrast, after irradiation V_{th} changes to the value of 0.3 V. This indicates an improvement of the sample operation parameters. I-V characteristics after treatment show decreasing channel conductance and superlinear behavior at T=280 K. The consequences of the irradiation are the decrease of the Fermi level energy and the expansion of the space distribution of the inversion layer resulting in a change of the I-V characteristic slope and strengthening of the gate coupling effect impact, as it will be shown below. The decrease of electron concentration in the Si layer can be explained by the formation of compensating acceptor centers after irradiation[160]. In our case of a rather low initial donor concentration (1×10^{15} cm^{-3}), the appearance of even a small concentration of compensating levels can lead to a decrease of the electron concentration in silicon. It should be noted that the slope decreases from 1 µA V^{-1} to 0.67 µA V^{-1}. This fact can also be explained by the difference in width of the

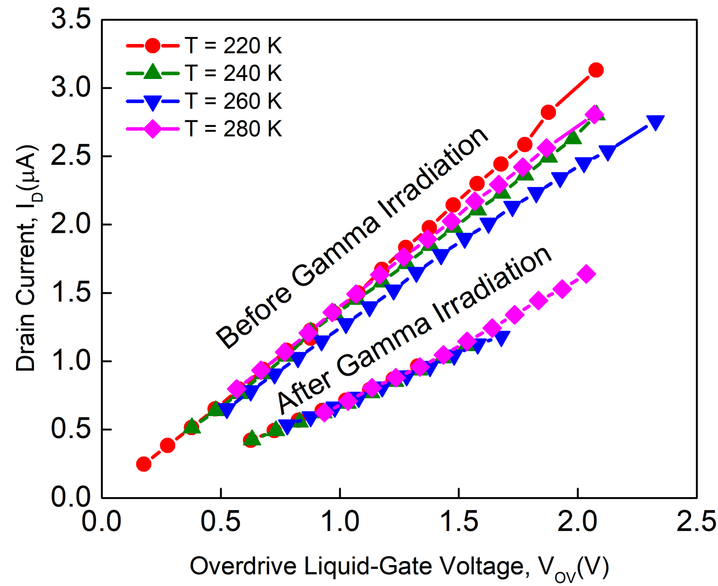

Figure 4.48: Transfer curves measured for Si NW FET before and after gamma irradiation.

conduction channel before (narrower) and after (broader) gamma radiation treatment. Increased gate coupling effect may influence on the balance between the trap centers in the front and back gate dielectrics on the transport and noise properties of the structure. The information about these processes can be extracted from the analysis of noise spectra behavior as a function of the back gate voltage. The spectra demonstrate 1/f behavior with a well-resolved bump corresponding to the RTS fluctuations (figure 4.49).

A convenient approach to analyze the flicker noise in the FET devices is to consider the dependence of the equivalent input noise ($S_U = S_I/g_m^2$). Here S_I is current noise power spectral density; g_m is the transconductance. Such dependencies obtained before and after gamma radiation treatment for temperature T = 280 K are shown in figure 4.50. The data demonstrate that in the accumulation regime the noise level is about the

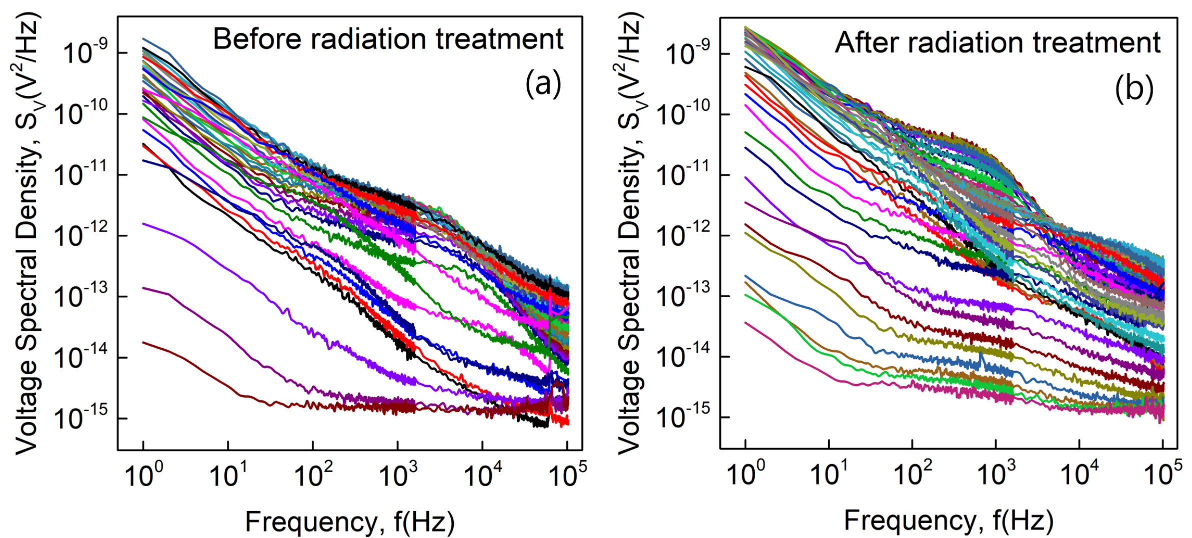

Figure 4.49: Noise voltage spectral density at different voltages in the range from −2 V to 2 V before(a) and after(b) gamma irradiation

same (figure 4.50(a)). With increasing positive overdrive gate voltage inversion layer of electrons forms in the channel and the noise behavior is different before and after gamma radiation. Our NW channel is only 50 nm thick, therefore the gate-coupling has to be considered.

The noise increase after gamma treatment can be explained by the spacial spread of the inversion layer and the enhanced coupling effect, causing the improved control of the channel conductivity by applied back gate voltage. We can show this by analyzing the flicker noise using the approach described in [130]. The contribution of the flicker noise of two interfaces Si / SiO2 (Δn fluctuations): front, f, and back, b, to the overall noise considering the values (g_m^2/I_D^2) as can be described by equation 4.28.

$$\frac{S_{I_D}}{I_D^2} = S_{U_f}\left(\frac{g_{m_f}}{I_D}\right)^2 + S_{U_b}\left(\frac{g_{m_b}}{I_D}\right)^2 \tag{4.28}$$

where I_D is the drain current; g_{mf} and g_{mb} is the transconductance of the FET for the front and back gate FET operation, respectively. S_{Uf} and S_{Ub} are the equivalent input noise values, where channel is located near front and back SiO2/Si interfaces, respectively. Since the NW FET is operated in current studies by the back gate, the value of $\left(g_{m_f}/I_D\right)^2$ does not change. The normalized noise densities of the drain current (S_{I_D}/I_D^2) as a function of $\left(g_{m_f}/I_D\right)^2$ before and after gamma radiation treatment are shown in figure 4.50(b). The two lines in the figure correspond to the linear relationship of equation 4.28 for two different dielectric interfaces. Note that the larger values (fS_{I_D}/I_D^2) correspond to noise normalized to a lower drain current value.

By increasing the gate voltage the FET transport in the channel is changed to the regime of strong inversion with increased electron density (for both classical and quantum considerations) shifted to the interface corresponding to the gate. It should be noted that in the accumulation regime the electron density is distributed widely over the entire thickness of the semiconductor layer and even shifts to the top interface. With respect to the inversion, the dependence before gamma treatment demonstrates the transition

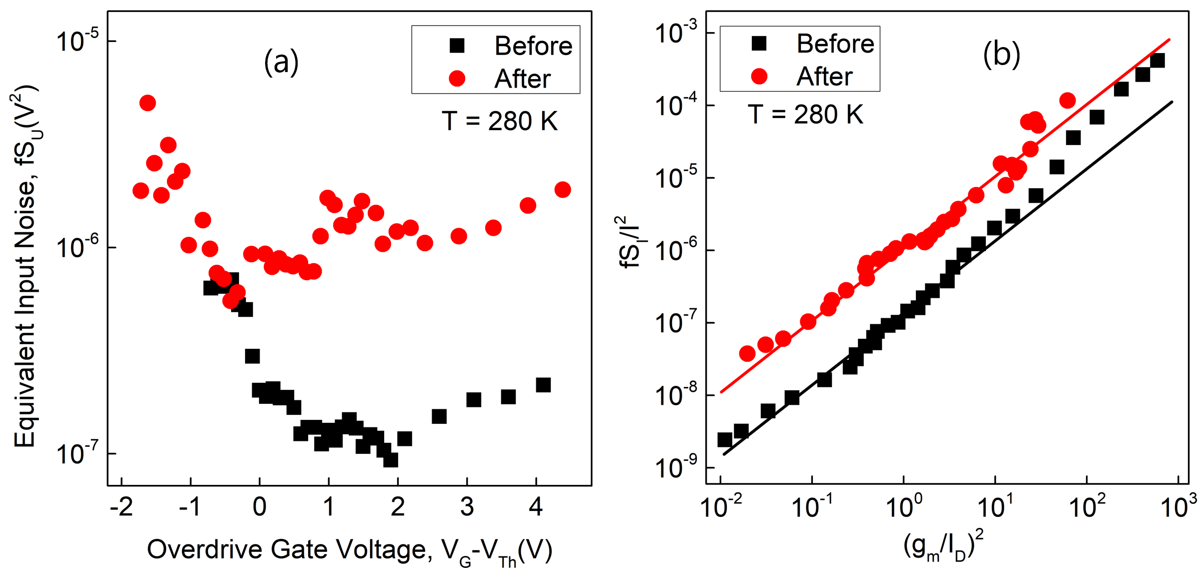

Figure 4.50: (a) Input-referred noise spectral density and (b) normalized flicker noise before and after gamma irradiation.

from one state to another, reflected in the point transition from one line to the other (black circles on the right). After irradiation such a transition is not observed. Before irradiation, in the accumulation regime, the noise behavior is mainly determined by front interface. This corresponds to a larger concentration of centers in the top dielectric layer close to the interface. When the inverting voltage increase, the channel shifts to the back interface. The electron density at the front interface is reduced, and the back interface noise, which is smaller, determines the noise properties. This is also clearly seen in figure 4.50. After irradiation, due to the increased role of the coupling effect, within the entire measured voltage range the condition when the back interface noise dominate is not reached. Considering the expression for the minimum length of the channel, in the absence of short-channel effects:

$$L_{min} = 0.4\left[r_j d(W_S + W_D)^2\right]^{\frac{1}{3}} = 0.4(\gamma)^{\frac{1}{3}} \tag{4.29}$$

,where L_{min} – is the minimum channel length when the subthreshold part displays long-channel behavior; $r_j d$ – junction depth; d – oxide thickness; $W_S + W_D$ – the sum of source and drain depletion regions depths, calculated as an approximation of a sharp one-dimensional p-n junction

$$W_D = \sqrt{\frac{2\epsilon_s}{qN_A}(V_D + V_{bi} + V_{BS})} \tag{4.30}$$

, where V_{bi} is the contact difference of junction, V_{BS} – substrate bias. At zero substrate bias $W_S = W_D$. The only parameter which can be changed in the equation 4.29 is the concentration of acceptor impurity, N_A. This parameter can be reduced by increasing the concentration of compensating (donor) impurity. It corresponds to a significant concentration of inverse electrons at the front interface, thus making no transition, as it was mentioned before (see figure 4.50(b)). We also investigated timetraces, corresponding to the bumps recorded in the noise spectra. Figure 4.51 demonstrates the behavior of the relative amplitude $\Delta I_D/I_D$ of the RTS noise as a function of the gate voltage V_G measured before and after irradiation at different temperatures. Monitoring the data of I_D serves as a measure of the electron concentration at the interface between the channel and the dielectric at a constant drain voltage, V_{DS}. As can be seen, at low current ($I_D < 1.3\,\mu\text{A}$), the value of $\Delta I_D/I_D$ is mostly independent of the current, and then decreases monotonically. In the subthreshold regime, the change in the charge state of the center causes the following current modulation processes. The trapped electron partially blocks the channel conductivity and simultaneously leads to the charge of the space-charge-region capacity. Therefore, the channel conductivity is determined not only by removing the complete charge of one electron, but also by the modulation of the space charge region. Decrease of relative current change, $\Delta I_D/I_D$, with increased current in the inversion regime is the result of the enhanced number of free electrons in the channel and, consequently, a decrease in the relative contribution of the charge of a single electron, captured on the trap, to the channel conduction [152]. The behavior of the relative amplitude of RTS pulses after irradiation is almost the same. A superlinear decrease of $\Delta I_D/I_D$ in the inversion regime is determined by increased screening of the charged center channel by free electrons and, consequently, a decrease in the modulation of conductivity in the local area. Strengthening of the charge screening is a phenomenon that is also responsible for the decrease of the Coulomb blockade energy with increasing carrier concentration in the inverse channel[151]. The observed superlinear $\Delta I_D/I_D$ decrease with current increase (see

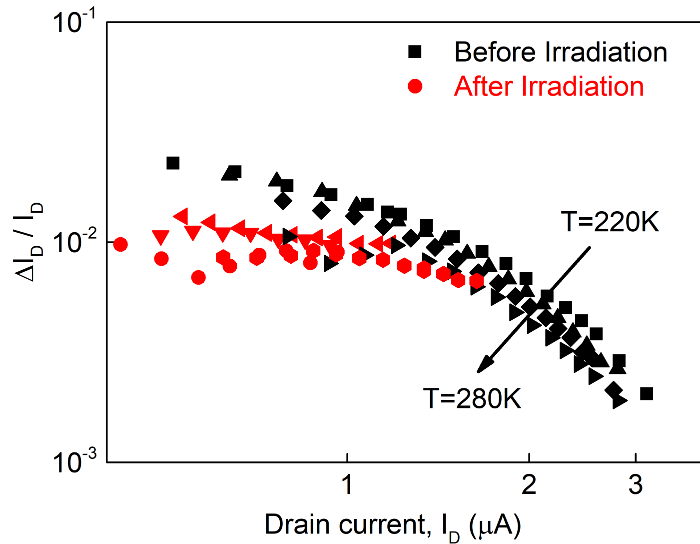

Figure 4.51: Normalized glsrts amplitude as a function of the drain current, measured at different temperatures.

figure 4.51) can be explained by the presence of a potential barrier associated with the charging of local capacities when moving the charge at a certain distance from the channel to the trap in the dielectric[98]. Normalized current generated by the single trap before and after irradiation almost coincides (see data shown in figure 4.51). Moreover, even though the current values after gamma radiation treatment are lower than those before irradiation, the dependence of $\Delta I_D/I_D$ on drain current follows the same pattern. Therefore, we can conclude that before and after irradiation we observe the same single trap. RTS noise characteristic time constants also changed under the influence of irradiation. Figure 4.52 shows the τ_c and τ_e dependences of the time constants on current in the linear regime. It should be emphasized that the slope of the τ_c equals (-5) and remains the same

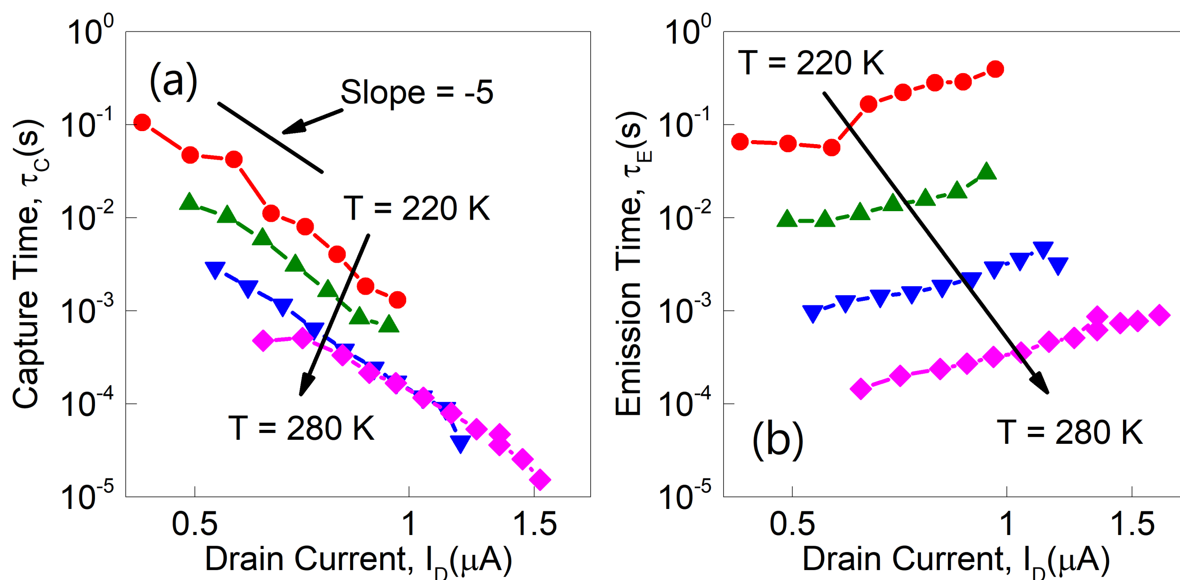

Figure 4.52: (a) Capture time constant, τ_c , and (b) emission time constant, τ_e , as a function of drain current, measured at different temperatures after gamma irradiation.

as before irradiation, but the value of the characteristic time constant decreases by one order of magnitude for the same values of the electron concentration (compare data of figure 4.43(a) and figure 4.52(a)). For example, at the drain current level of 1 µA at a temperature of 280 K the capture time reached a value of 5 ms. In contrast, after treatment the capture time was only 0.1 ms. Such decreased capture time reflects the change of capture probability to the trap center with decreased characteristic time, which is a manifestation of high-speed processes. Thus the effect may be utilized for the development of biosensors with a high-speed response. The temperature dependence of emission time is stronger after irradiation. The τ_e dependencies on the effective gate voltage before irradiation and after differ. The slope of the curves before gamma radiation treatment was relatively small (7.2 V dec^{-1}). However, after irradiation the slope increases by 4.7 times up to a value of 1.5 V dec^{-1}. At the same time, for certain selected temperature, the values of τ_e are higher by (5-10) times compared to the values measured before gamma treatment. The energy levels of the centers, calculated using Arrhenius plot, before irradiation - $E_t = 0.43$ eV, differ from the value after treatment - $E_t = 0.62$ eV (figure 4.53). We calculated the trap parameters at different temperatures after irradiation in the same way as prior to irradiation using the data of figure 4.52. There is the τ_e dependence on current, therefore the values of τ_e are determined as $I_D T^{3/2} = 3 \times 10^{-3} K^{3/2}$. The results are shown in table 4.1.

The value of the capture cross section increased by more than three orders of magnitude after gamma radiation treatment compared with the values obtained before exposure and corresponds to the characteristics of the attractive centers[158]. In this case, RTS noise demonstrates slightly different behavior, which can be described by equations [143]:

$$\frac{1}{\tau_C} = C_n N_C e^{-(E_C - \Delta E_F)/kT} \tag{4.31}$$

$$\frac{1}{\tau_E} = C_n N_C e^{-(E_b - \Delta E_{acc})/kT} \tag{4.32}$$

The expression for τ_e now also contains the additional energy ΔE_{acc}. This concept explains the growth of τ_e with increasing concentration of the conduction electrons in the channel (4.52(b)). The assumption that the observed center becomes an attractive center after

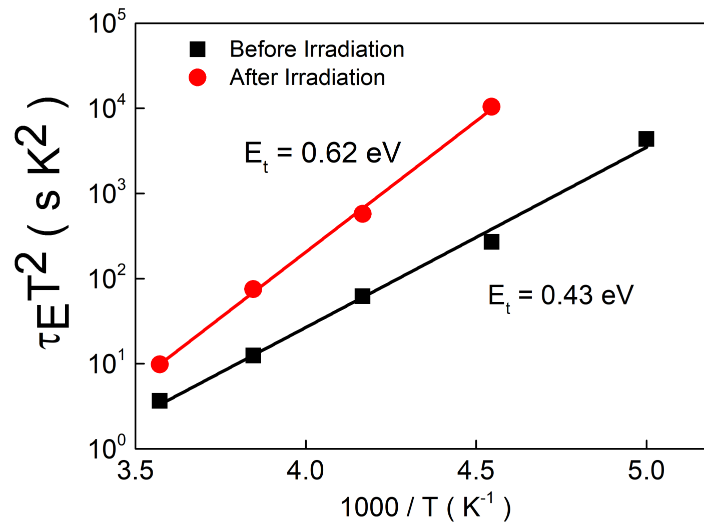

Figure 4.53: Arrhenius plot of the trap before and after gamma irradiation.

irradiation also explains the fact that the depth of the trap center increases significantly in relation to the energy of the conduction band at the Si/SiO_2 interface. Thus, the same trap determined the transport phenomena both before and after irradiation. The fact is also confirmed by the coincidence of the relative current generated by the single trap before and after gamma radiation treatment (figure 4.51). Irradiation of the sample results in the change of its initial charge state, from neutral to attractive, and in the increase of the center depth from 0.43 eV to 0.62 eV, before and after irradiation respectively. This fact confirms that we can considerably tune the parameters of a single trap by using low-dose gamma irradiation treatment. Capture time to the same single trap, measured at 1 µA current and $T = 280$ K, decreases from 5.0 µs to 0.1 µs after gamma radiation treatment. These results can be implemented for the development of the elementary basis components for a large number of applications in fundamental studies and applications in nanoelectronics and biosensors. It should be noted that RTS noise can be used as a signal for biosensors [1]. The signal-to-noise ratio in FET sensors is typically limited by well-established low-frequency noise models that show a scaling with the root mean square of the device area and the density of traps in the oxide [161]. As it was discussed above the stronger slope can be explained in frame of additional energy due to Coulomb interaction processes. Coulomb repulsion between charges located at nearby trapping sites can be beneficial for SNR improving [134]. The use of single trap phenomena, as a sensing technique in the case of strong Coulomb effects involving traps, can be considered as an attractive approach to overcome this SNR limitation and to get even higher sensitivities beyond the thermal limit.

4.7.4 Simulation of RTS Noise for Sensor Optimization

Simulations of random telegraph signal were performed for the silicon nanowire schematically shown in figure 4.54. In the model we considered that trap is located in SiO_2 gate dielectric of thickness t_{ox} at the distance of d_{trap} from the interface with silicon nanowire.

For simplicity the voltage was applied between gate and nanowire and is further called gate voltage. To evaluate the probabilities of electrons to be captured or emitted from the trap we utilized a method previously described in [162].The problem is similar to the electrochemical redox processes. The capture and emission rates may be evaluated in the

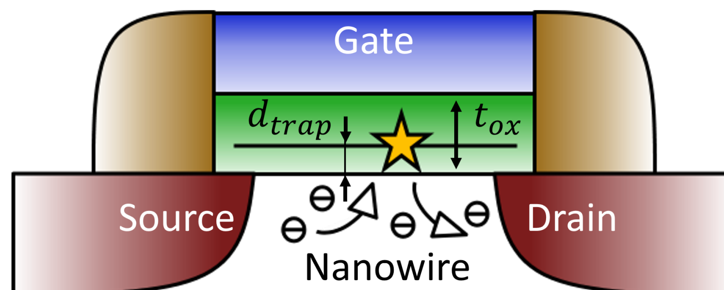

Figure 4.54: Schematic of the NW FET simulation system. The star represents the single trap, located at the distance d_{trap} from the nanowire in the gate dielectric of the thickness t_{ox}.

way similar to Butler–Volmer kinetic expressions:

$$k_{Red} = k(r)_{ET} exp\left[-\frac{\alpha nF}{RT}(E - E^{\circ})\right] \tag{4.33}$$

$$k_{ox} = k(r)_{ET} exp\left[-\frac{(1-\alpha)nF}{RT}(E - E^{\circ})\right] \tag{4.34}$$

Here $k(r)_{ET}$ is the distance-dependent electron transfer function, α is the transfer coefficient, E is applied potential and E° is the standard reduction potential of the molecule. Similarly we can express the capture and emission rates:

$$\frac{1}{\tau_C} = R_{coeff} \times \delta \times exp\left[-\frac{q}{kT}\gamma(E_{trap} - \alpha V)\right] \tag{4.35}$$

$$\frac{1}{\tau_E} = R_{coeff} \times \delta \times exp\left[-\frac{q}{kT}(1-\gamma)(E_{trap} - \alpha V)\right] \tag{4.36}$$

In this expression R_{coeff} is the adjustment coefficient which was introduced for the tuning of the probability in frequency domain thus making the frequency of Lorentzian shape component lover than sampling rate of data generation process. The sampling rate in all presented simulations was 50 kHz. For simulation purpose R_{coeff} was set to the constant value of 10. δ is degeneracy factor, in all shown here simulations it was set to 1. q is the elementary charge, kT is thermal energy, γ is the charge transfer coefficient, E_{trap} is the energy of trap, V is applied gate voltage, α is the ration of the capacitance C_G between the gate and trap site and tunneling capacitance C_J between the channel and trap site and often is close to the ratio between the trap depth d_{trap} and the dielectric thickness t_{OX}. For the RTS simulation we set $d_{trap} = 1\,\text{nm}$, $t_{ox} = 8\,\text{nm}$, thus $\alpha = 0.125$. The energy of trap was selected to be 0.1 eV. The probability of the electron been transferred from one state to the other after time t was calculated as

$$p_{C,E} = exp\left[-\frac{t}{\tau_{C,E}}\right] \tag{4.37}$$

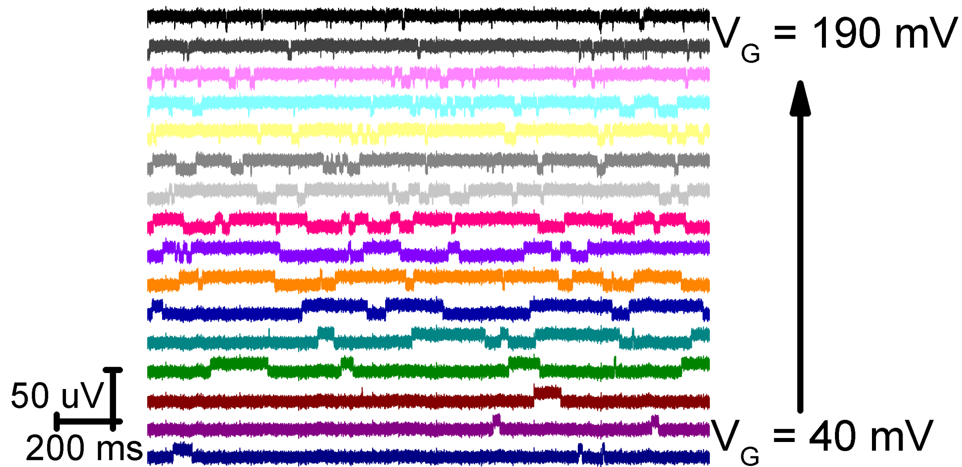

Figure 4.55: Simulated timetraces of RTS fluctuations at different applied gate voltages.

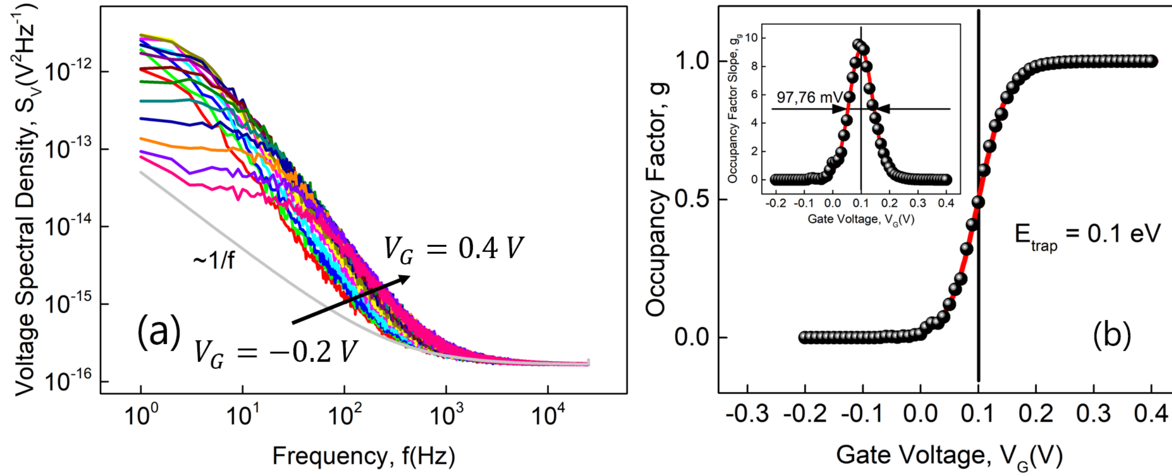

Figure 4.56: (a) Calculated voltage spectral density for corresponding timetraces. (b) Calculated occupancy factor using equation 4.38. Inset shows the slope of the occupancy factor, the width at half height equals to 97.76 mV

, where t is the time since the last transition. The randomness to the transition probabilities is introduced in the following way. At each time step the probability is compared to the uniformly generated random number. If it is smaller than the probability value the transition occurs, otherwise it the trap remains in the same state. The set of generated time series at various gate voltages is shown in figure 4.55.

For each timetrace we estimated the occupancy factor which indicates the probability of the trap to be occupied and is calculated as

$$g = t_{up}/(t_{up} + t_{down}) \tag{4.38}$$

The noise power spectral densities, calculated for the timetraces at different gate voltages are plotted in figure 4.56(a). The Lorentzian-shape component corresponds to the RTS noise fluctuations. Background noise was also artificially introduced into the simulation system. It should be noted that the background noise is the same for every timetrace and is not dependent on applied gate voltage. However this factor should also be considered as the background noise level can influence of the trap dynamics. The flicker noise component is simulated with the amplitude of $S_V = 5 \times 10^{-14}\,\mathrm{V^2\,Hz^{-1}}$ at 1 Hz, and the slope of flicker component is set to 1. Thermal noise was simulated for the channel resistance of 10 kOhm at temperature of 300 K.

Extracted occupancy factor behaves as a sigmoid function (see figure 4.56(b)) indicating that the trap is unoccupied at lower voltages and is permanently occupied at high voltages.

The slope of occupancy factor is a peak function with the width at half height of ≈ 97.76 mV, when the γ coefficient is set to 1 in equations 4.35, 4.36 (see figure 4.56(b)). This value corresponds to expected value since it is defined by the power of exponent taking into account equations 4.35, 4.36, and 4.38. Capture and emission times were evaluated from simulated timetraces.

Extracted value of capture and emission times are plotted in figure 4.57(a) and reflect typical exponential behavior of capture and emission times for FET device.

The distribution of time in up and down states for selected gate voltages where capture time is less then, equal and greater than the emission time are plotted in 4.57(b). As you

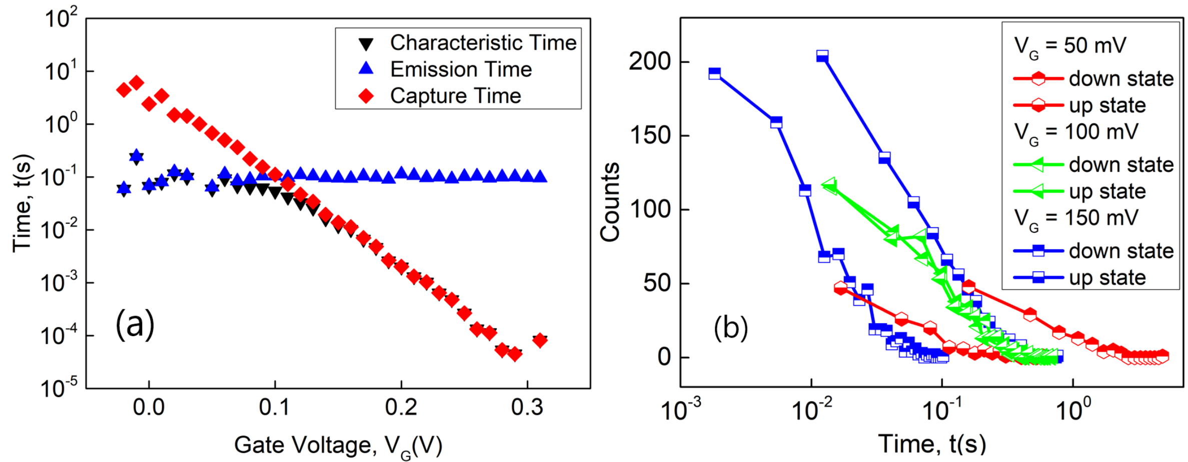

Figure 4.57: (a) Extracted capture and emission times as a function of gate voltage. (b) Statistics of capture(up state) and emission (down state) times.

can see the distributions for both times are the same for $V_G = 100\,\text{mV}$ which corresponds to the case when Fermi level and trap levels equalize. We selected this voltage for further analysis as RTS fluctuations at this point are the most pronounced, occupancy probability equals 0.5. When we are able to generate random telegraph signal noise as the next step we will try to answer another important question regarding the noise introduced by the calculation of occupancy factor. Now, when we are able to generate random telegraph signal noise fluctuations, we consider them as a useful signal and introduce a new method

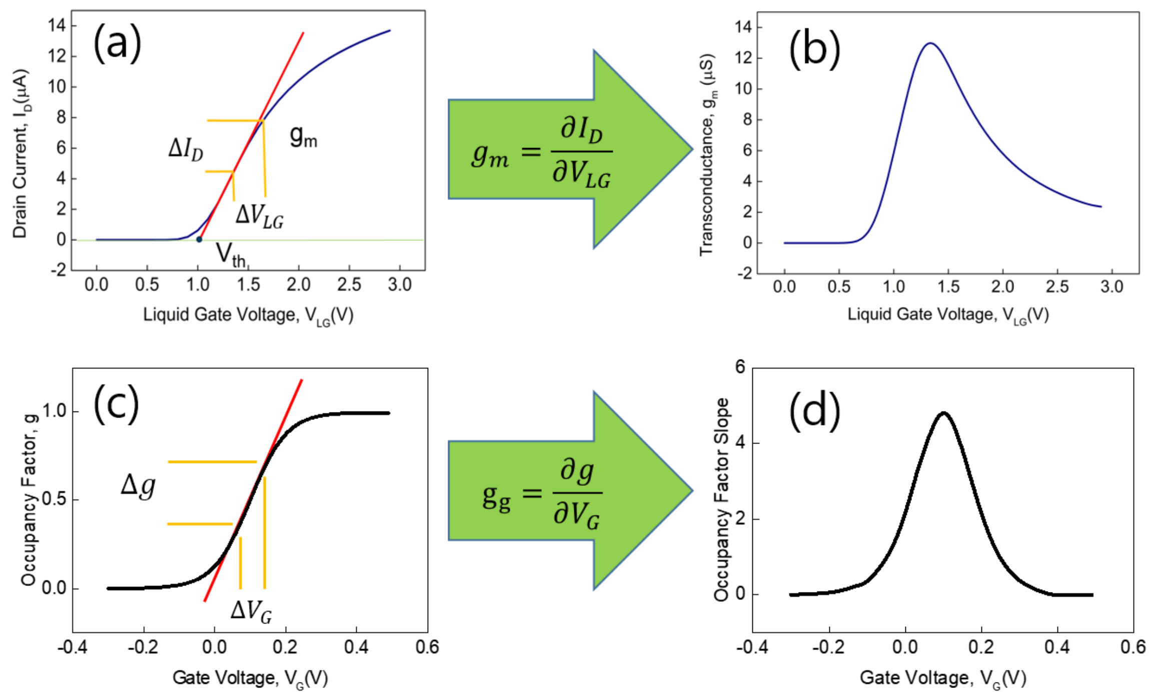

Figure 4.58: Schematic for the explanation of a new approach of occupancy factor equivalent input noise. (a) Typical transfer curve for liquid-gated nanowire FET. (b) Transconductance calculated from the transfer curve. (c) Occupancy factor calculated from simulated timetraces. (d) The slope of occupancy factor.

for noise evaluation of the trap occupancy probability as potential sensitive parameter.

In field-effect transistors the transconductance is calculated as a derivative of the drain current with respect to gate voltage (see figure 4.58$(a) \rightarrow (b)$). The input-referred fluctuations of the channel current can therefore be calculated as $\Delta V_{LG} = \Delta I_D / g_m$. In terms of power spectral density of noise fluctuations it can be written as $S_U = S_I / g_m^2$. Similarly to the transfer curve the occupancy factor also depends on the gate voltage. The occupancy factor slope is calculated as a derivative of the occupancy factor curve with respect to gate voltage as it is shown in figure 4.58$(c) \rightarrow (d)$). Therefore we can talk about equivalent input voltage fluctuations caused by the variation of occupancy factor, $\Delta V_G = \Delta g / g_g$. The fluctuations can also be presented in terms of power spectral density as $S_{gg} = S_g / g_g^2$. Such approach allows to compare the noise caused by the current fluctuations in the channel and fluctuations of occupancy factor.

In this respect we transform the voltage fluctuations into fluctuations of occupancy factor in time. For this purpose we select the window with predefined time duration and calculate occupancy factor within the time frame. By sliding the window along the timetrace we obtain the new timetrace with the occupancy factor fluctuations as it is shown in figure 4.59. From the timetraces of occupancy factor we calculate the power spectral density of occupancy factor in a similar manner as for voltage fluctuations. Calculated spectra are shown in 4.60(a). Each curve correspond to the different window duration starting from 10 ms ending up at 100 s. The longer window duration the lower noise can be obtained. This makes sense since the larger set of data points gives more precise estimation of the occupancy factor at each point and such approach is somehow similar to averaging filer. For FET device the transconductance indicates how drain current is controlled by the gate. Therefore current fluctuations can be recalculate as equivalent input voltage fluctuation. Similarly the occupancy factor fluctuations can be recalculated as equivalent input voltage fluctuations. If we replot caused by occupancy factor fluctuation equivalent input noise value at 10 Hz as a function of window duration

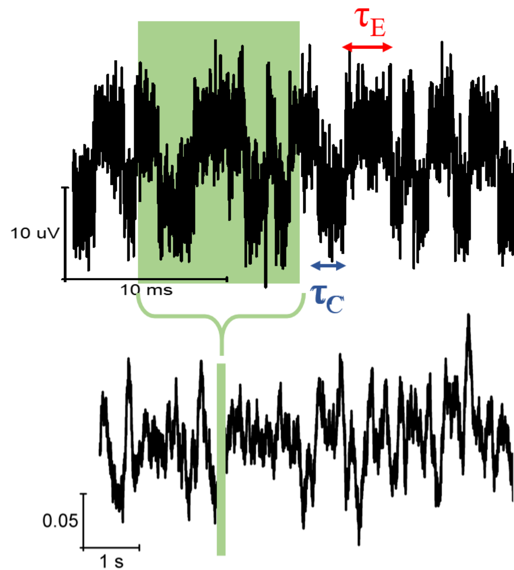

Figure 4.59: Illustration of the conversion from RTS voltage fluctuations into the fluctuations of occupancy factor using sliding window(green rectangle) with predefined width.

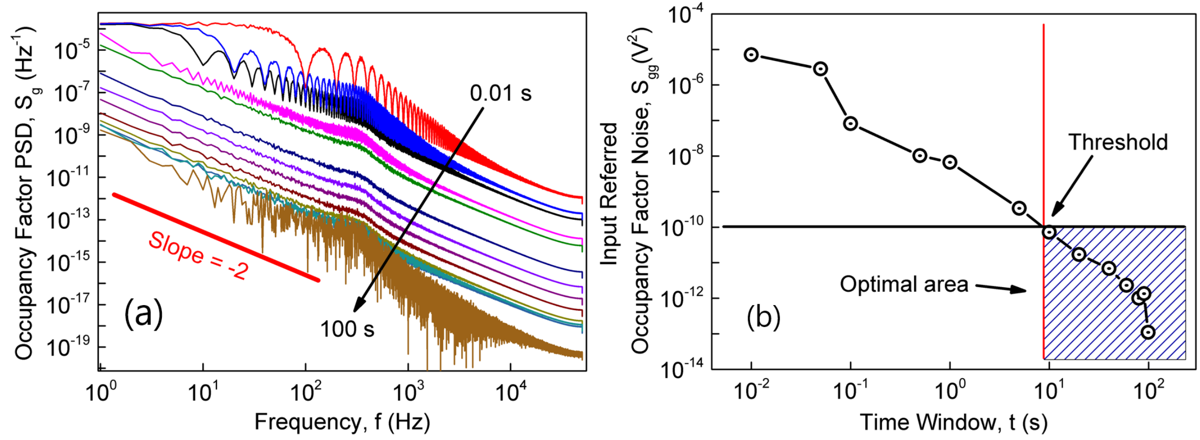

Figure 4.60: (a) Noise spectra of occupancy factor fluctuations calculated with different window width, from 10 ms to 100 s. (b) The equivalent input noise of the occupancy factor. The red line shows the window size when desired threshold noise level is reached.

we can see that the noise level decreases with the larger window size(see figure 4.60(b). From the graph we can estimate the amount of measurement time required in order to diminish the impact of occupancy factor noise on the precision of capture and emission time estimation. The typical noise value for transistor is around $1 \times 10^{-10}\,V^2$. From the graph we can estimate that the recording time should be greater than 10 seconds. The parameter is of critical importance when the single trap is used for biosensing applications.

To illustrate we compare our estimations with the results obtained from the measurements of RTS noise in liquid-gated nanowire FETs. The length of the nanowire was 200 nm and width 100 nm. The electrolyte solution was 10 mM PBS, pH = 7.4. Measured noise demonstrate lorentzian-shape component corresponding to the random telegraph signal noise fluctuations (see figure 4.61(a)). The frequency of the lorentzian component increase which is typical for all recorded RTS noise components The capture and emission times were extracted using method described in section 2.5.6. Calculated capture time demon-

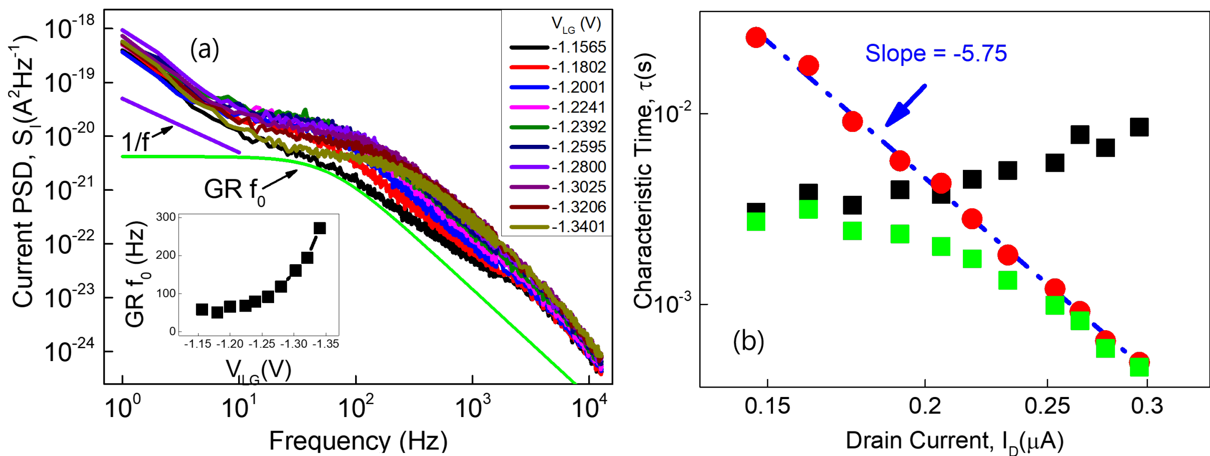

Figure 4.61: (a) Noise spectra measured for the liquid-gated Si NW FET. The Lorentzian-shape component is the result of RTS noise fluctuations. Inset shows the behavior of characteristic Lorentzian frequency. (b) Capture and emission times extracted from the timetraces. The capture time demonstrates high slope of -5.75.

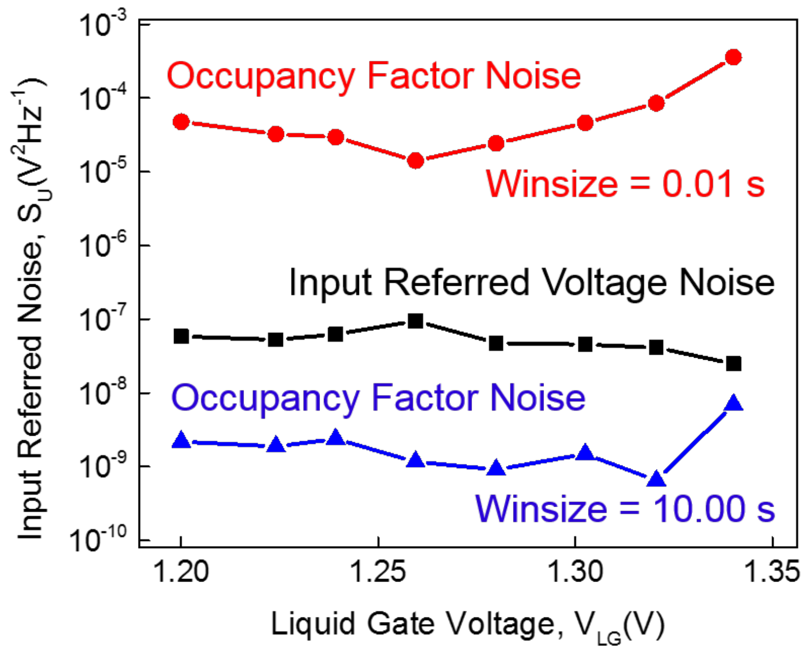

Figure 4.62: Input referred noise of voltage fluctuations in comparison to input referred occupancy factor fluctuations calculated for the window size of 10 ms and 10 s. The results demonstrate, that the window size of 10 s is enough for the accurate measurement and analysis of RTS signal.

strate non-SRH model behavior with the slope of -5.75 (figure 4.61(b)). We applied a new method of calculating input referred noise caused by occupancy factor fluctuation of the real measurement data. In the figure 4.62 we shown the input referred noise calculated for voltage as well as occupancy factor noise at 10 Hz. As we can see the small window size causes the large input referred noise while the large window size of 10 seconds demonstrate the lower level on input referred noise in comparison to the voltage noise. It should be noted that this is valid in the voltage range where occupancy factor slope is greater than one. It can be explained in terms of transition events - the more transitions occur in the time frame, the more accurate the fluctuations can be described statistically. The model suggests a new insight on the RTS fluctuations as useful signal, where capture dynamics is used as a sensing parameter. Furthermore it allows to estimate detection time parameters when single trap is employed as a biosensor.

4.8 Summary

In this chapter we have described the technological process steps required to fabricate liquid-gated silicon nanowires on the basis of SOI wafers. The protocol was optimized to reduce leakage currents and improve performance of devices. In addition, on-chip reference electrode and microfluidic system were introduced for biosensing experiments. High quality liquid-gated silicon nanowire FETs were fabricated in Helmholtz Nano Facility(HNF). Transport and noise properties of fabricated structures demonstrate excellent scaling abilities. Furthermore it was confirmed that mobility fluctuations are dominant

in $p^+ - p - p^+$ structures, while number fluctuations are typical for $n^+ - p - n^+$ structures.

Liquid-back gate coupling effect was revealed for the $n^+ - p - n^+$ inversion channel FET. The results demonstrate that number fluctuations caused by the interaction of charge carriers with the traps in the gate dielectric described by the McWhorter model is the dominant mechanism for the 1/f flicker noise component. Furthermore the application of back gate does not change the noise mechanism, but rather lower the noise level. Performed simulation of the FET device supports the results and demonstrate the possible cases when the conducting channel is located near the front-gate interface as well as back-gate interfaces. The application of gate coupling effect was evaluated from the viewpoint of the biosensor enhancement. The results demonstrate that noise lowering with applied back-gate voltage allows the optimization of silicon nanowire biosensor. In particular, enhanced signal-to-noise ratio of up to 100% was be achieved in the case of additionally applied back-gate bias.

The results of noise properties investigation demonstrate a good scaling with the gating area and follow generally known law. The charge noise demonstrate that single silicon nanowires are capable of single charge detection. During the studies a strong current modulation was observed as RTS fluctuations, which are caused by the single trap in the gate dielectric. A strong capture time dynamics with a power of up to (-14.37) was registered, which is not typical for standard SRH model. To explain such behavior several factors have to be considered, including quantization and specific distribution of charge carriers as well as their tunneling to the trap in gate dielectric. Single trap dynamics was studied in the temperature range from 200 K to 280 K. Coulomb blockade energy in terms of additional energy for overcoming the effective barrier in the accumulation regime was considered for understanding of the enhanced capture time dynamics. In addition we reveal that low doses of gamma irradiation result in changes of single trap dynamic processes by changing its charge state from neutral to attractive. The results demonstrate that gamma irradiation is an effective tool for controlling single trap parameters. Simulation model was developed to understand the parameters of the single trap and determine the application ranges, including the minimal time of recording to benefit from the single trap as a sensor. It should be emphasized that the gate area where nanowires demonstrate single charge detection coincide with the area where the probability of single trap appearance is very high.

In this respect, single trap phenomena is important for the broad range of fundamental studies as well as for the development of high-speed atomic-size biosensors with advanced functionality.

Chapter 5

Space-Charge Phenomena in GaN Nanostructures for Biosensing

5.1 Space-Charge Phenomena in GaN Nanowires

Semiconductor nanowires (NWs) and nanoribbons (NRs) are attracting more and more attention considering a variety of novel physical phenomena [163, 164] which are promising for applications in nanoelectronics, nanophotonics, sensing, etc. Major factors assisting appearance of novel effects include the utilization of different materials and fabrication techniques. Remarkable transport features often appear because of device geometry and high aspect ratio rather than material properties. The conductor of length, L, for instance, can be considered as a wire when two dimensions, normal to current flow, namely width, W, and thickness, D, are much smaller than the length. The effects involving the electric charging of NRs are very different from those in conducting-film structures ($W \gg L \gg D$) and bulk samples ($W, D \gg L$) due to weak screening of extra charges in NRs, appearing from the nonconductive dielectric surroundings [165]. The operation regime of such conductor typically transitions from linear or ohmic to nonlinear with increasing applied voltage. A superlinear current can be observed when uncompensated injected charge carriers limit the current, if not prevented by the contacts to the conductor. The charge-injection effects are more likely to appear at much lower voltages for nanoribbons (NRs) in comparison to conductive films and bulk samples.

For trap-free samples, space-charge limited current (SCLC) for bulk(B), film(F) and NR samples at large applied voltage follow the equations[166–169]:

$$I^B = \frac{9}{32}\frac{\varepsilon \mu V^2}{\pi L}\frac{WD}{L^2}, I^F = \zeta_2 \frac{\varepsilon \mu V^2}{4\pi L}\frac{W}{L}, I^{NR} = \zeta_1 \frac{\varepsilon \mu V^2}{4\pi L} \tag{5.1}$$

where ε is the dielectric constant of a material, μ is the mobility; ζ_2 and ζ_1 are numerical coefficients of the order of unity, depending on contact geometry. Equations for I^B and I^F are valid for $(W \times D)/L^2 \gg 1$ and $W/L \gg 1$, respectively.

Obviously, the current for all systems is proportional to V^2 and is independent on the system dimensionality (the Mott–Gurney law) [165]. The dependencies on the intercontact distance, L, considerably differ.

A simple comparison of the ohmic currents with those given by equation 5.1 allows the estimation of the voltage when the system transitions to the SCLC regime:

$$V_c^B = \frac{32\pi e}{9\varepsilon} n^B L^2, V_c^F = \frac{4\pi e}{\zeta_2 n} n^B DL, V_c^{NR} = \frac{4\pi e}{\zeta_1 \varepsilon} n^B DW \tag{5.2}$$

where for convenience of comparison, we introduce an electron volumetric concentration, n^B. The above-mentioned inequalities imply that $V_c^B \gg V_c^F \gg V_c^{NR}$. Similar relations are also valid for samples with trapping centers, although to provide trap filling for such samples the currents increase as V^{2+s} with $s > 0$ ([167, 170]). Meanwhile, the presence of surface states lime deep defect states influences on the space-charge redistribution across the NRs as a result of Fermi level pinning at the surface and electron band bending next to the surface. It is known that for n-type GaN NRs and nanowires (NWs) the electronic bands are bent upwards next to the surface and an electron depletion region forms near the surface [171–173]. Such mechanism was previously considered omitting possible depletion in the NR. Indeed depletion and SCLC effects represent the major mechanisms for charge-redistribution effects in the NR samples. For NRs and NWs, SCLC is a quite common phenomenon, which has been observed for samples fabricated by different techniques using variety of materials such as GaN [169, 174], InAs [175], CdS [176], Si [177] and GaAs [178]. The analysis of electrical properties inherent for such NRs, including space-charge distribution phenomena, has to be performed considering the NR characteristics, including dimensions, contact properties, carrier mobility and concentration. In current studies, we analyzed electronic edge-state and space-charge phenomena in planar AlGaN/GaN NRs with well defined basic characteristics. It has been found that the depletion effect is effectively observed not only at the edges of NR as influenced by deep charged edge states but also in the middle part of narrow NR samples. Furthermore, the effective depletion increases with NR width decrease which is in a good agreement with theoretical predictions. We reveal an important feature of spatial charge separation across the NR which produces an electrostatic potential patterns outside the NR with a large magnitude of the electric field. The effect is particularly important for two-dimentional materials, including graphene. In addition, we study electric noise in the NRs for the linear and nonlinear transport regime, which has not been reported previously. Noise results allow to analyze transport properties in NR structures and reflect diffusion processes, intensified as a result of space-charge-limited transport effect.

5.2 Patterning of AlGaN/GaN Nanoribbons

NR samples under study were fabricated on the basis of planar undoped AlGaN/GaN heterostructure wafers and patterned with different widths. Substrates were grown by metal-organic vapor-phase epitaxy on a (0001) Al_2O_3 substrate. The heterostructure consist of 3 µm-thick GaN layer followed by a 40 nm thick $Al_{0.1}Ga_{0.9}N$ top layer. The AlGaN/GaN NR structures were fabricated using electron-beam lithography and Ar^+ ion beam etching. The etching depth of 95 nm was well below the depth of the AlGaN/GaN interface. A schematic crosssection of the fabricated multi-NR samples is shown in the inset of figure 5.1.

Using ion beam etching six sets of devices with fixed length of 620 µm and different widths of 280, 360, 470, 720, 930 and 1110 nm as well as 100 µm-wide Hall-bar structures were patterned. Each device contained N=160 identical NRs connected in parallel. Ohmic contacts to NRs and Hall-bar structures were formed by a deposition of metal Ti/Al/Ni/Au stack followed by rapid thermal annealing at 900 °C for 30 s.

The current–voltage (I–V) characteristics showed linear behavior at voltages of less than 0.1 V. The contact resistivity measured on the test structure was estimated to be $2 \times 10^{-4}\,\Omega\,\mathrm{cm}^2$. The contact resistance was proven to be much smaller than the resistance of NRs. Even for a small Al content, the electrons are well confined near the

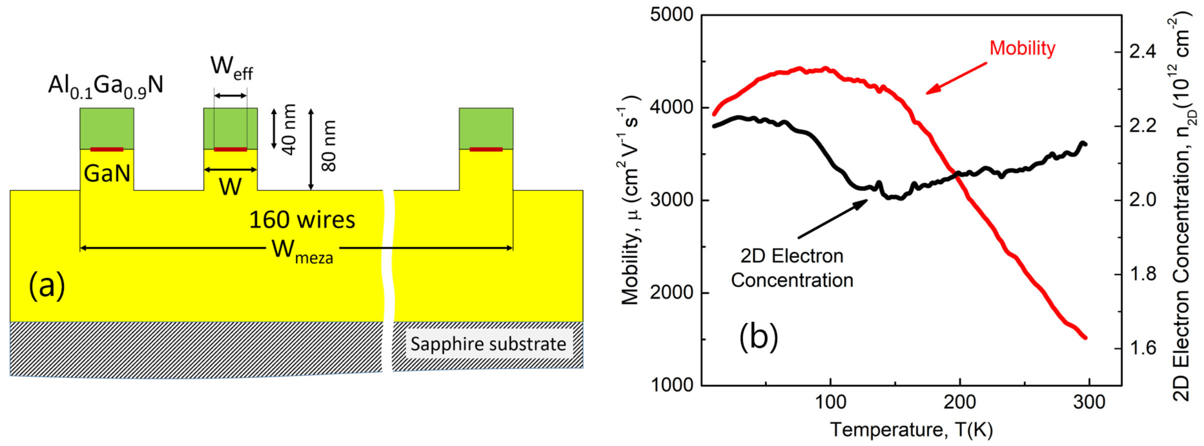

Figure 5.1: (a)A schematic cross-section of the heterostructure with parallel nanoribbons. (b)Mobility, μ, and two-dimensional electron concentration, n_{2D}, dependencies on the temperature for AlGaN/GaN heterostructure.

interface, although their two-dimensional electron gas (2DEG) concentration, n_{2D}, is not large. Temperature dependencies of n_{2D}, and the mobility, μ, were obtained from Hall measurements (figure 5.1). In particular, we found n-type conductivity of the 2DEG with $\mu = 1500\,\mathrm{cm}^2/\mathrm{V/s}$ and $n_{2D} = 2.1 \times 10^{12}\,\mathrm{cm}^{-2}$ at room temperature. The energy difference between the first excited and ground subbands in the quantum well were estimated to be 78 meV for studied heterostructure. It should be mentioned that the unique properties of AlGaN/GaN heterojunction of spontaneous and piezoelectric polarization fields provide the high density of the 2DEG at the interface between two materials without any modulation doping [179]. Fields assist the formation of a quantum well at the AlGaN/GaN interface. To analyze the electron dynamics within the two-dimensional system formed at the interface, electron energies and wave functions for the 2DEG were computed numerically from the self-consistent solution of the Schrödinger and Poisson equations (WinGreen simulation, Forschungszentrum Juelich, Germany). The results are presented in figure 5.2 where a potential profile and local density of states are shown. The concentration of 2DEG was calculated to be $2.5 \times 10^{12}\,\mathrm{cm}^{-2}$ by integration of the charge. It is clear that only electrons from the lowest sub-band of triangular well determine the transport in linear regime. Temperature dependencies of noise characteristics provide additional information on the structure transport properties. Noise properties were measured using noise measurement setup with dynamic signal analyzer (HP 35670A), similar to the one discussed in section 3.2. Measured spectra demonstrate both 1/f and generation-recombination noise behavior, where respective components are well resolved at temperatures lower than T=230 K (figure 5.3)

The characteristic frequency of the GR noise component (maximum position in figure 5.3(a)) obtained at T=130 K was about 1800 Hz and 630, 45, 2.5 [in Hz] for 110 K, 90 K, and 70 K, respectively. The shift of the GR maximum to lower frequencies with decreasing temperature (see figure 5.3(a)) is consistent with the model of temperature-activated processes in the AlGaN/GaN heterostructure. The analysis of temperature dependent GR noise components allows to estimate characteristic energy levels of the traps inside the bandgap responsible for the process in frame of theory, describing charge carrier recombination. In this case the GR noise spectrum can be described by two components with characteristic times τ_1 and τ_2 ,where $\tau_1 \gg \tau_2 s$ [180]. The first characteristic time constant

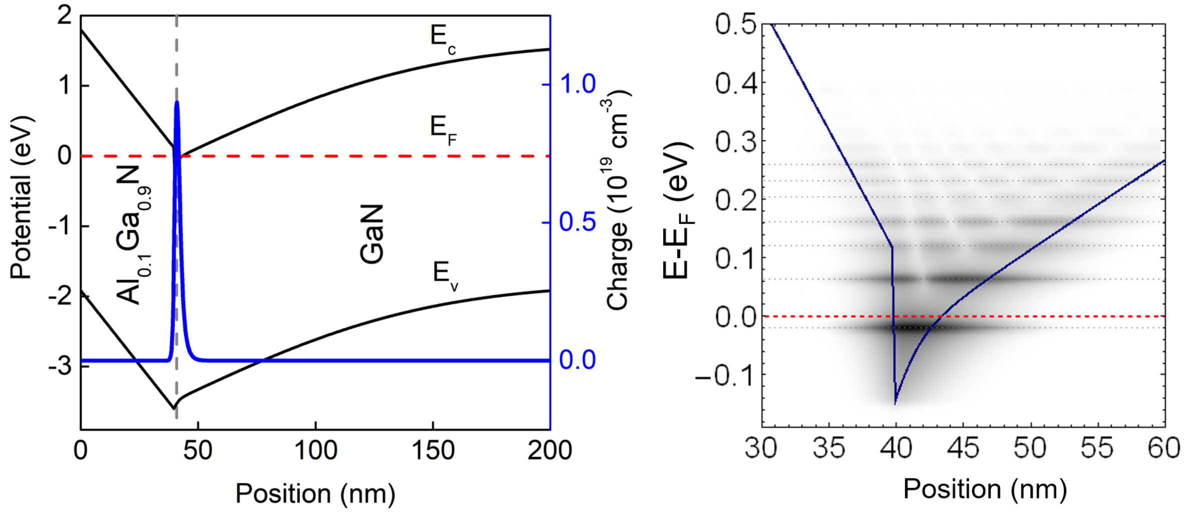

Figure 5.2: (a) The self-consistently calculated band diagram of the heterostructure. (b) Confinement energy levels in the quantum well with respect to Fermi energy, E_F, (in meV -20 64, 120, 162, 204, 232. E_t is a shallow defect-state level.

τ_1, also called "Shockley–Read time constant" (τ_{SR}) [181], depends on temperature as $\tau_{SR} \sim exp(-E_t/kT)$, where E_t is the trap energy level, k is the Boltzmann constant, and T is the temperature. The second characteristic time constant τ_2 corresponds to a considerably shorter time range and is, therefore, determined from measurements of noise spectra in the high-frequency range[182]. It should be noted that direct transitions between two quantum levels are very fast (with characteristic times of about ps), which corresponds to the THz frequency range. GR processes registered in low-frequency noise spectra are well described by the participation of trap levels. At small concentrations of Al content in AlGaN/GaN heterostructures the screening effect is small and the participation

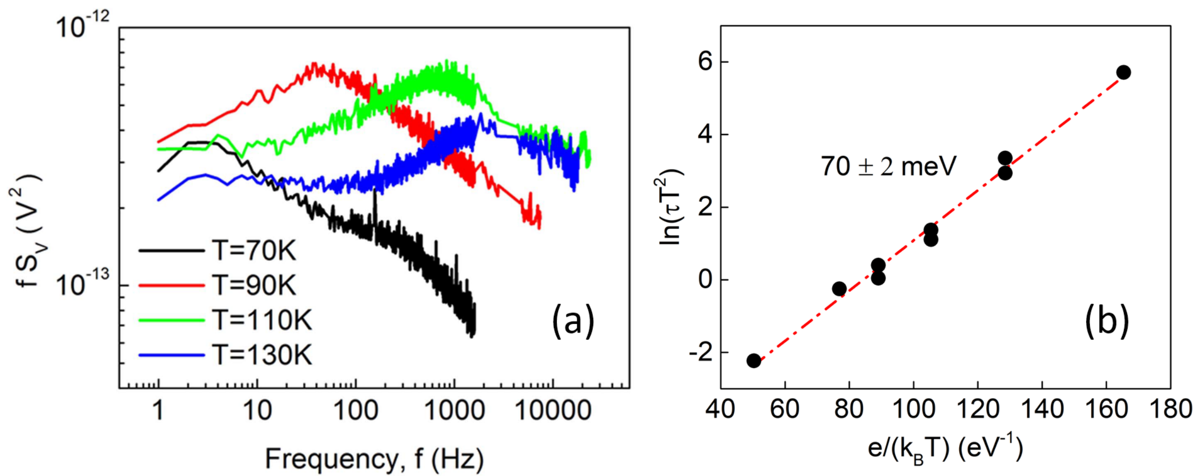

Figure 5.3: (a) Typical voltage noise power spectra, multiplied by frequency, f, measured at different temperatures. Spectra demonstrate the movement of generation-recombination (GR) component for NR with width $W = 1100$ nm at applied voltage, $V = 100$ mV. (b) Arrhenius plot obtained from temperature-dependent measurements of noise spectra.

of traps has to be considered.

GR processes include excitation of electrons from the first to the second quantum level in the quantum well followed by a recombination process, which consists of two stages with an intermediate state on the trap level (figure 5.2). From the measured noise spectra (figure 5.3(a)) we determine the characteristic frequency, f, of the GR component and the characteristic time τ_1 for each temperature as $\tau_1 = (2\pi f)^{-1}$. The characteristic energy, E_t, determined from an Arrhenius plot (figure 5.3(b)) equals $E_t = 70\,\mathrm{meV}$, which is in good agreement with the self-consistently calculated band diagram (figure 5.2(b)) and reflects the energy difference between the second level of the triangular quantum well and the trap energy level.

5.3 Depletion Effects in Low-Voltage Regime

5.3.1 Current–Voltage Characteristics of GaN NR Structures

We measured the current–voltage (I–V) characteristics for all NR sets. The results are shown in figure 5.4(a). As it is demonstrated in figure 5.4(b) the conductance of NRs depends linearly on the width. The extrapolation to zero conductance allows to determine the critical width of the NR where no current flow is expected. The extracted critical width was $W_c \approx 200\,\mathrm{nm}$. Indeed, for 185 nm wide structures the registered current was negligibly small. The critical width was also found to be slightly dependent on the temperature: W_c increases by 20% when the temperature decreases to 90 K. The slopes of fitting lines agree with temperature dependence of the mobility $\mu(T)$ within such accuracy. The existence of critical width for the NR conductivity(figure 5.4(b)) imply on the formation of depletion regions next to the edge of the NR. Indeed, surface-depletion effect for GaN NRs has been observed in experiments on conductivity [171], stationary and transient photoresponse [172, 173], and it has also been directly measured using Kelvin probe force microscopy [179]. The effect was observed for NRs fabricated by different methods. In general effect can be explained as pinning of Fermi level next to the surface due to

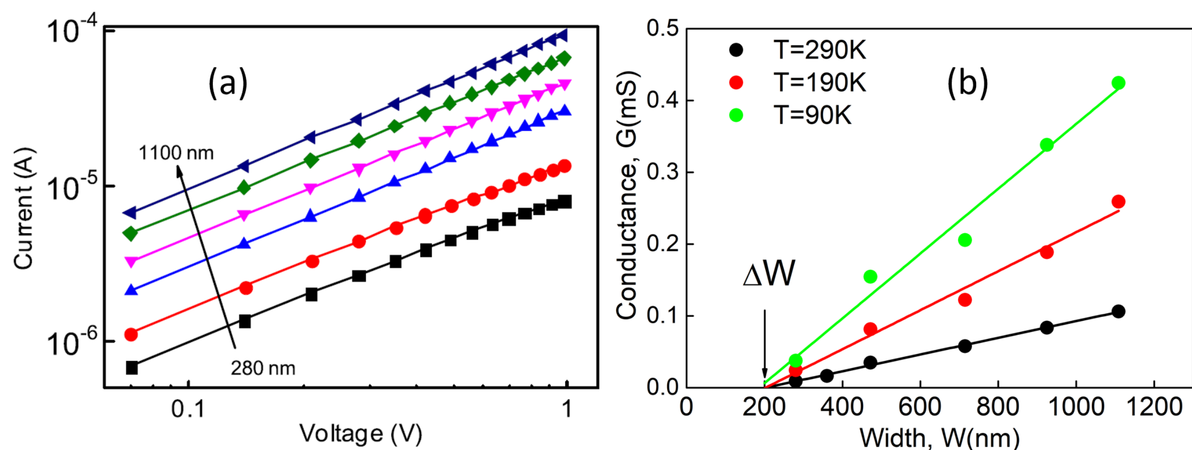

Figure 5.4: (a) The current-voltage(I-V) characteristics measured for sets of nanoribbons with different widths (W(nm): 280, 360, 470, 720, 930, 1100). (b) The low-voltage conductance versus the nanoribbon width measured at different temperatures, demonstrating critical width, W_C where 2DEG is formed in NR.

relatively deep surface defects. The surface of planar NR structures becomes negatively charged, forming an electron-depletion region in the NR via ionized positive donors. The space-distribution phenomena might be related to the existence of charged edge states likely originating from Ga vacancies [183–185]. It should be noted that in contrast to a bulk sample with an extended surface, the simple Schottky depletion space-charge model with an essentially constant space charge in the space-charge zone cannot be applied. By using a general approach with varying space-charge density across the NR we calculated the depletion effect in the planar NRs under consideration. It should be emphasized that simulation results demonstrate that electron concentration profiles considerably differ from previously suggested rectangular ones with depleted regions only at the edges of the NR structure, as will be shown below.

5.3.2 Electronic Edge-State Phenomena

To study the depletion effects in NRs and formation of the field patterns outside the NRs, a comprehensive model for the calculation of the electrostatic potential and the electron concentration distributions in the NR samples with edge traps had been developed. The theory was applied for the planar AlGaN/GaN NRs of different widths. Calculations were performed for samples with NR widths of 280 nm, 360 nm and 470 nm. In the theoretical model, the NR can be considered as infinitely long in the y-direction (see the sketch in figure 5.5(a)). The electron gas is strongly confined in the z-direction. The widths of the samples are much larger than the de Broglie wavelength of electrons and, therefore, the effects of electron quantization along the lateral x dimension can be neglected. Electron concentration, n_{2D}, and compensatory positive charge, N_D , were considered uniform and $n_{2D} = N_D$ for original heterosrtuctures. In NRs electrons are partially trapped by the very narrow regions near the edges of the ribbon, which are charged negatively. These regions are modeled as filaments with a linear electron concentration, N^{edge}. For the concrete

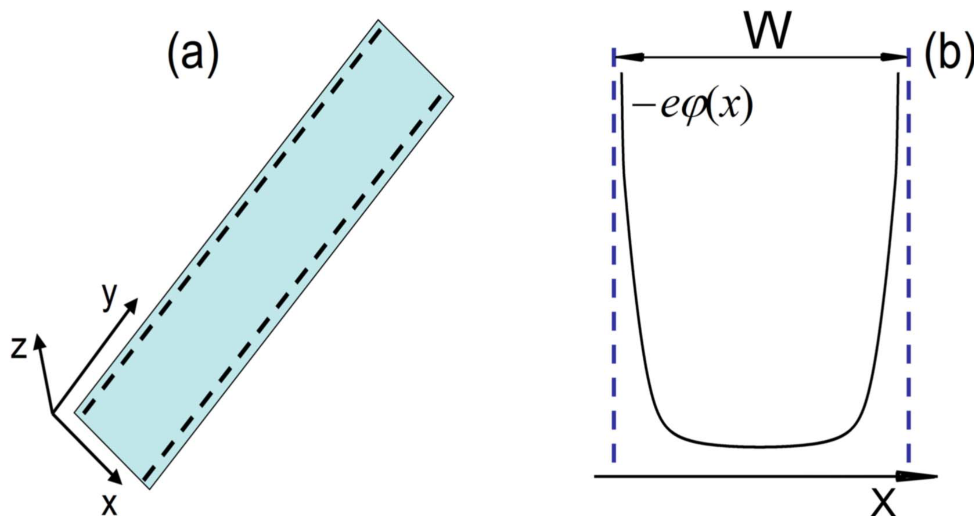

Figure 5.5: (a) Schematic geometry of NR sample considered for the calculation of electrostatic potential and electron concentration distribution. (b) Schematic potential distribution across the nanoribbon.

samples the value of N^{edge} is taken from experiment. The formation of such charged regions induces a redistribution of electron concentration, $n(x)$, inside the NR and the resulting electrostatic potential, ϕ, is also modified regarding the value of N^{edge}. The electrostatic potential caused by the charge redistribution in the NR induces electrical field in the space around the NR and, therefore is a function of two coordinates: x, z. To simplify the calculations the NR was assumed to be surrounded by air. In this case the electrostatic problem is reduced to the solution of equations system which includes 2D Poisson equation

$$\frac{\partial^2\phi}{\partial x^2}+\frac{\partial^2\phi}{\partial z^2}=-\frac{4\pi e}{\kappa_0}\delta_D(z)\left[N_D-n(x)-N^{edge}\times\left[\delta_D(x-W/2)+\delta_D(x+W/2)\right]\right] \quad (5.3)$$

,the definition of the equilibrium concentration of two dimensional free electrons obeying the Fermi statistics

$$n(x)=\frac{m^*k_BT}{\pi\hbar^2}log\left[1+exp\left(\frac{E_F+e\phi(x,0)}{k_BT}\right)\right] \quad (5.4)$$

and the charge-conservation law

$$N_DW=2N^{edge}+\int_{-W/2}^{W/2}n(x)dx \quad (5.5)$$

In equations 5.3,5.4, 5.5, e is the elementary charge, k_B and $\hbar$ are Boltzmann and Planck constants; κ_0 is the dielectric permittivity of the effective surroundings of the NR, m^* is the electron effective mass, T is temperature; E_F is the Fermi level relative to the bottom of the lowest sub-band and δ_D stands for the Dirac delta-function. In addition, we consider an NR with symmetric edges (N_{edge} is the same for the left and right edges). Using the Green's function

$$G(X-X',Z-Z')=-\frac{1}{2\pi}log\left[(X-X')^2+(Z-Z')^2\right] \quad (5.6)$$

corresponding to filament sources, the formal solution of the Poisson equation can be written as follows:

$$\phi(X,Z)=\frac{k_BT}{e}\frac{W_{sc}}{2}\left(\frac{N^{edge}}{WN_D}log\left[\left((X-1/2)^2+Z^2\right)\times\left((X+1/2)^2+Z^2\right)\right]-\right.$$
$$\left.-\int_{-1/2}^{1/2}dX'(1-n(X')/N_D)log\left[(X-X')^2+Z^2\right]\right) \quad (5.7)$$

where we introduced the dimensionless coordinates, $X=x/W, Z=z/W$. The parameter N^{edge}/WN_D reflects the percentage of trapped electrons on one of the interfaces. The dimensionless parameter $W_{sc}=2e^2WN_D/(\kappa_0k_BT)$ determines screening effects. Equation 5.7 allows to obtain the distribution of the electrostatic potential in the whole space surrounding the NR if $n(x)$ will be determined. Finally, with the use of equations 5.3,5.4, 5.5, the whole problem is reduced to the solution of the single nonlinear integral equation,

$$\zeta_F = log(exp(n(X)N_c)/-1) - W_{sc}\times$$
$$\times\, log\left(\sqrt{|X^2-1/4|}\right)\int_{-1/2}^{1/2} dX'(1-n(X')/N_D)\times$$
$$\times\int_{-1/2}^{1/2} dX' log(|X-X'|)(1-n(X')/N_D) \quad (5.8)$$

where $\zeta_F = E_F/k_BT$. The parameter $N_c = m^* k_B T/\pi\hbar^2$ is introduced as the effective density of states. The distribution of electron concentration $n(x)$ depends on three dimensionless parameters: N_c, W_{sc}, and ζ_F. Each of them is a function of the several physical parameters of the NR including initial doping N_D, temperature T, width of NR. For the given parameters of the NR we specify ζ_F, then solving equation (5.8) we find $n(x)$ and from equation (5.5) restore N^{edge}. Electrostatic potential profile, $\phi(x,0)$, can then be calculated inside the NR and afterwards around it, $\phi(x,z)$, using equation 5.7. Approximate solution to this reduced electrostatic problem can be found using variation method. The accuracy provided by the method depends on the successful selection of a trial function $g(x,a,b..)$, and a number of fitting parameters a, b, ... The latter are searched to minimize the squared residual $\Delta(a,b..) = \int(\hat{L}\{g(x,a,b..)\} - \hat{R}\{g(x,a,b..)\})^2 dx$, where $\hat{L}$ and $\hat{R}$ are the operators of the left and right parts of the equation. Another approach to solve the electrostatic proble is the iteration method which allows to obtain an exact solution with a given accuracy. Method works very well when the input parameter $W_{sc} \leq 1$, which corresponds to the compressive properties of the integral equation's core. However the more interesting case is when $W_{sc} \gg 1$, where the iteration procedure does not converge. In this respect to solve the integral equation 5.8 in both cases a more powerful "discretization" method had been developed. The main idea behind the method is the reduction of the integral equation to a system of algebraic nonlinear equations which can be solved numerically using known methods. Method is briefly described in [168, 186]. Using aforementioned approach electrostatic potential profiles , ϕ, can be calculated by solving a two-dimensional Poisson equation, self-consistently with the electron redistribution across the NRs. The only "free" parameter formulated in the problem was the one-dimensional density of the negative charge, eN^{edge}, accumulated on an edge of the NR. It was extracted from the conductance measurements(figure 5.4(a)). The fraction of the electrons trapped at the edges, $\delta = (1 - G/G_0)$ and $N_{edge} = \delta W n_{2D}/2$ were obtained by defining the conductance of the multi-NR structure as $G_0 = eN\mu n_{2D}W/L$, and using the measured conductance, G. The density of edge traps per unit NRNR length was estimated as $N_{tr} \approx 2.2\times10^7\,\mathrm{cm}^{-1}$. For samples with W=280, 360, 470 nm it was found $\delta \approx 0.7, 0.56, 0.42$, respectively.

Using these parameters, the distributions of the electron concentration and the dimensionless electrostatic energy (i.e. the electron band bending) across the NRs were calculated and are presented in figure 5.6. In central parts of the NRs the electrostatic potential is flat and the electron concentration is a smooth function of the coordinate x. A fast increase of the potential energy (an upward band bending: figure 5.6(b)) creates completely depleted zones near the edges (figure 5.6(a)) is observed in the direction toward the edges. The thicknesses of these depleted zones, with concentrations of less than $0.1n_{wD}$, can be estimated as $W_d \approx 50..70nm$. It should be noted, that the total size of depleted zones at both edges, $2W_d$, is less than the critical width, W_c, equal to 200 nm corresponding to almost zero conductance. This is explained by partially depleted

middle part of the NRs. The depletion effect is inherently large in narrow NRs. Indeed, for the examples presented in figure 5.6 the carrier concentrations reach maximal values $n_m/n_{2D} \approx 0.65, 0.76, 0.85$ at W=280, 360, 470 nm, respectively (the corresponding Fermi energies are small and change sign: $E_F/k_BT = -0.1, 0.16, 0.3$ (see figure 5.6(b)). It should be mentioned, that such approach can also be applied to graphene layers, which have charged edge states. In all cases wide depletion regions result in a decrease of the effective widths, W_{eff}, of the NR samples to the regions, which are essentially smaller than the geometrical sizes of the samples. The positive space charge is observed from experiment since carriers do not extend to the very borders of the NRs. The effect results in bond breaking and empties bulk donors with positive ionic charge in depletion regions, which is in good agreement with the depletion effect reported in cylindrical-geometry NWs [187, 188].

Self-consistently calculated distributions of the electrostatic energy around the planar nanostructures are shown in figure 5.7. The positive charge of edges is compensated by the negative charge of edge states. Remarkable feature of charge redistribution is the penetration of resulting electrostatic potential distribution outside of the NR at a distance of 1 µm from the NR into the surrounding environment. Such results have not been reported in literature previously. Mentioned above patterns are characteristic features for the planar NWs and NRs and does not appear in cylindrical geometry.

It should be emphasized, that the spatial distribution of positive charges in the NR and negatively charged wire edges induce the electrostatic potential and the field outside the wire, as illustrated in figure 5.8 for two NRs with W=280, 360 nm (corresponding potential and electron concentration distributions in the interior of these NRs are given in figure 5.6). Potential and field spread away from the NRs and form complex patterns. Electric fields of large magnitudes(tens of $kV cm^{-1}$) arise at distances of same orders as

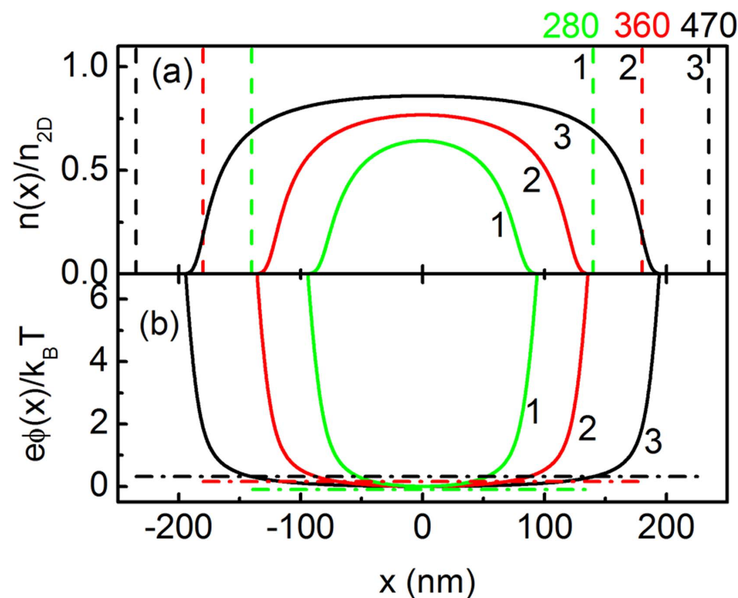

Figure 5.6: (a)The distribution of electron concentration across NRs. Vertical dashed lines indicate on the geometrical sizes of nanoribbons. Values in the top right include the ratio between depletion and conductive areas, correspondingly 200/80, 200/160, 200/270.(b) The distribution of the electrostatic energy of electrons at T = 290 K. The dashed lines show Fermi levels for curves, corresponding to different widths(1-280 nm, 2-360 nm, 3-470 nm).

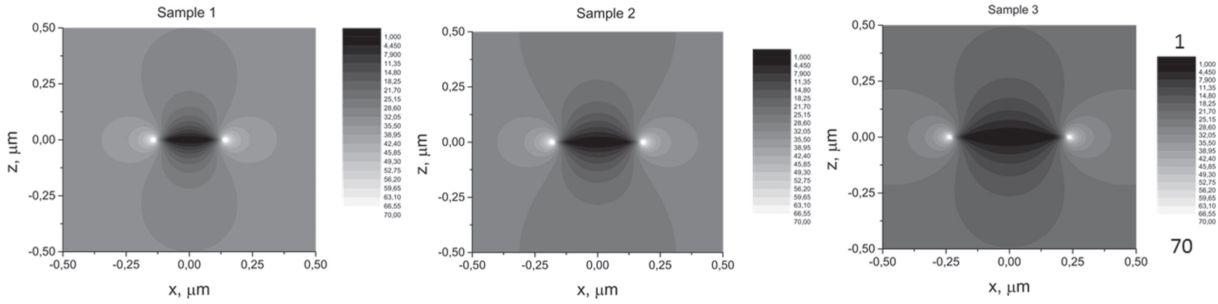

Figure 5.7: Distribution of electrostatic potential energy around NRs at z=0 in units of k_BT, calculated at $T = 300\,\mathrm{K}$ for samples with widths W=280 nm (sample 1), 360 nm (sample 2), 470 nm (sample 3). x = 0 corresponds to the middle of nanoribbon.

the NR width. It should be emphasized that phenomenon of field spreading outside the NR appears only for planar NR structures. The findings are interesting and important for applications in such fields as NR-based chemo- and bio-detectors where chemo- or bio-targets are typically delivered by diffusion processes. Existence of discussed above fields may assist the transport of target species towards the surface of sensor by enhancing or slowing the process dynamics. For example, it is easy to estimate that the flux of ions under the electric field and their diffusion flux both become comparable at the field k_BT/eZW (k_B and eZ are the Boltzmann constant and the ion charge, respectively: the diffusion flux is estimated for the characteristic spatial scale of the order of the wire width, W). Setting W=200 nm, T=300 K, Z=1, the field is estimated to be about $2.5\,\mathrm{kV\,cm^{-1}}$, which is much smaller than the electric fields induced by the depletion effect (see figure 5.8). In this respect we can expect that such electrostatic fields outside the NRs can be used for acceleration or slowing down ionic and molecular transport toward the NRs for enhancement of NR-based chemo- and bio-detector sensitivity as well as for decreasing the response time of these devices. It should be emphasized that air was considered as the

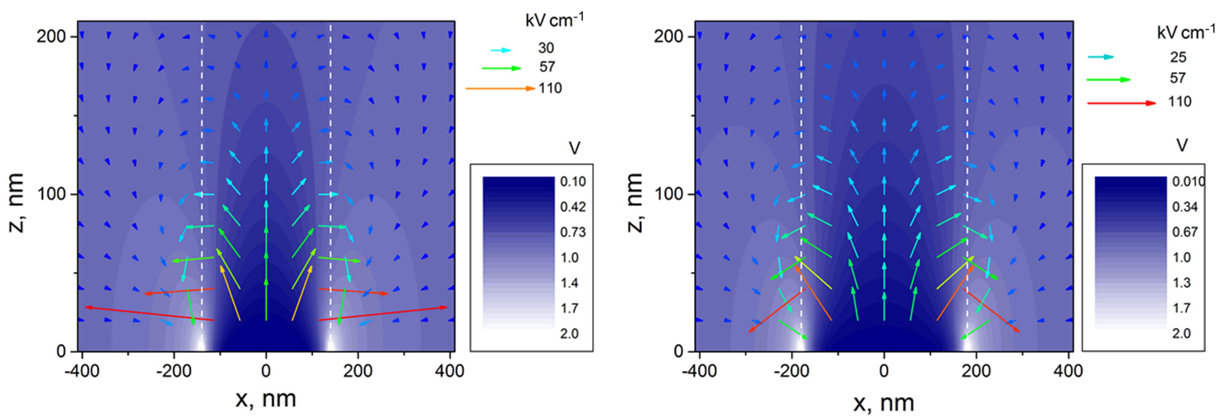

Figure 5.8: Electrostatic potential (contour plot) and electric-field strength (vector field) outside of the planar NRs, formed at the interface between AlGaN and GaN material at z = 0 calculated at $T = 300\,\mathrm{K}$ for two nanoribbons with $W = 280\,\mathrm{nm}$ (a) and $W = 360\,\mathrm{nm}$ (b), corresponding to the ratio between depletion and conductive channels 200/80 and 200/160, respectively. The origin or each vector corresponds to a space point where the electrical field vector was calculated.

outside environment for presented calculations. The dielectric constant of GaN layer has not been taken into account. Taking this into account will certainly modify the electric field below the NR. However the distribution on top, on the upper side of the NR with only a very thin AlGaN film (40 nm), might be assumed to be only weakly disturbed. This is a spatial region, where the external fields are of major interest because of their probable impact on adsorption processes.

5.4 Space-Charge Phenomena in Long GaN Nanoribbons

In this part nonlinear current regime(figure 5.9(a)), which was registered at high voltages ($V > 8\,\mathrm{V}$) of I-V characteristics, will be described. Interesting features in transport and noise properties were discovered after increasing the applied voltage. It should mentioned that for investigated voltage interval ($V = 0...25V$) electric fields in long NRs under study are small enough to neglect hot-electron effects and related current nonlinearities [189]. As it is shown in figure 5.9(a) the onset of nonlinear regime depends on the wire width. Such regime was most likely to observe for the three narrowest NRs. At high voltage, two NRs exhibit super-Mott-Gurney dependency, which is characteristic of a mature regime of SCLC: $I^{NR} \sim V^{2.4}$ at $W = 280\,\mathrm{nm}$ (shown in the inset of figure 5.9(a)), and $I^{NR} \sim V^{2.25}$ at $W = 360\,\mathrm{nm}$. For the NR with W=470 nm, $I^{NR} \sim V^{1.6}$. To understand such behavior, we note that in equation 5.2 for the critical voltage V_c^{NR}, the product $n^B DW$ corresponds to the number of electrons per wire unit length. For the planar NRs, this number can be estimated as $(1-\delta)n_{2D}W$. Using the parameters, δ(defined above), critical voltages were calculated for three NRs: $V_c \approx 3.7, 5.5, and 12.5V$ at W=280, 360, and 470 nm, respectively. Such voltages are in good agreement with nonlinear phenomena registered in I–V characteristics (figure 5.9(a)). It should be noted that effective conductive width of

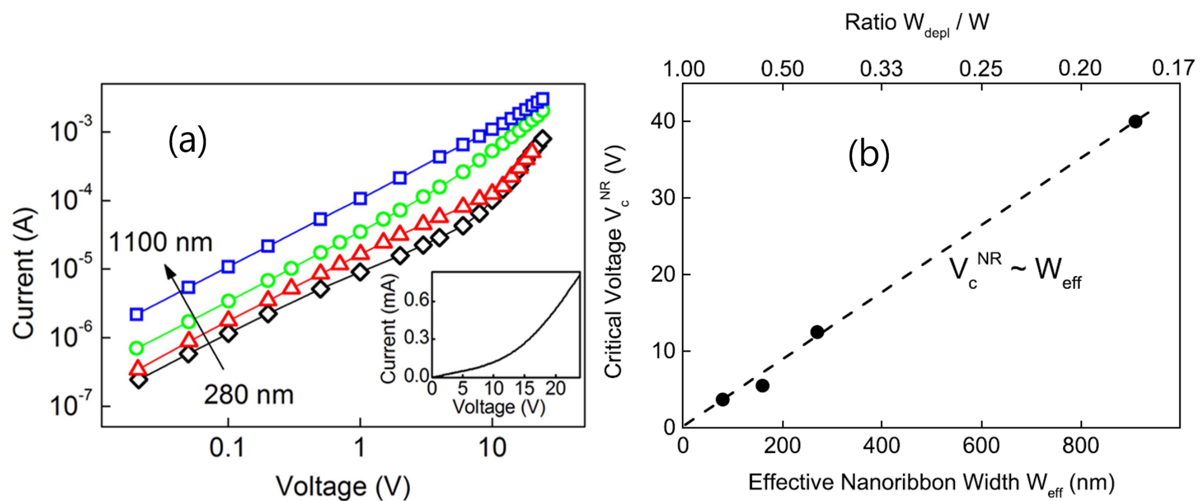

Figure 5.9: (a) Current-Voltage (I-V) characteristics measured for four sets of NWs with different widths, W(nm): 280, 360, 470, 1100. Inset shows the I-V characteristic for NR with $W = 280\,\mathrm{nm}$ at $T = 290\,\mathrm{K}$. (b) Critical voltage dependence on the effective NR width(bottom axis) and ratio between depletion and conductive channel (top axis). Dashed line reflects the behavior according to equation [**eq:gan2**].

the samples differs for linear and nonlinear regions of I–V characteristics. In linear region, conductivity of the NR is determined by $W_{eff} = W - W_{depi}$. However, in nonlinear regions injected current flows through the entire cross-section of the sample. Figure 5.9(b) shows the results of critical voltage for different samples taking into account the above-mentioned peculiarity. The critical voltage strongly depends on the ratio between depletion and conductive channel regions. The smaller the ratio (the larger the effective width) the larger the critical voltage. For the NR with a 1100 nm width, it was calculated $V_c \approx 40V$, i.e. the SCLC regime was not reached. Whereas, for the first two NRs, SCLC was observer in our experiment, while for the third NR only the transient regime for the SCLC transport was reached. This explains the behavior of I–V characteristics shown in figure 5.9(a). The most prominent features of the current corresponding to the nonlinear regime were revealed in fully depleted sample with the narrowest width of 185 nm at different temperatures down to $T = 77$ K.

For this NR sample, I–V characteristics measured at different temperatures are presented in figure 5.10. The temperature-dependent data confirm the formation of the space-charge-limited current transport [170, 176] in the NR structures at high voltages. Characteristics exhibit the following typical behavior with three stages: an initial slow rise followed by a sharp rise by a few orders of magnitude at a critical voltage of about 1 V, when the Mott–Gurney limit ($I\ V^{2+s}$) is attained. Interestignly, the three stages of this scenario are similar to those found in an early paper [170] and discussed in a recent paper [190] devoted to the analysis of diodes with deep traps. The behavior of the I–V characteristics of NR structures can be understood in the framework of depletion and SCLC phenomena at several stages. Firstly, I-V characteristics measured at $T = 77$ K should be considered. For the 185 nm-wide NR, the total number of electrons supplied by donors per wire unit length is less than the density of the edge defects, $n_{2D}W < N^{tr}$, making NR practically depleted. Small residual concentration of electrons is determined by thermal ionization of the deep-edge defects and substantially depends on the temperature. Then, at low voltages (¡1 V), very small currents are observed(less than 'nominal' currents $\mu(T)n_{2D}WV/L'$ by a factor in the range of 10^2 to 10^3), as it can be seen from figure 5.8.

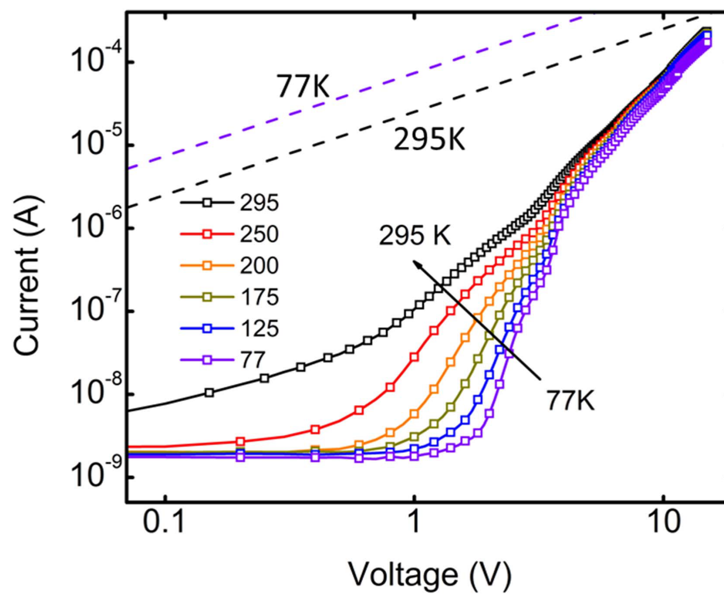

Figure 5.10: Current-voltage characteristics of the narrow NR structure with $W = 185$ nm. Dashed lines are nominal I-V characteristics for 77 and 295 K.

With increasing voltage, electrons injected from the contact fill the empty edge traps and the current slowly rises, until the edge traps become totally filled at a voltage V_on, equal to 5 V at $T = 77$ K. Further increase of applied voltage provides more injected electrons and a sharp magnification of the current. At low temperatures, this sharp magnification of current has the character of a switching effect — at a small variation in the voltage, the high-resistance state of the NR is reset to the well-conducting state. At higher voltages, the current behavior reflects the SCLC transport with $I\ V^{2+s}$ dependence. The voltage, V_on, decreases with temperature increase and is estimated to be for other temperatures in the voltage range from 5 V to 2 V. The I–V characteristics corresponding to high-voltage range (above 8 V) reflect weak temperature dependence.

5.5 Noise Spectroscopy of GaN Nanoribbons

The study of electric currents in NRs was validated by measurements of the current noise spectral density, $S_I(f)$, in the frequency range from 1 Hz to 100 kHz. A detailed description of noise measurement procedure can be found in the section 3.2. In planar AlGaN/GaN heterostructures, the current noise demonstrate two main components: the flicker noise (with the Hooge parameter $\alpha_H \approx 5 \times 10^{-4}$) and GR (generation–recombination) components [191–194]. Indeed, noise measurements for the planar AlGaN/GaN structure revealed flicker noise with a modest value of $\alpha_H \approx 2.9 \times 10^{-4}$ and a GR component.

Figure 5.11 shows isolines obtained at constant frequencies from normalized current noise spectra, measured at different voltages for NR structure with $W = 280$ nm. GR noise component reflects recombination processes related to excess electrons injected into the NR structure at voltages exceeding 1 V. We found that, compared to the planar heterostructures, the NRs are more noisy. For the linear current regime, at $T = 300$ K, the flicker component (f^{-1}) is dominant and the characteristic parameter α_H increases when the NR width decreases: $\alpha_H \approx 8.7 \times 10^{-3}$, 0.02, and 6.2 for W=470, 360, and 280 nm, respectively. The high level of noise can be explained as follows. The low-frequency electric fluctuations are related to capture/decapture processes related to defect states. The presence of defects in extended AlGaN/GaN heterostructures determines a moderate

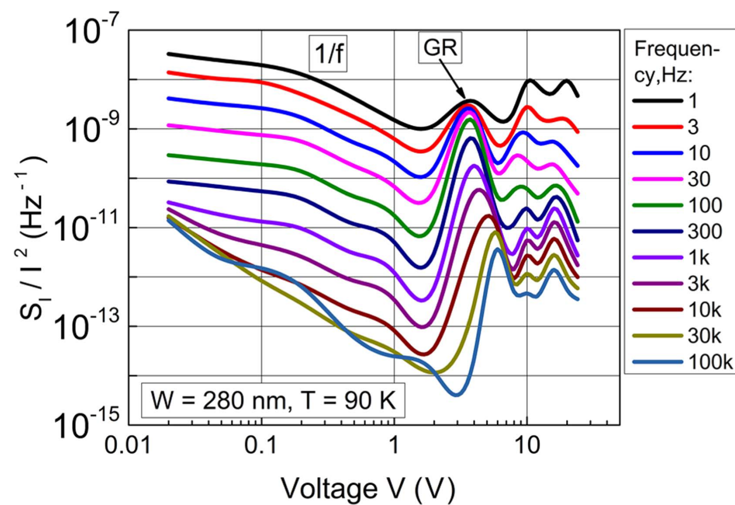

Figure 5.11: Typical normalized current noise spectra measured at different voltages for the NR structure with $W = 280$ nm.

flicker noise and the respective value of the Hooge parameter. Additionally, there are deep-edge defects in the NRs, which participate in both stationary phenomena, determining depletion effects and stochastic capturing/decapturing processes generating additional noise. The smaller the NR width, the larger the contribution of the edge defects to the noise, such that in the narrow NRs, the processes involving the edge defects are dominant. Analysis of the measured noise spectra revealed two features of the noise generally found for all NRs: an increase of the noise intensity and a modification of the spectral density, $S_I(f)$, with increasing voltage/current. The noise increase with the voltage was stronger for NRs with lower 1/f noise at small voltages. To illustrate this effect we analyzed the normalized spectral density, $S_I(f)/I^2$, as a function of the voltage for a given frequency, f.

The results are presented in figure 5.12 for the NRs with W=360 nm and 1100 nm. The normalized noise spectral density increases by three to four orders of magnitude. For the NR with W=360 nm, a steady noise increase appears in the voltage interval $V = 1...10V$. For the wider NR (with W=1100 nm), the noise intensity increases considerably at the larger voltages, $V > 10V$. As the voltage increases, the spectral dependencies, $S_I(f)$, of the NRs are modified.

Particularly, at $V \geq V_c$ the dependencies $S_I(f)$ show a faster decay with f, as illustrated by the inset of figure 5.12(a), for the narrow NR at the voltage $V = 8\,\mathrm{V}$. At the same voltage, the wider NR shows only the 1/f dependence (see the inset of figure 5.12(b)). The noise features of the NRs discussed above reflect the SCLC effects. The low-frequency noise is mainly determined by fluctuations of the free-electron concentration. Under the conditions of the experiments presented here, the hot-electron effects are negligible and distributions of free electrons over the momenta and energies are almost at equilibrium. However, both free-electron concentration and that of electrons captured by the defects are far from equilibrium in the SCLC regime. Indeed, the main attributes of this regime are the electron injection, nonuniform electrostatic potential, development of a potential barrier near the cathode [165–167] and redistribution of the electrons along

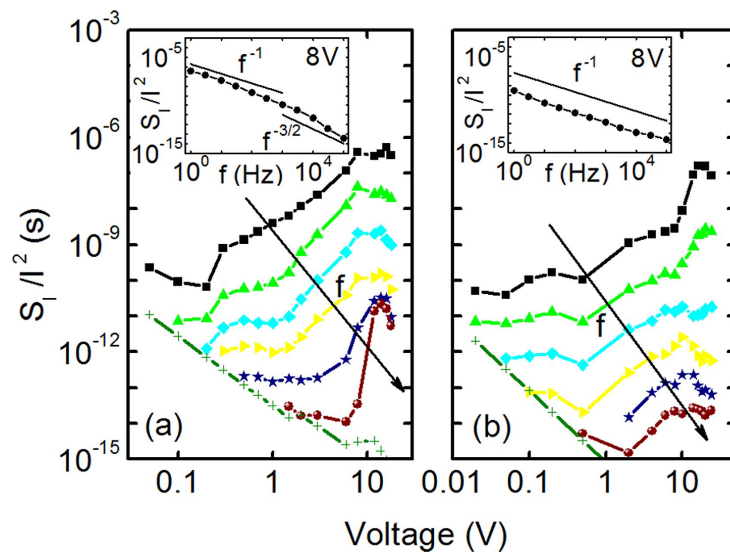

Figure 5.12: Normalized noise spectral density, S_I/I^2, as a function of applied voltage for $1, 10, 10^2, 10^3, 10^4, 10^5 Hz$ for nanoribbon widths (a) $W = 360\,\mathrm{nm}$ and (b) $W = 1100\,\mathrm{nm}$. Crosses indicate estimated level of thermal noise. The inset shows frequency dependencies of $S_I(f)/I^2$ for NRs with corresponding widths at $V = 8\,\mathrm{V}$.

the conductor. Near the injecting electrode, particularly, a zone with excess electron concentration is formed, while a zone near the anode is depleted due to exclusion processes. Both factors, excess and deficit of free electrons, obviously give rise to intensified capture/decapture processes and to an increase of the noise intensity. The additional mechanism of the fluctuations is provided by stochastic capture/decapture processes in the vicinity of the potential barrier: they randomly modulate the injection current and contribute to the noise. Highly nonuniform electron distribution along the NRs in the SCLC regime explains the above-mentioned modification of the noise spectral density, $S_I(f)$ at $V \geq V_c$. In fact, the 1/f noise dependence develops as a result of stochastic GR processes with distributed characteristic times of capture/decapture events. This interpretation is valid for macroscopically uniform bulk samples [193] and for surface/edge noise in uniform conductive channels [195, 196]. However, for a nonuniform distribution of the electrons and, consequently, nonuniform noise sources, temporal evolution of a fluctuation involves diffusion processes. The latter results in so-called diffusion noise [180], for which $S_I(f)\ f^{-3.2}$ [197]. Spectra with slope 3/2 reflect fluctuation processes determined by a characteristic time of electron diffusion with recombination at the surface or in the region of high concentration of recombination centers. Thus, the observed noise in the nonlinear regime corresponds to diffusion of nonequlibrium electrons from the injection region of space charge toward borders of the NRs with an increased concentration of defect states. The decreasing time constant (time decrease of diffusion) as well as the plateau of the GR noise component in low-frequency regions with increasing voltage can be explained by the spread of the space-charge region toward the NR borders, which results in a decrease of the distance of electron diffusion. For NRs of length L, the characteristic diffusion time in the SCLC regime is estimated to be $\tau_D = L^2/D$, with $D = k_B T\mu/e$ being the diffusion coefficient. The corresponding characteristic frequency is $f_D = 1/(2\pi\tau_D)$. For the experiments at $T = 300\,\mathrm{K}$, it was found that $D \approx 37\,\mathrm{cm}^{-2}\,\mathrm{s}^{-1}$,$\tau_D \approx 1 \times 10^{-4}\,\mathrm{s}$, $f_D \approx 1.5\,\mathrm{kHz}$. This indicates that at $f > f_D$, the spectral density, $S_I(f)$, shows faster decay with f, as is shown in the inset of figure 5.12(a) for the narrow NR at the voltage $V = 8\,\mathrm{V}$. Data shown in figure 5.11 demonstrate the diffusion time decrease with voltage increase from 3 V to 8 V due to carrier distribution spread in the direction of depleted regions at the edges. As a result of increased recombination processes on defects of depletion regions decreases the effective diffusion length. Consequently, the characteristic time constant as well as plateau level of the GR noise component decreases. At higher voltages for $V > 15\,\mathrm{V}$(figures 5.11, 5.12) decreasing noise can be explained by scattering of electrons on optical phonons [198]. The noise spectra with 1/f 3/2 dependence reflect SCLC phenomena accompanied by diffusion processes due to gradients in electron concentrations.

5.6 Summary

Electron-charge phenomena are analyzed with respect to both static edge-trap-induced charge redistribution and transport phenomena in the range of space-charge-limited currents. The results obtained for planar GaN NRs of different widths at low voltages allowed an estimation of the depletion effects in the NRs. We have shown that, for the planar NWs and NRs, the spatial separation of the positive and negative charges due to the depletion effects induces an electrostatic potential and a field outside the samples. The electric fields of large amplitude (tens of $kV cm^{-1}$) spread out over distances of the order of the width of the planar NWs and NRs Low-frequency noise spectra studied at different applied voltages allowed us to analyze the mechanisms of current formation in the NRs

structures in linear and nonlinear regimes. The GR noise components in the noise spectra observed at different temperatures allow an estimation of the energy of exchange processes between trap states and quantum-confinement levels. The activation energy is in good agreement with the self-consistently calculated band diagram. For low voltages, we found a relatively large noise intensity for the narrow NRs, which is explained by the substantial contribution of the deep-edge defects to stochastic capturing/decapturing processes generating additional noise. For higher voltages, the current nonlinearities allow us to study peculiarities of the SCLC effect in planar NW and NR structures. The onset of this effect clearly correlates with the NR width. For the narrow NRs (W=280, 360 nm), the mature SCLC regime was reached. An extreme behavior of the current of the switching type was observed for the narrower 185 nm NR with decreasing temperature. In this case, both space-charge-related phenomena studied are important. We found a change in the shape of the noise spectra with increasing voltage. In particular, the spectra show faster decay with frequency for the narrow NR with a tendency toward a slope of (3/2), as is typical for the diffusion noise, and which is characteristic of highly nonuniform conductive channels. It has been shown that, with increasing applied voltage, the noise spectra reflect evidence of the SCLC phenomena. Finally, we suggest that the features of the electric current and noise in the NRs and NWs studied are of a general character. This knowledge might be important for the development of different NR-based devices, including bio-sensors with enhanced sensitivity.

Chapter 6

Silicon Nanostructures Toward the Development of Biosensors

6.1 pH Sensitivity

Over the past decade, nanosized silicon structures have been under intensive study [163] due to their promising electrical, optical, chemical, thermal, and mechanical properties. Compared to larger structures, nanoscale field-effect transistors (FETs) allow measuring electrical, optical, and other often very small signals due to increased surface-to-volume ratio of the sample. The nanostructures became ideal for sensing of small sample volumes with low analyte concentrations. Silicon nanoribbon (NR) and nanowire (NW) FET structures open prospects for label-free, real-time, and high-sensitive detection of biomolecules using affinity-based binding principles [199] New features and functions are continuously added to the electronic devices, such as health monitoring mobile systems and wearable devices. Despite the success of such personal health monitoring systems [200], the next generation of wearable devices is expected to include also a portable "lab-on-a chip"—set of medical biosensors, which can be used for the detection and diagnosis of various medical substances [201, 202]. In order to be able to monitor and detect the early stages of disease in ideal case at the level of single molecule, the size of the sensor transducer has to be comparable with the biological markers under test. Therefore, biosensors based on NWs and NRs have to be developed for the monitoring of biological events that occur at very small dimensions. With size decrease, the limitations regarding current and voltage have to be also considered. For devices operating at weak signal levels, internal noise plays crucial role [132, 203, 204]. It determines one of the most important parameters of sensor's signal-to-noise ratio (SNR). As it is shown for double-gated Si NW sensors, pH sensitivity increases with the liquid gate voltage and SNR has higher value ($\sim 10^5$) [205, 206]. State-of-the-art research on nanoscale materials has revealed that electronic, magnetic, thermal, and optical properties may differ dramatically when their one-dimensional forms are synthesized. In this section we study FETs based on silicon nanostructures, including nanowires and nanoribbons from the viewpoint of pH sensitivity. Effects of channel length influence on the source-drain currents as well as pH sensitivity. We demonstrate that silicon nanowires, fabricated from the thin silicon layer, on the basis of silicon-on-insulator (SOI) wafets, can have high pH sensitivity fairly close to the Nernst limit.

The sensitivity of the Si NR FET sensor to changes in pH can be quantified by measuring the shift of the threshold voltage of the device and is defined by the Nernst equation

[207]:

$$\frac{\delta\psi_0}{\delta pH} = -2.3\frac{kT}{q}\alpha \leq 59\,\mathrm{mV\,pH^{-1}} \tag{6.1}$$

where, $\delta\psi_0$, is the potential at the surface. The dimensionless parameter, α, depends on the intrinsic buffer capacity of the oxide surface and the differential double layer capacitance can vary from 0 to 1. Changes in the pH of the solution induce variations in the surface charge density and surface potential. It leads to a change in the NR channel conductance. In general, sensitivity is defined as the largest possible output response to a certain biological event. The pH sensitivity of biologically sensitive field-effect transistors (BioFETs) arises from the acid/base reactions at the oxide/electrolyte interface and the maximum pH response achievable by a conventional ion sensitive field-effect transistor (ISFET) is the Nernst limit of $59\,\mathrm{mV\,pH^{-1}}$.

A response of $p^+ - p - p^+$ NR FET to surface potential changes were studied with respect to solution pH varying in the range from 2 to 12. Microfluidic system described in section 4.3.2 has been employed to provide a continuous flow of the liquid and enable an easy way to change the pH. For 10 µm long and 5 µm wide nanoribbon changes of pH

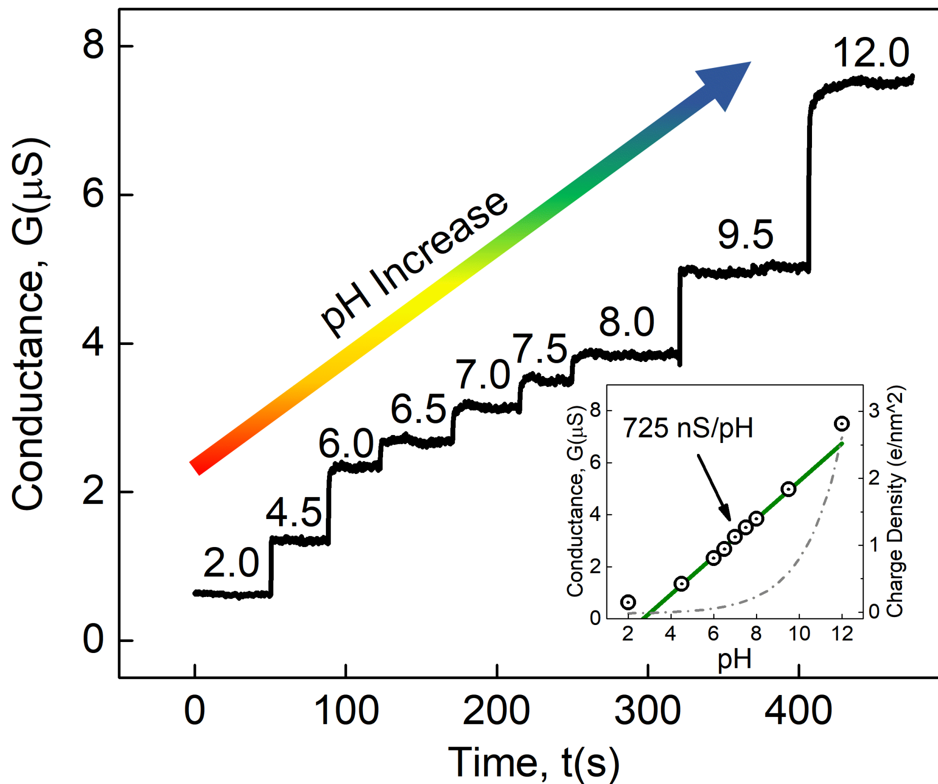

Figure 6.1: The timetrace demonstrating the stepwise conductance change with pH of the solution. Inset shows recalculated sensor response of the sensor together with the surface charge density, which explains lower and higher sensitivity at lower and higher pH, correspondingly.

appeared as a step-like conductance response of the NR sensor as it is shown in figure 6.1. It should be emphasized that the conductance changes are reversible - it returns back to its initial level in the same stepwise manner. Averaged values of the conductance for each step corresponding a unique value of pH are plotted as a dependence on the pH value in the inset to figure 6.1. The region from pH 4.5 to 9.5 can be highlighted as the dependence

exhibits linear behavior with the slope of 725 nS pH^{-1}. Obtained sensitivity is considerably higher the ones reported for Si NWs [208]. It should be noted that conductance change is lower for low pH value(2) and slightly higher for high pH value(12). The results correlate with measurements of surface charge density dependencies on the pH for silica [209]. The surface charge density has been reconstructed from [209] for the ion concentration of 10 mM and plotted in the inset to figure 6.1 along with conductance response.

Over the years, there have been numerous reports on devices with near Nernstian response [210–218]. The most popular platform for chemical modification of SiO2 surface is chemisorption of a few nanometer thick self-assembled monolayers [219], not only to enhance the pH sensitivity of Si/SiO2 gated nanosensors [220], but also because biomolecules such as proteins [221] or deoxyribonucleic acid (DNA) [222], which can be coupled to the other functional end of certain monolayers. Authors of [223] discussed the results concerning the functionalization and modification of Si NW FET sensors. A high sensitivity was achieved either by optimization of the intrinsic device transfer characteristics (such as lowering of the subthreshold swing or by tuning the gate potential) or by chemical surface modifications. Decreasing silicon thickness leads to higher surface charge sensitivity [217]. In [199], it was shown that at an optimum thickness of 30 nm the sensitivity reaches maximum value, and for a thicker device layer the pH response decreases and the largest response is obtained from the widest NR FET with the highest surface area. In this respect we performed the investigation of size-dependent pH sensitivity to determine the optimal parameters of the sensor.

6.1.1 Effect of the Channel Length on pH Sensitivity

In this section, we present the results of channel length influence on the pH sensitivity of the Si NR-based sensors. As the response of NR FET sensor to pH change is linear in the range from pH 5 to 9 we performed studies of surface potential changes in solution with pH = 6.2, 7, and 8.3. Typical transfer curves for aforementioned pH values are shown in figure 6.2. Measurements were performed four times for each pH value. The repeatability was within 7%.

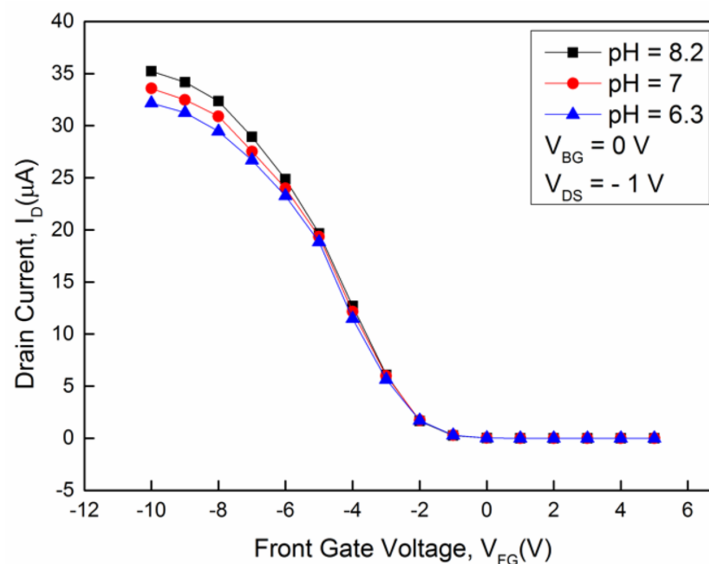

Figure 6.2: Transfer curves measured at different pH values

For $p^+ - p - p^+$ type structure we can see that increasing pH value results in the increase of the channel current, I_D. This is in a good agreement with model of the solution contact with the oxide layer surface, then on the oxide/solution interface caused hydroxyl groups SiOH. Concentration and behavior of those hydroxyl groups depend on value of the pH. The case when the surface is not charged is called zero charge point. For the SiO_2 dielectric layer, the point is reached at pH = 2.2. At the pH values lower than 2.2, the oxide surface is charged positively; at higher values of the pH, oxide surface is charged negatively. In the case of buffer solution with pH = 7, silicon oxide surface charge will be charged negatively. Therefore, at the applied negative gate potential, the absolute value of the negative charge on the surface oxide increases. As a result, the majority carrier concentration increases in the current channel (holes in p-Si) and thus channel current increases. pH sensitivity of the biochemical sensors is given as:

$$R_{pH} = \frac{R_{ch}\Delta I_D}{\Delta pH} \tag{6.2}$$

Here, ΔI_D and ΔpH are the elementary changes in I_D and pH. A typical response values of the sensor were in the range from 35 mV pH^{-1} to 59.5 mV pH^{-1}. To check the idea of the sensor size impact on the pH sensitivity we performed measurement using relatively large silicon nanoribbons with lengths 2 µm to 10 µm, width 10 µm and thickness of 50 nm. The dielectric covering silicon nanoribbon was thermally grown silicon dioxide of 8 nm.

The magnitude of the current is inversely proportional to the length of the current channel, which justifies the application of the drift approximation for transport mechanism, as well as the assumption of a uniform distribution of the electric field strength along the length of the current channel). The pH sensitivity increases with the current channel length and tends to the Nernst limit of 59.5 mV pH^{-1} (figure 6.3), which is in good agreement with values obtained for micro-size sensors [214]. Our results support also observations of the pH sensitivity behavior obtained for NW samples with different geometries [199] The length effect studied systematically in our work can be explained in terms of the surface charge density. Since the length of the channel decreases, the area of

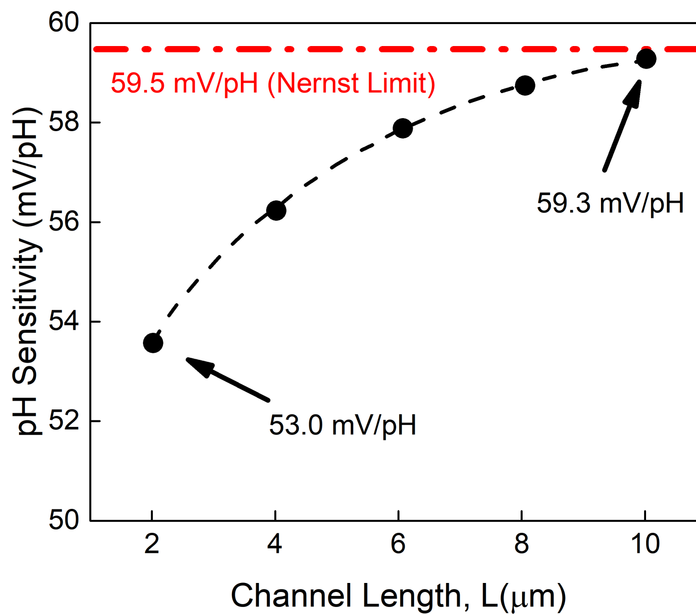

Figure 6.3: pH sensitivity as a function of channel length.

the pH-sensitive surface decreases, and consequently the number of measurable H+ ions in the aqueous solution decreases. According to equation 2.1, the current I_{ds} increases with decreasing length, which leads to a decrease in the resistance of the current channel at constant voltage, V_{DS} . As the resistance of the channel R_{ch} decreases, its modulation is hampered under the influence of the H^+ ions, hence, the pH sensitivity decreases.

6.1.2 Simulation of pH Biosensor

pH sensitivity of ideal nanowire FET biosensor has also been confirmed by the simulation in Sentaurus TCAD software. The model has been adapted from [224] and implemented in 3D (figure 6.4(a)). It should be mentioned that solution has been implemented as a custom material derived from semiconductor. The permittivity was set to reproduce the behavior of water. To make the semiconductor function as a solution mobility of charge carriers was tuned to reproduce the behavior of ions in the solution. In simulated liquid, electrons and holes describe the mobile ions in the solution. The major parameters which bring the similarity between the solution and intrinsic semiconductor are the semiconductor state densities, N_C and N_V, in conduction and valence bands, correspondingly. The values can be described as molar concentrations of ionic content of the solution. It is known that water can be represented as an equilibrium of ions as $2H_2O \rightarrow H_3O^+ + OH^-$. The concentrations of $[H_3O^+]$ and $[OH^-]$ determine the pH of the solution and can be represented as concentrations of holes and electrons in the simulated liquids. Taking into account that concentrations of electrons and holes can be approximated by the Boltzmann distribution:

$$n \approx N_C e^{-\dfrac{E_C - E_F}{kT}} \tag{6.3}$$

$$p \approx N_V e^{-\dfrac{E_F - E_V}{kT}} \tag{6.4}$$

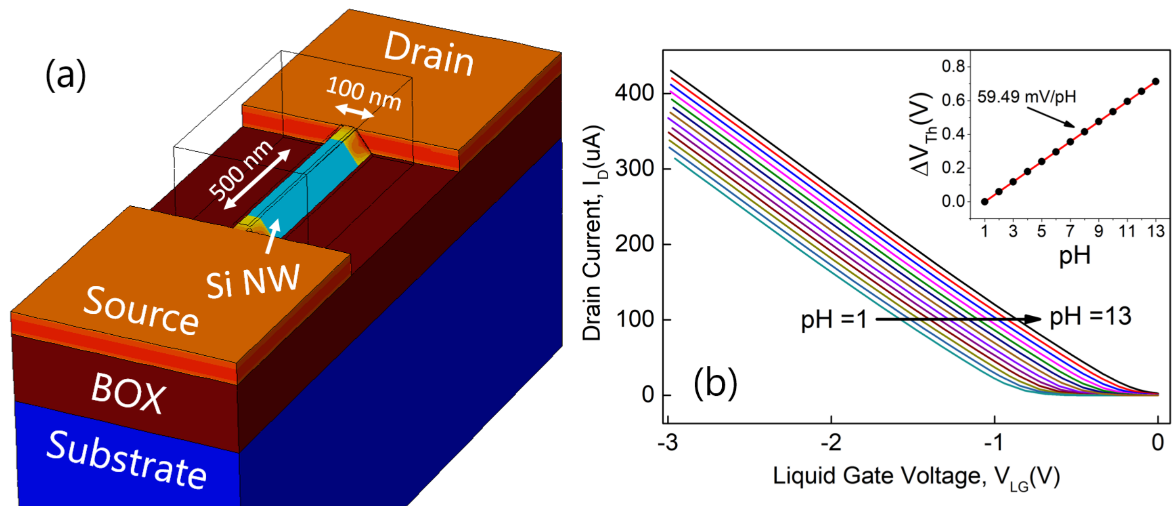

Figure 6.4: (a) Simulated silicon nanowire device. The liquid gate is shown as a frame on top of the nanowire. (b) Transfer curves simulated for different pH values. The inset shown the threshold voltage shift due to different pH of the simulated solutions. The sensor demonstrate the ultimate sensitivity at the Nernst limit of 59.5 mV pH^{-1}

Considering the relations between concentrations of electrons and holes,

$$np = N_C N_V e^{-\frac{E_G}{kT}} \tag{6.5}$$

different pH solutions can be simulated by calculating the densities of states, considering the Avogadro constant $N_A = 6.022 \times 10^{23}\ mol^{-1}$. Simulated transfer curves corresponding to the different pH of the solutions are plotted in figure 6.4(b). The results were obtained for $p^+ - p - p^+$ FET structure with 500 nm long and 100 nm wide nanowire. The increase of pH resulted in the shift of threshold voltage towards lower values, which was also confirmed by the experiment. The sensitivity was estimated as 59.49 mV pH^{-1} which is at Nernst limit. The model describes well the behavior of liquid-gate FETs. However, it should be mentioned that the model does not take into account surface effects and concentrations of charge states at the liquid-solid interface, and therefore demonstrate high sensitivity despite the relatively small area of the nanowire. The model can be further optimized for investigation of the impact of different molecules on the nanowire channel.

6.2 Single Trap Phenomena for Enhanced Biosensing

While the traditional biosensing approach of FET threshold voltage shift suffers from the Nernst limit novel approaches can be employed to struggle for better sensitivities and dynamic ranges. Here we consider two-level random telegraph signal noise fluctuations originating from the single trap at the interface with the nanowire channel as a process highly sensitive the the changes of surface potential. Indeed the impact of the gate voltage change on the dynamics of the trap can be extremely strong as it was shown in section 4.6. We investigated silicon nanowire FET with length of 100 nm and width of 100 nm where two-level random telegraph signal (RTS) fluctations was recorded and performed experiment with different pH solutions starting from pH = 3 to 7. The corresponding timetraces are shown in figure 6.5(a). Histograms recalculated for each timetrace are plotted in figure 6.5(b). On the histograms for each pH value it is possible to distinguish two gaussian peaks corresponding to the stable states of the single trap. Noise spectra demonstrate pronounced generation-recombination (GR) component corresponding

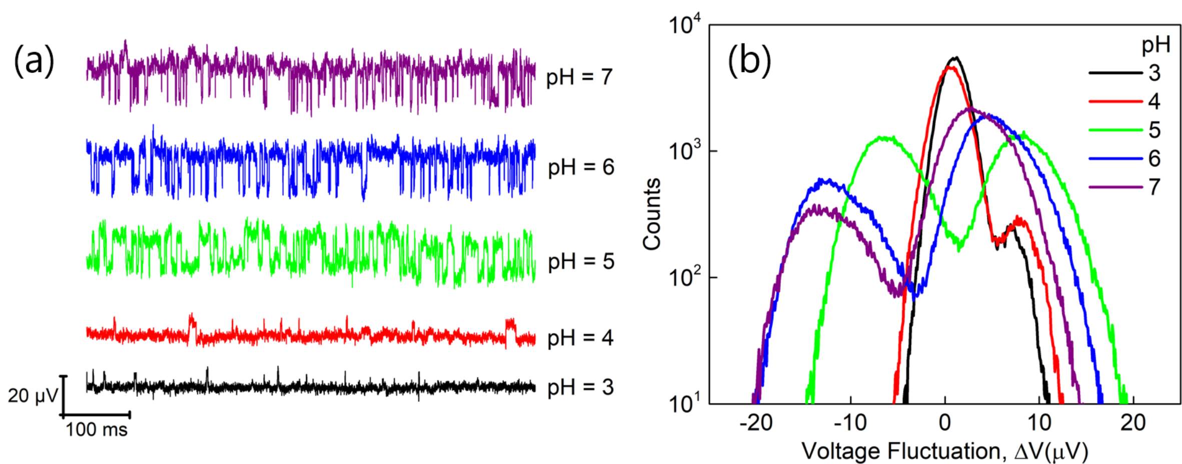

Figure 6.5: (a) Two-level RTS timetraces recorded for different pH values. (b) Histograms recalculated form corresponding timetraces.

to RTS fluctuations of the drain current (figure 6.6(a)). The behavior of the noise amplitude and characteristic Lorentzian frequencies follow typical for RTS noise behavior as it was previously discussed in the section 2.5.6. Characteristic capture and emission times

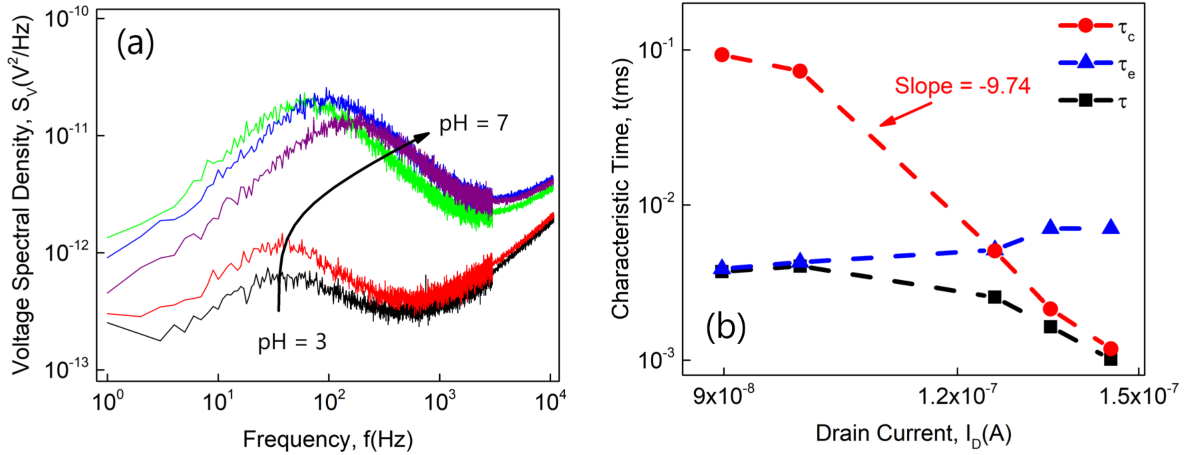

Figure 6.6: (a) Multiplied by frequency measured noise spectra. Pronounced Lorentzian-shape components, represented as peaks, correspond to the RTS fluctuations. (b) Dependencies of characteristic GR time, τ, capture time, τ_c, and emission time,τ_e, on the drain current. The capture time demonstrate a strong dependence with the slope of -9.74, indicating the enhanced sensitivity.

for the single trap were extracted using method described in section 2.5.6 using noise spectra and histograms of timetraces. The dependence of capture and emission times are plotted versus drain current in figure 6.6(b). It should be mentioned that in frame of the standard Shockley-Read-Hall (SRH) model the trap capture time dependence on current behaves as $\tau_c \propto I_D^{-1}$. In our case the capture time demonstrate extremely high slope indicating that $\tau_c \propto I_D^{-9.74}$, which is far beyond the standard SRH model. The fact shows that single trap phenomena is extremely sensitive to the surface potential changes. Capture and emission times are plotted depending on the pH of the solution in figure 6.7(a).

Using data presented in figures 6.6 and 6.7, we can recalculate the relative current shift as I_D/I_D^{max} and capture time change as τ_c/τ_c^{min}. Values of the relative sensor response of channel current and capture time are plotted versus pH in figure 6.7(b). The response curves compare the sensitivity of two approaches, including current and capture time changes. It should be noted that for pH = 3 the relative change of drain current is around 1.6, while for capture time the gain is 78 which is 48.5 times larger. The capture time curve demonstrate much stronger dependence on the pH of the solution in comparison to the current change. The enhanced behavior can be explained by the high slope of the capture time dependence on the surface potential. In this respect the trapping/detrapping dynamics of a single trap appears as a useful signal which is promising for enhanced biosensing. Furthermore a single trap phenomena has a huge potential to become a smallest ever sensor.

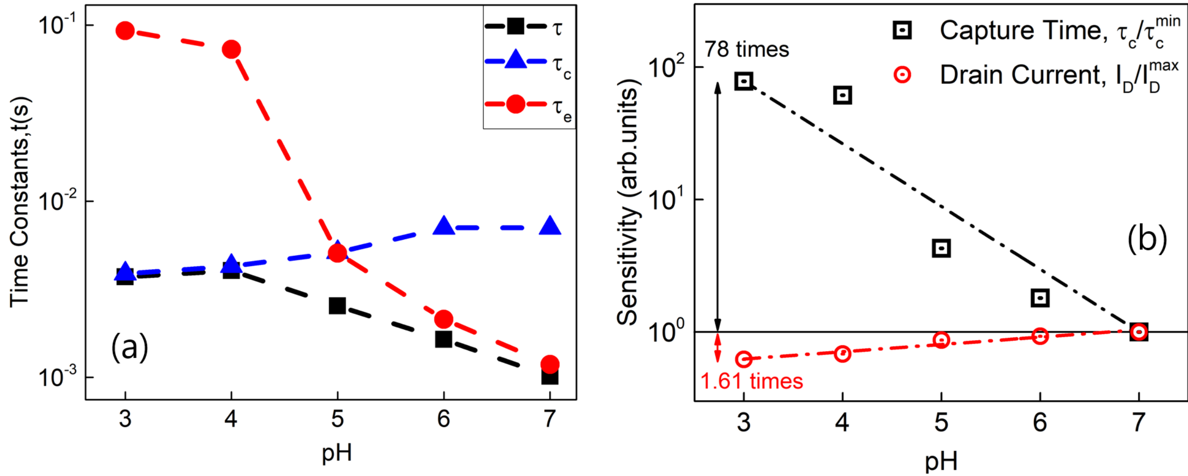

Figure 6.7: (a) Dependencies of characteristic GR time, τ, capture time, τ_c, and emission time,τ_e, on pH of the solution. (b)Sensitivity extracted from the pH dependence of the drain current and RTS capture time constant.

6.3 Cardiac Troponin Detection

Cardiac Troponin I(cTnI) has become a gold standard for detection of myocardial necrosis because of high cardio-specificity, fast release time and high elevation level[225, 226]. In present studies we used liquid-gated silicon nanowire FETs as a label-free biosensors. Drain and source contacts were highly implanted with arsenic dopants resulting in $n^+ - p - n^+$ structure. We demonstrate that not only the channel current can be used as an indication of target molecule binding event but also noise spectroscopy, being an excellent tool for biosensor performance characterization, is a promising analytical method for electrical sensing of target biomolecules. We demonstrate that Si NW FETs can be considered as reusable transducers, allowing multiple cTnI detection cycles, resulting in a possibly more cost-efficient point of care solution enabling the most effective medical treatment of cardiac injury. The proposed method involving excess noise analysis allows to calculate the density of cTnI molecules, causing fluctuation while binding to the NW FET surface. An analysis of the noise spectra and input-referred noise behavior indicates that additional noise reflecting changes in dynamic process is related to the binding of target molecules with increased effective gate voltage. To perform the troponin detection experiment silicon nanowires were functionalized with monoclonal cTnI antibodies using the protocol described in section 3.4, providing specific antibody-antigen detection principle.

Si NW FETs with modified surface were used for the sensing experiment to detect various concentrations of troponin I (TnI) antigens in 1 mM phosphate-buffered saline (PBS) solution with pH = 7.4 ($\lambda_D \approx 7.6\,\mathrm{nm}$). Transfer curves for Si nanowires with modified surface in buffer solution as well as curves corresponding to the addition of certain TnI antigen concentration are plotted in the figure 6.8.

The transfer curve measured before the injection of cTnI antigen molecules was used as a baseline (black curve in figure 6.8)(a).

After introducing a buffer of $\sim 20pM$ cTnI (about $0.5\,\mathrm{ng\,ml^{-1}}$), the change in the I_D–V_{LG} characteristic was observed (red curve in 6.8)(a) — a threshold voltage shift in the positive voltage direction.

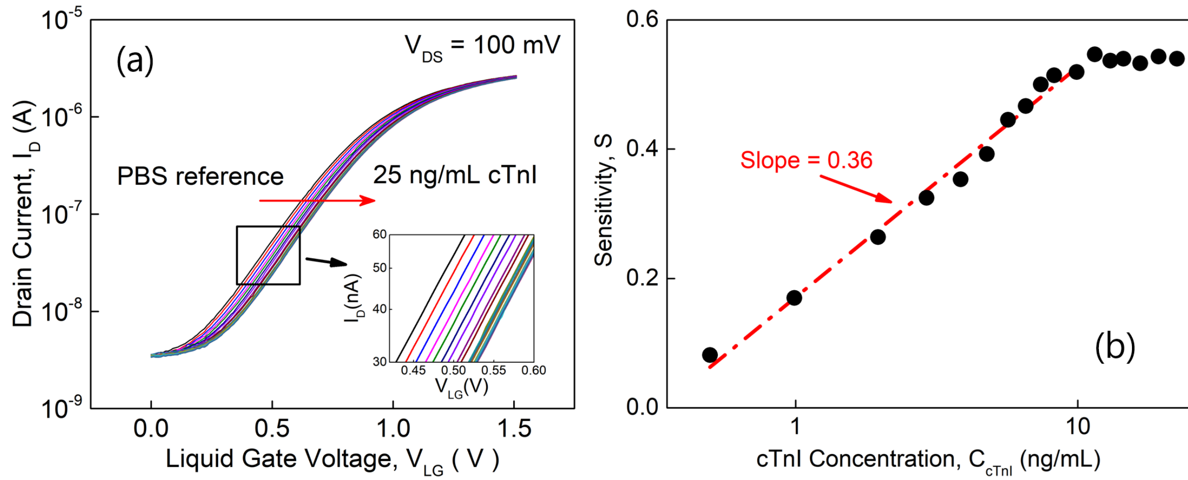

Figure 6.8: (a) Transfer characteristics of the functionalized Si NW FET biosensor for various cTnI concentrations in 1 mM PBS solution. (b) Average sensitivity versus logarithm of cTnI for the values of $I_{D_0} = 100\,\text{nA}$. The dash-dot line reflects the calibration curve to show the linear-log behavior of device sensitivity.

The device response, i.e. the transistor transfer curve, was measured after a time period of about two minutes to achieve stable sensor output and an equilibrium state after introducing analyte molecules into the buffer solution. The isoelectric point(pI) of cTnI molecules is around 5.2, which means that they carry negative charge in physiological solutions with pH=7.4.

Therefore the binding of negatively charged troponin molecules onto the surface of n-type Si NW FET results in the depletion of the conducting channel due to the gate effect, leading to an increase of threshold voltage. It should be noted that the result obtained is consistent with the results reported in the literature [227].

With further increasing of troponin concentration, pronounced shifts of transfer curves were observed upon sequential protein injections reflecting the concentration-dependent binding behavior. As it follows from figure 6.8)(a) transfer curves remained at the same position after the injection of a certain troponin concentration ($\sim 10\,\text{ng}\,\text{ml}^{-1}$). The fact indicates on the sensor surface saturation where no more molecules can be attached to the sensor. The sensitivity of the Si NW device is defined as the normalized current change after the binding event of the target molecules:

$$S = \frac{\mid I_D - I_{D0} \mid}{I_{D0}} \tag{6.6}$$

,where I_{D0} and I_D are the drain current of the functionalized transistor before and after binding of the biomolecules. It is plotted in figure 6.8(b) as a function of the log cTnI antigen concentration.

The surface potential of Si NW FET biosensors depends on the charge of biomolecules next to the surface. Because of field effect molecules influence on the threshold voltage of the device accordingly to the number of attached molecules. When all antibodies are occupied by antigen molecules the number of charges on the surface is not increasing anymore, thus resulting in no further transfer curve shift corresponding to the saturation in figure 6.8)(b). Vertical error bars in the figure represent statistical error obtained using least square root method while analyzing obtained experimental points for the entire

concentration range.

The sensor demonstrates logarithmic response upon injection of a small concentration of target molecules and saturates at higher concentrations, when no free binding sites left on the nanowire surface. The calibration curve can be extracted by a linear fit on the semilogarithmic scale as $S = 0.36log\,[C_{cTnI}] + 0.17$. It should be noted that a logarithmic response of a Si NW FET-based sensor for the detection of cTnI antigen molecules is observed for a wide concentration range and covers the elevated concentration range of troponin release during the development of acute myocardial infarction (AMI).

Thus, during the biosensing experiment, the cTnI antigens binding with appropriate monoclonal antibodies on the silicon nanowire surface resulted in an I_D–V_{LG} characteristic shift to a higher voltage with $\Delta V_T = 100\,\mathrm{mV}$ in total.

6.3.1 Sensor Reusability

A variety of methods for target molecule detection has been established over decades of extensive research in biosensor industry. One of the major challenges remaining is the development of cost-efficient system with high enough sensitivity and time resolution, which is affordable for everyday usage. An effective way to overcome the problem is to use biosensor multiple times. It has been demonstrated in the literature [228, 229] that reusability of Si NW FET-based biosensors can be achieved by reversible association– dissociation between glutathione (GSH) and glutathione S-transferase (GST). The dissociation of the GSH-GST complex on the surface of Si NW FETs makes the sensor reusable. However, the increased ($\sim$ 6 nm) GSH-GST molecule chain considerably decreases the sensitivity of the device due to the screening effect[227, 230]. In the work of Chiang [231] it was demonstrated that reversible functionalization can be performed using a cleavable disulfide bond between the receptor and Si NW FET surface. The approach had been demonstrated for H_5N_2 avian influenza virus proving the possibility for reusable sensors. A drawback is obviously the requirement for re-immobilization of antibodies onto the surface of biosensor. This does not guarantee the initial state of the sensor and thus requires additional calibration of the device before the measurement.

To develop a reusable biosensor several issues should be addressed. Firstly, the solution for the surface regeneration should be non-destructive and favor to the biosensor surface, gate dielectric, in the case of Si NW FET-based device, as well as the recognition layer, immobilized antibodies. Secondly, in the case of antigen-antibody approach, the complex has to be completely dissociated during regeneration process. Based on these considerations, glycine-HCl buffer was chosen in the studies of cardiac troponin as the optimal regeneration reagent for renewal of the functionalized surface of the sensors. We demonstrate for the first time for cTnI antigen that applying glycine amino acid solution after detection of cTnI target molecules allows the receptor-analyte complex to dissociate and restore the initial sensor state.

The mild regeneration solution contained 10mM glycine diluted in 1 mM PBS solution. The pH was adjusted to pH = 4.0 with 1%-HCl. In such an environment, glycine molecules at the isoelectric point (pI) of 5.97 carry a positive charge. The isoelectric point(pI) of cTnI is around 5.2 which means that antigen molecules are positively charged at pH =4.0. The addition of glycine buffer with low pH results in a change of attractive van der Waals and electrostatic (Coulombic) forces into repulsive which make the antigen-antibody complex to separate. In this case, the proteins unfold leading to a dissociating effect between antigen and antibody molecules. The glycine-HCl buffer with pH = 4.0 also

satisfies the requirement for the reversible biosensors since the solution is not harmful for the biosensor surface and does not cause any irreversible changes, but assists the decrease of bonding strength thus supporting the natural activity of the immobilized antibodies. It should be mentioned that glycine-HCl buffer has not yet been reported as a regeneration solution for cTnI biosensor based on Si NW FETs. After the sensing experiment, the analyte solution was replaced by regeneration buffer and incubated for 10 min at room temperature allowing the cTnI antigen-antibody complex to dissociate (figure 6.9).

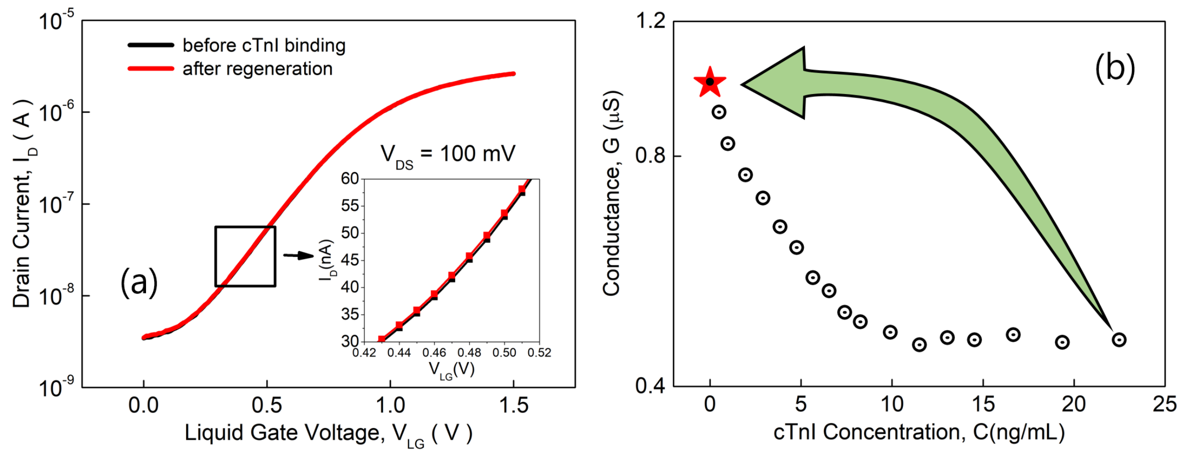

Figure 6.9: (a) Transfer curves before binding of troponin molecules and after application of glycine regeneration solution. (b) Conductance decreases as a function of cTnI concentration for the values of $I_{D_0} = 100\,\text{nA}$. The conductance returns to the same level after applying glycine-HCl buffer.

Device was rinsed with deionized water after the regeneration procedure with low pH glycine buffer. Afterwards transfer curve was measured again under the same conditions to compare with the initial curve. As it is shown in the figure 6.9(a) the curve returned to the initial state indicating on the successful device regereration process and biosensor stability.

It is noteworthy that the leakage current through the front-gate dielectric layer when measured in a liquid environment remained negligibly small (below 10 pA). It should also be emphasized that the conductance of the Si NW FET returned to the original level after removing the antigen (see figure 6.9(b))

6.3.2 Noise Spectroscopy for Biomolecular Detection

Usually, a noise of nanoscale FETs originates from the interactions occurring inside the conducting channel and provides useful information about internal processes and allows to study the device performance in a non-destructive manner [132, 232]. There are, however, other noise sources when considering transistor operation in a liquid environment, as a part of the biosensing system. In such a configuration, additional excess noise is a result of charge exchange reactions at the interface between electrolyte solution and insulator. This is particularly relevant when target biomolecules attach to immobilized on the surface receptor molecules. Fluctuations caused by such a process might significantly contribute to the overall device noise.

Typical normalized noise power spectra of liquid-gate Si NW FET measured in 1 mM phosphate buffered saline (pH = 7.4) before and after binding of cardiac troponin molecules are presented in figure 6.10(a). Noise spectra were measured under the same conditions for both cases in order to compare the noise-generating mechanisms. Applied drain-source voltage of 100 mV insured the operation of the device in a linear regime. The back gate contact was grounded.

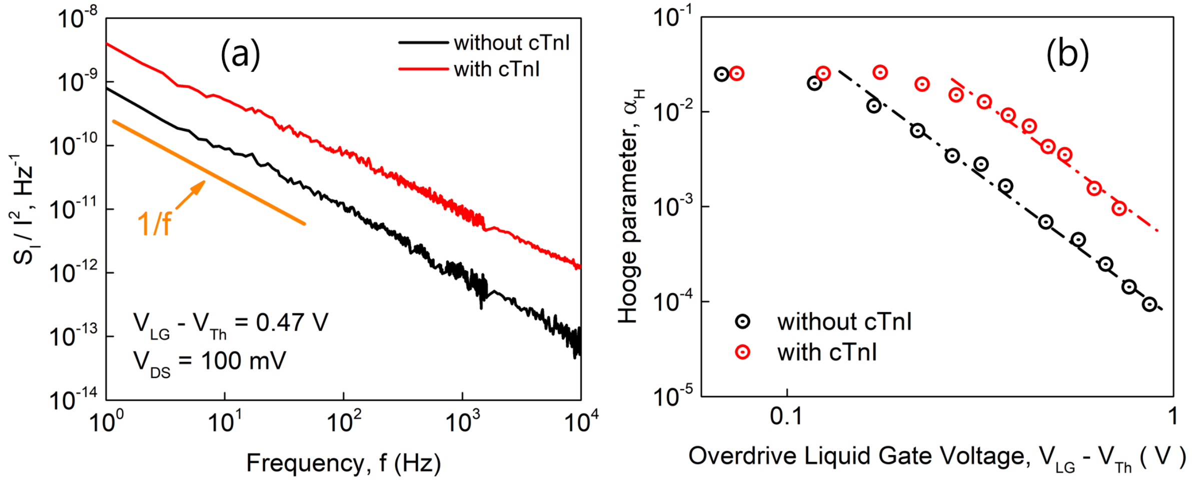

Figure 6.10: (a) Typical noise spectra measured for the liquid-gated Si NW FET at a drain bias of 0.1 V and overdrive gate voltage of 0.47 V before and after cTnI binding. (b) Dimensionless Hooge parameter α_H obtained from 1/f noise spectra for solutions with and without troponin molecules as a function of the overdrive liquid gate voltage (V_{LG} -V_{th}) for the same Si NW FET biased at $V_{DS} = 100$ mV. The lines are guides for the eye.

Noise spectra demonstrate a dominant flicker noise behavior at low frequencies in cases both with troponin molecules and without. The noise amplitude is, however, almost one order of magnitude larger after cardiac troponin molecule binding (figure 6.10(a)), which is in a good agreement with literature [233]. The origin of such noise increase still has to be discussed.

Hooge parameter, α_H , the dimensionless parameter is known as an indicator of sample "noisiness" for systems exhibiting 1/f noise behavior[234, 235]. We demonstrate that α_H reaches the values of 10^{-4} indicating on a good quality of fabricated structures [236]. Meanwhile we demonstrate Hooge's parameter increase almost one order of magnitude at overdrive liquid gate voltage greater than 0.3 V when troponin molecules are present in the solution (figure 6.10(b)). To understand the impact of molecular binding on the noise level the molecular interaction in antibody-antigen complex should be considered as well as the surface coverage with target molecules. Debye screening length plays a crucial role determining the distance from the surface where the charge of target molecule will influence on the surface without screening by counter ions. In turn the charge brought by the target molecule redistributes over the receptor-biomolecule complex and influences on the surface potential. The impact of single molecule on the surface potential can be estimated by considering it as a point charge. Taking into account that molecule is bound to the SiO_2 dielectric surface in low-molar PBS solution with permittivity about 80 surface dipole potential of the liquid and thus threshold voltage shift can be calculated by solving Maxwell's equation: $div\vec{D} = 4\pi\rho$, where ρ is the charge introduced by the target molecule, $\vec{D}$ is the electric flux density defined as $\vec{D} = \varepsilon\vec{E}$, $\vec{E}$ is the electric field $\vec{E} = -\nabla\phi$. By solv-

ing linear partial differential equations numerically using Chebyshev method the maximal shift of FET biosensor threshold voltage was estimated to be 0.6 mV C^{-1}. Considering the fact that threshold voltage shift is caused by the layer of uniformly distributed over the nanowire surface charged biomolecules with the spacing around 7.6 nm, corresponding to Debye length, where molecules do not interact with each other and are considered as point charges, the density of bound molecules can be estimated as $n_m = 4.3 \times 10^5\ \mu m^{-2}$. On the other hand taking into account threshold voltage shift caused by the saturated layer of troponin molecules($\Delta V_T = 100$ mV) the density of antigen-bounded molecules equals to $n_m = 7.2 \times 10^7\ \mu m^{-2}$.

Now noise level can be analyzed with the knowledge about the troponin molecule concentration and compare the case with molecules and without. Normalized drain current noise, fS_{I_D}/I_D^2, at 30 Hz against $(g_m/I_D)^2$ is shown in figure 6.11(a), where g_m is the transconductance.

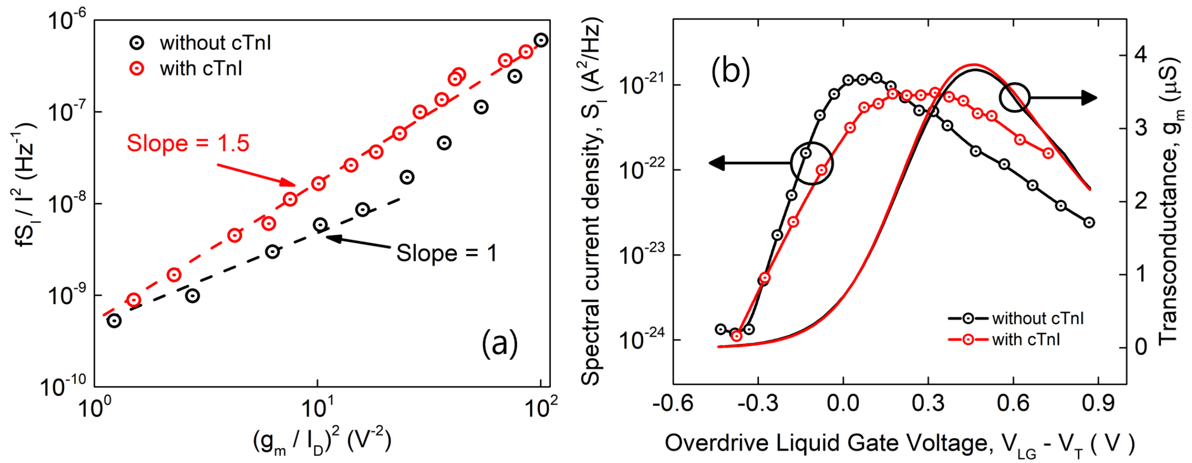

Figure 6.11: (a) The normalized drain current noise of the same transistor extracted at f = 30 Hz as a function of $(g_m/I_D)^2$. (b) On the left axis, the drain current noise amplitude extracted at f = 30 Hz as a function of overdrive liquid-gate volatage. On the right axis, the transconductance of the Si NW FETFET extracted from the transfer curves before and after binding of cTnI molecules.

Typically the slope of such curve equals to 1 and indicates on the linear operation regime of FET device according to the number fluctuation noise model[98, 114]. According to the model current fluctuations are caused by the interaction of charge carriers in the conductive channel with the traps in gate dielectric through the trapping/detrapping process. In the case with negatively charged cTnI molecules the slope considerably differs from 1 and equals 1.5. The fact indicates on different origins of noise in liquid environment with troponin molecules. The current noise power spectra with and without troponin molecules are shown in figure 6.11(b) as a function of overdrive gate voltage. Obviously the noise behavior differs considerably for the case with and without troponin molecules while the transconductance remains almost the same. This suggests that noise characteristics are highly sensitive to troponin molecules and dynamic binding processes happening next to the surface of the biosensor.

The input referred noise (figure 6.12) recalculated from noise spectra is independent on the overdrive gate voltage at $V_{LG} - V_T > 0.3$ V for the case without troponin molecules. This confirms the applicability of carrier number fluctuation model. On the contrary the

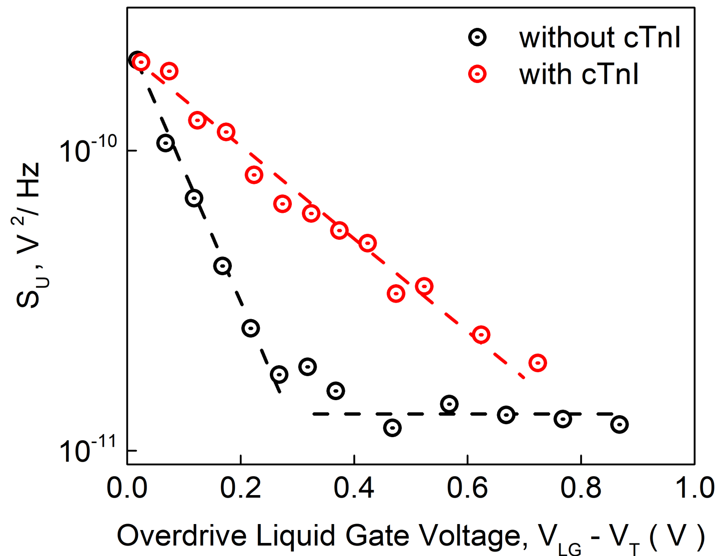

Figure 6.12: The equivalent input noise SU of the Si NW FET at different liquid gate voltages V_{LG} in 1 mM PBS solution before and after binding of troponin molecules. The lines are guides for the eye.

presence of troponin molecules causes substantial increase of the input-referred noise. The deviation from expected by the McWhorter model [98] is not caused by the changes in gate dielectric but is related to the dynamic processes from the liquid side where ions are moving through the membrane formed by cTnI molecules attached to the antibodies on the surface of biosensor. According to Donnan's theory [237, 238] the detection in antibody-antigen system is possible by considering that antibodies form a membrane on the dielectric layer. The opacity of such membranes varies considerably with the target molecule concentration. Increased input-referred noise in the case with troponin molecules can be explained in terms of aforementioned membrane formed by the antibodies. The membrane prevents a part of ions present in the solution from penetrating throught the membrane to the surface of biosensor. Attached troponin antigens influence on the flow of small ions resulting in measurable current fluctuations in the channel of the transistor. Increased amplitude and behavior of input referred noise for solutions with troponin molecules of our biosensor provide evidence for the ion kinetic change as a result of troponin molecules attachment responsible for perturbation of a membrane. Furthermore we demonstrate that the noise level slightly depends on the ion concentration in the solution [238], which also proves that excess noise originates from attached troponin molecules. It should be emphasized that input-referred noise in case with troponin molecules decreases when increasing effective gate voltage. The fact indicates that the flow of the ions through the membrane can be effectively controlled by applied liquid gate voltage. This means that troponin binding to the antibody causes not only a surface potential change but also influences on ion kinetics at the interface between membrane and solution. And this process can be tuned by liquid-gate voltage. Withal we demonstrate that noise spectroscopy characteristics allow analyzing of dynamic processes in biomolecular solutions. The results open prospects for studies of the molecular dynamic and interaction processes taking place in the liquid gate in terms of sensor response to antibody-antigen binding events. Our results demonstrate high sensitivity of noise characteristics to bio-chemical reactions taking place in biosensors.

6.4 Nanostructures for the Detection of Ascorbate and Gluthathione Solutions

Reactive oxygen species (ROS), reactive molecules containing oxygen, are found essential for the aerobic organisms. The molecules are produced as a result of numerous reduction-oxidation reactions as well as cellular signaling in both developmental and stress responses. The imbalance of the ROS level, caused by the oxidative stress, makes system to detoxify and repair injured cells[239, 240]. The processes causing the instability of the internal cellular conditions with consequent release of ROS species are known to play the crucial role in aging processes. Furthermore the increased levels of ROS contribute to the development of a various diseases including cancer, diabetes, cardiovascular and neurodegenerative diseases, including Alzheimer's and Parkinson's [241–243]. In this respect any cellular dysfunctions can be recognized by the elevated ROS levels. On the other hand the regulatory pathways activate when stress conditions appear. In this case antioxidants arise to reduce and compensate the oxidative stress and bring the system to balanced state. Therefore activation of regulatory system and increase of antioxidant concentrations indicate on increased ROS generation and thus on the existence of the oxidative stress. The understanding of the ROS dynamics and oxidative stress conditions plays a crutial role in cellular signaling and exchange processes. Among a variety of components, sodium ascorbate and gluthathione are known as a central items in ROS regulation system in cells [244, 245]. Sodium ascorbate is an antioxidant appearing as a result of aerobic metabolism. It neutralizes the toxic effect of superoxide, singlet oxygen, ozone and hydrogen peroxide by reacting with them through sodium ascorbate peroxidase. Gluthathione is a redoxactive molecule which plays important role in detoxification, antioxidant biochemistry and biosynthetic pathways. Both molecules participate in oxidation-reduction balance and play important role in regulation of cellular reactions on various diseases. Therefore it is important to develop a highly sensitive real-time detection method of such species playing role in ROS reactions. In our studies we used $p^+ - p - p^+$ silicon nanowire FETs to detect L(+)-ascorbic acid sodium salt with molecular weight of 198.11 and gluthathione with molecular weight of 307.32 from aqueous solutions. Different concentrations were prepared by the dilution of ascorbate and gluthathione in deionized water. Microfluidic

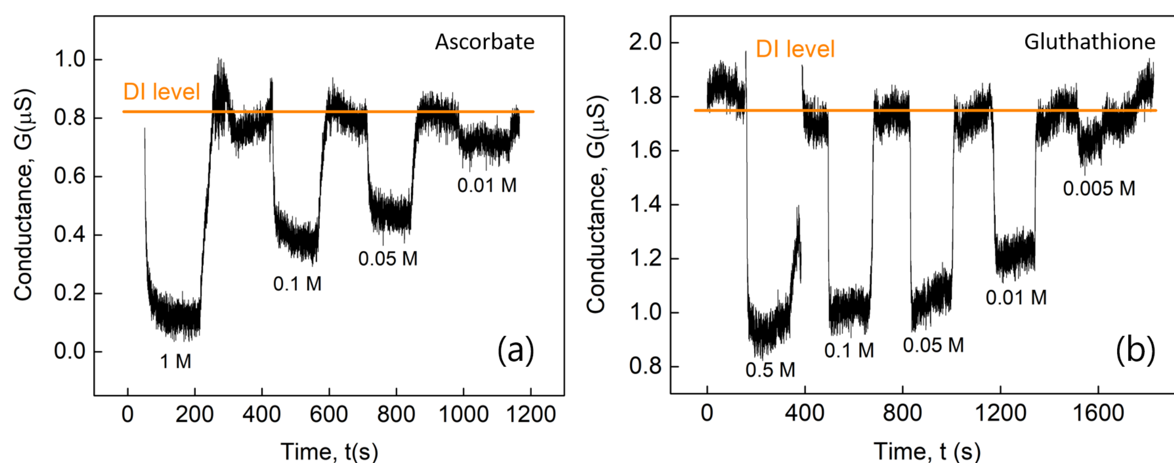

Figure 6.13: Silicon nanowire FET conductance changes in time caused by flushing different concentrations of (a)ascorbate (b) gluthathione.

system was employed to apply different concentrations to the nanowires. Typical response from nanowires are shown in the figure 6.13 as conductance change in time.

It should be mentioned that no specific functionalization has been performed prior to the detection of molecules. However we can assume that the changes of nanowire conductivity is the result of molecule concentration influence as no other components were present in the solution mixture. After each concentration nanowires were washed with deionized water thus bringing the conductivity to the initial level. It should be emphasized that conductivity decreased in experiments for both ascorbate and gluthathione molecules. This indicates that molecules bring positive charge to the surface, resulting in threshold voltage increase.

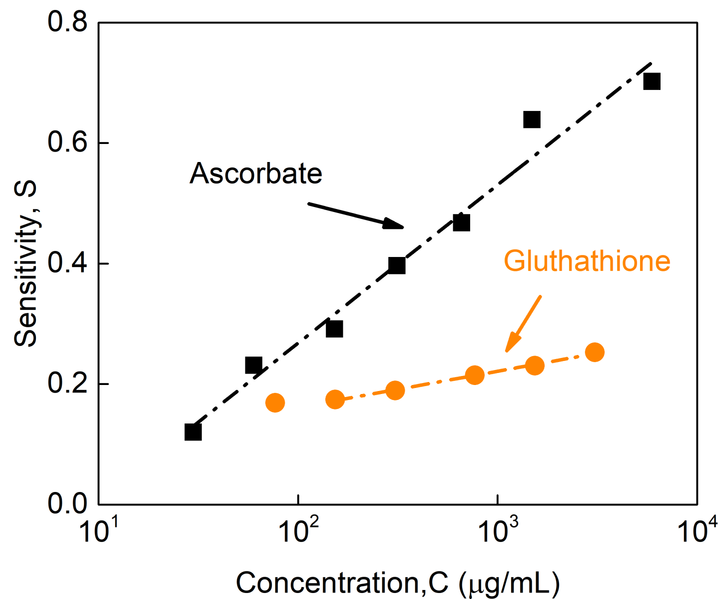

Figure 6.14: Sensitivity extracted from transfer curves for ascorbate(black squares) and gluthathione(orange circles).

The relative changes of conductance under the influence of ascorbate and gluthathione are shown in figure 6.14. Sensors demonstrate higher sensitivity to ascorbate molecules in comparison to gluthathion. The results correlate with the difference in molecular weight. Therefore such difference can be employed for classification of different species in the liquid after calibrations with sufficient amount of liquids. To summarize, the low-molecular-weight antioxidants, sodium ascorbate and gluthathione dissolved in deionized water, were investigated. The nanowire sensors are highly sensitive to such molecules and can be utilized for studying the processes of biochemical processes involving reactive oxygen species. The sensitivity and selectivity can be optimized by applying chemical treatment to the nanowire surface.

6.5 Silicon NW FET Structures for Analysis of Cellular Activity

Signal recordings from individual electrically active living cells (e.g. cardiomyocytes or neurons) represent the general approach for understanding biological processes in living systems on different levels, from the cell network to the single-cell level. The heart is a

particularly important system to study since it is the engine of the human body, ensuring a continuous flow of blood and providing the organism with oxygen and nutrients. Heartbeat fluctuations may be caused by a variety of factors, among which cardiac dysfunction and cardiac diseases occupy the highest priority for medical treatment and healthcare applications. Despite the current progress in developing recording electrodes for cell activity monitoring [246–248], there is still a huge requirement for devices to allow stable and reproducible in vitro evaluation of the effect of pharmacologically active agents on the tissue. multielectrode array (MEA) chips have attracted much attention in this field and have replaced large-scale electrodes as they are capable of gaining more detailed information [249] than conventional electrodes. Even though high-resolution MEAs have been developed, the SNR is still limited while electrodes are becoming smaller [74, 75]. This creates a number of challenges in terms of achieving cellular and subcellular resolution for recording functional signals.

Silicon (Si)-based devices, on the contrary, fabricated using technology compatible with modern complementary metal-oxide-semiconductor (CMOS) process, possess a lot of advantages due to their unique properties, which have been demonstrated by extensive research over the past few decades. Furthermore, a transition from conventional planar devices to nano-scaled structures such as NWs may improve the sensitivity down to the single molecule level. An enhanced sensitivity of biosensors based on Si NWs was confirmed for a variety of biological test objects, including proteins, nucleic acids, and viruses [65, 76]. The characteristic sizes of such structures allow much denser packaging, resulting in higher spatial resolution. It should be emphasized that recent research on interfacing between living cells and nanoscale objects demonstrates improved interface properties, with a smaller cleft between a cell and nanoscale structure in comparison to large-scale planar devices [4]. Furthermore, the investigation of gate coupling effect in nanowire transistors demonstrate the possibility of enhanced SNR for cellular recordings [77]. Modern drug design and delivery is not possible without fully understanding the drug-related metabolism and reactions as well as its ability to penetrate cells, its interaction with the target, and its pharmacological effect [250, 251]. In particular, heart failure treatment requires a comprehensive and complex investigation of the functional activity of heart tissue. Dysfunction is typically caused by biochemical changes in metabolic processes on the cellular and subcellular level. Such processes are supported by and highly interconnected with the calcium content in cells and the cellular Ca^{2+} stores in mitochondria [252, 253]. The investigation of different aspects of drug delivery and calcium transport monitoring on the cellular and subcellular levels is possible using fluorescence microscopy [250, 251]. A method for simultaneously measuring mitochondria Ca^{2+} uptake and mitochondria membrane potential in living cells using fluorescent dyes is described in [254]. However, studies of noradrenaline (NorA) influence on cell activity using this method in combination with Si NW FET sensors have not yet been reported. In this work, we combine in vitro monitoring of cardiomyocyte cell culture action potential (AP) activity using Si NW FETs with fluorescence microscopy to develop a bio-platform that enables us to reveal the effect of pharmacologically active agents on the living cell community by tracking the cell calcium content, mitochondrial membrane potential, and cellular electrical spiking activity. We demonstrate the high-quality material and electrical properties of fabricated Si NW FET structures. We show that transistors operate without leakage current in culture media due to multi-stage fabrication process optimization. We applied the novel approach of using Si NW structures as a bio-platform in combination with fluorescence microscopy techniques to monitor the effects of pharmacologically ac-

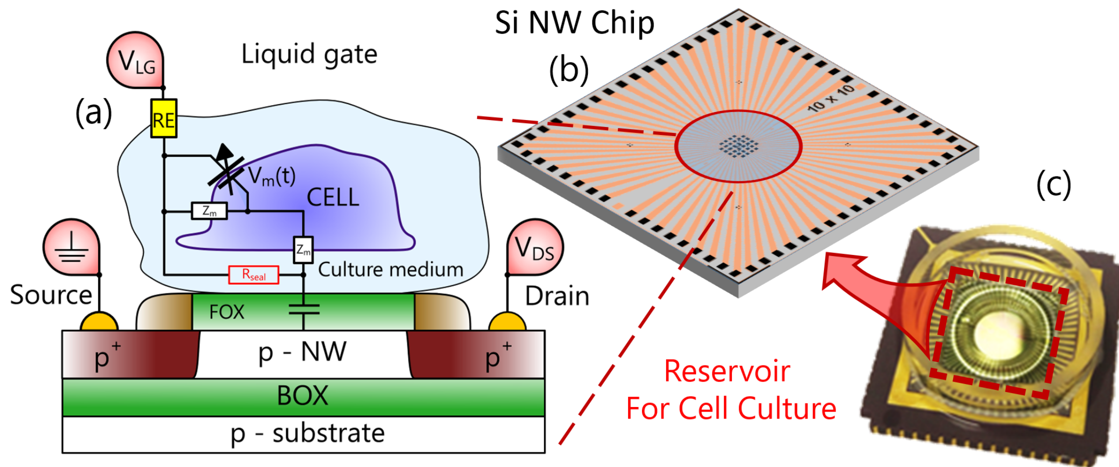

Figure 6.15: (a) Schematic cell-nanowire interface with the measurement configuration for cardiomyocyte electrical activity monitoring using NW FET biosensor. (b) Nanowire chip with a grid layout containing 32 measurement channels. (c) Chip encapsulated within a glass ring and polydimethylsiloxane (PDMS) as a reservoir for the medium and cell culture.

tive agents such as NorA on the functional activity of cells. The results of studies on the pharmacological treatment and electrical activity of HL-1 cells demonstrate that Si NW FETs can be used to investigate and select biologically active solutions to tune and control cardiac activity from the viewpoint of different physiological and pathological conditions of cardiac activity.

6.5.1 Chip Characterization for Cellular Measurements

For the in vitro studies of cellular activity we used silicon nanowire array FETs fabricated using a CMOS-compatible top-down approach described in section 4.2. Schematic representation of electrical activity recording from cardiac cells is shown in figure 6.15. The structures were 20 µm long, and each NW in the array was 150 nm wide with a spacing of 250 nm (see figure 6.16). Source and drain contacts were highly implanted with boron ions, resulting in $p^+ - p - p^+$ type structure. After the fabrication process, wafers were cut into chips, wire-bonded to chip carriers, and subsequently encapsulated with PDMS and glass rings to form a reservoir for cells and culture medium. Liquid-gate voltage was applied to the sample using an Ag/AgCl reference electrode. To measure the confluent cell layer formed on the chip, we used a multichannel measurement setup. The system enables I–V characterization to be performed as well as time-series recordings in parallel from all 32 transistors on the chip [111]. The setup consist of an amplification cascade which includes a pre-amplifier and a main amplifier. For AC-coupled measurements, filters were used to prevent aliasing effects. The amplified signal was then passed to the data acquisition system for readout and further data processing on the computer. The pre-amplifier consists of a corresponding operational amplifier and a Si NW FET on the chip (the “channel”). The resulting amplification depends on the feedback resistance (R_{FB}) connected to the operational amplifier and the actual transconductance of the FET defined by the selected working point: $V_{out} = V_{LG} \times g_m \times R_{FB}$. It should be noted

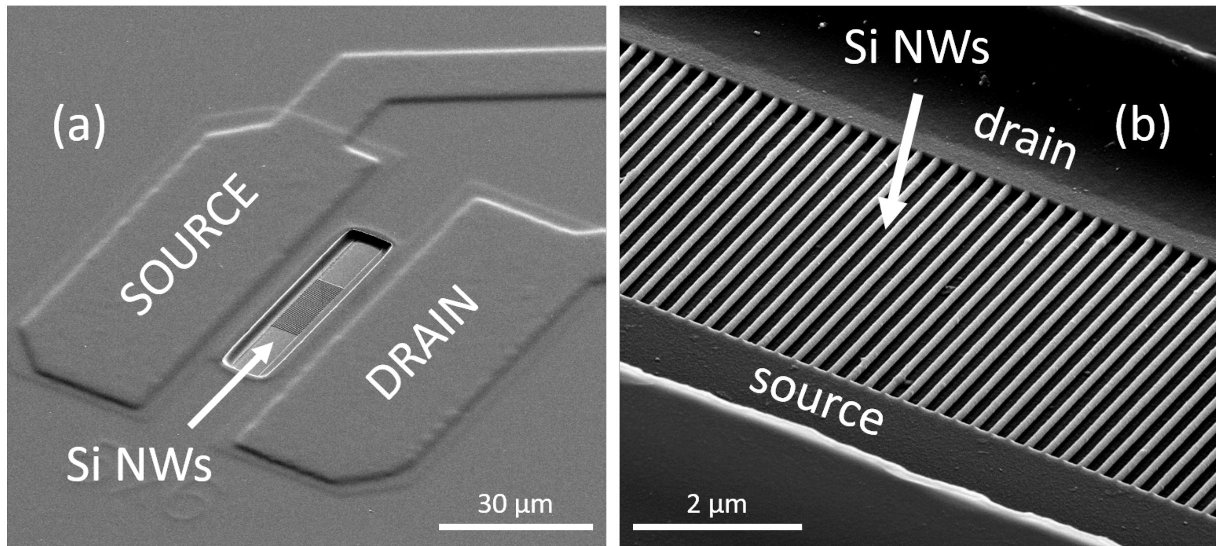

Figure 6.16: (a)SEM image of a Si NW FET biosensor. The entire surface including metal feedlines is covered with polyimide passivation layer while only the active area with nanowires is exposed to cell culture medium. (b) SEM image, enlarged part of active sensing area with nanowire array.

that for optimal signal amplification, R_{FB} corresponds approximately to the FET channel resistance.

In order to select the working point with the highest transconductance for the FETs, I–V characteristics were measured prior to the time trace studies. The measured transfer characteristics, as shown in figure 6.17, demonstrate typical behavior for p-type transistors. Transfer curves were measured in the linear (V_{DS}= -0.1 V) and saturation (V_{DS}= -1.1 V) regimes. The average transconductance curves for both linear and saturation regimes with an average deviation of 12% for different FETs is shown in the inset of figure 6.17(a). In the linear regime with V_{DS}= -0.1 V and V_{LG}= -1.58 V the maximum transconductance obtained was about $(1.88\pm0.23)\mu S$ for our FETs. In the other working point near the saturation regime FETs demonstrated higher transconductance values (figure 6.17(b)), with the maximum equal to $(10.57\pm1.91)\mu S$ at V_{DS}= -1.1 V and V_{LG}= -1.9 V. Optimized values for drain-source, liquid-gate, and back-gate voltages were selected based on re-plotted derivative (dI_{DS}/dV_{LG}) curves. Further reported time series had already been recalculated into the input voltage fluctuations using the equation: $dV_G = dV_{out}/(g_m \times R_{FB})$. A cardiomyocyte HL-1 cell community was cultured on NW FET chips. The confluent layer formed on the Si NW FET was characterized using fluorescence microscopy visualization. The high viability of cells was assessed using calcium-sensitive fluorescent dye Calcein AM and DNA-binding fluorescent dye DAPI. Performed electrical measurements demonstrate stable recordings with high SNR of recorded AP signals. An analysis of the recordings showed the propagation of APs across the cell community with a speed of 13 mm/sec, which is in good agreement with the speeds reported in the literature on MEAs for cardiac cells [255, 256]. Analyzing signal propagation allowed us to estimate the position of pacemaker cells, which provides important information on the functional activity and communications of the entire cell community, as will be shown below.

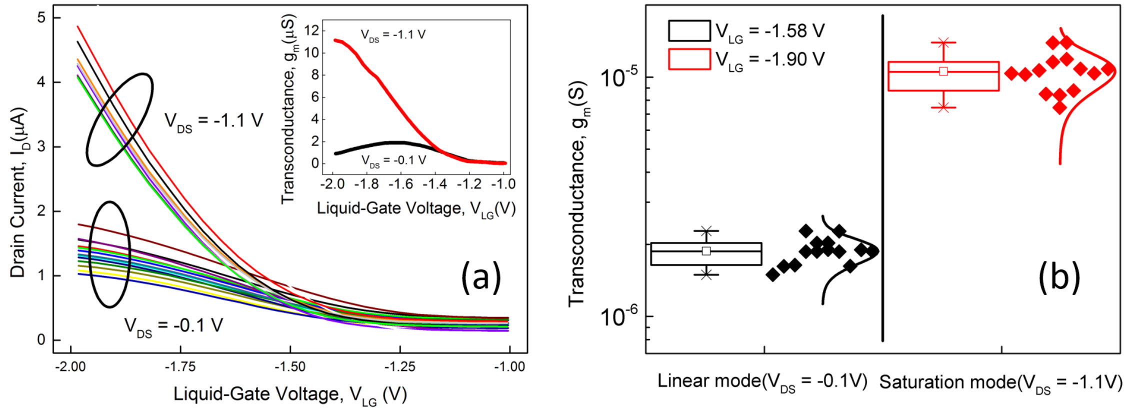

Figure 6.17: (a) Transfer characteristics measured for different FETs at $V_{DS} = -0.1\,\text{V}$ and $V_{DS} = -1.1\,\text{V}$. Inset demonstrates the transconductance averaged for all FETs. (b) The distribution of transconductance values for different FETs. Values demonstrate improved transconductance in saturation mode in comparison to linear mode, which is more favorable for cell activity monitoring.

6.5.2 In Vitro HL-1 Cell Measurement

The recording of extracellular APs from cardiac cells is important for fundamental studies of AP propagation features reflecting cardiomyocyte activity as well as the influence of pharmacological substances on the signal. We applied the fabricated Si NW FETs as a bio-platform to monitor the APs and to evaluate the effects of pharmacological and electrical stimulations on cardiac cell activity. The cardiomyocyte cell community was cultured on the chip for 3–4 days (figure 6.18). This time frame was sufficiently long for the cells to create a dense confluent layer that already demonstrated beating activity. This was supported by the spontaneous generation of APs by the pacemaker cell. Usually, pacemaker cells are the strongest and they set the beating rate for the entire monolayer, providing a stable beating rhythm for the cell community as well as the synchronization between cells [257]. Since the HL-1 cells form a syncytium, the electrical signals propagate geometrically along the tissue. It is therefore important to record not only the electrical activity of cells but also the propagation of the signal across the community. We demonstrate that our NW sensors satisfy these requirements and contain multiple Si NW FETs on the chip. This enabled us to record electrical fluctuation from all 32 FETs simultaneously. Prior to time-dependent measurements, we performed I–V characterization of transistors on the chip (see data of figure 6.17). We recorded time traces at a sampling rate of 1 kHz with the working point set in the linear regime with V_{DS} = -0.1 V and V_{LG} = -1.58 V. The maximum transconductance obtained was about $(1.88 \pm 0.23)\mu S$ for our FETs. We then performed time-series measurements at another working point near the saturation regime. The FETs demonstrated higher transconductance values (figure 6.17), with the maximum equal to $(10.57 \pm 1.91)\mu S$ at V_{DS} = -1.1 V and V_{LG} = -1.9 V. In this working regime, clear APs were recorded with an improved 3-5 times peak-to-peak values of SNR, compared to the low-voltage regime. Typical recorded time trace and APs extracted for the different channels are shown in figure 6.19, where colored lines correspond to the mean value of multiple APs and black background shows the standard deviation of the APs recorded over the entire measurement time. The shape of the signal was in

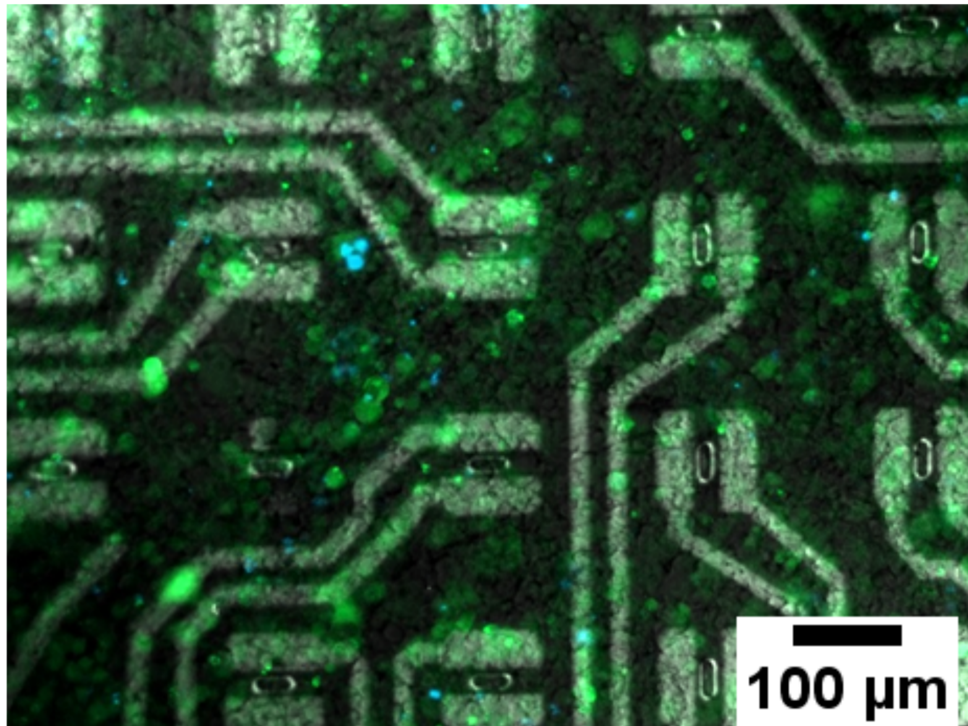

Figure 6.18: Live-dead staining of HL-1 cardiac cells on Si NW chips using green fluorescent Calcein AM dye and blue fluorescent DAPI dye

good agreement with the processes taking place in the cell membrane and corresponded to current flows through ion channels [258]. The beating frequency was about 2–3 Hz.

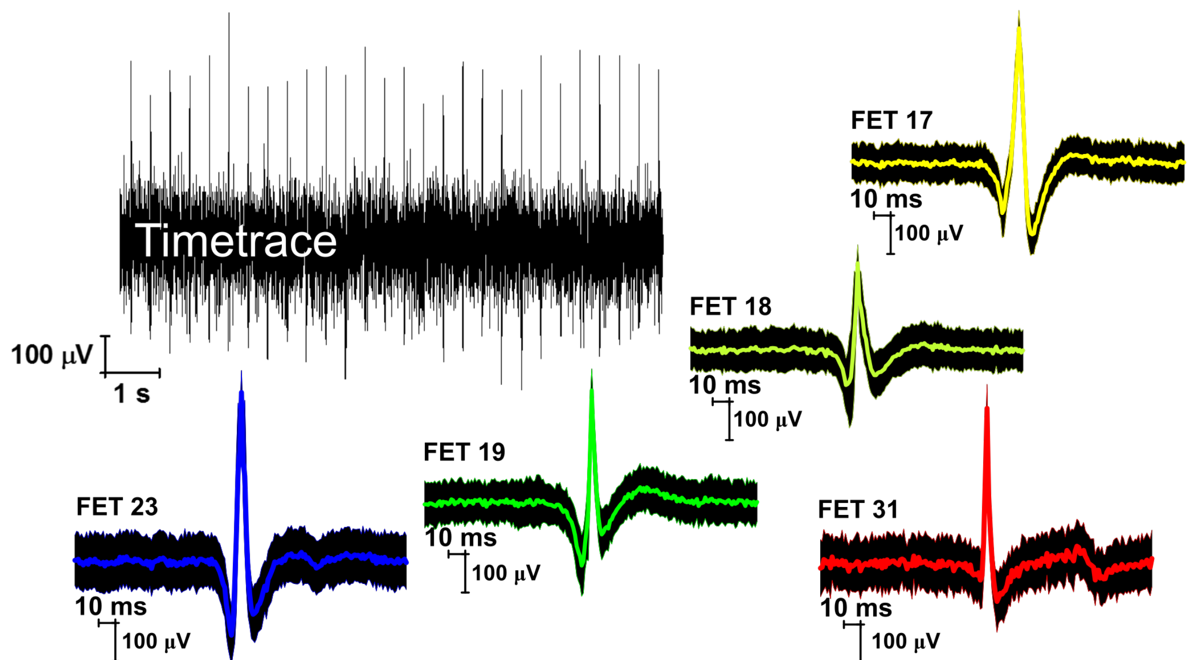

Figure 6.19: Typical recorded timetrace with action potential activity, and extracted action potential shapes for FETs 17,18, 19, 23, 31. Colored line shows averaged values for action potentials found in the time trace, while the black background shows the standard deviation.

High peak-to-peak SNR values ranging from 3 to 5 were obtained. In general, noise may be caused by several factors [132], including the quality of cell–chip coupling, sealing resistance, and junction resistance, which may also influence the transconductance of the FET itself. AP propagation across the tissue was also registered using spatially separated FETs. For the studies of signal propagation in 1D along the single line of transistors and 2D over the surface of the chip we employed linear and grid chip layouts correspondingly. Timetraces measured for the linear chip layout are shown in the figure 6.20, sorted correspondingly to the peak appearance delay. From measured data we recalculated the time delay of pulses for the FET channels and plotted it as a function of the transistor position in the Y direction (figure 6.21). Time delays for seven of the transistors fitted with linear dependence, demonstrating signal propagation without distortion. Extracted AP propagation speed in the Y direction was calculated to be 13 mm/sec, which is in good agreement with the values obtained for MEA sensors [255, 256]. As shown in figure 6.21(b), one of the transistors reflected signal propagation in the opposite direction to that previously discussed. Indeed, a single pacemaker cell in the cell network caused excitation of the whole network. We estimated the position of this pacemaker cell by plotting another line with a slope corresponding to the same propagation speed. As it is shown in 6.21(b), the relevant pacemaker cell was located close to FET #23.

For the propagation over the chip surface measurements were performed on the chip with grid layout (figure 6.22). In this case, transistors were distributed over the surface of the chip in 2D and we recorded spiking activity on the majority of transistors. Figure 6.22(b) shows, that the signal also propagated over the surface of the chip with a speed of 10 mm/sec, which is also in good agreement with previous measurements. This demonstrates that we obtained high-quality signal propagation within the cellular layer, where the confluent layer was established over the entire chip sensing area. To determine the influence of pharmacological solutions on AP and to test the biological response to the pharmacological effect on the cultured cells, we utilized NorA, which is a drug used for

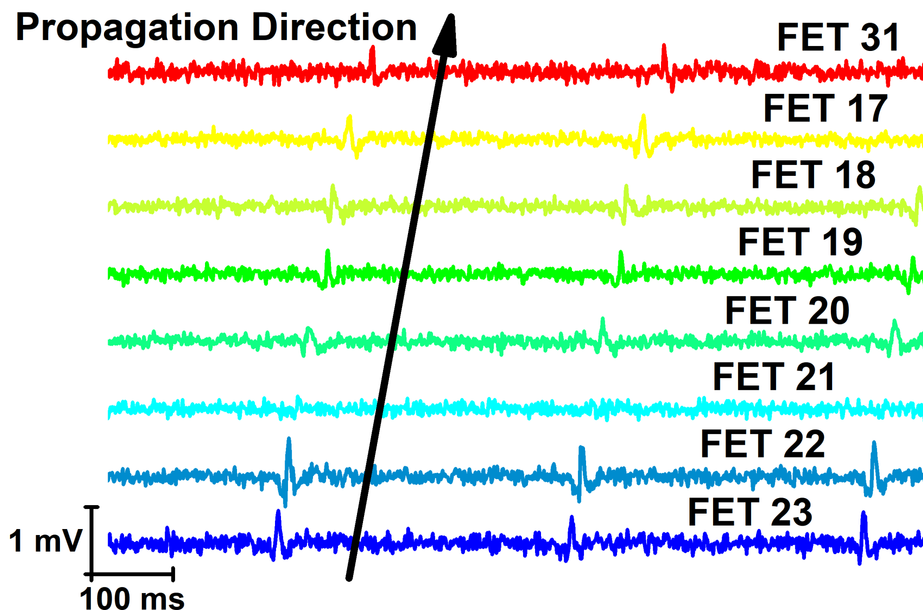

Figure 6.20: The time traces recorded on different transistors where the action potential activity was detected. Time series are sorted corresponding to the time delay.

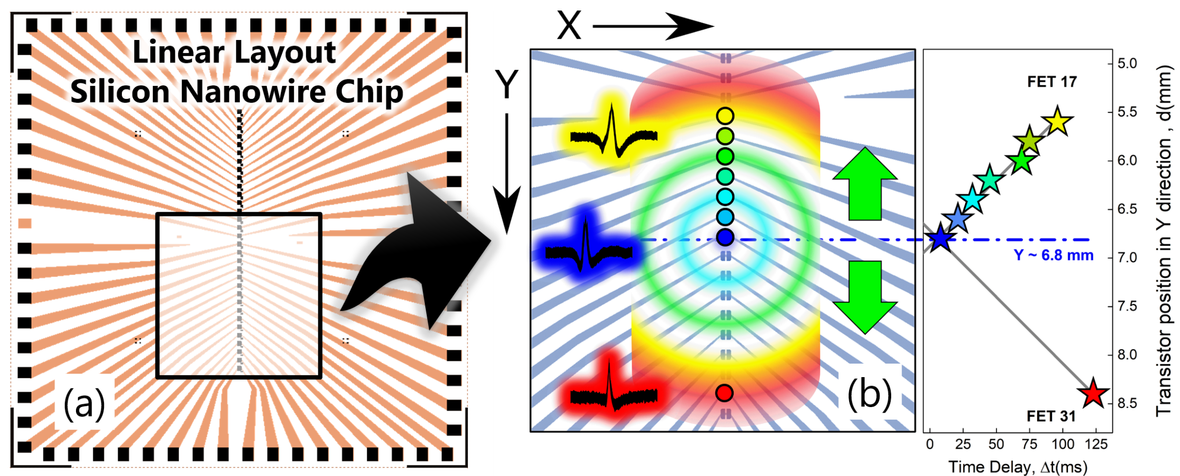

Figure 6.21: (a)Silicon nanowire chip with linear layout. (b)) (left) Zoomed in nanowire chip and schematically demonstrated action potential propagation along the line of transistors. (right) The plot of action potential delay in time versus the position of transistor which recorded the action potential. Color is used for visual representation of the time delay. The blue line shows the approximate position of the pacemaker cell and green arrows show the directions of action potential propagation.

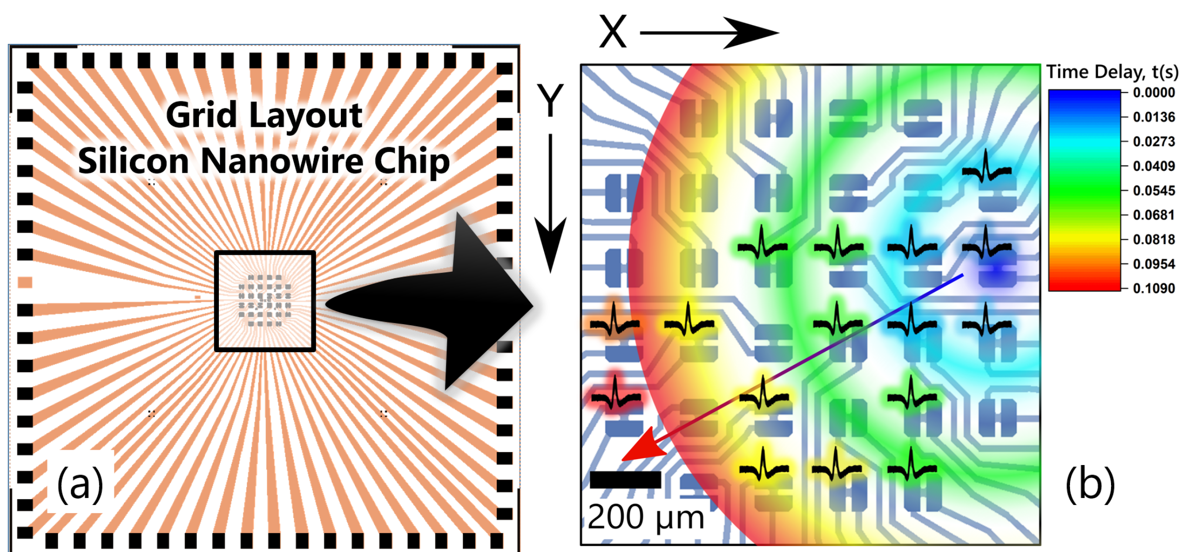

Figure 6.22: (a) Silicon nanowire chip with grid layout. (b) Zoomed in nanowire chip and schematical demonstration of action potential propagation across the surface of the chip. Action potential symbol indicates that the transistor at this position was recording action potential activity. Color indicates the time delay of the action potentials at different positions on the chip. Arrow shows the radial direction of action potential propagation.

heart stimulation and a substance that is released as a reaction to stress or danger. Cell beating depends on a direct stimulation effect caused by NorA on pumping Na^+ and K^+ cell channels. As shown in figure 6.23(a), the addition of NorA to the medium resulted in almost doubling the beating frequency, which is in good agreement with the literature [259]. Additionally sodium dodecyl sulfate (SDS) was selected as the surfactant, as it dissolves the cell membrane and may be used to model critical stage of AMI. Supplying

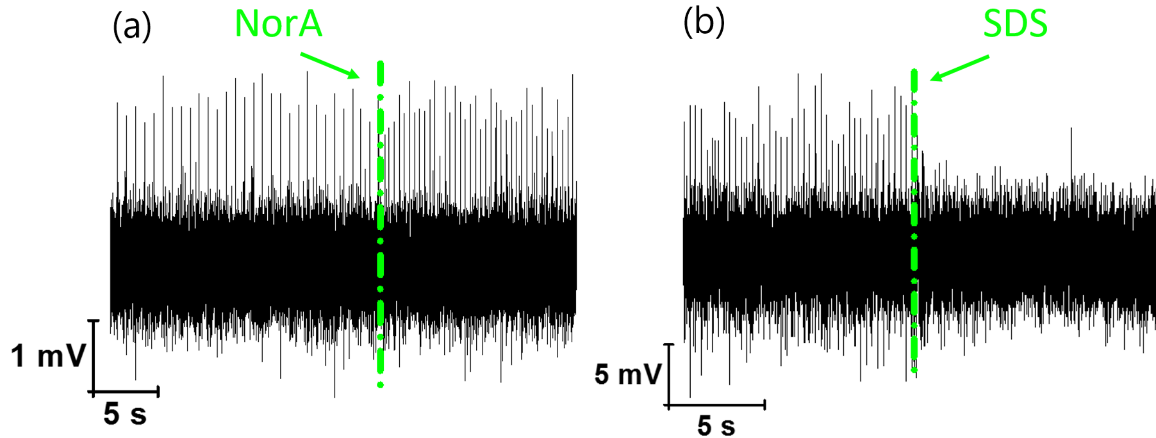

Figure 6.23: (a) The influence of NorA on AP activity makes the beating rate almost twice as fast. (b) The addition of SDS results in the complete AP activity ceasing.

SDS to the medium perforates the cellular layer. These processes cause the AP activity to vanish, as it is demonstrated in figure 6.23(b). Performed experiments show that Si NW FETs are the perfect candidates for studying cell network behavior at different conditions.

6.5.3 Combination of Electrical Monitoring with Fluorescent Microscopy

The monitoring of AP spiking activity is not only required to evaluate cellular functional activity but also to estimate the intracellular calcium content as well as membrane potential of mitochondria, which are the main calcium storage inside the cell. In a wide range of cardiac diseases, alterations in Ca^{2+} handling, energetic deficit, and oxidative stress in cardiac myocytes are important pathophysiological hallmarks [260]. Cellular functional activity studies were accomplished by applying the fluorescent markers technique. Intracellular calcium level and mitochondria membrane potential of HL-1 cardiomyocyte cells were evaluated using a combination of Fluo-4 AM and tetramethylrhodamine, methyl ester, perchlorate (TMRM) fluorescent dyes. These fluorescent dyes were used for simultaneous fluorescence imaging of the calcium level and mitochondrial membrane potential of the HL-1 cells. Green fluorescent Fluo-4 AM dye (10 µM) was loaded into cells at 37 °C for a 30-min incubation period and red fluorescent TMRM dye (200 nM) was loaded into cells at room temperature for a 5-min incubation period. Before loading, the cell samples were washed 3 times with PBS and then incubated under appropriate conditions and concentration of the probes. After loading with Fluo-4 AM and TMRM, the stain solutions were removed and the cell samples were washed with PBS 3 times for 3 minutes. We used a combination of calcium-sensitive Fluo-4 AM and membrane potential-sensitive TMRM fluorescent dyes to evaluate the effect of NorA on the functional activity of HL-1 cardiac cells on Si NW chips. The results obtained are shown in figure 6.24. Cardiac cell functional activity depends on metabolic biochemical changes on the cellular and subcellular level and is closely connected with both calcium content of cells and calcium stores in cells, particularly in mitochondria. Calcium is an important second messenger in cardiac function [261]. In heart failure and in a wide range of cardiac diseases, alterations in Ca^{2+} handling, energetic deficit, and oxidative stress in cardiac myocytes are important

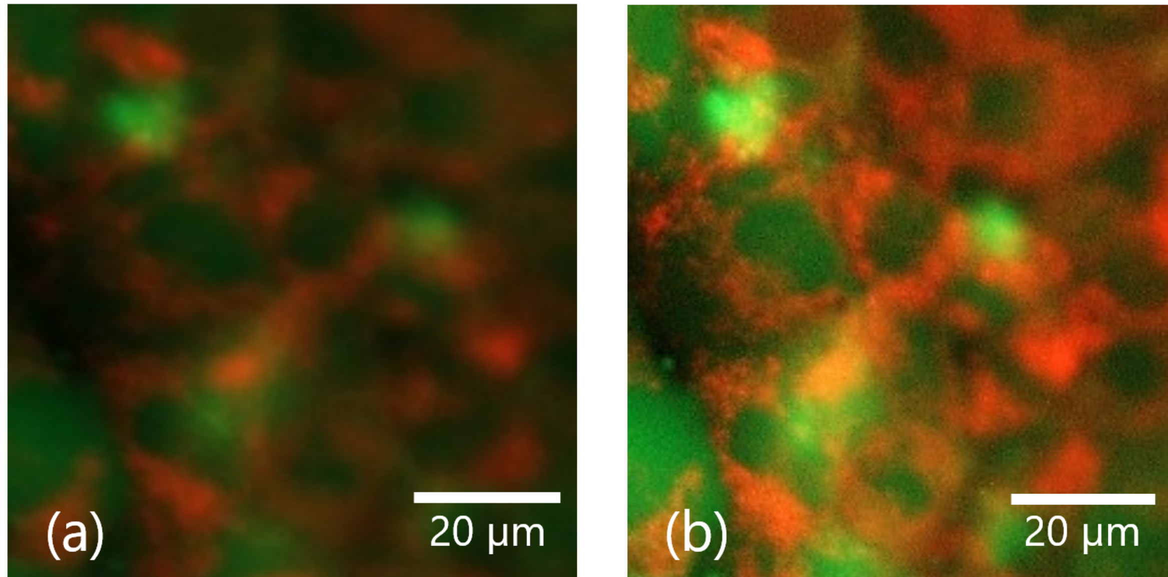

Figure 6.24: (a) Evaluation of the functional activity of HL-1 cardiac cells on Si NW chips using green fluorescent Fluo4 AM dye and red fluorescent TMRM dye before NorA treatment. (b) The effects of NorA on the polarization of mitochondria and on the calcium level in HL-1 cells on Si NW FETs after NorA treatment.

pathophysiological hallmarks [262]. Mitochondria, among the most important calcium stores in cardiac cells, play the central role within these processes since they are the main source of adenosine triphosphate (ATP) and ROS. Their function is critically controlled by Ca^{2+} and the polarization of mitochondrial membrane potential [252]. The resting concentration of Ca^{2+} in the cytoplasm is in the range of 10–100 nM. To maintain this low concentration, Ca^{2+} is pumped from the cytosol to the extracellular space and into the subcellular calcium stores of mitochondria. Signaling occurs when the cell is stimulated to release Ca^{2+} from intracellular stores, and/or when Ca^{2+} penetrates the cell through ion channels of plasma membrane. Specific signals and stimulations can trigger an increase in the cytoplasmic Ca2+ level, leading to change of mitochondrial membrane potential Specific signals and stimulations can trigger an increase in the cytoplasmic Ca^{2+} level, leading to change of mitochondrial membrane potential. In view of the abovementioned, the monitoring of cardiac cell activity has to be coupled with the study of the functional activity of cells and the evaluation of the Ca^{2+} content as well as membrane potential of cardiomyocytes and cardiac mitochondria [263]. The functional activity of HL-1 cardiac cells on Si NW chips and the effect of NorA on this activity were studied using a combination of Fluo-4 AM and TMRM fluorescent dyes. Fluo-4 AM is a membrane-permeant AM ester form of Fluo-4 that can penetrate inside cells via incubation. It does not bind extracellular calcium, but it is readily hydrolyzed to Fluo-4 by endogenous esterases once the dye is inside the cells. Fluo-4 AM ester is very useful for measuring and visualizing the intracellular calcium level in high-throughput drug screening. It is optimally excited at the 494 nm wavelength of light and emits effectively at 506 nm. TMRM is a membrane potential-sensitive cell-permeant dye which accumulates in active mitochondria with intact membrane potentials. It can be used to measure the membrane potential of mitochondria in living cells. TMRM does not form aggregates in cell membranes and interacts minimally with membrane proteins. Thus, the transmembrane distribution of the

dye is directly related to the membrane potential in accordance with the Nernst equation [264, 265]. We applied the combination of calcium-sensitive Fluo-4 AM and membrane potential-sensitive TMRM fluorescent dyes to evaluate the functional activity of HL-1 cardiac cells on Si NW chips. The green fluorescence of Fluo-4 AM represents the level of calcium in living cells, while the red fluorescence of TMRM represents the membrane potential of mitochondria in living cells (figure 6.24(a)). It was shown that the HL-1 cells, cultured on the sensing surface of the Si NW FETs, were functionally active. This was confirmed by the polarization of the mitochondrial membrane (TMRM red fluorescence) as well as by the calcium content (Fluo-4 AM green fluorescence) in cells. The results are in good agreement with those reported in the literature [254]. Moreover, in further experiments, we used this combination of calcium-sensitive Fluo-4 AM and membrane potential-sensitive TMRM fluorescent dyes to evaluate the effect of NorA on the functional activity of HL-1 cardiac cells on Si NW chips. These experiments showed that the addition of NorA led to changes in both the mitochondrial membrane potential and the calcium level in cells (figure 6.24(b)). Therefore the effects of NorA on the polarization of mitochondria were clearly registered as increased fluorescence response, and visualized by the green fluorescent Fluo-4 AM dye and red fluorescent TMRM dye. Our results confirm the crucial role of calcium content in the functionality of cardiomyocytes with regard to the biochemical influence of NorA as an effector of heart stimulation and as a substance biomarker of stress reactions in cells. As proof that spiking activity corresponds to cellular activity we used SDS, which dissolves the cell membrane and can be used to model critical stages of AMI. Adding SDS to the medium resulted in the cellular layer being perforated and thus suppressed cellular activity, causing AP activity to cease completely. Performed studies showed that Si NW FETs are perfect candidates for the investigation of cell network behavior under different conditions. Furthermore, in combination with calcium-sensitive fluorescent markers, they represent a novel approach for studies of cellular response to a variety of pharmacological treatments. Such experimental tools are particularly relevant for monitoring the states and stages of cardiac diseases, including AMI.

6.6 Neuronal Interfacing

Along with cardiomyocyte cells we studied the compatibility of our Si NW FETs with neuronal cell networks for electrical activity recording, targeting the applications for in vivo signal monitoring. Rat cortical neurons were cultured on chip in the reservoir under proper conditions in the incubator, following developed in the institute protocols. The experiments were performed after 12 to 18 days in vitro(DIV). A typical microscope image of the neurons on silicon nanoribbon structures is shown in figure 6.25(a). The live-dead staining of the neurons cultured on chip was performed using fluorescent dyes allowing to distinguish between live and dead cells. The green fluorescent dye, calcein-AM, and the red fluorescent dye, ethidium homodimer, stain live and dead cells, correspondingly. Typical fluorescent image made using different light sources and filters is shown in figure 6.25(b). The location of transistors is highlighted with yellow rectangles. It should be emphasized that live cells (colored in greed) grow also on the sensing area of transistors. The bio-compatibility of silicon nanoribbons was approved by the scanning electron microscopy. Developed in the institute cell fixation protocol, employing the critical point drying technique, has been performed to preserve the shape of cells under the electron beam. Typical SEM pictures of neuronal network on the chip are shown in figure 6.25(c-

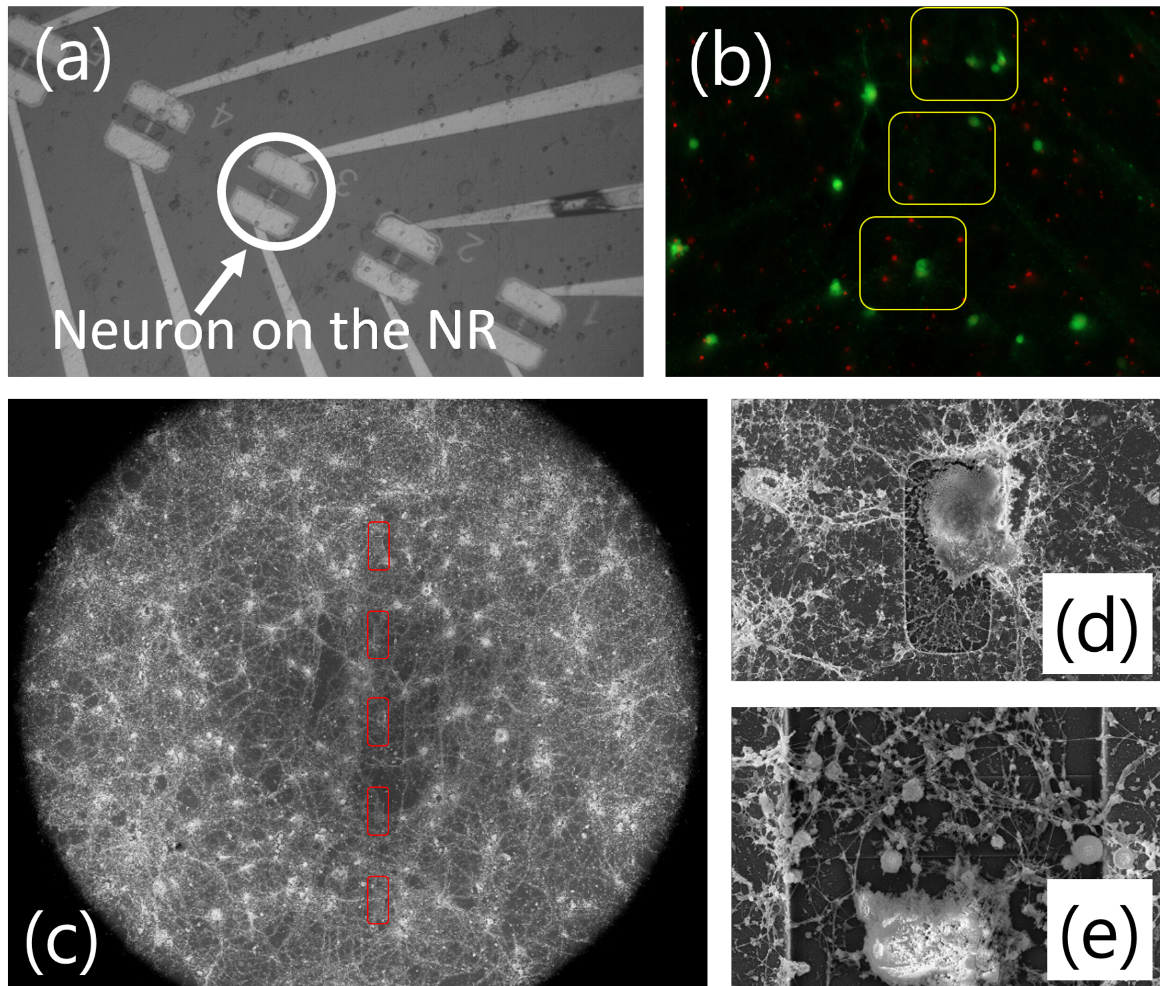

Figure 6.25: (a) Optical image of neuronal cells after 12 DIV. White circle shows neurons directly grown on the transistor channel. (b) Live-dead staining of neurons on Si NR after 18 DIV. Live cells appear colored in green, dead - in red. Transistors are highlighted with yellow squares. (c) The overview scanning electron microscopy (SEM) picture, showing neuronal networks covering the chip. Transistors are highlighted with red rectangles. (d) Neuron, grown on the nanoribbon. (e) Neuron, grown close to the transistor, and the net of axons and dendrites covering the transistor.

e). In current studies neurons were grown on the chip surface homogeneously with a high cell density. SEM investigation confirms that neurons and neurites grow on the majority of transistors covered with silicon dioxide dielectric layer. Obtained results demonstrate a good bio-compatibility of silicon nanostructures with neuronal and cardiac cells and prove the ability of recording the electrical signals from cellular layers.

6.7 Summary

In this chapter we discussed the application of silicon nanostructures for the biosensing applications. For fabricated silicon nanostructures we demonstrated a good pH sensitivity, approaching the Nernst limit of $59.5\,\mathrm{mV\,pH^{-1}}$ with increase of channel length. The fact indicates that larger sensing area devices are more suitable for pH sensing. In addition, single trap phenomena with enhanced capture time behavior was employed for the detection of solution pH. We show that capture time is much more sensitive than the current change. The results demonstrate that single trap phenomena is a powerful method for the ultra-high sensitive and real-time biosensing.

Silicon nanowire FETs were applied for the selective detection of cardiac troponin I molecules as a biomarkers, used for the diagnosis of AMI. We demonstrate a high sensitivity to the target molecules. Furthermore, noise properties were shown to reflect the molecular binding to the surface of the sensor. We reveal that the additional excess noise originates originates from ion dynamic processes related to the antibody-antigen binding events. In addition we show that the initial state of the biosensor can be recovered after sensing experiment using glycine-HCl buffer at low pH. In this respect silicon nanowire FETs are applicable as a label-free reusable biosensor for the development of healthcare diagnostic platform.

ROS are important substances, playing an important role in various processes including cellular signaling. Excess concentrations might indicate on the development of such diseases as Alzheimer's and Parkinson's. Therefore we employed silicon nanowires for the detection of antioxidant solutions which appear to balance the increased ROS concentrations. Silicon nanowires demonstrate high sensitivity to such molecules. Furthermore it is different for the molecules with different molecular weight, which can be utilized to distinquish the species.

We designed and developed a bio-platform based on Si NW FETs, which enables the monitoring of AP spiking activity of HL-1 cells. Fabricated devices demonstrate demonstrate a good stability in liquid environment. Cardiomyocyte cells were cultured on the nanowires in the reservoir. A novel approach of fluorescent imaging was applied along with electrical measurements. High quality AP recordings as well as signal propagation across the HL-1 cell community were demonstrated. We studied the functional activity of the HL-1 cells and demonstrated the pharmacological and biochemical effects of NorA by tracking changes in AP frequency and using Fluo-4 AM and TMRM fluorescent dyes. This novel approach opens up prospects with regard to evaluating the effect of pharmacologically active agents on cardiac tissue. In addition silicon nanowires were approved as biocompatible sensors for studying neuronal networks as well. Obtained results demonstrate the prospects of NW FETs utilization as a bio-platform for studying cellular activity and the impact of various pharmacological agents.

Chapter 7

Conclusions and Outlook

In this thesis nanostructures including single nanowires, nanowire arrays and nanoribbons were designed, fabricated and studied to determine appropriate operation modes and highlight the transport features for advanced biosensing. The transport properties were investigated using I-V characterization as well as noise spectroscopy to determine the device geometry, where novel sensitive parameters are more beneficial, and optimal working regimes with improved noise properties for advanced biosensing of soluiton pH , various biomarkers as well as action potentials from electrogenic cells.

High-quality liquid-gated silicon nanostructures with several geometries for studying biological objects were fabricated using the combination of conventional optical and e-beam lithographies on the basis of silicon-on-insulator (SOI) wafers. Wet chemical etching was utilized for patterning of the nanostructures as it results in the improved noise properties of fabricated devices. Silicon nanowires demonstrate excellent scaling abilities. Extracted values of charge carrier mobility were in the range from $40\,\mathrm{cm}^2/\mathrm{V\,sec}$ to $116\,\mathrm{cm}^2/\mathrm{V\,sec}$ for $p^+ - p - p^+$ structures and from $230\,\mathrm{cm}^2/\mathrm{V\,sec}$ to $500\,\mathrm{cm}^2/\mathrm{V\,sec}$, indicating the high quality of fabricated devices. The equivalent input noise was estimated to be in the range from the level corresponding to the thermal limit determined by the dielectric-polarization noise of silicon dioxide and the noise level characteristic for trap density of $N_a = 1 \times 10^{10}\,\mathrm{cm}^{-2}$.

A liquid-back gate coupling effect was revealed in the case of $n^+ - p - n^+$ inversion field-effect transistor (FET), considering the optimization impacts on the sensitivity of the biosensor. Equivalent input noise was shown to be independent of both liquid- and back-gate voltages. The results demonstrate that the dominant mechanism of 1/f noise can be described in the McWhorter model of number fluctuations and is caused by the charge carrier trapping/detrapping in the liquid gate dielectric. Simulation data support the results and show the possibility of conduction channel localization near the front- and back-gate as well as charge carrier redistribution between both interfaces. Because of conductive channel position tuning the signal-to-noise ratio (SNR) increased up to 100%, which represents almost twofold improvement in comparison to the SNR enhancement in p+-p-p+ structures.

Noise properties were studied for nanowires of several geometries. We demonstrate that input-referred noise scales with the sensor area as it is estimated from theory. Furthermore $p^+ - p - p^+$ devices fit well to mobility fluctuation model, while $n^+ - p - n^+$ fit to the number fluctuations, which is explained by the dynamic processes dependent on the location of conducting channel withing the nanowire. The fact has been also confirmed by the simulation using technology computer-aided design (TCAD) software.

When scaling nanowires down a strong modulation effects were recorded as two-level fluctuations due to charge carrier capturing to the single traps at the interface with gate dielectric. The recorded slopes reached extremely high values of (-14.37), indicating on the enhanced sensitivity to the surface potential change. For a more accurate explanation of the strong capture time slope dependence on the drain current in nanowire FETs, several components have to be taken into account: quantization of the mobile carriers in the channel; specific distribution of free carriers in the channel and tunneling of the electrons into the oxide single trap; sharp growth of the electron cross-section with the decrease of electron concentration at the oxide-nanowire (NW) interface.

It should be noted that first two factors are determined by the electron concentration distribution in the plane perpendicular to the NW-front oxide (FOX) interface. The last factor plays a significant role in the formation of the capture time slope versus drain current in the strong accumulation regime. The value of the capture time slope as a function of drain current strongly increases with a decrease of the oxide thickness. It was shown that increased values of the slope can be explained by the strong increase of the effective capture cross-section with a decrease of the concentration of minor carriers in the channel. Our calculations shown that the high surface electric field plays an insignificant role in capture dynamics in the accumulation regime.

Single trap dynamics was studied in the temperature range from 200 K to 280 K as well as under gamma radiation treatment. Characteristics of the trap were extracted form temperature measurements. The deviation of the single trap dynamics in Si NW FETs from the classical Shockley-Read-Hall (SRH) law was observed not only before, but also after gamma radiation treatment. The difference was explained in the framework of Coulomb blockade energy. Our results demonstrate, that low-dose gamma irradiation results in changes of dynamical processes determined by the single trap in the gate dielectric of the Si NW FET. It was shown, that the charge state changes from the neutral state before gamma radiation to the attractive state after treatment, although the additional energy remains the same. The results demonstrate that gamma radiation is an effective tool for controlling single trap parameters. The observed effects are important for a broad range of Si NW FET fundamental studies and applications utilizing single trap phenomena as well as for development of a single-trap-based devices and high-speed biosensors with advanced functionality.

In addition, AlGaN/GaN nanoribbons as a promising wide bandgap structures were investigated aiming the application in biosensing. Electron-charge phenomena were analysed for GaN nanoribbons with respect to static edge-trap-induced charge redistribution and transport phenomena in the range of space-charge-limited currents. The results obtained for planar GaN nanoribbons (NRs) of different widths at low voltages allowed an estimation of the depletion effects in the NRs. For planar NWs and NRs, the spatial separation of positive and negative charges due to the depletion effects induces an electrostatic potential and a field outside the samples. The electric fields of large amplitude spreads into the surrounding space for the distances comparable with the width of planar nanoribbons and nanowires. Low-frequency noise spectra studied at different applied voltages allowed us to analyze the mechanisms of current formation in the NR structures in linear and nonlinear regimes. The generation-recombination (GR) noise components in the noise spectra observed at different temperatures allow an estimation of the energy of exchange processes between trap states and quantum-confinement levels. The activation energy is in good agreement with the one, obtained from the self-consistently calculated band diagram. For higher voltages, the current nonlinearities allow to study peculiar-

ities of the space-charge limited current effect in planar NW and NR structures. The onset of this effect clearly correlates with the NR width. For the narrow NRs (W = 280, 360 nm), the mature space-charge limited current (SCLC) regime was reached. It has been shown that, with increasing applied voltage, the noise spectra reflect evidence of the SCLC phenomena. The features of the electric current and noise in the NRs and NWs studied might be important for the development of different NR-based devices, including bio-sensors with enhanced sensitivity.

Liquid-gated silicon nanostructures were utilized as biosensing platform. We reveal high pH sensitivity of Silicon nanoribbons. It should be emphasized that increasing the sensing area resulted in the sensor response approaching the Nernst limit. Single trap phenomena with high degree of modulation has been employed for the detection of pH using nanowires with pronounced random telegraph signal (RTS) fluctuations. As the capture time is a large power function (in experiment the slope = -9.74) of channel current the changes of single trap dynamics are around 10 times more sensitive to changes of surface potential in comparison to conductance change.

Liquid-gated Si NW array FETs were applied for the selective detection of cardiac troponin I (TnI) molecules as cardiac biomarkers, which can be used for the early-stage diagnosis of acute myocardial infarction (AMI). After detailed analysis of measured noise spectra of liquid-gated Si NW FETs before and after the binding of cardiac TnI molecules we observed that surface potential fluctuations related to the charge fluctuations of troponin molecules result in additional excess noise component. The noise component has characteristics which strongly differ from conventional transistor noise behavior. We found that the excess noise originates from ion dynamic processes associated with the biomolecular antibody-antigen binding events. We have also shown that utilization of low pH glycine-HCl buffer leads to antigen-antibody dissociation allowing the recovery of the sensors' initial state indicating that the devices can be reused. Thus, we have demonstrated that the fabricated Si NW FETs with appropriate surface functionalization are applicable as label-free reusable biological sensors and have considerable potential to be a powerful tool in point of care diagnostics.

Such molecular objects as reactive oxygen species (ROS) play important role in numerous reduction-oxidation reactions as well as cellular signaling in both developmental and stress responses. The increased ROS concentrations impact into the development of a various diseases, including Alzheimer's and Parkinson's. As the response to elevated ROS levels, the concentration of antioxidants increases to bring the system back to the balanced state. We performed experiments for the detection of such important components as sodium ascorbate and gluthathione. Silicon nanowires demonstrate high sensitivity to the species while it is higher to the ascorbate molecules.

On the basis of Si NW array FETs we designed and developed a bio-platform for monitoring the cellular AP spiking activity of cardiomyocyte (HL-1) cells. In order to evaluate the functional activity of cardiomyocyte cells the fluorescent imaging and electrical measurements were performed before as well as after pharmacological treatment. This novel approach opens up prospects with regard to evaluating the effect of pharmacologically active agents on cardiac tissue. Fabricated structures demonstrated stable and high-quality FET behavior with a sufficiently high transconductance to record action potentials (APs) of HL-1 cells in a culture medium. Sensing devices were used for in vitro electrical activity monitoring of the cardiomyocyte cell community, which was cultured directly in a reservoir on the chip. High SNR values of 3–5 were demonstrated for the fabricated FETs. AP propagation across the cell layer was reliably recorded and propa-

gation speed of $13\,\mathrm{mm\,s^{-1}}$ was extracted. Spatially separated FETs allow to extract the position of pacemaker cells, which is important for studies of HL-1 cell communication and their responses to external treatments. High-quality confluent layers of cardiomyocytes were grown on Si NW chips with high cell viability and vitality, which was confirmed by fluorescence imaging with Calcein AM and DAPI fluorescent markers, which color living cells in green and dead cells in red, correspondingly We studied the functional activity of the HL-1 cells on the Si NW FET platforms and demonstrated the pharmacological and biochemical effects of noradrenaline (NorA) by tracking changes in AP frequency and using calcium-sensitive Fluo-4 AM and membrane potential-sensitive TMRM fluorescent dyes. The increased fluorescence response as well as doubling of the beating frequency was revealed after adding NorA, which is a biochemical stimulator of cell activity. The spiking activity of the cardiomyocytes ceased after the addition of sodium dodecyl sulfate (SDS) solution. Performed experiments show that Si NW FETs are promising candidates as a tool for the studies of cellular responses to a variety of pharmacological influences. The results demonstrate the prospects of using the fabricated Si NW FETs as a bio-platform for studying HL-1 cells as well as to monitor cellar functional activity based on the analysis of the biochemical and electrophysiological properties of the cells. Furthermore the prospects of living systems interfacing and monitoring the activity of cells, including neurons, has been revealed using Si NW FETs. The results obtained represent a new approach for the investigation of various diseases, including myocardial dysfunctions.

As a future directions of the investigations we suggest to focus on the studies of Si NW FET biosensor stability in liquid environment. For the improvement of such properties the gate dielectric layers have to be improved. There are several ways to achieve this. Firstly the gate dielectric can be grown thicker, which is known to possess higher stability in liquids. Secondly, the atomic layer deposition (ALD) can be additionally applied. Such approach allows to improve stability drastically while keeping the dielectric layers thin enough to achieve high biosensor performance. Another way employs novel passivation materials which form almost monolayer on the surface of the sensor while being chemically stable in the liquid environment. In the current work we demonstrated the geometries of nanowires where single trap phenomena is observed relatively often. There is, however, a large chance where active single trap is not achieved. Therefore a research has to be performed in order to define the single traps in nanowire FETs with predefined parameters. This can be achieved by tuning the cross-section of the nanowire, including the triangular cross-section. Due to the enhanced fields in the top edge of such nanowires the probabilities of single trap might increase. As a modification of previous statement the novel nanowire configurations with enhanced fields and "weak" places can be developed. Another possibility is the single impurity implantation which is expected to produce the predefined and reproducible trap parameters. When this is accomplished the dynamic range of single trap has to be investigated for the biosensing applications. Speaking about nanostructures for cellular activity monitoring, the geometry of the nanowires has to be optimized to achieve better transconductance values, that would enable the detection of even smaller signals, such as neuronal action potentials. This can be achieved by tuning the access resistance of the nanowires, adjusting the ion implantation profiles as well as geometry optimization.

Appendices

Appendix A

Silicon Nanowire Fabrication Protocol

The up to date version of fabrication procedure used for the fabrication of silicon nanowires (SOI#17L,SOI#17R,SOI#19L,SOI#19R). The process is similar to the one used for silicon nanowire arrays and nanoribbons fabrication.

1. RCA clean

- **Piranha**
  - $H_2O_2 : H_2SO_4 = 2 : 1$ for 10 min
  - DI water rinse(10 min or 14 MΩ conductivity)
  - HF 1% for 10 s
  - DI water rinse(10 min or 14 MΩ conductivity)
- **SC-1**
  - $NH_4OH : H_2O_2 : DI = 1 : 4 : 20$ for 10 min
  - DI water rinse(10 min or 14 MΩ conductivity)
  - HF 1% for 10 s
  - DI water rinse(10 min or 14 MΩ conductivity)
- **SC-2**
  - $NH_4OH : H_2O_2 : DI = 1 : 1 : 20$ for 10 min
  - DI water rinse(10 min or 14 MΩ conductivity)
  - Drying with nitrogen gun

2. SiO_2 hard mask formation

- **PECVD or thermal oxydation**(900 °C for 56 min in dry oxygen atmosphere) for 20 nm SiO_2 . Check the results using ellipsometer.

3. Definition of e-beam markers

- **Dehydration:** 5 min at 180 °C on the hotplate. Cool down with nitrogen gun.
- **Spin-coating:** Cover wafer with AZ nLOF-2020 (approx. 4 mL), spin at 4000 rpm with pre-acceleration.
- **Soft bake:** 1 min at 110 °C on the hotplate.
- **Exposure:** i-line 40 mJ
- **Post-exposure bake:** 1 min at 110 °C on the hotplate.
- **Development:** 45 s in AZ 326 MIF.
- **Rinsing:** cascade DI water rinse, drying with nitrogen gun.

4. Reactive ion etching of markers

- $O2$**:** 30 sccm for 3 s, RF power.
- CHF_3/Ar: 50/50 sccm for 40 s RF power.

- SF_6/O_2**:** 100/8 sccm for 15 s RF power.
- CHF_3/Ar**:** 50/50 sccm for 7 min RF power.
- SF_6/O_2**:** 30/10 sccm for 20 s RF power.
- $O2$**:** 30 sccm for 90 s, RF +ICP power.

Resulting thickness is around 595 nm

5. Patterning of nanowires

- **Dehydration:** 5 min at 180 °C on the hotplate. Cool down with nitrogen gun.
- **Spin-coating:** Cover wafer with PMMA 649.04 200K (approx. 3 mL), spin at 4000 rpm with pre-acceleration.
- **Soft-bake:** 5 min at 180 °C on the hotplate.
- **E-beam lithography:** nanowire pattern with the dose of 270 µC with the step of 5 nm and current of 500 pA.
- **Development:** 1 min AR 600-55, 1 min IPA, cascade DI water rinse, drying with nitrogen gun.
- **RIE etching of nanowires:**
  - $O2$**:** 30 sccm for 3 s, RF power.
  - CHF_3/Ar**:** 50/50 sccm for 40 s RF power.
  - $O2$**:** 30 sccm for 40 s, RF with ICP power.

6. Patterning of meza structure in SiO_2 hard mask.

- **Dehydration:** 5 min at 180 °C on the hotplate. Cool down with nitrogen gun.
- **Apply adhesion promoter:** HMDS evaporation at 130 °C.
- **Spin-coating:** Cover wafer with AZ 5214 E (approx. 4 mL), spin at 4000 rpm with pre-acceleration.
- **Soft-bake:** 1 min at 110 °C on the hotplate.
- **Exposure:** i-line 75 mJ
- **Development:** 55 s AZ 326 MIF, DI water cascade, drying with nitrogen gun.
- **RIE etching of meza in SiO_2 hard mask**
  - $O2$ 30 sccm for 3 s, RF power.
  - CHF_3/Ar 50/50 sccm for 40 s RF power.
  - $O2$ 30 sccm for 30 s, RF +ICP power.

7. Wet etching of nanowires and meza

- **Strip native oxide:** HF 1% for 30 s
- **Rinsing:** DI water for 30 s
- **Etching:** TMAH 5% for 15 s at 80 °C
- **Rinsing:** DI water rinse(10 min or 14 MΩ conductivity)

8. RCA clean

- **Piranha**
  - $H_2O_2 : H_2SO_4 = 2 : 1$ for 10 min
  - DI water rinse(10 min or 14 MΩ conductivity)
  - HF 1% for 10 s
  - DI water rinse(10 min or 14 MΩ conductivity)
- **SC-1**
  - $NH_4OH : H_2O_2 : DI = 1 : 4 : 20$ for 10 min
  - DI water rinse(10 min or 14 MΩ conductivity)
  - HF 1% for 10 s
  - DI water rinse(10 min or 14 MΩ conductivity)

- **SC-2**
  - $NH_4OH : H_2O_2 : DI = 1 : 1 : 20$ for 10 min
  - DI water rinse(10 min or 14 MΩ conductivity)
  - Drying with nitrogen gun

9. Protective oxidation

- **Thermal oxidation** for 5 nm of SiO_2 .

10. Ion Implantation

- **Dehydration:** 5 min at 180 °C on the hotplate. Cool down with nitrogen gun.
- **Apply adhesion promoter:** HMDS evaporation at 130 °C.
- **Spin-coating:** Cover wafer with AZ 5214 E (approx. 4 mL), spin at 4000 rpm with pre-acceleration.
- **Soft-bake:** 1 min at 110 °C on the hotplate.
- **Exposure:** i-line 40 mJ
- **Development:** 55 s AZ 326 MIF, DI water cascade, drying with nitrogen gun.
- **Ion implantation:**
  - for $p^+ - p - p^+$ structures: Boron, energy = 6 keV, dose = $1 \times 10^{15}\,\text{cm}^{-2}$
  - for $n^+ - p - n^+$ structures: Arsenic, energy = 8 keV, dose = $5 \times 10^{14}\,\text{cm}^{-2}$
- **Acetone overnight**

11. RCA clean

- **Piranha**
  - $H_2O_2 : H_2SO_4 = 1 : 3$ for 10 min
  - DI water rinse(10 min or 14 MΩ conductivity)
  - HF 1% for 10 s
  - DI water rinse(10 min or 14 MΩ conductivity)
- **SC-1**
  - $NH_4OH : H_2O_2 : DI = 1 : 4 : 20$ for 10 min
  - DI water rinse(10 min or 14 MΩ conductivity)
  - HF 1% for 10 s
  - DI water rinse(10 min or 14 MΩ conductivity)
- **SC-2**
  - $NH_4OH : H_2O_2 : DI = 1 : 1 : 20$ for 10 min
  - DI water rinse(10 min or 14 MΩ conductivity)
  - Drying with nitrogen gun

12. Post-implantation rapid thermal annealing

- **Purge nitrogen:** 5 ln/min for 2 min
- **Conditioning nitrogen:** 0.5 ln/min for 30 sec
- **Rapid thermal annealing:**
  - for Arsenic 30 s at 950 °C
  - for Boron 5 s at 1000 °C
- **Fast cooling down:** fast cool down to 700 °C
- **Complete cooling down:** cool down to 200 °C

13. Gate Oxide formation

- **Strip oxide:** HF 1% for 40 s
- **Rinsing:** DI water rinse(10 min or 14 MΩ conductivity)
- **Thermal oxidation:** at 850 °C for 44 min in dry oxygen atmosphere
- **Ellipsometer check**

14. Back Gate opening

- **Dehydration:** 5 min at 180 °C on the hotplate. Cool down with nitrogen gun.
- **Applying adhesion promoter:** HMDS evaporation at 130 °C.
- **Spin-coating:** Cover wafer with AZ 5214 E (approx. 4 mL), spin at 4000 rpm with pre-acceleration.
- **Soft-bake:** 1 min at 110 °C on the hotplate.
- **Exposure:** i-line 75 mJ
- **Development:** 45 s AZ 326 MIF, DI water cascade, drying with nitrogen gun.
- **Bake:** 2 min at 120 °C on the hotplate.
- **Wet chemical etching**:
  - BOE (HF:NH_4F = 12.5:87.5) etching for 70 s
  - DI water rinse(10 min or 14 MΩ conductivity)
  - drying with nitrogen gun
- **Strip resist:** Acetone for 20 min (if possible in ultrasonic bath), Isopropanol for 1 min

15. Open meza pads for metallization

- **Dehydration:** 5 min at 180 °C on the hotplate. Cool down with nitrogen gun.
- **Applying adhesion promoter:** HMDS evaporation at 130 °C.
- **Spin-coating:** Cover wafer with AZ 5214 E (approx. 4 mL), spin at 4000 rpm with pre-acceleration.
- **Soft-bake:** 1 min at 110 °C on the hotplate.
- **Exposure:** i-line 75 mJ
- **Development:** 45 s AZ 326 MIF, DI water cascade, drying with nitrogen gun.
- **Bake:** 2 min at 120 °C on the hotplate.
- **Wet chemical etching:**
  - BOE (HF:NH_4F = 12.5:87.5) etching for 70 s
  - DI water rinse(10 min or 14 MΩ conductivity)
  - drying with nitrogen gun
- **Strip resist:** Acetone for 20 min (if possible in ultrasonic bath), Isopropanol for 1 min. If required additional Piranha cleaning can be applied.
- **Optical microscope and/or SEM check**

16. Metallization

- **Dehydration:** 5 min at 180 °C on the hotplate. Cool down with nitrogen gun.
- **Spin-coating:** Cover wafer with AZ nLOF-2020 (approx. 4 mL), spin at 4000 rpm with pre-acceleration.
- **Soft bake:** 1 min at 110 °C on the hotplate.
- **Exposure:** i-line 40 mJ
- **Post-exposure bake:** 1 min at 110 °C on the hotplate.
- **Development:** 45 s in AZ 326 MIF.
- **Rinsing:** cascade DI water rinse, drying with nitrogen gun.
- **Strip native oxide:**
  - HF 1% for 15 s
  - DI water rinse(10 min or 14 MΩ conductivity)
- **Sputtering** of 5 nm TiN / 200 nm Aluminum.
  OR
- **E-beam assisted metal evaporation** of 200 nm Aluminum.
- **Lift-off:** in acetone overnight. Note: If the problem with complete resist

removal exists oxygen plasma cleaning can be used in Barrel Reactor TePla Gigabatch 310M (300W, 200 sccm, 3 min)

- **Optical microscope and/or SEM check**
- **Rapid thermal annealing:** 10 min at 450 deg in formin gas atmosphere.
- **Resistance check**

17. Passivation

- **Warm up resist:**Take PI out of the fridge overnight
- **Dehydration:** 20 min at 180 °C on the hotplate. Cool down with nitrogen gun.
- **Apply adhesion promoter:**
  - Spin-coat wafer with VM-652 (always use fresh) at 3000 rpm with closed lid
  - Bake at 110 °C for 60 s on the hotplate
- **Apply PI-2545:** spin at 5000 rpm with closed lid.
- **Soft bake:** at 140 °C for 6 min on the hotplate
- **Spin-coating:** Apply AZ nLOF-2020 at 4000 rpm with closed lid
- **Soft bake:** at 110 °C for 60 s on the hotplate
- **Exposure:** Dose - 40 mJ
- **Post-exposure bake:** at 110 °C for 60 s on the hotplate
- **Development:** in AZ 326 MIF for 18 s to 35 s(should be tested prior on dummy wafer).
- **Rinsing:** cascade DI water rinse, drying with nitrogen gun.
- **Removing resist:** Acetone for 60 s properly stirring(ensure that AZ nLOF-2020 is removed)
- **Rinsing:** cascade DI water rinse, drying with nitrogen gun.
- **Hard bake in a convension furnace:**
  - Ramp up to 200 °C with the speed of 4 °C/ min
  - Hold for 30 min at 200 °C
  - Ramp up to 350 °C with the speed of 2.5 °C/ min
  - Hold for 30 min at 350 °C
  - Cool down to room temperature overnight(slowly).

18. Protective coating and wafer cutting

- **Dehydration:** 5 min at 180 °C on the hotplate. Cool down with nitrogen gun.
- **Spin-coating:** Cover wafer with PMMA 649.04 200K (approx. 3 mL), spin at 4000 rpm with pre-acceleration. Note: It is advisable to used e-beam resist, for easier removal after storing under normal light conditions.
- **Soft-bake:** 1 min at 180 °C on the hotplate.
- **Cutting wafer with dicing saw**
- **Packaging chips into boxes**
- **Note:**When required chips should be washed with Acetone and Isopropanol.

Appendix B

Silicon Nanowire Description

In this appendix the we describe the chip layouts, including the nanowire dimensions, and their location on the wafer. Presented tables and layouts are valid for the recent fabrication process (SOI#17L,SOI#17R,SOI#19L,SOI#19R), described in appendix A.

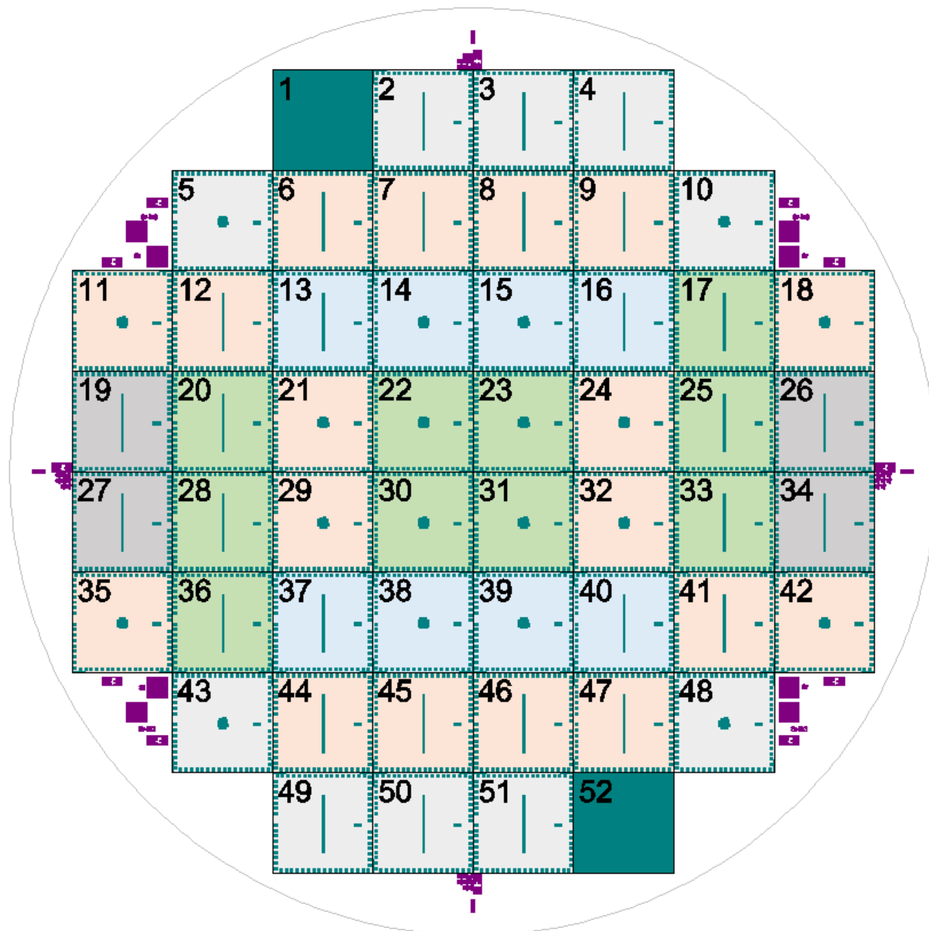

Figure B.1: Visual representation of chip location over the wafer. There are 52 chips on the wafer, marked with corresponding number. The color indicates on the chip configuration. The circle around shown the bounds of the 4-inch wafer.

Chip Type	Layout	Chip Numbers									
Chip2	Linear	13	16	37	40						
	Grid	14	15	38	39						
Chip3	Linear	17	20	25	28	33	36				
	Grid	22	23	30	31						
Chip4	Linear	6	7	8	9	12	41	44	45	46	47
	Grid	11	18	21	24	29	32	35	42		
Chip5	Linear	19	26	27	34						
Chip6	Linear	2	3	4	49	50	51				
	Grid	5	10	43	48						
TLM		1	52								

Table B.1: Table matches the chip number on the wafer(see figure B.1 to predefined layout of the chip and type. There are two layouts(linear and grid) and 6 types of chips(Chip2-6, TLM). Each chip type contains different sets of nanowire transistors.

Transistror #	Chip 2		Chip 3		Chip 4		Chip 5		Chip 6	
	Width	Length	Width	Length	Width	Length	Width	Length	Width	Length
1	70	100	100	100	100	200	70	100	70	1
2	80	100	100	200	100	200	70	200	80	1
3	90	100	100	400	100	200	70	400	90	1
4	100	100	100	600	100	200	70	600	100	1
5	100	200	100	800	100	200	70	800	150	1
6	90	200	100	1	100	200	70	1	200	1
7	80	200	100	2	100	200	70	2	250	1
8	70	200	100	4	100	200	70	4	500	1
9	70	400	100	4	100	400	80	4	500	1
10	80	400	100	2	100	400	80	2	250	1
11	90	400	100	1	100	400	80	1	200	1
12	100	400	100	800	100	400	80	800	150	1
13	100	1	100	600	100	400	80	600	100	1
14	90	1	100	400	100	400	80	400	90	1
15	80	1	100	200	100	400	80	200	80	1
16	70	1	100	100	100	400	80	100	70	1
17	70	1	200	100	100	600	90	100	70	2
18	80	1	200	200	100	600	90	200	80	2
19	90	1	200	400	100	600	90	400	90	2
20	100	1	200	600	100	600	90	600	100	2
21	100	400	200	800	100	1	90	800	150	2
22	90	400	200	1	100	1	90	1	200	2
23	80	400	200	2	100	1	90	2	250	2
24	70	400	200	4	100	1	90	4	500	2
25	70	200	200	4	100	2	100	4	500	2
26	80	200	200	2	100	2	100	2	250	2
27	90	200	200	1	100	2	100	1	200	2
28	100	200	200	800	100	2	100	800	150	2
29	100	100	200	600	100	4	100	600	100	2
30	90	100	200	400	100	4	100	400	90	2
31	80	100	200	200	100	4	100	200	80	2
32	70	100	200	100	100	4	100	100	70	2

Table B.2: Summary of the chip types, showing the width and length of a corresponding transistor on the chip. Corresponding chip numbers can be found in the table B.1

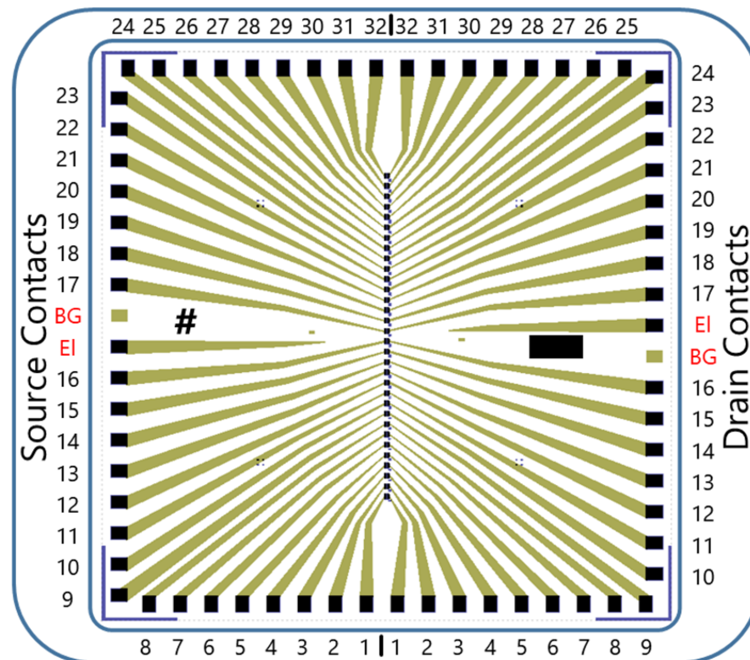

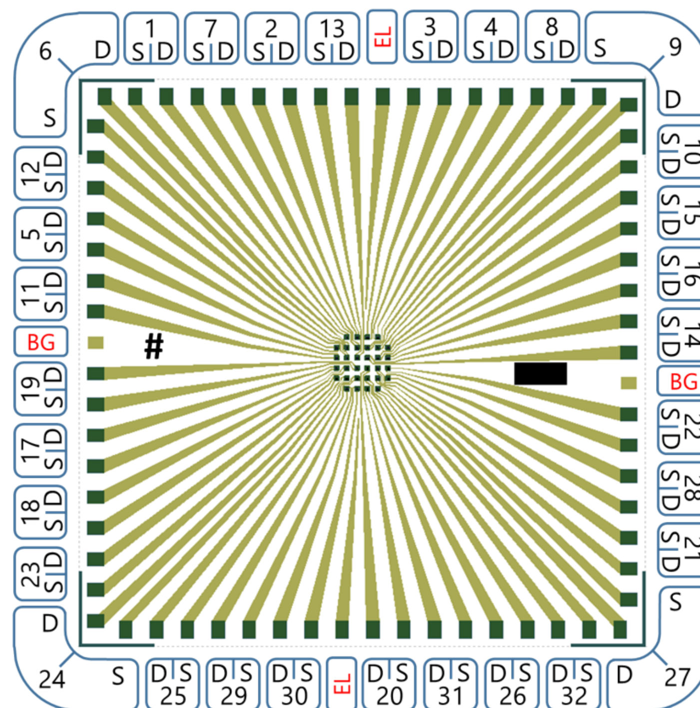

Figure B.2: Description of linear and grid layouts, used for characterization of silicon nanostructures. S stands for source contact, D - drain contact, BG - back gate contact, El - electrode. On the real chip instead of # symbol there is a chip number, and in the black rectangle there is an information about the process.

Appendix C

Software Development

During the PhD thesis we developed a variety of software for automation of measurement process as well as for simplification of data analysis. The software is stored in the Institute of Complex Systems(ICS-8), Forschungszentrum Juelich. The major developed programs are:

- **PyFANS**(including **PyFANS Analyzer**) - Python Fully Automated Noise measurement System, allows to acquire and analyze noise data from the device under test (DUT).
- **PyIV** - program for measurement of current-voltage characteristics of DUT.
- **BioMAS Analyzer** - developed program, specific for FET analysis in our research group (Do NOT confuse with other software packages in the institute).

For the development we used Python(version 3.4.3) programming language and packages, listed below:

Package	Version
Cython	0.25.2
decorator	4.0.10
future	0.16.0
Gnosis	0.1.1
imageio	2.2.0
imagesize	0.7.1
lazy-object-proxy	1.2.2
lazyxml	1.2.1
lmfit	0.9.5
lxml	4.1.1
matplotlib	2.2.2
neo	0.5.2
numpy	1.11.2+mkl
pandas	0.20.3
pandocfilters	1.4.1
PeakUtils	1.1.0
Pillow	4.3.0
Pint	0.8.1

Package	Version
playsound	1.2.2
py-expression-eval	0.3.4
PyCmdMessenger	0.2.4
pyparsing	2.2.0
PyQt4	4.11.4
pyqt2waybinding	0.3
pyqtgraph	0.9.10
pyserial	3.3
PyVISA	1.8
QDarkStyle	2.5.4
qrcode	5.3
QtAwesome	0.3.3
QtPy	1.1.2
Qt	5.5.0
scikit-learn	0.20.0
scipy	0.18.1
SIP	4.16.8
tqdm	4.11.1

List of Abbreviations

ALD	Atomic Layer Deposition.
AMI	Acute Myocardial Infarction.
AP	Action Potential.
ATP	Adenosine Triphosphate.
BIOFET	Biologically Sensitive Field-Effect Transistor.
BOE	Buffered Oxide Etch.
BOX	Buried Oxide.
CMOS	Complementary Metal-Oxide-Semiconductor.
DAQ	Data Acquisition.
DNA	Deoxyribonucleic Acid.
DUT	Device Under Test.
EDL	Electrical Double Layer.
ELISA	Enzyme-Linked Immunosorbent Assay.
FET	Field-Effect Transistor.
FOX	Front Oxide.
GR	Generation-Recombination.
HMDS	Hexamethyldisilazane.
HNF	Helmholtz Nanoelectronic Facility.
ISFET	Ion Sensitive Field-Effect Transistor.
JFET	Junction Field-Effect Transistor.
MEA	Multielectrode Array.
MOS	Metal-Oxide Semiconductor.
MOSFET	Metal-Oxide Semiconductor Field-Effect Transistor.
NORA	Noradrenaline.
NR	Nanoribbon.
NW	Nanowire.
PBS	Phosphate-Buffered Saline.
PDMS	Polydimethylsiloxane.
PECVD	Plasma-Enhanced Chemical Vapor Deposition.
PGA	Programmable-Gain Amplifier.
PSD	Power Spectral Density.
RIE	Reactive-Ion Etching.
RNA	Ribonucleic Acid.
ROS	Reactive Oxygen Species.
RTA	Rapid Thermal Annealing.
RTS	Random Telegraph Signal.
SCLC	Space-Charge Limited Current.
SDS	Sodium Dodecyl Sulfate.
SEM	Scanning Electron Microscopy.

SMU Source-Meter Unit.
SNR Signal-To-Noise Ratio.
SOI Silicon-On-Insulator.
SRH Shockley-Read-Hall.
TCAD Technology Computer-Aided Design.
TLM Transmission Line Measurement.
TMAH Tetramethylammonium Hydroxide.
TNC Troponin C.
TNI Troponin I.
TNT Troponin T.
UTB Ultra Thin Body.

References

[1] J. Li et al. “Sensitivity enhancement of Si nanowire field effect transistor biosensors using single trap phenomena”. *Nano Letters* 14.6 (2014), pp. 3504–3509.

[2] N. S. Ramgir, Y. Yang, and M. Zacharias. “Nanowire-Based Sensors”. *Small* 6.16 (2010), pp. 1705–1722.

[3] F. Patolsky, G. Zheng, and C. M. Lieber. “Nanowire-based biosensors.” *Analytical chemistry* 78.13 (2006), pp. 4260–9.

[4] K. Y. Lee et al. “Coupling of semiconductor nanowires with neurons and their interfacial structure”. *Nanoscale Research Letters* 5.2 (2010), pp. 410–415.

[5] F. Patolsky. “Detection, Stimulation, and Inhibition of Neuronal Signals with High-Density Nanowire Transistor Arrays”. *Science* 313.5790 (2006), pp. 1100–1104.

[6] A. Nakajima. “Application of single-electron transistor to biomolecule and ion sensors”. *Applied Sciences* 6.4 (2016).

[7] J Salfi et al. “Direct observation of single-charge-detection capability of nanowire field-effect transistors.” *Nature nanotechnology* 5.10 (2010), pp. 737–741.

[8] M Xiao et al. “Electrical detection of the spin resonance of a single electron in a silicon eld-effect transistor”. *Nature* 430.July (2004), pp. 435–439.

[9] E. Simoen. *Random telegraph signals in semiconductor devices.* 2016, pp. 1–217.

[10] S. Pud et al. “Modulation phenomena in Si nanowire field-effect transistors characterized using noise spectroscopy and gamma radiation technique”. *Journal of Applied Physics* 113.12 (2013).

[11] S. J. Pearton and F. Ren. “Wide Bandgap Semiconductor One-Dimensional Nanostructures for Applications in Nanoelectronics and Nanosensors”. *Nanomaterials and Nanotechnology* 3 (2013), p. 1.

[12] J. Juan Colás and J. Juan Colas. *Dual-Mode Electro-photonic Silicon Biosensors.* Vol. 1. Springer Theses. Cham: Springer International Publishing, 2017.

[13] S. Sang et al. “Progress of new label-free techniques for biosensors: a review”. *Critical Reviews in Biotechnology* 36.3 (2015), pp. 1–17.

[14] A. Rhouati et al. *Label-Free Aptasensors for the Detection of Mycotoxins.* 2016.

[15] S. Harz et al. “Fluorescence optical spectrally resolved sensor based on molecularly imprinted polymers and microfluidics”. *Engineering in Life Sciences* 11.6 (2011), pp. 559–565.

[16] Y. Li, W. Xie, and G. Fang. “Fluorescence detection techniques for protein kinase assay”. *Analytical and Bioanalytical Chemistry* 390.8 (2008), pp. 2049–2057.

[17] J. Ma et al. “Speciation and detection of arsenic in aqueous samples: A review of recent progress in non-atomic spectrometric methods”. *Analytica Chimica Acta* 831 (2014), pp. 1–23.

[18] C. P. Toseland and M. R. Webb. “Fluorescence tools to measure helicase activity in real time”. *Methods* 51.3 (2010), pp. 259–268.

[19] W. Xu et al. “Rational Design of Phosphorescent Chemodosimeter for Reaction-Based One- and Two-Photon and Time-Resolved Luminescent Imaging of Biothiols in Living Cells”. *Advanced Healthcare Materials* 3.5 (2014), pp. 658–669.

[20] U. S. Akshath, L. Sagaya Selvakumar, and M. S. Thakur. “Detection of formaldehyde in food samples by enhanced chemiluminescence”. *Analytical Methods* 4.3 (2012), pp. 699–704.

[21] C. Ma et al. “Highly sensitive detection of microRNA by chemiluminescence based on enzymatic polymerization”. *Analytical and Bioanalytical Chemistry* 402.6 (2012), pp. 2217–2220.

[22] X. Wang et al. “Hybridization chain reaction-based instantaneous derivatization technology for chemiluminescence detection of specific DNA sequences”. *The Analyst* 138.9 (2013), p. 2691.

[23] B. Wu et al. “Sensitive ECL immunosensor for detection of retinol-binding protein based on double-assisted signal amplification strategy of multiwalled carbon nanotubes and Ru(bpy)32+ doped mesoporous silica nanospheres”. *Biosensors and Bioelectronics* 50 (2013), pp. 300–304.

[24] J. Yu et al. “A novel chemiluminescence paper microfluidic biosensor based on enzymatic reaction for uric acid determination”. *Biosensors and Bioelectronics* 26.7 (2011), pp. 3284–3289.

[25] N. Gibson et al. “Radiolabelling of engineered nanoparticles for in vitro and in vivo tracing applications using cyclotron accelerators”. *Archives of Toxicology* 85.7 (2011), pp. 751–773.

[26] Y. Qi et al. “A cancer-targetable copolymer containing tyrosine segments for labeling radioactive halogens”. *Reactive and Functional Polymers* 71.4 (2011), pp. 390–394.

[27] Y. M. Shlyapnikov et al. “Detection of microarray-hybridized oligonucleotides with magnetic beads”. *Analytical Biochemistry* 399.1 (2010), pp. 125–131.

[28] S. Sang Dr.-Ing. “An approach to the design of surface stress-based PDMS micromembrane biosensors - concept, numerical simulations and prototypes”. PhD thesis. 2011.

[29] G MacBeath and S. L. Schreiber. “Printing proteins as microarrays for high-throughput function determination.” *Science (New York, N.Y.)* 289.5485 (2000), pp. 1760–3.

[30] N. J. Goddard, D. Pollard-Knight, and C. H. Maule. “Real-time biomolecular interaction analysis using the resonant mirror sensor”. *The Analyst* 119.4 (1994), p. 583.

[31] N. J. Goddard et al. “Internally-referenced Resonant Mirror devices for dispersion compensation in chemical sensing and biosensing applications”. *Sensors and Actuators A: Physical* 100.1 (2002), pp. 1–9.

[32] G. Yuan et al. “Improvement of optical sensing performances of a double-slot-waveguide-based ring resonator sensor on silicon-on-insulator platform”. *Optik* 125.2 (2014), pp. 850–854.

[33] O. Gaathon et al. “Enhancing sensitivity of a whispering gallery mode biosensor by subwavelength confinement”. *Applied Physics Letters* 89.22 (2006), p. 223901.

[34] V. Goral et al. “Label-free optical biosensor with microfluidics for sensing ligand-directed functional selectivity on trafficking of thrombin receptor”. *FEBS Letters* 585.7 (2011), pp. 1054–1060.

[35] S. M. Grist et al. “Silicon photonic micro-disk resonators for label-free biosensing”. *Optics Express* 21.7 (2013), p. 7994.

[36] I. M. White and X. Fan. “On the performance quantification of resonant refractive index sensors”. *Optics Express* 16.2 (2008), p. 1020.

[37] F. J. Blanco et al. “Microfluidic-optical integrated CMOS compatible devices for label-free biochemical sensing”. *Journal of Micromechanics and Microengineering* 16.5 (2006), pp. 1006–1016.

[38] R. Heideman, R. Kooyman, and J. Greve. “Performance of a highly sensitive optical waveguide Mach-Zehnder interferometer immunosensor”. *Sensors and Actuators B: Chemical* 10.3 (1993), pp. 209–217.

[39] Á. Lavín et al. “Efficient design and optimization of bio-photonic sensing cells (BICELLs) for label free biosensing”. *Sensors and Actuators B: Chemical* 176 (2013), pp. 753–760.

[40] F. Sanza et al. “Bio-Photonic Sensing Cells over transparent substrates for anti-gestrinone antibodies biosensing”. *Biosensors and Bioelectronics* 26.12 (2011), pp. 4842–4847.

[41] F. Cunin et al. “Biomolecular screening with encoded porous-silicon photonic crystals”. *Nature Materials* 1.1 (2002), pp. 39–41.

[42] G. Gaur, D. S. Koktysh, and S. M. Weiss. “Immobilization of Quantum Dots in Nanostructured Porous Silicon Films: Characterizations and Signal Amplification for Dual-Mode Optical Biosensing”. *Advanced Functional Materials* 23.29 (2013), pp. 3604–3614.

[43] M. Hiraoui et al. “Towards a biosensor based on anti resonant reflecting optical waveguide fabricated from porous silicon”. *Biosensors and Bioelectronics* 36.1 (2012), pp. 212–216.

[44] I. Rendina et al. “Porous silicon-based optical biosensors and biochips”. *Physica E: Low-dimensional Systems and Nanostructures* 38.1-2 (2007), pp. 188–192.

[45] A.-L. Kang et al. “A wireless pressure sensor based on surface transverse wave”. In: *2011 Symposium on Piezoelectricity, Acoustic Waves and Device Applications (SPAWDA)*. IEEE, 2011, pp. 231–235.

[46] K. Länge, B. E. Rapp, and M. Rapp. “Surface acoustic wave biosensors: a review”. *Analytical and Bioanalytical Chemistry* 391.5 (2008), pp. 1509–1519.

[47] D. Ballantine et al. “Acoustic Wave Sensors and Responses”. In: *Acoustic Wave Sensors*. Ed. by D. S. Ballantine et al. Applications of Modern Acoustics. Burlington: Elsevier, 1997, pp. 36–149.

[48] K. Lawrence et al. "Functionalized Carbon Nanoparticles, Blacks and Soots as Electron-Transfer Building Blocks and Conduits". *Chemistry - An Asian Journal* 9.5 (2014), pp. 1226–1241.

[49] U. von Ah, D. Wirz, and A. Daniels. "Isothermal micro calorimetry – a new method for MIC determinations: results for 12 antibiotics and reference strains of E. coli and S. aureus". *BMC Microbiology* 9.1 (2009), p. 106.

[50] M. M. F. Choi. "Progress in Enzyme-Based Biosensors Using Optical Transducers". *Microchimica Acta* 148.3-4 (2004), pp. 107–132.

[51] G. Denuault. "Electrochemical techniques and sensors for ocean research". *Ocean Science* 5.4 (2009), pp. 697–710.

[52] D. Grieshaber et al. "Electrochemical Biosensors - Sensor Principles and Architectures". *Sensors* 8.3 (2008), pp. 1400–1458.

[53] H. Yang. "Enzyme-based ultrasensitive electrochemical biosensors". *Current Opinion in Chemical Biology* 16.3-4 (2012), pp. 422–428.

[54] World Health Organization. *The top 10 causes of death.*

[55] S. K. James et al. "Troponin and C-reactive protein have different relations to subsequent mortality and myocardial infarction after acute coronary syndrome". *Journal of the American College of Cardiology* 41.6 (2003), pp. 916–924.

[56] R. Dhingra and R. S. Vasan. "Biomarkers in cardiovascular disease: Statistical assessment and section on key novel heart failure biomarkers". *Trends in Cardiovascular Medicine* 27.2 (2017), pp. 123–133.

[57] V. L. Filatov et al. "Troponin: Structure, Properties, and Mechanism of Functioning". *Biochemistry (Moscow) Translated from Biokhimiya Original Russian Text* 64.9 (1999), pp. 969–985.

[58] A. Streng. *The path of life of cardiac troponin T.* 2017.

[59] M. A. Daubert, A. Jeremias, and D. L. Brown. "Diagnosis of Acute Myocardial Infarction". In: *Cardiac Intensive Care.* Elsevier, 2010, pp. 97–105.

[60] G. K. Dhoot, P. G. Gell, and S. V. Perry. "The localization of the different forms of troponin I in skeletal and cardiac muscle cells." *Experimental cell research* 117.2 (1978), pp. 357–70.

[61] S. V. Perry. "Troponin I: Inhibitor or facilitator". *Molecular and Cellular Biochemistry* 190.1 (1999), pp. 9–32.

[62] J. Liu, M. Agarwal, and K. Varahramyan. "Glucose sensor based on organic thin film transistor using glucose oxidase and conducting polymer". *Sensors and Actuators B: Chemical* 135.1 (2008), pp. 195–199.

[63] T. Sekiguchi et al. "Immunological Helicobacter pylori urease analyzer based on ion-sensitive field effect transistor". *Sensors and Actuators B: Chemical* 67.3 (2000), pp. 265–269.

[64] T. M. Anh et al. "Development of tyrosinase biosensor based on pH-sensitive field-effect transistors for phenols determination in water solutions." *Talanta* 56.4 (2002), pp. 627–34.

[65] W. Zhou, X. Dai, and C. M. Lieber. "Advances in nanowire bioelectronics". *Reports on Progress in Physics* 80.1 (2017), p. 016701.

[66] A. GOLDUP, S. OHKI, and J. DANIELLI. “Black Lipid Films”. In: *Recent Progress in Surface Science*. 1970, pp. 193–260.

[67] J. V. Raimondo et al. “Ion dynamics during seizures”. eng. *Frontiers in cellular neuroscience* 9 (2015), p. 419.

[68] J Dudel. “Innerneurale Homeostase und Kommunikation, Erregung BT - Neuro- und Sinnesphysiologie”. In: ed. by R. F. Schmidt. Berlin, Heidelberg: Springer Berlin Heidelberg, 1998, pp. 31–58.

[69] E. Kandel, J. Schwartz, and T. Jessell. *Principles of neural science*. 4th Editio. New York: McGraw-Hill, 2000.

[70] A. L. Hongkin and A. F. Huxley. “A quantitative description of membrane current and its application to conduction and excitation in nerve”. eng. *The Journal of physiology* 117.4 (1952), pp. 500–544.

[71] J. T. Koivumäki, T. Korhonen, and P. Tavi. “Impact of sarcoplasmic reticulum calcium release on calcium dynamics and action potential morphology in human atrial myocytes: a computational study”. eng. *PLoS computational biology* 7.1 (2011), e1001067–e1001067.

[72] K. Schmidt-Nielsen. *Animal physiology : adaptation and environment*. 5th ed. Cambridge : Cambridge University Press, 1997.

[73] R. Kim et al. “Recent trends in microelectrode array technology for in vitro neural interface platform”. *Biomedical Engineering Letters* 4.2 (2014), pp. 129–141.

[74] D. J. Banks et al. “Instrumentation to evaluate neural signal recording properties of micromachined microelectrodes inserted in invertebrate nerve”. *Physiological Measurement* 23.2 (2002), pp. 437–448.

[75] O. J. Prohaska et al. “Thin-Film Multiple Electrode Probes: Possibilities and Limitations”. *IEEE Transactions on Biomedical Engineering* BME-33.2 (1986), pp. 223–229.

[76] P. Namdari, H. Daraee, and A. Eatemadi. “Recent Advances in Silicon Nanowire Biosensors: Synthesis Methods, Properties, and Applications”. *Nanoscale Research Letters* 11.1 (2016), p. 406.

[77] S. Pud et al. “Liquid and back gate coupling effect: Toward biosensing with lowest detection limit”. *Nano Letters* 14.2 (2014), pp. 578–584.

[78] P. Fromherz et al. “Junction : A Retzius Cell of the”. *Science* 252 (1991), pp. 1290–1293.

[79] D. Braun and P. Fromherz. “Fluorescence Interferometry of Neuronal Cell Adhesion on Microstructured Silicon”. *Physical Review Letters* 81.23 (1998), pp. 5241–5244.

[80] M. Voelker and P. Fromherz. “Signal Transmission from Individual Mammalian Nerve Cell to Field-Effect Transistor”. *Small* 1.2 (2005), pp. 206–210.

[81] C. G. Sodini, T. W. Ekstedt, and J. L. Moll. “Charge accumulation and mobility in thin dielectric MOS transistors”. *Solid State Electronics* 25.9 (1982), pp. 833–841.

[82] W. Zhu, J. P. Han, and T. P. Ma. “Mobility measurement and degradation mechanisms of MOSFETs made with ultrathin high-k dielectrics”. *IEEE Transactions on Electron Devices* 51.1 (2004), pp. 98–105.

[83] A. Gao et al. “Signal-to-Noise Ratio Enhancement of Silicon Nanowires Biosensor with Rolling Circle Amplification”. *Nano Letters* 13.9 (2013), pp. 4123–4130.

[84] S. S. Buchholz et al. “Noise thermometry in narrow two-dimensional electron gas heat baths connected to a quasi-one-dimensional interferometer”. *Physical Review B - Condensed Matter and Materials Physics* 85.23 (2012), pp. 10–15. arXiv: `1111.1591`.

[85] N. Clément et al. “Evaluation of a gate capacitance in the Sub-aF range for a chemical field-effect transistor with a Si nanowire channel”. *IEEE Transactions on Nanotechnology* 10.5 (2011), pp. 1172–1179. arXiv: `1101.4088`.

[86] W. Schottky. “Über spontane Stromschwankungen in verschiedenen Elektrizitätsleitern”. *Annalen der Physik* 362.23 (1918), pp. 541–567.

[87] Y. M. Blanter et al. “Shot noise in mesoscopic conductors”. *Physics Reports* 336.1-2 (2000), pp. 1–166. arXiv: `9910158 [cond-mat]`.

[88] F. Hooge. “1/f noise sources”. *IEEE Trans. Electron Devices* 41.11 (1994), pp. 1926–1935.

[89] E. Simoen and C. Claeys. “On the flicker noise in submicron silicon MOSFETs”. *Solid-State Electronics* 43.5 (1999), pp. 865–882.

[90] L. K. Vandamme and F. N. Hooge. “What do we certainly know about 1/f noise in MOSTs?” *IEEE Transactions on Electron Devices* 55.11 (2008), pp. 3070–3085.

[91] T. G. M. Kleinpenning and A. H. de Kuijper. “Relation between variance and sample duration of 1/ f noise signals”. *Journal of Applied Physics* 63.1 (1988), pp. 43–45.

[92] F. N. Hooge, T. G. M. Kleinpenning, and L. K. J. Vandamme. “Experimental studies on 1/f noise”. *Reports on Progress in Physics* 44.5 (1981), pp. 479–532.

[93] M. Toshimitsu, B. Gábor, and S. Minoru. “1/ f phonon-number fluctuations in quartz observed by laser light scattering”. *Physical Review Letters* 64.20 (1990), pp. 2394–2397.

[94] T. Musha and G. Borbély. “1/ f Fluctuations of Phonon Energy in Water”. *Japanese Journal of Applied Physics* 31.Part 2, No. 3B (1992), pp. L370–L371.

[95] F. N. Hooge and F. Hooge. “1/f noise is no surface effect”. *Phys. Lett* 29.3 (1969), pp. 139–140.

[96] A. L. McWhorter. “1/f noise and related surface effects in germanium.” (1955).

[97] M. Surdin. “Fluctuations de courant thermionique et le « Flicker effect »”. *Journal de Physique et le Radium* 10.4 (1939), pp. 188–189.

[98] M. J. Kirton and M. J. Uren. “Noise in solid-state microstructures: A new perspective on individual defects, interface states and low-frequency (1/f) noise”. *Advances in Physics* 38.4 (1989), pp. 367–468.

[99] K. S. Ralls et al. “Discrete Resistance Switching in Submicrometer Silicon Inversion Layers: Individual Interface Traps and Low-Frequency (1/f) Noise”. *Physical Review Letters* 52.3 (1984), pp. 228–231.

[100] K. Hung et al. “Random telegraph noise of deep-submicrometer MOSFETs”. *IEEE Electron Device Letters* 11.2 (1990), pp. 90–92.

[101] N. B. Lukyanchikova et al. “Non-trivial GR and 1/ f noise generated in the p-Si layer of SOI and SOS MOSFETs near the inverted front or buried p-Si/SiO 2 interface”. *Semiconductor Science and Technology* 14.9 (1999), pp. 775–783.

[102] N. V. Amarasinghe, Z. Çelik-Butler, and A. Keshavarz. “Extraction of oxide trap properties using temperature dependence of random telegraph signals in submicron metal–oxide–semiconductor field-effect transistors”. *Journal of Applied Physics* 89.10 (2001), pp. 5526–5532.

[103] K. Georgakopoulou, A. Birbas, and C. Spathis. “Modeling of fluctuation processes on the biochemically sensorial surface of silicon nanowire field-effect transistors”. *Journal of Applied Physics* 117.10 (2015), pp. 0–8.

[104] G. Ghibaudo, O. Roux-dit Buisson, and J. Brini. “Impact of Scaling Down on Low Frequency Noise in Silicon MOS Transistors”. *Physica Status Solidi (a)* 132.2 (1992), pp. 501–507.

[105] N. B. Lukyanchikova et al. “RTS capture kinetics and Coulomb blockade energy in submicron nMOSFETs under surface quantization conditions”. *Microelectronic Engineering* 48.1 (1999), pp. 185–188.

[106] R. Huang et al. “Characterization and analysis of gate-all-around Si nanowire transistors for extreme scaling”. In: *2011 IEEE Custom Integrated Circuits Conference (CICC)*. IEEE, 2011, pp. 1–8.

[107] I. Zadorozhnyi et al. “Effect of Gamma Irradiation on Dynamics of Charge Exchange Processes between Single Trap and Nanowire Channel”. *Small* 14.2 (2018), p. 1702516.

[108] S. Machlup. “Noise in Semiconductors: Spectrum of a Two-Parameter Random Signal”. *Journal of Applied Physics* 25.3 (1954), pp. 341–343.

[109] V. Sydoruk. “Low-frequency noise and transport characteristics of nanostructures” (2011), p. 168.

[110] S. Pud. “Silicon nanowire structures for neuronal cell interfacing”. PhD thesis. Jülich, 2015, 153 pp.

[111] M. Jansen. “Silizium Nanoribbon Feld-Effekt Transistoren zur Kopplung an elektroaktive Zellen”. PhD thesis. Jülich: RWTH Aachen, 2014, xvi, 181 p.

[112] N. K. Rajan, X. Duan, and M. A. Reed. “Performance limitations for nanowire/nanoribbon biosensors”. *Wiley Interdisciplinary Reviews: Nanomedicine and Nanobiotechnology* 5.6 (2013), pp. 629–645.

[113] Z Xie and Y Liu. “and Y. Liu, Zhongguo Youse Jinshu Xuebao, 1998, 8, (4),” *Zhongguo Youse Jinshu Xuebao* 8.4 (1998), p. 668.

[114] I. Zadorozhnyi et al. “Single-trap kinetic in Si nanowire FETs: effect of gamma radiation treatment”. *MRS Advances* 1.56 (2016), pp. 3755–3760.

[115] S Takagi et al. “On the universality of inversion layer mobility in Si MOSFET’s: Part I-effects of substrate impurity concentration”. *IEEE Transactions on Electron Devices* 41.12 (1994), pp. 2357–2362.

[116] S Takagi et al. “On the universality of inversion layer mobility in Si MOSFET’s: Part II-effects of surface orientation”. *IEEE Transactions on Electron Devices* 41.12 (1994), pp. 2363–2368.

[117] H Irie et al. “In-plane mobility anisotropy and universality under uni-axial strains in nand p-MOS inversion layers on (100), [110], and (111) Si”. In: *IEDM Technical Digest. IEEE International Electron Devices Meeting, 2004.* 2004, pp. 225–228.

[118] O. Gunawan et al. “Measurement of Carrier Mobility in Silicon Nanowires”. *Nano Letters* 8.6 (2008), pp. 1566–1571.

[119] L. Su et al. “Deep-submicrometer channel design in silicon-on-insulator (SOI) MOSFET’s”. *IEEE Electron Device Letters* 15.5 (1994), pp. 183–185.

[120] E. Suzuki et al. “Highly suppressed short-channel effects in ultrathin SOI n-MOSFETs”. *IEEE Transactions on Electron Devices* 47.2 (2000), pp. 354–359.

[121] H.-S. Wong, D. Frank, and P. Solomon. “Device design considerations for double-gate, ground-plane, and single-gated ultra-thin SOI MOSFET’s at the 25 nm channel length generation”. In: *International Electron Devices Meeting 1998. Technical Digest (Cat. No.98CH36217).* IEEE, 1998, pp. 407–410.

[122] H.-K. Lim et al. “Threshold voltage of thin-film Silicon-on-insulator (SOI) MOSFET’s”. *IEEE Transactions on Electron Devices* 30.10 (1983), pp. 1244–1251.

[123] J.-P. Colinge. *Silicon-on-Insulator Technology: Materials to VLSI.* Boston, MA: Springer US, 2004.

[124] T. Poiroux et al. “New and accurate method for electrical extraction of silicon film thickness on fully-depleted SOI and double gate transistors”. In: *2004 IEEE International SOI Conference (IEEE Cat. No.04CH37573).* IEEE, 2004, pp. 73–74.

[125] V. P. Trivedi, J. G. Fossum, and W. Zhang. “Threshold voltage and bulk inversion effects in nonclassical CMOS devices with undoped ultra-thin bodies”. *Solid-State Electronics* 51.1 (2007), pp. 170–178.

[126] J. Mazellier et al. “Threshold voltage in ultra thin FDSOI CMOS : Advanced triple interface model and experimental devices”. In: *2008 9th International Conference on Ultimate Integration of Silicon.* IEEE, 2008, pp. 31–34.

[127] T. Rudenko et al. “A review of special gate coupling effects in long-channel SOI MOSFETs with lightly doped ultra-thin bodies and their compact analytical modeling”. *Solid-State Electronics* 117 (2016), pp. 66–76.

[128] T Rudenko et al. “Revision of interface coupling in ultra-thin body silicon-on-insulator MOSFETs”. *Semiconductor Physics Quantum Electronics and Optoelectronics* 16.3 (2013), pp. 300–309.

[129] G. Ghibaudo et al. “Improved Analysis of Low Frequency Noise in Field-Effect MOS Transistors”. *Physica Status Solidi (a)* 124.2 (1991), pp. 571–581.

[130] C. G. Theodorou et al. “Impact of front-back gate coupling on low frequency noise in 28 nm FDSOI MOSFETs”. *European Solid-State Device Research Conference (ESSDRC)* 2.September (2012), pp. 334–337.

[131] T. Rudenko et al. “Experimental study of transconductance and mobility behaviors in ultra-thin SOI MOSFETs with standard and thin buried oxides”. *Solid-State Electronics* 54.2 (2010), pp. 164–170.

[132] S. Vitusevich and I. Zadorozhnyi. “Noise spectroscopy of nanowire structures: fundamental limits and application aspects”. *Semiconductor Science and Technology* 32.4 (2017), p. 043002.

[133] Y. Akue Allogo et al. “1/f noise in 0.18 nm technology n-MOSFETs from subthreshold to saturation”. *Solid-State Electronics* 46.7 (2002), pp. 977–983.

[134] N. Clément et al. “A silicon nanowire ion-sensitive field-effect transistor with elementary charge sensitivity”. *Applied Physics Letters* 98.1 (2011), pp. 2009–2012. arXiv: 1010.1232.

[135] K. Bedner et al. “Investigation of the dominant 1/f noise source in silicon nanowire sensors”. *Sensors and Actuators B: Chemical* 191 (2014), pp. 270–275.

[136] N. K. Rajan et al. “Limit of detection of field effect transistor biosensors: Effects of surface modification and size dependence”. *Applied Physics Letters* 104.8 (2014), p. 84106.

[137] S. Chen, A. Van Den Berg, and E. T. Carlen. “Sensitivity and detection limit analysis of silicon nanowire bio(chemical) sensors”. *Sensors and Actuators, B: Chemical* 209 (2015), pp. 486–489.

[138] A. M. Janssens et al. “Charge Noise in Liquid-Gated Single-Wall Carbon Nanotube Transistors”. *Nano Letters* 8.2 (2008), pp. 685–688.

[139] L. J. Chen. “Silicon nanowires: The key building block for future electronic devices”. *Journal of Materials Chemistry* 17.44 (2007), pp. 4639–4643.

[140] H. Zhu. “Semiconductor Nanowire MOSFETs and Applications”. In: *Nanowires - New Insights*. Vol. i. tourism. InTech, 2017, p. 13.

[141] H. J. Fan, P. Werner, and M. Zacharias. “Semiconductor nanowires: From self-organization to patterned growth”. *Small* 2.6 (2006), pp. 700–717.

[142] A. Zhang and C. M. Lieber. “Nano-Bioelectronics”. *Chemical Reviews* 116.1 (2016), pp. 215–257. arXiv: 15334406.

[143] M. Schulz. “Coulomb energy of traps in semiconductor space-charge regions”. *Journal of Applied Physics* 74.4 (1993), pp. 2649–2657.

[144] C. R. Helms and B. E. Deal, eds. *The Physics and Chemistry of SiO2 and the Si-SiO2 Interface 2*. Boston, MA: Springer US, 1993.

[145] H. H. Mueller, D. Wörle, and M. Schulz. “Evaluation of the Coulomb energy for single-electron interface trapping in sub-μm metal-oxide-semiconductor field-effect transistors”. *Journal of Applied Physics* 75.6 (1994), pp. 2970–2979.

[146] N. B. Lukyanchikova et al. “Impact of the free electron distribution on the random telegraph signal capture kinetics in submicron n -metal–oxide–semiconductor field-effect transistors”. *Applied Physics Letters* 73.17 (1998), pp. 2444–2446.

[147] E. Simoen et al. “Single Defect Studies by Means of Random Telegraph Signals in Submicron Silicon MOSFETs”. *Solid State Phenomena* 69-70 (1999), pp. 467–472.

[148] N. Lukyanchikova et al. “Influence of the substrate voltage on the random telegraph signal parameters in submicron n -channel metal-oxide-semiconductor field-effect transistors under a constant inversion charge density”. *Applied Physics A: Materials Science & Processing* 70.3 (2000), pp. 345–353.

[149] S. Pud et al. “Single trap dynamics in electrolyte-gated Si-nanowire field effect transistors”. *Journal of Applied Physics* 115.23 (2014).

[150] E Simoen and C Claeys. “Substrate bias effect on the capture kinetics of random telegraph signals in submicron p-channel silicon metal–oxide–semiconductor transistors”. *Applied Physics Letters* 66.5 (1995), pp. 598–600.

[151] H. H. Mueller and M. Schulz. “Conductance modulation of submicrometer metal–oxide–semiconduct field-effect transistors by single-electron trapping”. *Journal of Applied Physics* 79.8 (1996), p. 4178.

[152] L. K. Vandamme, D. Sodini, and Z. Gingl. “On the Anomalous Behavior of the Relative Amplitude of Rts Noise”. *Solid-State Electronics* 42.6 (1998), pp. 901–905.

[153] F.-C. Hung, J.-J. Sze, and S.-G. Wuu. *Transistors, methods of manufacturing thereof, and image sensor circuits with reduced rts noise.* 2006. arXiv: `arXiv:1208.5721`.

[154] W Shockley and W. T. Read. “Statistics of the Recombinations of Holes and Electrons”. *Physical Review* 87.5 (1952), pp. 835–842.

[155] R. N. Hall. “Electron-Hole Recombination in Germanium”. *Physical Review* 87.2 (1952), p. 387.

[156] M Schulz and A Karmann. “Single, individual traps in MOSFETs”. *Physica Scripta* T35 (1991), pp. 273–280.

[157] M Schulz and A Karmann. “Individual, attractive defect centers in the SiO2-Si interface of μm-sized MOSFETs”. *Applied Physics A* 52.2 (1991), pp. 104–111.

[158] A. G. Milnes. *Deep impurities in semiconductors.* New York, 1973.

[159] W. Shockley and W. T. Read. “Statistics of the Recombination of Holes and Electrons”. *Physical Review* 87.46 (1952), pp. 835–842.

[160] D. Wilson et al. *Effects of radiation on semiconductor materials and devices.* Tech. rep. New York 10038: Bell Telephone Laboratories, 1966.

[161] N. Clément et al. “One-by-one trap activation in silicon nanowire transistors.” *Nature communications* 1.May (2010), p. 92. arXiv: `1010.4456`.

[162] Y.-W. Huang et al. “Real-time and label-free detection of the prostate-specific antigen in human serum by a polycrystalline silicon nanowire field-effect transistor biosensor.” *Analytical chemistry* 85.16 (2013), pp. 7912–8.

[163] N. P. Dasgupta et al. “25th anniversary article: Semiconductor nanowires - Synthesis, characterization, and applications”. *Advanced Materials* 26.14 (2014), pp. 2137–2183.

[164] B. A. Danilchenko et al. “High-field quasi-ballistic transport in AlGaN/GaN heterostructures”. *Applied Physics Letters* 104.7 (2014), p. 72105.

[165] F. Léonard and J Tersoff. “Novel Length Scales in Nanotube Devices”. *Physical Review Letters* 83.24 (1999), pp. 5174–5177.

[166] S. Mott N. F. (Nevill Francis) and R. W.R. W. Gurney. *Electronic processes in ionic crystals.* 2nd ed. Oxford : Clarendon Press, 1948.

[167] M. A. Lampert and R. B. Schilling. “Chapter 1 Current Injection in Solids: The Regional Approximation Method”. In: *Injection Phenomena.* Ed. by R. K. Willardson, A. C.B.T. S. Beer, and Semimetals. Vol. 6. Elsevier, 1970, pp. 1–96.

[168] A. A. Grinberg et al. “Space-charge-limited current in a film”. *IEEE Transactions on Electron Devices* 36.6 (1989), pp. 1162–1170.

[169] A. A. Talin et al. “Unusually Strong Space-Charge-Limited Current in Thin Wires”. *Physical Review Letters* 101.7 (2008), p. 76802.

[170] A Rose. “Space-Charge-Limited Currents in Solids”. *Physical Review* 97.6 (1955), pp. 1538–1544.

[171] P. Lehnen et al. “Enhanced spin-orbit scattering length in narrow AlxGa(1-x)N/GaN wires”. *Physical Review B* 76.20 (2007), p. 205307.

[172] R. Calarco et al. “Size-dependent Photoconductivity in MBE-Grown GaN-Nanowires”. *Nano Letters* 5.5 (2005), pp. 981–984.

[173] N. Sanford et al. “Steady-state and transient photoconductivity in c-axis GaN nanowires grown by nitrogen-plasma-assisted molecular beam epitaxy”. *Journal of Applied Physics* 107.3 (2010), pp. 34314–34318.

[174] B. S. Simpkins et al. “Space-charge-limited currents and trap characterization in coaxial AlGaN/GaN nanowires”. *Journal of Applied Physics* 110.4 (2011), p. 44303.

[175] A. A. Talin et al. “Transport characterization in nanowires using an electrical nanoprobe”. *Semiconductor Science and Technology* 25.2 (2010), p. 24015.

[176] Y Gu and L. J. Lauhon. “Space-charge-limited current in nanowires depleted by oxygen adsorption”. *Applied Physics Letters* 89.14 (2006), p. 143102.

[177] K. Rasool et al. “The role of surface states in modification of carrier transport in silicon nanowires”. *Journal of Applied Physics* 113.19 (2013), p. 193703.

[178] A. D. Schricker et al. “Space charge limited currents and trap concentrations in GaAs nanowires”. *Nanotechnology* 17.10 (2006), pp. 2681–2688.

[179] O Ambacher et al. “Two dimensional electron gases induced by spontaneous and piezoelectric polarization in undoped and doped AlGaN/GaN heterostructures”. *Journal of Applied Physics* 87.1 (1999), pp. 334–344.

[180] K. M. van Vliet and J. R. Fassett. “Fluctuations due to electronic transitions and transport in solids”. In: *Fluctuation Phenomena in Solids*. Ed. by R. E. Burgess. New York, London: Academic Press, 1965.

[181] R. A.R. A. Smith. *Semiconductors*. 2nd ed. Cambridge ; New York : Cambridge University Press, 1978.

[182] S. A. Vitusevich et al. “Origin of noise in AlGaN/GaN heterostructures in the range of 10-100MHz”. *Journal of Applied Physics* 99.7 (2006), p. 73706.

[183] J. Neugebauer and C. G. Van de Walle. “Gallium vacancies and the yellow luminescence in GaN”. *Applied Physics Letters* 69.4 (1996), pp. 503–505.

[184] T Mattila and R. M. Nieminen. “Point-defect complexes and broadband luminescence in GaN and AlN”. *Physical Review B* 55.15 (1997), pp. 9571–9576.

[185] S. Vitusevich et al. “Improvement of interface properties of AlGaN/GaN heterostructures under gamma-radiation”. *Applied Surface Science* 255 (2008), pp. 784–786.

[186] V. V. Korotyeyev et al. “Steady-state and high-frequency electron transport in GaN nanowires”. *Journal of Physics: Conference Series* 647 (2015), p. 12033.

[187] H.-Y. Chen et al. “Size-dependent photoconductivity and dark conductivity of m-axial GaN nanowires with small critical diameter”. *Applied Physics Letters* 95.14 (2009), p. 143123.

[188] R. Calarco et al. "Surface-induced effects in GaN nanowires". *Journal of Materials Research* 26.17 (2011), pp. 2157–2168.

[189] S. A. Vitusevich et al. "Separation of hot-electron and self-heating effects in two-dimensional AlGaN/GaN-based conducting channels". *Applied Physics Letters* 82.5 (2003), pp. 748–750.

[190] X.-G. Zhang and S. T. Pantelides. "Theory of Space Charge Limited Currents". *Physical Review Letters* 108.26 (2012), p. 266602.

[191] S. A. Vitusevich et al. "Excess low-frequency noise in AlGaN/GaN-based high-electron-mobility transistors". *Applied Physics Letters* 80.12 (2002), pp. 2126–2128.

[192] A Balandin et al. "Flicker noise in GaN/Al/sub 0.15/Ga/sub 0.85/N doped channel heterostructure field effect transistors". *IEEE Electron Device Letters* 19.12 (1998), pp. 475–477.

[193] S Rumyantsev et al. "Low-frequency noise in AlGaN/GaN heterojunction field effect transistors on SiC and sapphire substrates". *Journal of Applied Physics* 87.4 (2000), pp. 1849–1854.

[194] J. A. Garrido et al. "Low-frequency noise and mobility fluctuations in AlGaN/GaN heterostructure field-effect transistors". *Applied Physics Letters* 76.23 (2000), pp. 3442–3444.

[195] S. Kogan. *Electronic Noise and Fluctuations in Solids*. Cambridge: Cambridge University Press, 1996.

[196] V. A. Kochelap et al. "Theory of surface noise under Coulomb correlations between carriers and surface states". *Journal of Applied Physics* 92.9 (2002), pp. 5347–5358.

[197] N. B.N. B. Lukyanchikova and B. K. Jones. *Noise research in semiconductor physics*. Amsterdam : Gordon and Breach Science Publishers, 1996.

[198] V Bareikis et al. "Hot electron noise and diffusion in micron-long n+-n-n+ structures of GaAs and InP". *Lithuanian Journal of Physics* 27 (1987), pp. 511–21.

[199] R. Afrasiabi. "Silicon Nanoribbon FET Sensors: Fabrication, Surface Modification and Microfluidic Integration". PhD thesis. KTH Royal Institute of Technology, Stockholm, 2016.

[200] K. S. McKeating, A. Aubé, and J.-F. Masson. "Biosensors and nanobiosensors for therapeutic drug and response monitoring". *Analyst* 141.2 (2016), pp. 429–449.

[201] H. Craighead. "Future lab-on-a-chip technologies for interrogating individual molecules". *Nature* 442.7101 (2006), pp. 387–393.

[202] S. S. Bhinder and P. Dadra. "Application of nanostructures and new nano particles as advanced biomaterials". *Asian Journal of Chemistry* 21.10 (2009), pp. 167–171.

[203] T. Wu et al. "Experimental Study of the Detection Limit in Dual-Gate Biosensors Using Ultrathin Silicon Transistors". *ACS Nano* 11.7 (2017), pp. 7142–7147.

[204] F. V. Gasparyan et al. "Low-Frequency Noise in Field-Effect Devices Functionalized With Dendrimer/Carbon- Nanotube Multilayers". *IEEE Sensors Journal* 11.1 (2011), pp. 142–149.

[205] F. Gasparyan et al. "Double-gated Si NW FET sensors: Low-frequency noise and photoelectric properties". *Journal of Applied Physics* 120.6 (2016).

[206] M Bruno et al. “First-principles optical properties of silicon and germanium nanowires”. *Surface Science* 601.13 (2007), pp. 2707–2711.

[207] R. van Hal, J. Eijkel, and P. Bergveld. “A novel description of ISFET sensitivity with the buffer capacity and double-layer capacitance as key parameters”. *Sensors and Actuators B: Chemical* 24.1-3 (1995), pp. 201–205.

[208] Y. Cui et al. “Nanowire Nanosensors for Highly Sensitive and Selective Detection of Biological and Chemical Species”. *Science* 293.5533 (2001), pp. 1289–1292.

[209] G. H. Bolt. “Determination of the Charge Density of Silica Sols”. *The Journal of Physical Chemistry* 61.9 (1957), pp. 1166–1169.

[210] S. Chen et al. “Al 2 O 3 /Silicon NanoISFET with Near Ideal Nernstian Response”. *Nano Letters* 11.6 (2011), pp. 2334–2341.

[211] L. Mu et al. “Direct, Rapid, and Label-Free Detection of Enzyme–Substrate Interactions in Physiological Buffers Using CMOS-Compatible Nanoribbon Sensors”. *Nano Letters* 14.9 (2014), pp. 5315–5322.

[212] B. Reddy et al. “High-k dielectric Al2O3 nanowire and nanoplate field effect sensors for improved pH sensing”. *Biomedical Microdevices* 13.2 (2011), pp. 335–344.

[213] R Kühnhold and H Ryssel. “Modeling the pH response of silicon nitride ISFET devices”. *Sensors and Actuators B: Chemical* 68.1 (2000), pp. 307–312.

[214] O. Knopfmacher et al. “Nernst limit in dual-gated Si-nanowire FET sensors”. *Nano Letters* 10.6 (2010), pp. 2268–2274.

[215] S. Zafar et al. “Optimization of pH sensing using silicon nanowire field effect transistors with HfO2as the sensing surface”. *Nanotechnology* 22.40 (2011), p. 405501.

[216] M.-P. Lu, M.-Y. Lu, and Y.-J. Wang. “Low-frequency electrical fluctuations in metal–nanowire–metal phototransistors”. *Nanotechnology* 25.28 (2014), p. 285202.

[217] N Elfström and J Linnros. “Sensitivity of silicon nanowires in biosensor applications”. *Journal of Physics: Conference Series* 100.5 (2008), p. 52042.

[218] A. Tarasov et al. “True reference nanosensor realized with silicon nanowires”. *Langmuir* 28.25 (2012), pp. 9899–9905.

[219] S. Onclin, B. J. Ravoo, and D. N. Reinhoudt. “Engineering Silicon Oxide Surfaces Using Self-Assembled Monolayers”. *Angewandte Chemie International Edition* 44.39 (2005), pp. 6282–6304.

[220] Y Cui et al. “Nanowire nanosensors for highly sensitive and selective detection of biological and chemical species.” *Science* 293.5533 (2001), pp. 1289–1292.

[221] S. Guha Thakurta and A. Subramanian. “Fabrication of dense, uniform aminosilane monolayers: A platform for protein or ligand immobilization”. *Colloids and Surfaces A: Physicochemical and Engineering Aspects* 414 (2012), pp. 384–392.

[222] Y.-L. Wu et al. “Highly sensitive polysilicon wire sensor for DNA detection using silica nanoparticles/γ-APTES nanocomposite for surface modification”. *Sensors and Actuators B: Chemical* 155.2 (2011), pp. 709–715.

[223] A. Nazarov et al., eds. *Functional Nanomaterials and Devices for Electronics, Sensors and Energy Harvesting.* Engineering Materials. Cham: Springer International Publishing, 2014.

[224] D. Passeri et al. “Numerical simulation of ISFET structures for biosensing devices with TCAD tools”. *BioMedical Engineering OnLine* 14.Suppl 2 (2015), S3.

[225] G. Boriani et al. “Evaluation of Myocardial Injury Following Repeated Internal Atrial Shocks by Monitoring Serum Cardiac Troponin I Levels”. *Chest* 118.2 (2000), pp. 342–347.

[226] S. Korff, H. A. Katus, and E. Giannitsis. “Differential diagnosis of elevated troponins”. eng. *Heart (British Cardiac Society)* 92.7 (2006), pp. 987–993.

[227] K. Kim et al. “Silicon nanowire biosensors for detection of cardiac troponin I (cTnI) with high sensitivity”. *Biosensors and Bioelectronics* 77 (2016), pp. 695–701.

[228] T.-W. Lin et al. “Label-free detection of protein-protein interactions using a calmodulin-modified nanowire transistor”. *Proceedings of the National Academy of Sciences* 107.3 (2010), pp. 1047–1052.

[229] S.-P. Lin et al. “A reversible surface functionalized nanowire transistor to study protein–protein interactions”. *Nano Today* 4.3 (2009), pp. 235–243.

[230] E. Stern et al. “Importance of the Debye Screening Length on Nanowire Field Effect Transistor Sensors”. *Nano Letters* 7.11 (2007), pp. 3405–3409.

[231] P.-L. Chiang et al. “Nanowire Transistor-Based Ultrasensitive Virus Detection with Reversible Surface Functionalization”. *Chemistry - An Asian Journal* 7.9 (2012), pp. 2073–2079.

[232] V. A. Sydoruk et al. “Electronic edge-state and space-charge phenomena in long GaN nanowires and nanoribbons”. *Nanotechnology* 28.13 (2017), p. 135204.

[233] Q. Guo et al. “Noise spectroscopy as an equilibrium analysis tool for highly sensitive electrical biosensing”. *Applied Physics Letters* 101.9 (2012).

[234] A Balandin et al. “The fundamental 1/f noise and the Hooge parameter in semiconductor quantum wires”. *IEEE Transactions on Electron Devices* 46.6 (1999), pp. 1240–1244.

[235] L. K. Vandamme, X. Li, and D. Rigaud. “1/f Noise in MOS Devices, Mobility or Number Fluctuations?” *IEEE Transactions on Electron Devices* 41.11 (1994), pp. 1936–1945.

[236] C Wei et al. “Investigation of Low-Frequency Noise in Silicon Nanowire MOSFETs in the Subthreshold Region”. *IEEE Electron Device Letters* 30.6 (2009), pp. 668–671.

[237] M. Kaisti. “Detection principles of biological and chemical FET sensors”. *Biosensors and Bioelectronics* 98.July (2017), pp. 437–448.

[238] Y Kutovyi et al. “Low-frequency noise in Si NW FET for electrical biosensing”. In: *2017 International Conference on Noise and Fluctuations (ICNF)*. IEEE, 2017, pp. 1–4.

[239] H Sato et al. “Differential cellular localization of antioxidant enzymes in the trigeminal ganglion”. *Neuroscience* 248 (2013), pp. 345–358.

[240] J. Navarro-Yepes et al. “Antioxidant gene therapy against neuronal cell death”. *Pharmacology & Therapeutics* 142.2 (2014), pp. 206–230.

[241] S. T. Teoh and S. Y. Lunt. “Metabolism in cancer metastasis: bioenergetics, biosynthesis, and beyond”. *Wiley Interdisciplinary Reviews: Systems Biology and Medicine* 10.2 (2018), e1406.

[242] R. A. Huynh and C. Mohan. *Alzheimer’s Disease: Biomarkers in the Genome, Blood, and Cerebrospinal Fluid*. 2017.

[243] M. Colamartino et al. “A multi-biomarker analysis of the antioxidant efficacy of Parkinson’s disease therapy”. *Toxicology in Vitro* 47 (2018), pp. 1–7.

[244] N. Naumova et al. “Microwave characterization of low-molecular-weight antioxidant specific biomarkers”. *Biochimica et Biophysica Acta - General Subjects* 1863.1 (2019), pp. 226–231.

[245] L. A. H. Shereefa and M. Kumaraswamy. “Reactive oxygen species and ascorbate–glutathione interplay in signaling and stress responses in Sesamum orientale L. against Alternaria sesami (Kawamura) Mohanty and Behera”. *Journal of the Saudi Society of Agricultural Sciences* 15.1 (2016), pp. 48–56.

[246] T. Kaneko et al. “Extracellular field potential recording of single cardiomyocytes in agarose microchambers using microelectrode array”. *Japanese Journal of Applied Physics* 57.3S2 (2018), 03EB03.

[247] J. K. Y. Law et al. “The use of microelectrode array (MEA) to study the protective effects of potassium channel openers on metabolically compromised HL-1 cardiomyocytes”. *Physiological Measurement* 30.2 (2009), pp. 155–167.

[248] F. Santoro et al. “On chip guidance and recording of cardiomyocytes with 3D mushroom-shaped electrodes”. *Nano Letters* 13.11 (2013), pp. 5379–5384. arXiv: arXiv:1011.1669v3.

[249] B. P. Timko et al. “Electrical recording from hearts with flexible nanowire device arrays”. *Nano Letters* 9.2 (2009), pp. 914–918. arXiv: NIHMS150003.

[250] T. Etrych et al. “Fluorescence optical imaging in anticancer drug delivery”. *Journal of Controlled Release* 226 (2016), pp. 168–181.

[251] N. White and R. Errington. “Fluorescence techniques for drug delivery research: theory and practice”. *Advanced Drug Delivery Reviews* 57.1 (2005), pp. 17–42.

[252] E. Bertero and C. Maack. “Calcium Signaling and Reactive Oxygen Species in Mitochondria”. *Circulation Research* 122.10 (2018), pp. 1460–1478.

[253] R. Bravo-Sagua et al. “Calcium Transport and Signaling in Mitochondria”. In: *Comprehensive Physiology*. Hoboken, NJ, USA: John Wiley & Sons, Inc., 2017, pp. 623–634.

[254] M. McKenzie, S. C. Lim, and M. R. Duchen. “Simultaneous Measurement of Mitochondrial Calcium and Mitochondrial Membrane Potential in Live Cells by Fluorescent Microscopy”. *Journal of Visualized Experiments* 119 (2017), pp. 2–7.

[255] B. Hofmann et al. “Light induced stimulation and delay of cardiac activity”. *Lab on a Chip* 10.19 (2010), pp. 2588–2596.

[256] V. Maybeck et al. “Boron-Doped Nanocrystalline Diamond Microelectrode Arrays Monitor Cardiac Action Potentials”. *Advanced Healthcare Materials* 3.2 (2014), pp. 283–289.

[257] K. Kojima, T. Kaneko, and K. Yasuda. “Role of the community effect of cardiomyocyte in the entrainment and reestablishment of stable beating rhythms”. *Biochemical and Biophysical Research Communications* 351.1 (2006), pp. 209–215.

[258] P. Fromherz. “Extracellular recording with transistors and the distribution of ionic conductances in a cell membrane”. *European Biophysics Journal* 28.3 (1999), pp. 254–258.

[259] A. R. Natarajan et al. “Intrinsic cardiac catecholamines help maintain beating activity in neonatal rat cardiomyocyte cultures”. *Pediatric Research* 56.3 (2004), pp. 411–417.

[260] J. C. Kim, M. J. Son, and S. H. Woo. “Regulation of cardiac calcium by mechanotransduction: Role of mitochondria”. *Archives of Biochemistry and Biophysics* 659 (2018), pp. 33–41.

[261] T. L. Rosenbaum Emir. *Neurobiology of TRP Channels*. Ed. by E. Tamara Luti Rosenbaum. 2nd. Boca Raton : CRC Press, 2017.: CRC Press, 2017. Chap. Chapter 9. Pp. 149–185.

[262] M. Franzoso, T. Zaglia, and M. Mongillo. “Putting together the clues of the everlasting neuro-cardiac liaison”. *Biochimica et Biophysica Acta - Molecular Cell Research* 1863.7 (2016), pp. 1904–1915.

[263] N. Tribulova et al. “Disordered myocardial Ca2+homeostasis results in substructural alterations that may promote occurrence of malignant arrhythmias”. *Physiological Research* 65 (2016), S139–S148.

[264] D. Farkas et al. “Simultaneous imaging of cell and mitochondrial membrane potentials”. *Biophysical Journal* 56.6 (1989), pp. 1053–1069.

[265] A. A. Gerencser et al. “Quantitative measurement of mitochondrial membrane potential in cultured cells: Calcium-induced de- and hyperpolarization of neuronal mitochondria”. *Journal of Physiology* 590.12 (2012), pp. 2845–2871.

Personal Publication List

Peer-Reviewed Journals

[1] **I. Zadorozhnyi**, H. Hlukhova, Y. Kutovyi, V. Handziuk, N. Naumova, A. Offenhaeusser, and S. Vitusevich. “Towards pharmacological treatment screening of cardiomyocyte cells using Si nanowire FETs ”, **Biosensors and Bioelectronics**, (**2019**) DOI: 10.1016/j.bios.2019.04.038

[2] M. Petrychuk, **I. Zadorozhnyi**, Y. Kutovyi, S. Karg, H. Riel, and S. Vitusevich, “Noise spectroscopy to study the 1D electron transport properties in InAs nanowires ”, **Nanotechnology**, *30*, 305001, (**2019**) DOI: 10.1088/1361-6528/ab175e

[3] Y. Kutovyi, **I. Zadorozhnyi**, V. Handziuk, H. Hlukhova, N. Boichuk, M. Petrychuk, and S. Vitusevich. “Temperature-Dependent Noise and Transport in Silicon Two-Layer Nanowire FETs”, **Physica Status Solidi B**, 1800636 (**2019**) DOI: 10.1002/pssb.201800636

[4] Y. Kutovyi, **I. Zadorozhnyi**, V. Handziuk, H. Hlukhova, N. Boichuk, M. Petrychuk, and S. Vitusevich. “Liquid-Gated Two-Layer Silicon Nanowire FETs: Evidence of Controlling Single-Trap Dynamic Processes”, **Nano Letters**, *18*(11), 7305-7313 (**2018**) DOI: 10.1021/acs.nanolett.8b03508

[5] F. Gasparyan, **I. Zadorozhnyi**, H. Khondkaryan, A. Arakelyan, and S. Vitusevich. “Photoconductivity, pH Sensitivity, Noise, and Channel Length Effects in Si Nanowire FET Sensors”, **Nanoscale Research Letters**, *13:87* (**2018**) DOI: 10.1186/s11671-018-2494-5

[6] Y. Kutovyi, **I. Zadorozhnyi**, H. Hlukhova, V. Handziuk, M. Petrychuk, A. Ivanchuk, and S. Vitusevich. “Origin of noise in liquid-gated Si nanowire troponin biosensors”, **Nanotechnology**, *29*(17), 175202 (**2018**) DOI: 10.1088/1361-6528/aaaf9e

[7] **I. Zadorozhnyi**, J. Li, S. Pud, H. Hlukhova, V. Handziuk, Y. Kutovyi, M. Petrychuk, and S. Vitusevich. “Effect of Gamma Irradiation on Dynamics of Charge Exchange Processes between Single Trap and Nanowire Channel”, **Small**, *14*(2), 1702516 (**2018**) DOI: 10.1002/smll.201702516

[8] V. Sydoruk, **I. Zadorozhnyi**, H. Hardtdegen, H. Lüth, M. Petrychuk, A. Naumov, V. Korotyeyev, A. Belyaev, and S.Vitusevich. “Electronic edge-state and space-charge phenomena in long GaN nanowires and nanoribbons”, **Nanotechnology**, *28*, 135204 (**2017**) DOI: 10.1088/1361-6528/aa5de3

[9] S. Vitusevich, and **I. Zadorozhnyi**. “Noise spectroscopy of nanowire structures: Fundamental limits and application aspects”, **Semiconductor Science and Technology**, *32*, 043002 (**2017**) DOI: 10.1088/1361-6641/aa5cf3

[10] D. Kireev, **I.Zadorozhnyi**, T. Qiu, D. Sarik, F. Brings, T. Wu, S. Seyock, V. Maybeck, M. Lottner, B. Blaschke, J. Garrido, X. Xie, S. Vitusevich, B. Wolfrum, and A. Offenhäuesser. "Graphene Field-Effect Transistors for In Vitro and Ex Vivo Recordings", **IEEE Transactions on Nanotechnology**, *16*(1), 140-147 (**2017**) DOI: 10.1109/TNANO.2016.2639028

[11] F. Gasparyan, H. Khondkaryan, A. Arakelyan, **I. Zadorozhnyi**, S. Pud, and S. Vitusevich. "Double-gated Si NW FET sensors: Low-frequency noise and photoelectric properties Optimal signal-to-noise ratio for silicon nanowire biochemical sensors Double-gated Si NW FET sensors: Low-frequency noise and photoelectric properties", **Journal of Applied Physics**, *120*(98), 064902 (**2016**) DOI: 10.1063/1.4960704

[12] **I. Zadorozhnyi**, J. Li, S. Pud, M. Petrychuk, and S. Vitusevich. "Single-trap kinetic in Si nanowire FETs: effect of gamma radiation treatment", **MRS Advances**, Available on CJO (**2016**) DOI: 10.1557/adv.2016.347

[13] F. Gasparyan, **I. Zadorozhnyi**, and S. Vitusevich. "Single trap in liquid gated nanowire FETs: Capture time behavior as a function of current", **Journal of Applied Physics**, *117*, 174506 (**2015**) DOI: 10.1063/1.4919816

Conference Publications

[1] V. Handziuk, Y. Kutovyi, H. Hlukhova, **I. Zadorozhnyi**, N. Boichuk, M. Petrychuk, and S. Vitusevich. "Nanoimprint Technology for Liquid-Gated Si Nanowire FET Biosensors: Noise Spectroscopy Analysis" **Accepted for 25$^{\text{th}}$ International Conference on Noise and Fluctuations (ICNF 2019)**, *Neuchâtel, Switzerland 2019*

[2] Y. Kutovyi, **I. Zadorozhnyi**, S.H. Kim, T. Fujii, A. Offenhäusser, S. Vitusevich, and N.Clement. "Noise in single-trap punctual nanobiosensors" **Accepted for International Conference on Noise and Fluctuations (ICNF 2019)**, *Neuchâtel, Switzerland 2019*

[3] Y. Kutovyi, **I. Zadorozhnyi**, N. Naumova, N. Boichuk, M. Petrychuk, and S. Vitusevich. "Ascorbate detection using single trap phenomena in two-layer Si NW FETs" **Accepted for International Conference on Noise and Fluctuations (ICNF 2019)**, *Neuchâtel, Switzerland 2019*

[4] Y. Kutovyi, **I. Zadorozhnyi**, V. Handziuk, N. Boichuk, H. Hlukhova, M. Petrychuk, and S. Vitusevich. "Single Electron Dynamics in Liquid-Gated Two-Layer Silicon Nanowire Structures: Towards Biosensing with Enhanced Sensitivity" **International Conference on Solid State Devices and Materials (SSDM-2018)**, *Tokyo, Japan 2018*

[5] Y. Kutovyi, **I. Zadorozhnyi**, V. Handziuk, H. Hlukhova, M. Petrychuk, N. Boichuk, and S. Vitusevich. "Nanowire field-effect transistor structures for the detection of cardiac biomarkers: troponin and C-reactive protein" **DPG Spring Meeting**, *Berlin, Germany 2018*

[6] Y. Kutovyi, **I. Zadorozhnyi**, V. Handziuk, H. Hlukhova, M. Petrychuk, and S. Vitusevich. "Temperature-dependent noise and transport in two-layer silicon nanowire FETs" **34$^{\text{th}}$ International Conference on the Physics of Semiconductors**, *Montpellier, France 2018*

[7] Y. Kutovyi, **I. Zadorozhnyi**, V. Handziuk, H. Hlukhova, M. Petrychuk, and S. Vitusevich. "The impact of biomolecules binding on low-frequency noise in Si NW FET biosensors" **8th International Conference on Unsolved Problems on Noise (UPON 2018)**, *Gdańsk, Poland 2018*

[8] M. Petrychuk, **I. Zadorozhnyi**, M. Kutovyi, S. Karg, H. Riel, and S. Vitusevich. "1D electron transport in InAs nanowires" **8th International Conference on Unsolved Problems on Noise (UPON 2018)**, *Gdańsk, Poland 2018*

[9] **I. Zadorozhnyi**, H. Hlukhova, Y. Kutovyi, M. Petrychuk, V. Sydoruk, V. Handziuk, and S. Vitusevich. "Analysis of charge states in GaN-based nanoribbons using transport and noise studies" **24th International Conference on Noise and Fluctuations (ICNF 2017)**, *Vilnius, Lithuania 2017*

[10] Y. Kutovyi, **I. Zadorozhnyi**, H. Hlukhova, M. Petrychuk, and S. Vitusevich. "Low-frequency noise in Si NW FET for electrical biosensing" **24th International Conference on Noise and Fluctuations (ICNF 2017)**, *Vilnius, Lithuania 2017*

[11] **I. Zadorozhnyi**, Y. Kutovyi, H. Hlukhova, M. Petrychuk, and S. Vitusevich. "Hooge's parameter in Si NW FET with different widths" **24th International Conference on Noise and Fluctuations (ICNF 2017)**, *Vilnius, Lithuania 2017*

[12] **I. Zadorozhnyi**, and S. Vitusevich. "Signal-to-noise ratio enhancement using the gate coupling effect" **46th European Solid-State Device Research Conference (ESSDERC 2016)**, *Lausanne, Switzerland 2016*

[13] **I. Zadorozhnyi**, S. Pud, M. Petrychuk, and S. Vitusevich. "Features of the gate coupling effect in liquid-gated Si nanowire FETs" **23th International Conference on Noise and Fluctuations (ICNF 2015)**, *Xian, China 2016*